UNIAXIAL TENSILE TESTING TECHNIQUE TO OBTAIN SOFTENING RESPONSE OF ULTRA-HIGH PERFORMANCE CONCRETE UNDER CONFINING PRESSURES

A Thesis
Presented to
The Academic Faculty

By

Brett David Reichard

In Partial Fulfillment
Of the Requirements for the Degree
Master of Science in Civil Engineering

Georgia Institute of Technology

August 2015

UNIAXIAL TENSILE TESTING TECHNIQUE TO OBTAIN SOFTENING RESPONSE OF ULTRA-HIGH PERFORMANCE CONCRETE UNDER CONFINING PRESSURES

Approved by:

Dr. Lauren Stewart, Advisor
School of Civil Engineering
Georgia Institute of Technology

Dr. Lawrence Kahn
School of Civil Engineering
Georgia Institute of Technology

Dr. David Frost
School of Civil Engineering
Georgia Institute of Technology

Date Approved: May 8, 2015

ACKNOWLEDGEMENTS

I would like to first thank all of the professors at the Georgia Institute of Technology, especially within the Civil and Environmental Engineering Department that I have had the opportunity to learn from during my undergraduate and graduate studies. They have not only built my engineering foundation, but have instilled the importance of critical thinking and the responsibility that comes with calling oneself an engineer. I also owe much gratitude to Dr. Julian Rimoli and Dr. David Frost for having faith in an undergraduate student and giving him the opportunity to participate in their research.

In regards to this thesis, I want to express my thanks to all of the researchers who have developed and studied fracture mechanics of concrete. Much of my understanding on the subject was gained through their reports, theses, and academic articles. Special thanks are necessary to the following people who made this thesis possible:

Dr. Lauren Stewart, my advisor, for the great opportunity and for her guidance, support, and patience throughout the entire project.

Dr. Lawrence Kahn and Dr. David Frost, my committee members, for their time, support, and detailed remarks.

Mr. Ken Morrill and Mr. Mark Weaver at Karagozian & Case for their work and advice on the project.

U.S. Army Engineer Research and Development Center for sponsoring and funding the project.

Mr. James Huggins and Kyle Brindley for their continued assistance in the Hi-Bay Laboratory at the Manufacturing Research Center (MARC Building).

Guillaume Pelletier for his help in the transitioning phase of the project from the University of California, San Diego to Georgia Tech.

Catherine Benson for her help with recreating figures and for her patience, support, and understanding during this process.

I could not have completed this thesis without the unconditional love and support from my parents, Jim and Linda, and sister, Kristen. To my family goes my sincere love and deepest appreciation. This thesis is dedicated to them.

TABLE OF CONTENTS

LIST OF TABLES

LIST OF FIGURES

LIST OF SYMBOLS AND ABBREVIATIONS

List of Symbols

A	current output (amperage) from controller to regulate servo-valves at Georgia Tech
C	strain rate
c_1, c_2	material constants for Reinhardt et al.'s nonlinear softening function
D	displacement of: (a) machine actuator or (b) hollow plunger cylinder, used to apply loading at Georgia Tech
d	diameter of cylindrical specimen
d_{max}	maximum size aggregates
E	tensile elastic modulus of concrete, unless stated otherwise
E_r	displacement error signal to allow for closed-loop testing at Georgia Tech
e	eccentricity of loading
F	axial force, designation used in multiple references
f_{cc}	cube compression strength of concrete
f_{st}	ultimate tensile strength of concrete for split cylinder/Brazilian test
f_t	ultimate tensile strength of concrete for flexural and direct tensile tests
f_c'	compressive strength of concrete
G_f	fracture energy of concrete, defined as the area under the stress - crack opening curve
h	height distance between the front and rear perimeter cracks at the start of ligament bending, described by Van Mier for fixed boundary phenomenon
k_0	stiffness of lower steel posts, machine actuator, lower wedge grip, and lower load train, for uniaxial test setup design
k_1	stiffness of upper load train, upper wedge grip, load cell, machine crosshead, and upper steel posts, for uniaxial test setup design
k_2	stiffness of donut-shaped piece, hydraulic plunger cylinder, and crosshead channel, for uniaxial test setup design
k_s	stiffness of test specimen, for uniaxial test setup design
k_{sys_0}	system stiffness for Phase II, Test Type 0 of experimental program
$k_{sys\_1,2}$	system stiffness for Phase II, Test Type 1 & 2 of experimental program
L_C	characteristic size of the structure, defined as the smallest dimension of the cross section where a crack will likely initiate and propagate
L_{st}	length of cylindrical concrete specimen for split cylinder/Brazilian test
l_{ch}	characteristic length of material, used as a measure of brittleness
l_{meas}	measured gage length
M_{sec}	secondary moment, defined as the closing bending moment resulting from use of fixed boundaries during uniaxial tensile testing
P	axial force, designation used in multiple references

P_R	residual load marking the end of perimeter cracking and beginning of ligament bending, described by Van Mier for fixed boundary phenomenon
P_{max}	maximum axial force, designation used by Van Mier for fixed boundary phenomenon
P_{st}	maximum applied load during split cylinder / Brazilian test
Q	hydraulic flow from servo-valves to regulate machine actuator and hydraulic cylinder plunger displacement at Georgia Tech
R_s	fractal roughness, defined as fractured surface area divided by projected area
SD_E	standard deviation of elastic modulus of concrete
SD_{ft}	standard deviation of ultimate tensile strength of concrete for flexural and direct tensile tests
SD_{st}	standard deviation of ultimate tensile strength of concrete for splitting tensile/Brazilian test
t	time, used in loading rate determinations
V	voltage output from controller to regulate servo-valve at Georgia Tech
W_o/C	water-cement ratio
w	crack opening displacement ahead of crack tip
w_1	crack width ahead of crack tip at which the tensile stress has fallen to zero
w_c	maximum crack opening displacement at end of softening diagram
α	fixed value dependent on material and test type, used in the combination of stress and strain for feedback and load rate determination
β	level of minor compressive stresses in true triaxial tests (0, 0.05, and 0.1)
δ	axial displacement, for uniaxial tensile test
δ_0	residual deformation at the ultimate tensile stress point on the axial stress-deformation curve
δ_{ax}	axial displacement, for tensile test under confining pressure
$\delta_{ax,0}$	axial displacement due to hydrostatic preload, for tensile test under confining pressure
δ_e	elastic deformation outside the fracture zone at any point on the axial stress-deformation curve
δ_p	deformation at the ultimate tensile stress point on the axial stress-deformation curve
$\dot{\delta}$	axial displacement rate
ε	axial strain, axial displacement divided by measured gage length, for uniaxial tensile test
$\varepsilon_1, \varepsilon_2, \varepsilon_3$	principal strains under multi-axial loadings
$\varepsilon_x, \varepsilon_y$	strain along the x and y-axis for three-jack solution control
σ	nominal axial stress, load divided by original area
σ_0	circumferential stress of hydrostatic preload, for tensile test under confining pressure
$\sigma_1, \sigma_2, \sigma_3$	principal stresses under multi-axial loadings
σ_{ax}	nominal axial stress, for tensile test under confining pressure

σ_{rad}	circumferential stress, for tests only under confining pressure
σ_{cp}	applied compressive preloading stress
σ_p	ultimate tensile stress of concrete for direct tensile tests, designation used in multiple references
φ_{op}, φ_{ip}	out-of-plane and in-plane-rotations
ϑ	temperature at which uniaxial tension test is performed

List of Abbreviations

ACI	American Concrete Institute
AE	acoustic emissions
ASTM	American Society for Testing and Materials
CT	compact tension
CM	centering mechanism
ERDC	US Army Corps of Engineers' Research and Development Center
FA	fixed adapter
FCM	fictitious crack model
FEM	finite element method
FRC	fiber reinforced concrete
GFRC	glass fiber reinforced concrete
GT	Georgia Institute of Technology
HPC	hydraulic plunger cylinder
HPFRCC	high performance fiber reinforced cementitious composites
HSHDC	high strength high ductility concretes
K&C	Karagozian & Case, Inc.
LC	lightweight concrete
LCSS	linear combination of sample stress and strain
LVDT	linear variable differential transformer
MTS	Material Testing Systems
NC	normal weight concrete
NSC	normal strength concrete
PVC	polyvinyl chloride
SD	sample displacement
TPBT	three point bending test
TMD	testing machine displacement
SIFCON	slurry infiltrated fiber concrete
UCSD	University of California, San Diego
UHPC	ultra-high performance concrete
UHPFRC	ultra-high-performance fiber-reinforced concrete
USBR	United States Bureau of Reclamation
WST	wedge splitting test

SUMMARY

Fracture mechanic theory for normal strength plain concrete has thoroughly been studied over the past decades. Through indirect and direct tensile testing techniques, the post-peak softening response of concrete has been established and utilized in finite element method (FEM) models to improve analysis simulations and to better understand concrete tensile behavior. However for more intricate concrete materials (e.g. fiber reinforced, high performance) under complex loading conditions, the required fracture properties are extremely limited and in need of further investigation.

Considering this lack of research, the objective of this thesis was to develop a uniaxial tensile testing technique to attain the post-peak softening response for ultra-high performance concrete (UHPC) under confining pressure. This particular multi-axial behavior is valuable in improving material models for US Army applications into hardened target structures.

To meet the goal of this thesis, a detailed literature review was initially performed. Understanding the development and background behind basic concrete fracture mechanic models as well as the previous approaches and techniques that have been used in performing uniaxial tensile tests, allowed this researcher to properly analyze the work completed earlier in the experimental program. A new testing methodology was then developed which enabled for the testing frame itself to apply a stiffening force, while an external hydraulic plunger cylinder (HPC) performed the uniaxial tensile test. Eight tests were performed on UHPC specimens with half maintaining stability throughout their entirety. The positive and negative aspects of these tests were analyzed and improvements were described which would provide increased testing stability and accuracy of measurements.

This unique testing scheme enables for tensile testing under confining pressures in the US Army Corps of Engineers' Engineer Research and Development Center (ERDC) compression-only pressure vessel. In addition, the developed testing scheme can be implemented into typical testing frames to perform stability-critical uniaxial tensile tests on concrete specimens.

CHAPTER 1: INTRODUCTION

Concrete is one of the most widely used structural, building materials. It is relatively inexpensive with readily available constituent materials, provides great fire resistance and durability, and has large compressive strengths. However, its tensile capacity is low, roughly one-tenth of that in compression. Because of this, concrete design in the past, and even still in some large structures today, was based on an elastic, zero tensile capacity approach (*Figure 1.1a)*. In actuality, under uniaxial tension, concrete is a quasibrittle material that exhibits a non-linear, post-peak softening response similar to that shown in *Figure 1.1c*. It has notable tensile toughness and energy dissipation ability, which is typically not taken into consideration for design. The post-peak tensile strength is provided from crack-face bridging. Bridging can result from friction, aggregate crack interference which can leave undamaged ligaments between overlapping cracks, or from fiber inclusion [2:203-207]. This response falls under the realm of fracture mechanics and is directly related to crack initiation and energy release during crack propagation. While the utilization of this toughness may be insignificant in typical building design, it is valuable in improving the analysis of dynamic and repeated (i.e. fatigue) loadings, high-performance concretes, bar anchorage, punching shear, penetration simulations, and thus is essential for improving modeling capabilities.

The development of the fictitious crack model (FCM) in 1976 enabled for an adequate parameterization of the softening response of concrete. The nonlinear

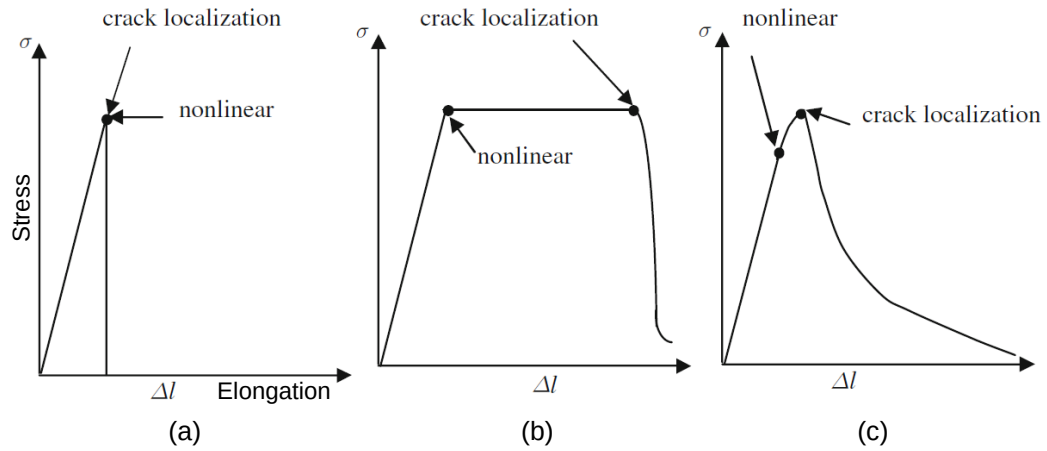

Figure 1.1: *Stress-displacement under uniaxial tension for different material types: (a) brittle, (b) ductile, and (c) quasibrittle (modified from [1:21])*

softening curve as well as the FCM parameters can be used to update concrete finite element method (FEM) models, such as the smeared crack model and concrete damage plasticity approach utilized in FEM analysis programs (e.g. Abaqus, DIANA, LS-DYNA, etc.) [3, 4, 5:367-387]. Various modeling techniques for simulating the nonlinear behavior are advancing as computational systems are improving. For example, the FCM parameters have been implemented to create complicated FEM models to more accurately predict behavior of reinforced concrete members strengthened with carbon fiber sheets [6].

The nonlinear tensile properties of varying types of concrete have been thoroughly researched utilizing both direct and indirect, tensile testing techniques. However in the field of multi-axial behavior, the tensile softening response of concrete is extremely limited and in need of exploration for modeling purposes. The US Army Corps of Engineers' Engineer Research and Development Center (ERDC) is interested in characterizing tensile post-peak softening properties for ultra-high performance concrete (UHPC), similar to Cor-Tuf, under confining pressure. During triaxial compression testing using an in-house pressure vessel, this specific UHPC remained intact even when the axial compressive force was relieved. Since their specific pressure vessel is only capable of applying axial compressive forces, the tensile softening under confining pressure was unable to be examined.

This particular multi-axial behavior is valuable in improving current material models in FEM simulations for US Army applications into hardened target structures among other applications. In a joint effort with Karagozian & Case (K&C), the Georgia Institute of Technology (GT) has researched and developed a uniaxial testing procedure for eventual implementation into ERDC's triaxial pressure vessel, similar to *Figure 1.2*. The purpose of this thesis was to develop a novel uniaxial tensile testing scheme for concrete specimens and to determine whether GT uniaxial testing can be used to implement into ERDC's triaxial testing system for future extension, multi-axial behavioral investigations. The research scope was limited to a review of concrete's nonlinear tensile behavior as well as ERDC's previous experimentation on UHPC. The methodology undertaken throughout previous and current phases of the project will be discussed, followed by the results from GT's uniaxial tensile testing method. To conclude, this method is analyzed and discussed for future implementation into ERDC's triaxial testing system.

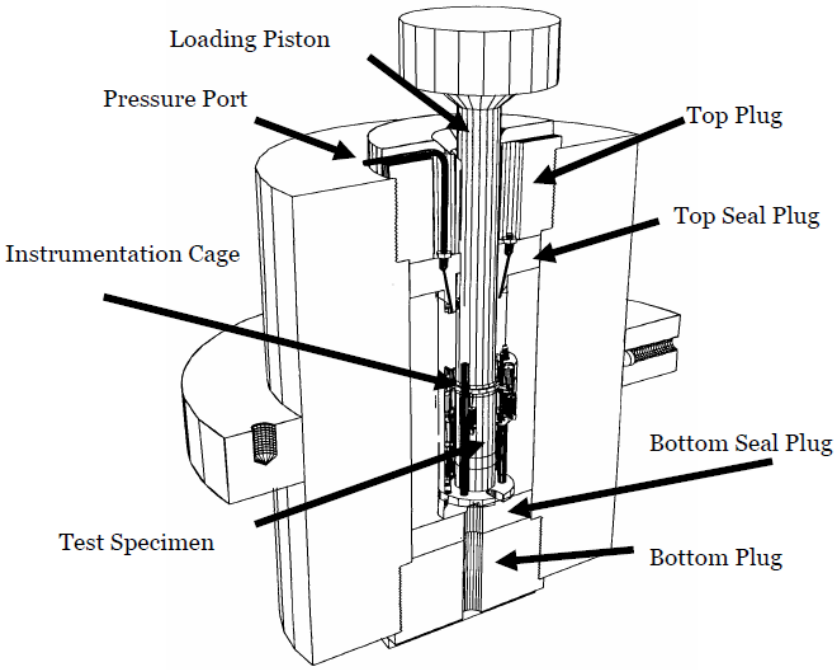

Figure 1.2: *ERDC Pressure Vessel Schematic (from [7])*

CHAPTER 2: LITERATURE REVIEW

In what follows is a literature review on the development of the FCM and the effectiveness of different tensile testing techniques to accurately capture the tension softening response that is required for the model. Since this project utilizes the direct tension test method, a further detailed and up-to-date literature review of the specific method was essential in order to understand the complexities in determining concrete's post-peak softening curve and the factors that affect it. The current state of multi-axial research on concrete softening curves and past work performed on UHPC is also reviewed.

2.1 DEVELOPMENT OF FRACTURE MECHANIC THEORY FOR CONCRETE

Various fracture mechanic models have been derived throughout the past century based on the nonlinear zones that occur near the crack tip for differing material behavior. *Figure 2.1* shows the overall size and shape of these zones for linear elastic, nonlinear plastic, and nonlinear quassibrittle materials (e.g. concrete). Experimental results have validated this nonlinear fracture process zone in concrete through acoustic emission (AE), as shown in *Figure 2.2,* and x-ray techniques [9]. *Figure 2.2b* shows that once the lower energy events are filtered out, the progression of AE occurrences reflects that of the nonlinear fracture zone for quasibrittle materials.

Linear elastic fracture mechanics was developed in the early 1900s under the assumption of a small and concentrated nonlinear behavior zone at the crack tip. In the

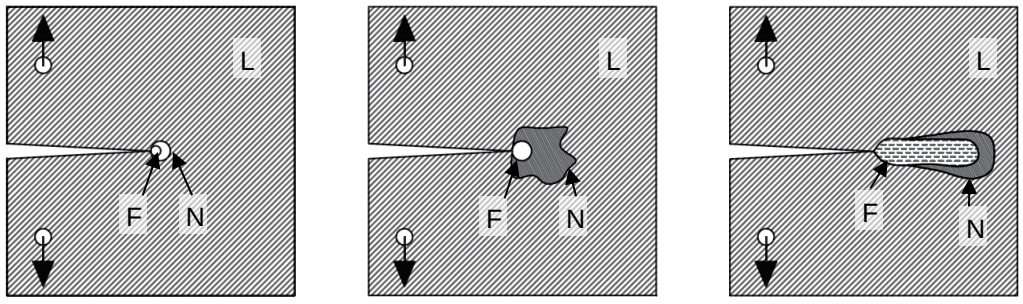

Figure 2.1: *Linear (L), Nonlinear (N), and Fracture Process (F) Zones in (a) Linear elastic, (b) Nonlinear plastic, and (c) Nonlinear quasibrittle materials (after [8:29])*

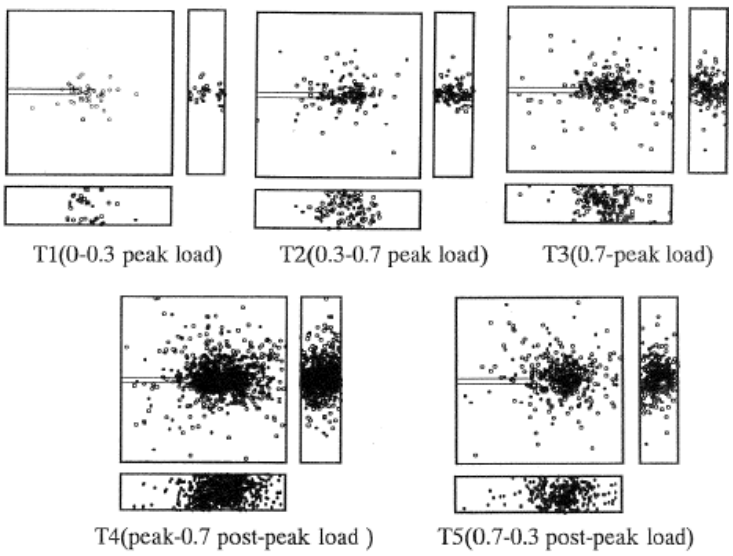

(a)

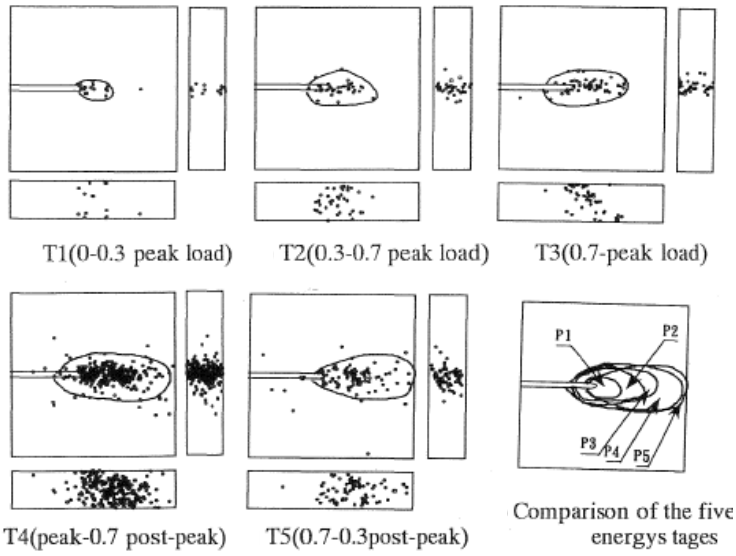

(b)

Figure 2.2: *AE Inspection Results of Concrete Fracture Zone in Tension Specimen, (a) Complete Data, (b) Energy Higher than 1000 $V^2\mu s$ (modified from [9])*

1960s, to account for more ductile materials that exhibit nonlinear plastic behavior, the crack-tip opening displacement method and J-integral approach were established [1:9-18]. These elastic plastic fracture mechanic models were much better suited for analyzing concrete fracture and have been applied to determine the tension softening response in cementitious composites [10]. While adequate for some applications, it was not until the development of the FCM, an improvement on the cohesive crack method

[11], by Hillerborg, Modeer, and Petersson, were the nonlinear mechanics for concrete truly quantified and thus able to be simulated.

The FCM was proposed in 1976 on the basis of energy absorption per unit crack area. As the tip of a crack begins to reach its ultimate tensile strength, f_t, the crack starts to propagate and loses its cohesive stress capability. As shown in *Figure 2.3,* from Hillerborg et al. original proposal, the larger the crack width, w, the lower the cohesive stress. This is true up until a width of w_1, at which the crack can no longer support any stress [12]. The FCM splits the tensile failure of concrete into two separate

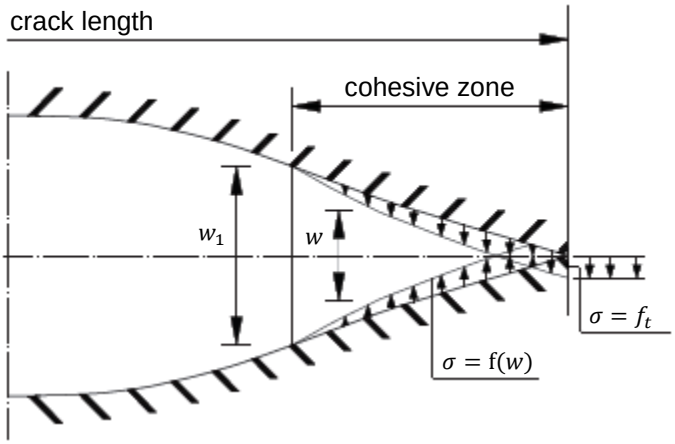

Figure 2.3: *Hillerborg et al. Proposed Fictitious Crack Model (after [12])*

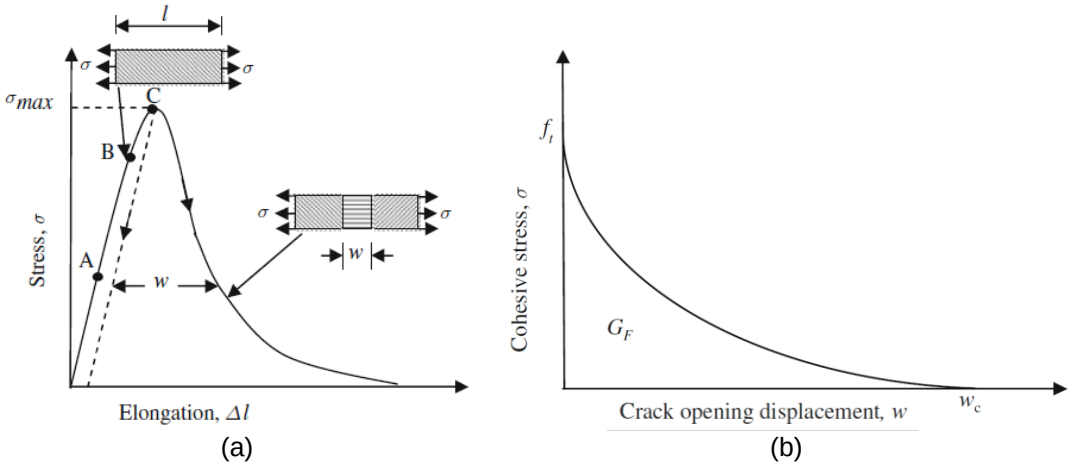

Figure 2.4: *Fictitious Crack Model Processes and Parameters: (a) Total Stress Displacement Curve and (b) Stress-Crack Opening Displacement Curve (from [1:17, 1:32])*

processes as exhibited by the specimen representations in *Figure 2.4a.* One of these is the mostly linear, stress-strain relationship that occurs outside the fracture zone. The other process is the nonlinear, stress-crack displacement relationship that occurs in the fracture zone (*Figure 2.4b).* The area under this tensile stress versus nonlinear crack opening response is used to determine the fracture energy parameter, G_f, in the FCM.

The total stress-displacement curve of concrete shown in *Figure 2.4a* can be explained in relation to points A, B, and C. From the start of the test up until point A (~30% of f_t), the propagation of microcracks is assumed negligible. Between points A and B (~80% of f_t), microcracking increases but is randomly distributed so that a uniform tensile stress remains along the entire length of the specimen. The microcracks begin to localize between points B and C (f_t) into a macrocrack. In this range the strain distribution along the specimen is no longer uniform and crack propagation occurs with increasing load. Upon reaching point C, a localized fracture zone develops. As the uniaxial test continues past the peak load, the fracture zone width increases while the concrete material outside unloads elastically [1:17-19].

Utilizing the modulus of elasticity in tension, E, along with the previously mentioned material parameters (G_f and f_t), the brittleness of the material could be quantified into a single property called the characteristic length, l_{ch}. Hillerborg et al. defined this property in *Eq. 2-1* [12]. Typical characteristic lengths in mm for various materials are: glass = 10^{-6} [13:60, 14], hardened cement paste = 5-15 [13:60, 15], mortar = 100-200 [13:60, 15], high strength concrete (42-103MPa) = 300-500 [16], normal concrete = 200-500 [13:60, 15], and dam concrete (e.g. d_{max}= 38mm) = 700 [17].

$$l_{ch} = \frac{E G_f}{{f_t}^2} \qquad (2\text{-}1)$$

In his PhD thesis, Petersson examined the results of applying linear-elastic, elastic-plastic, and nonlinear (i.e. FCM) fracture mechanics to cementitious materials. He concluded that the FCM was clearly the most accurate approach, while the others were unsuitable methods resulting in conflicting results [18:55-99]. After many tensile tests he proposed a more realistic relationship between stress and crack displacement than the linear trend previously assumed by Hillerborg et al [18:151-169]. His bi-linear approximation was determined to be suitable for most normal concretes and is shown compared to the linear relationship in *Figure 2.5.* Since its development, the FCM has

been altered and adjusted into specific models for a wide variety of unique conditions [1:25-30]. More recently, Van Mier has proposed a four stage fracture model as a possible successor to the FCM. Instead of a single post-peak softening phase, Van Mier splits the response into two stages: (1) Macrocrack propagation and (2) Bridging, which is limited to the tail end of the softening diagram. The latter can be described for typical aggregate bridging in plain concrete or aggregate and fiber bridging in fiber-reinforced concrete [2:197-211]. However in all expansions and improvements of the FCM model, the parameters to characterize the tensile softening response of concrete have remained of utmost importance. They are necessary to incorporate into FEM models, which may lead to better predictions of true concrete structural behavior.

The FCM developed by Hillerborg et al. was described for the tensile opening mode of fracture, Mode I. In fracture mechanics three modes exist to characterize crack propagation: Mode I, Mode II (in-plane-shearing), and Mode III (out-of -plane shearing). These are illustrated in *Figure 2.6*. While the FCM was intended for Mode I loadings, the developers saw no limitations in applying it to the other modes or combinations of these. After an extensive review of research performed on Mode II and Mode III fracture in concrete, Van Mier determined that in practice Mode I is the most significant. Results showed that even under Mode II, Mode III, and mixed mode experiments, direct tensile mechanisms (Mode I) seemed to govern on the micro-scale [5:114-132]. Therefore to adequately characterize concrete fracture, the parameters in the FCM model are most important to be determined for crack opening (i.e. Mode I loadings).

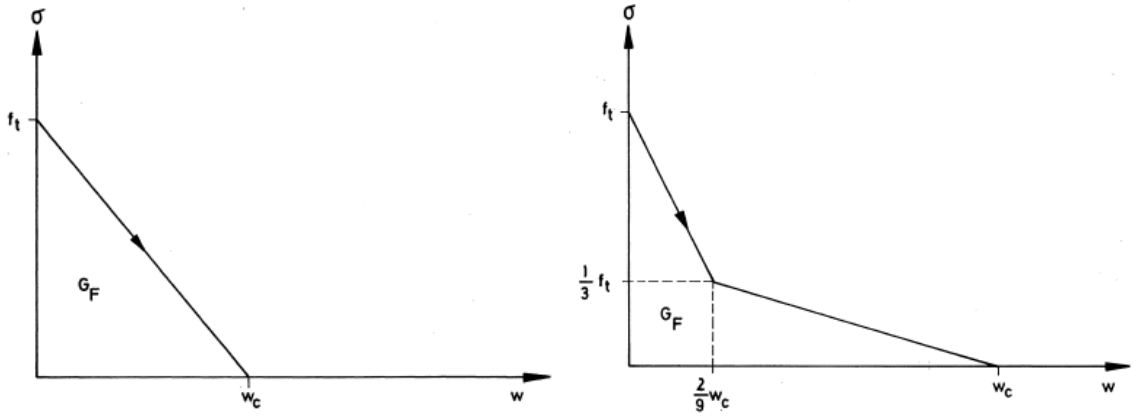

Figure 2.5: *Hillerborg et al. Linear Approximation vs. Petersson 2-Line Approximation for stress-crack displacement curve (from [18:56-57])*

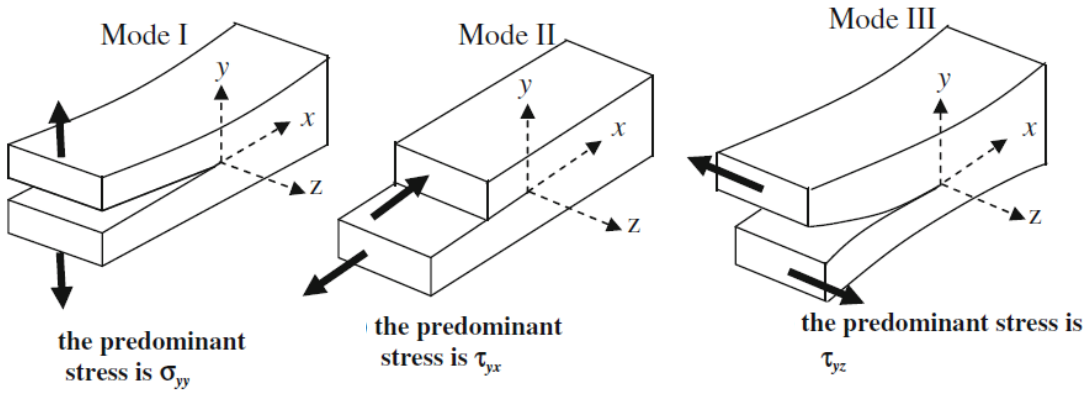

Figure 2.6: *Fracture Modes in Fracture Mechanics (from [1:10])*

2.2 BASIC TENSILE TESTING TECHNIQUES

Tensile tests of concrete are carried out in multiple ways: split cylinder/Brazilian, flexural (e.g. three-point bending), compact tension, wedge splitting, and direct/uniaxial tension tests. The first four methods are indirect methods, meaning a non-tensile loading is applied to gain an understanding of tensile capacities; the latter is a direct method. All of the methods have their shortcomings, but it is widely acknowledged that the uniaxial tensile test is the most accurate and direct in gaining concrete's true response under tensile stress.

2.2.1 Split-Cylinder/Brazilian Test

The split-cylinder test was officially introduced in 1943 at the 5th meeting of the Brazilian Association for Technical Rules by Professor Fernando L.L.B. Carneiro [19]. It is one of the most widely used methods to determine tensile strength of concrete due to its simplicity. In brief, a vertical compressive force is applied perpendicular to the cylindrical axis of the specimen introducing a tensile force perpendicular to the applied load. The load is increased until the specimen ruptures. *Figure 2.7* contains a series of schematics that show a representation of the test setup as well as force and stress states that develop on a specimen during testing. A detailed procedure is covered in ASTM C496 [21]. Based on the assumption of linearly elastic behavior, the tensile strength can be determined by:

$$f_{st} = \frac{2P_{st}}{\pi L_{st} d} \qquad (2\text{-}2)$$

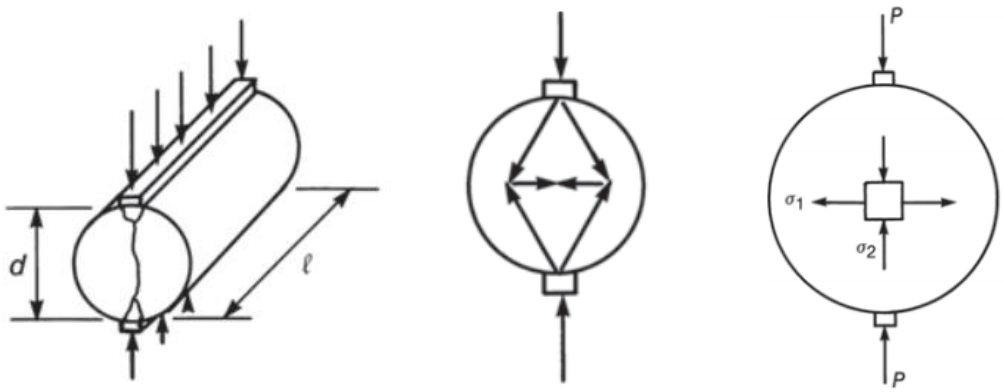

Figure 2.7: *Split Cylinder Test Schematics (from [20:60])*

The split-cylinder method is a good approximation of tensile strength, but due to its instability and non-uniform, steep stress gradient, attaining a softening response and ultimately the total fracture energy needed for the fictitious crack model would be difficult. Because of this, early experiments in the field had to utilize other methods.

2.2.2 Three Point Bend Test and other Indirect Methods

When the FCM was developed, computing speed and overall machine stiffness were rarely adequate to perform a stable direct tensile test, which is the only test that can determine all required parameters for the method. Because of this Hillerborg et al. developed a three point bend test (TPBT) on a notched beam to indirectly determine the fracture energy parameter [22, 23]. While not necessary, Hillerborg et al. advised the use of a high stiff load frame and close-loop test for the most accurate and stable results. For the tensile strength determination and elastic modulus, the Brazilian test mentioned above was still used. *Figure 2.8* contains a schematic of the typical TPBT layout.

Like any experiment, the TPBT has its shortcomings. These include shape and size dependency, strict support requirements, self-weight effects, and the use of global response and a nonuniform, linear stress-gradient to inversely measure activity near the crack tip. Over the years, the issues on the TPBT were examined, and in some cases, procedures were introduced to mitigate these issues. A true material parameter should be independent of specimen size, however the TPBT exhibits an increase in G_f with increasing specimen size [24, 25]. Two solutions for this problem are the size-effect method [26] and hinge model [27], which enable G_f to be determined independently of

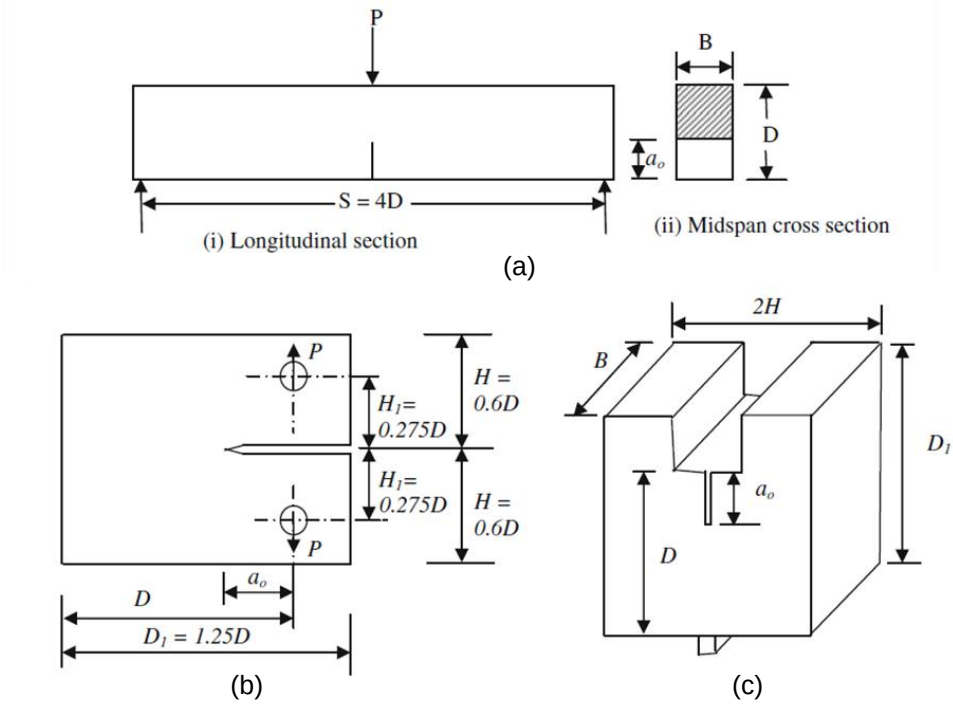

Figure 2.8: *Indirect Tensile Methods: (a) Three-point Bending Test, (b) Compact Tension Test, and (c) Wedge Splitting Test Specimens (from [1:23])*

the shape and size of the test specimen. One of the requirements of the TPBT is frictionless supports (i.e. rollers) [5:188-189]. It was determined that even when using rollers, the effects from rolling friction were significant [28]. This error will always be present during experimentation. Self-weight introduces uncontrollable load to the test, which may lead to instability. As one would expect, this effect is worse for larger beams. To negate the self-weight, a counterweight can be added as a cantilever over the roller supports [18:115-123, 29]. TPBT uses global responses to measure something as local as crack propagation, which results in questionable accuracy and reliability. One technique devised to improve the issue in relation to tension softening curves of mortar was the incremental displacement collocation method, which utilizes both global and local displacements [30]. This method has since been applied to plain concrete [31].

In place of the original proposed TPBT, other indirect methods have been utilized to capture concrete's softening response. Four-point bending tests, similar to the ASTM standards [32, 33], have been used so that a support would not be in-line with the fracture zone [34:33-37, 34:124-138]. Two relatively smaller scale testing methods typically used are compact tension (CT) [10, 35] and wedge splitting tests (WST) [1], which are also displayed in *Figure 2.8*. These smaller scale tests help limit the higher

stresses that are exhibited in the extreme fibers of large beam tests compared to that of uniform tests.

One additional limitation of these inverse procedures is their inability to be implemented for multi-axial loading situations. Under these circumstances a direct uniaxial tensile test must be utilized.

2.2.3 Uniaxial Tensile Test

Uniaxial or direct tensile tests are generally agreed to be the most representative tests for determining the parameters needed to characterize concrete in fracture mechanics. Unlike splitting tensile, TPBT, compact tension, and others discussed in the previous section, uniaxial tensile tests do not rely on inverse techniques, measure both f_t and G_f in a single test, and also can exhibit a uniform stress distribution over the fracture plane. While advantageous in some respects, the uniaxial tensile test can be difficult to perform correctly. At the time of the development of the FCM, improvements were needed in the fields of computing and electronics before it was to become a viable test.

Figure 2.9 shows a coarse progression of uniaxial tension/compression tests from left to right. Initially only concrete's pre-peak response was able to be determined by loading the machine at a specific rate (*Figure 2.9a)*. These tests did not take into

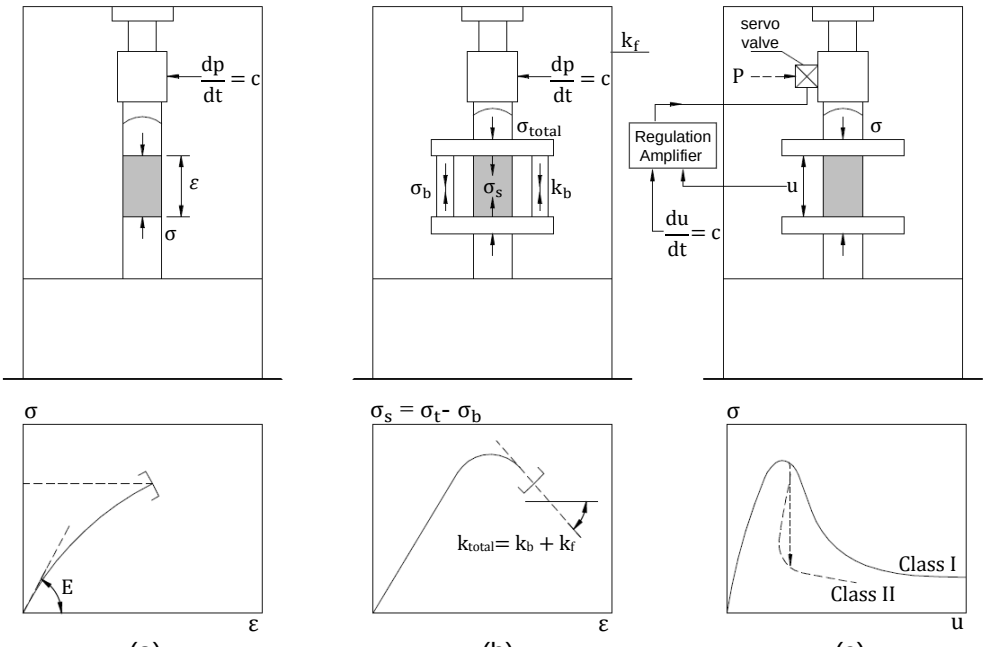

Figure 2.9: *Progression of Uniaxial Tensile Tests (after [5:158])*

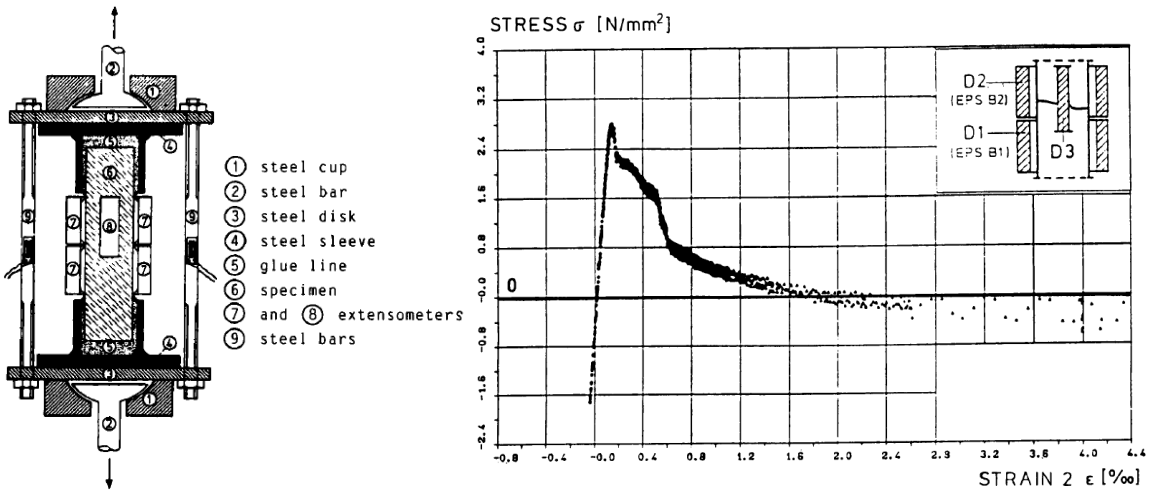

Figure 2.10: *Experimental Test Setup and Results Using Steel Bars for Stability (from [36])*

account local occurrences in the specimen and thus abruptly failed with only speculation into concrete's and other quasibrittle materials' nonlinear softening behavior. To allow for a more stable test, steel bars were placed into the testing setup to take excess load from the sample during crack initiation. While *Figure 2.9b* shows an abrupt end in the stress-strain curve under this technique, Schorn and Berger-Bocker were able to capture it in its entirety [36], and the results are shown in *Figure 2.10*. While their test setup was successful, this method is typically limited, because the total stiffness of the testing machine (i.e. combined stiffness of the load frame and steel bars) is greater than the negative stiffness of the descending branch of the stress-strain curve. More brittle materials are ultimately affected by this due to their steep descending branch and will fail when the two inverse stiffnesses coincide. Failure will also occur if the steel bars are not designed properly [5:158-159]. Petersson developed a unique load frame to increase testing stability that preceded the setup of Schorn and Berger-Bocker (*Figure 2.11)*. Instead of using steel bars to take excess load, he heated large aluminum columns, roughly 4.75 inches in diameter, to induce a tensile force and deformation between two large concrete blocks [18:157-161]. This extremely stiff load frame enabled Petersson to perform many stable uniaxial tension tests and compare the effects of material properties, notches, and reliability. The results from these tests are discussed in later sections.

Uniaxial tensile tests ultimately became feasible with advances in electronics and the development of closed-loop control servo-testing systems [37, 38]. Unlike open-loop

test systems used in the indirect tensile concrete tests, closed-looped systems provided the ability to use feedback from local activity on a specimen to control the loading rate of the testing machine, greatly improving the stability of a test. Basic schematics of open and close-loop tests are shown in *Figure 2.12*. When utilizing closed-loop tests, the softening curves in *Figure 2.9c* can be gained.

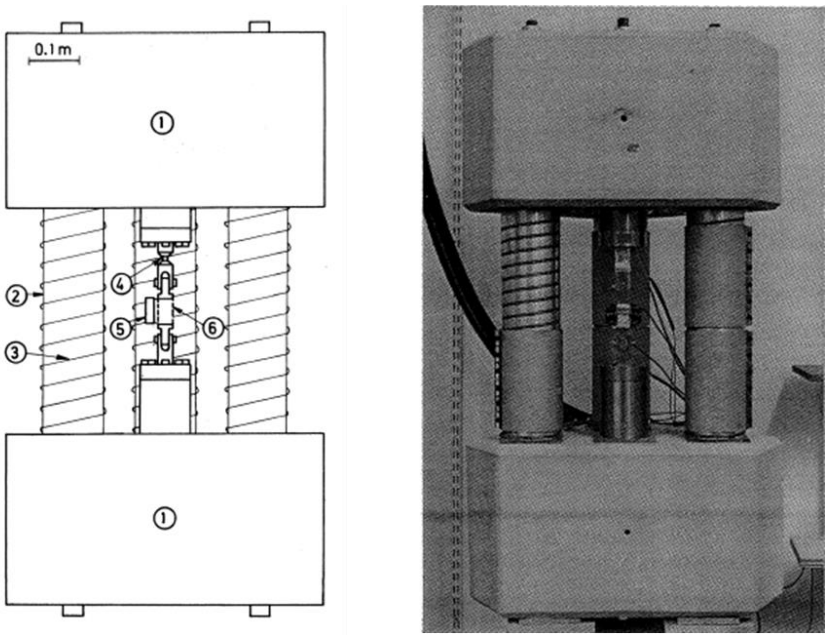

Figure 2.11: *Stiff Testing Frame Developed by Petersson: 1-concrete blocks, 2-aluminum columns, 3-heating coils, 4-strain gauges, 5- inductive deformation transducer, 6-specimen (from [18:158-169])*

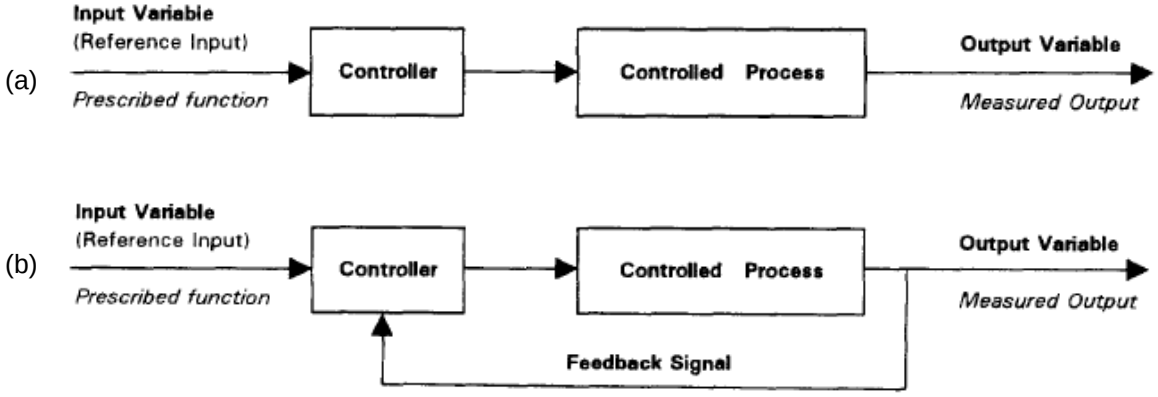

Figure 2.12: *Open-Loop Control (a) vs. Closed-Loop Control (b) Diagrams (from [37])*

It has been shown in compressive rock fracture mechanics that two classes of softening behaviors exist. Class I is characterized as stable fracture propagation where further crack opening is required for a decrease in a sample's load carrying capability. Unstable failure is labeled as Class II behavior, where energy is unable to be removed from the sample resulting in an imbalance in elastic energy [39]. If a test is controlled off of the fracture zone displacement rate, the Class II snap-back effect will never manifest, but instead will see a vertical drop until the test regains stability.

Even with the improvements in controls and electronics, uniaxial tension tests are still complicated with many issues that need to be considered. These issues include: effects of notches, size effects, boundary conditions and their relation to secondary flexure, gripping techniques, material structure, specimen alignment, and environmental conditions [40, 41, 42]. In addition to these, the testing methods and techniques, such as loading rate and control variable selection, also greatly affect the results of uniaxial tensile tests. Understanding the effects of these issues is vital to correctly devise an experiment and interpret results. The next section will look at the specific effects these factors have on the outcome of a uniaxial tension test.

2.3 Factors affecting Softening Response of Uniaxial Tensile Test

2.3.1 Testing Methodology

The tensile softening curve during uniaxial testing is partially a function of the testing procedure. Some of the choices that need to be made are concerned with the length of the gage used to measure the deformations of the fracture process zone, the feedback used to control the experiment, the loading rate, and also temperature.

2.3.1.1 Measured Gage Length

Concrete fracture in tension is dependent on the ability to capture crack propagation and is thus a local phenomenon. Therefore to correctly measure the tensile softening curve, not only is locating the crack location necessary, but the measured length must be small enough. *Figure 2.13a* shows that if the process zone (i.e. fracture zone) is not captured, only the displacements in the elastic portion of the sample will be measured. Once a larger crack forms and begins to propagate, this elastic region will unload with little to no residual strain as shown in curve II. If the crack is caught within the measured zone, the descending branch is dependent on the measuring length as displayed in *Figure 2.13b* for normal strength concrete. While the crack opening contribution remains unchanged under differing measuring lengths, the elastic

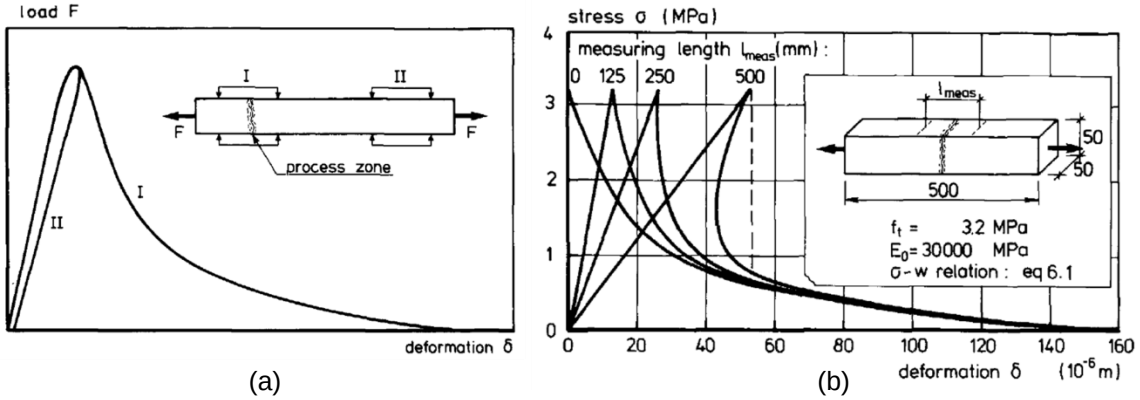

Figure 2.13: *Measured Length Effects, (a) Load-deformation curves for captured and uncaptured fracture zone, (b) Stress-deformation and measured gage length relation (from [34:8-10])*

deformation in this range is altered. If the measured length becomes too large, a "snap-back" behavior occurs. This is due to a greater amount of deformation lost in elastic unloading than gained in crack opening. All in all, the smaller the measured length over the fracture zone, the better the tensile softening curve represents the real material behavior [34:8-10].

2.3.1.2 Control Parameters

The earliest tensile tests were controlled based off force loading. Due to the uncertainty in the ultimate tensile strength, using force control to produce a softening curve in a closed-loop test is impossible unless excess load is removed from the specimen, such as through parallel steel bars. Therefore, stable uniaxial tensile tests are performed utilizing displacement control based off of feedback from LVDT or strain gage readings at slow rates (e.g. 4-6με/min [25], 0.08μm/s [43], 0.007μm/s [44]). Because of this, the measured length is significant. As shown by the dashed line in *Figure 2.13b*, if the controlling length is too large, the test is likely to become unstable. Even if the testing machine remains stable under large control gage lengths, the softening response will not be representative of the true material property. If notches are used to force the fracture zone location, small gage lengths can easily be used as the control parameter. This minimizes the possibility of snap-back behavior and testing instability and is the reason why many tests have been performed with notched specimens.

Tests can be controlled off of average gage readings or specific readings that are at critical locations. Hordijk performed many uniaxial tests on samples with LVDT and

strain gage arrangement as shown in *Figure 2.14*. Some of the tests were controlled off of the average of the two long LVDTs and others used the average readings of the 4 small LVDTs located at the crack corners, which better analyzed three-dimensional crack opening behavior. In addition to these tests, uniaxial tensile tests were performed on single notched plates. *Figure 2.15* shows the results of the experiment and overall

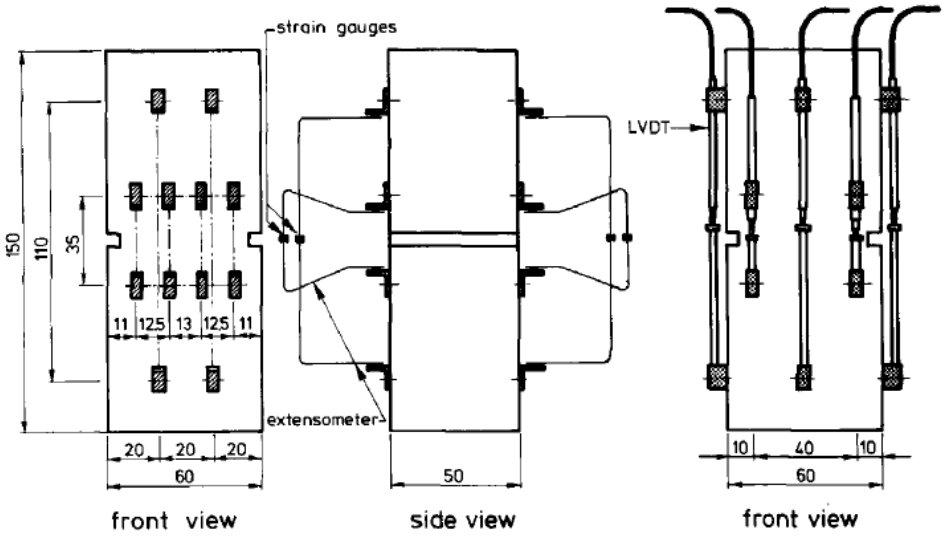

Figure 2.14: *LVDT and Gage Placement on Uniaxial Tension Specimen (from [34:32])*

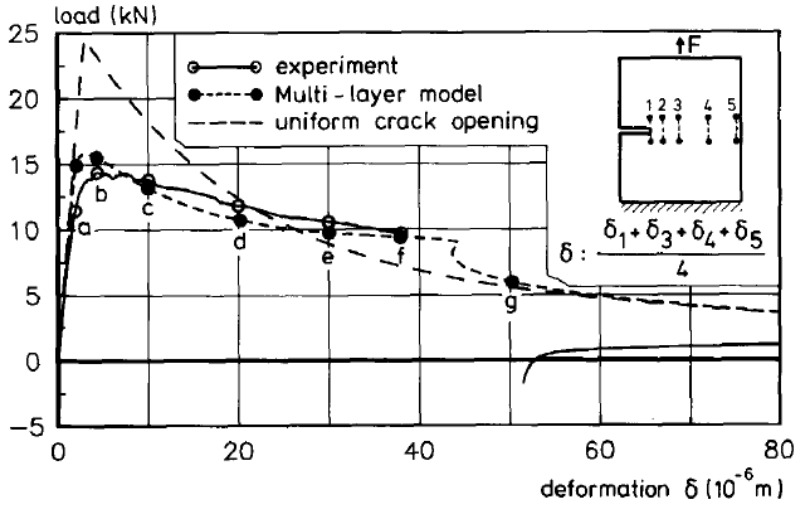

Figure 2.15: *Experimental, Multi-layer model, and Theoretical Load vs. Displacement Curves for Single Notch Tensile (from [34:139])*

layout of LVDTs. During testing, the two LVDTs at location 3 were used to control the test. The results show a snap-back occurring around a deformation of 40 µm. [34:138-144]. If the gauges used at either location 1 or 2 were used to control, this instability may not have occurred.

The typical deformation rate applied during a uniaxial concrete tensile test is extremely slow. To help streamline the amount of time required to perform a test, slower deformation rates can be utilized to control at stability critical stages (e.g. fracture zone initiation and development) and faster rates at less critical zones (e.g. elastic range and gradual end of softening curve) [44]. Also to increase the stability of a test, the deformation rate can be controlled based off of a function of strain and axial stress as shown in *Eq. 2-3,* where ε = axial strain, σ = axial stress, E = young's modulus, C = deformation rate, and t =time [45].

$$\varepsilon - \frac{\sigma}{E} = C \cdot t \qquad (2\text{-}3)$$

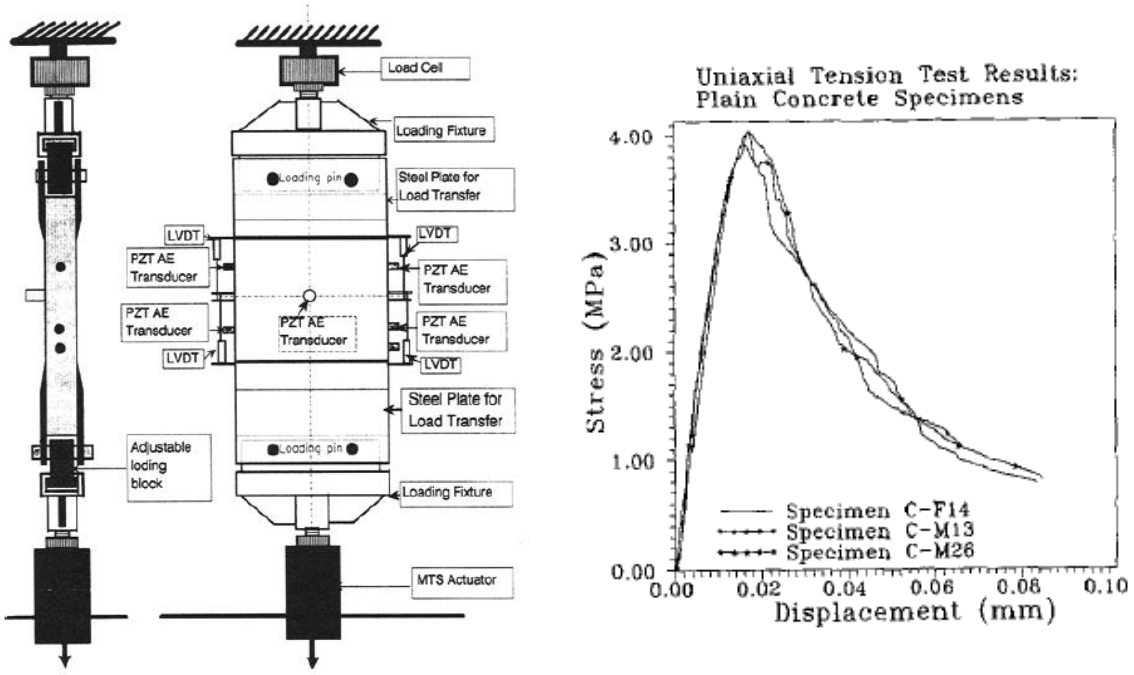

Figure 2.16: *Uniaxial Tension Test Setup and Stress-displacement Results from Li et al. (from [46])*

One downside of using unnotched specimens is the uncertainty in the location of the fracture zone. For a stable uniaxial tensile test, it is vital to capture crack initiation and then control the crack propagation based on a designated displacement rate. To ensure this with unnotched specimens, multiple gauges are needed at varying locations. During testing the gage with the largest displacement rate will be used to control. Li et al. performed uniaxial tensile tests on unnotched specimens using this exact method and were able to capture the entire stress-displacement softening curve for concrete as shown in *Figure 2.16* on the previous page [46]. *Figure 2.17a* displays the displacement

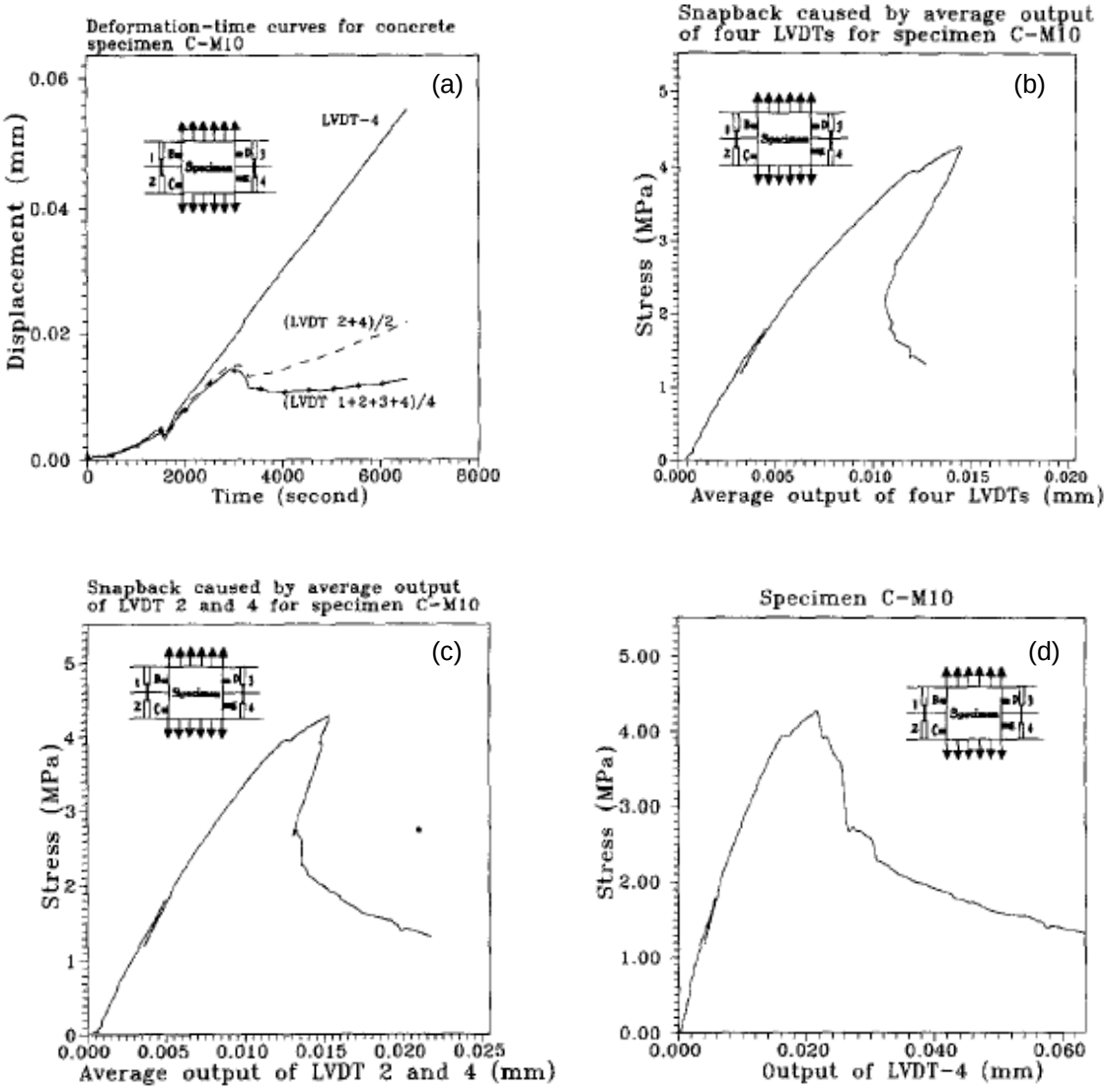

Figure 2.17: *Unnotched Specimen Stress-Displacement Response, (a) LVDTs displacement vs. time, (b)-(d) Stress-displacement for differing measured length combinations (from [46])*

of each of the four LVDTs over the duration of one of their tests. Around a little less than 2000 sec, LVDT 4 began to open at a much faster rate than the others and was thus selected as the controlling length. *Figure 2.17b-d,* show the resulting stress-displacement curves of the average of all four LVDTs, average of LVDT2 and LVDT4, and LVDT4 respectively. It is obvious that the stability of the test was dependent on controlling LVDT4's displacement rate. The snap-back effect is evident in *Figure 2.17b* and *Figure 2.17c.* In addition to controlling off the maximum opening, the above tests also utilized AE techniques (*Figure 2.18)* to assist in selecting the governing LVDT. The

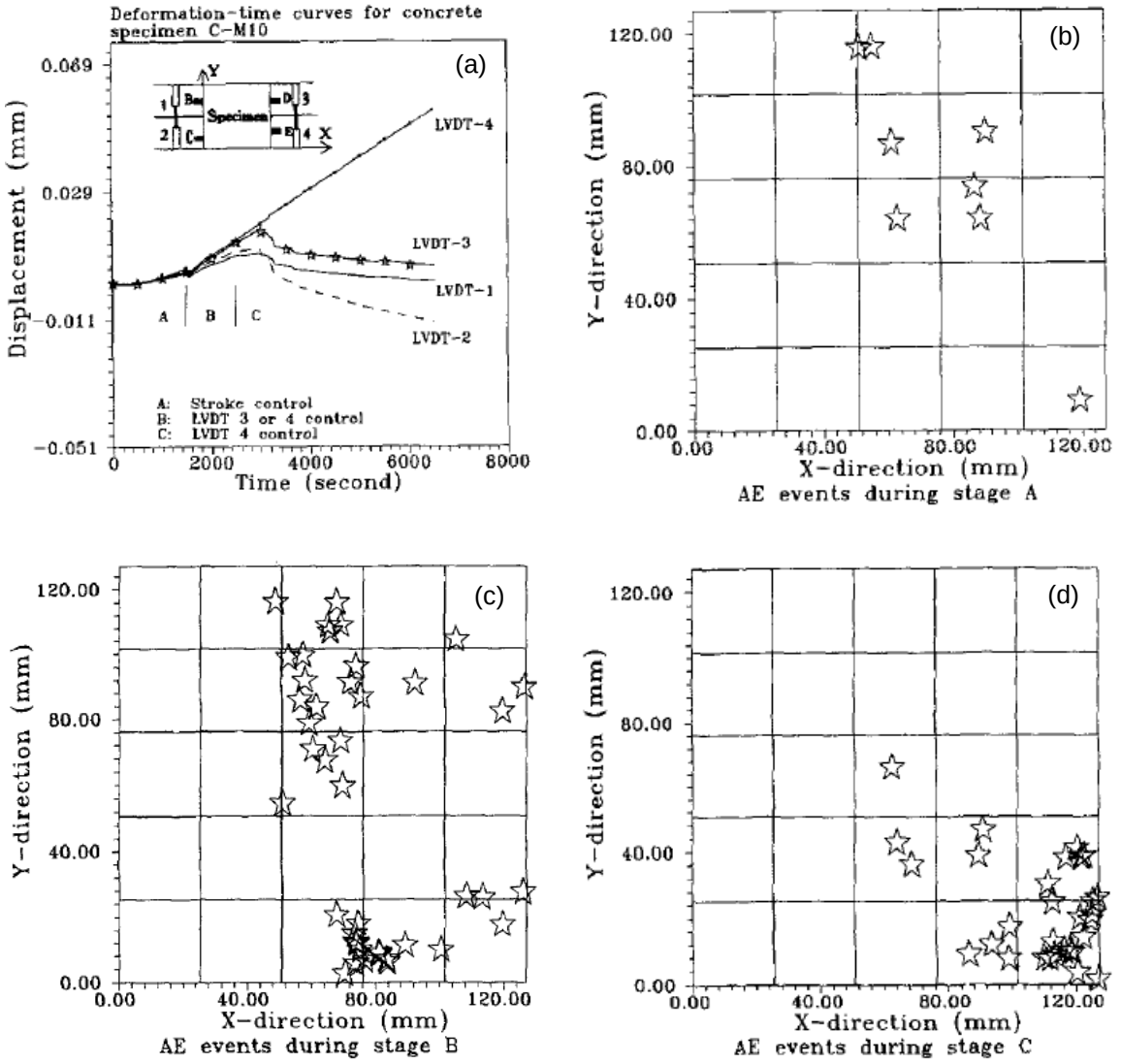

Figure 2.18: *Unnotched Specimen AE Activity, (a) Stages of plots, (b)-(d) Stage A-C respectively (from [46])*

acoustic activity during the test also shows evidence that LVDT4 was indeed the governing gage during crack propagation.

The controlling LVDT during the tests by Li et al. were manually selected based on the LVDT displacement rate and acoustic activity [46]. With current computing and electronic capability all of this can be included in the closed-loop testing code. Eventually visual strain imaging techniques will be improved and can be used in place of LVDTs to select the governing location on an unnotched specimen.

2.3.1.3 Loading Rate

The shape of concrete's stress-displacement or force-displacement softening curve is directly related to the path of crack propagation. If the path is tortuous, the load-displacement curve will reflect more ductile properties. Increasing the load rate results in a more uniform and direct fracture plane, which decreases ductility. Therefore E, f_t, and the slope of the descending branch of the softening curve should increase [47, 48]. This result is presented in *Figure 2.19* and *Figure 2.20a.* The displacement rates of 5E-3 mm/s and 5E-5 mm/s in *Figure 2.19* resulted in fractal roughnesses, R_s, (i.e. fractured surface area divided by projected area) of 1.192 and 1.204 respectively [47].

Differences in softening curves also result from whether the loading is applied monotonically or in a stepwise manner (*Figure 2.20b)*. When the force is relaxed during stepwise loading it allows time for microcracks to propagate in the elastic range. This ultimately decreases the stiffness of the specimen and possibly contributes to multiple crack formation. Therefore stepwise loading will increase ductility during a test [48].

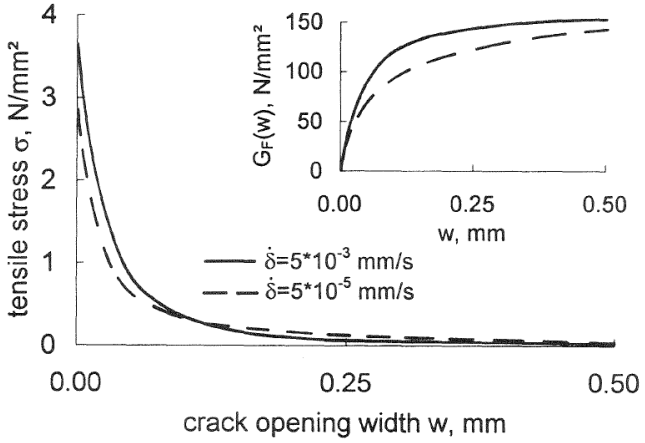

Figure 2.19: *Load Rate Effects on Stress-Displacement Curve (from [47])*

Concrete uniaxial tensile tests typically use low loading rates for stability, however, much faster rates can be applied using numerical examples and FEM models. These models give insight into the effects of high deformation rates on concrete fracture patterns. *Figure 2.21* shows that the ultimate tensile strength of concrete under direct tension increases exponentially with a logarithmic increase in loading rate from static loads to 1500 mm/s. Therefore under slow loading rates, the difference in ultimate tensile strength is slight. *Figure 2.22* shows uniaxial concrete failure patterns under the differing load rates where fracturing is marked in red and yellow. Under lower rates (i.e.

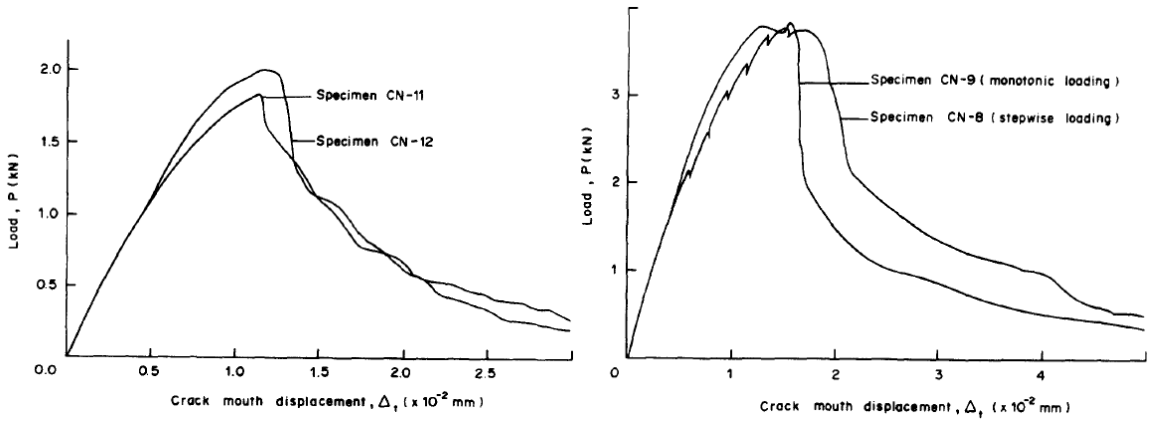

(a) (b)

Figure 2.20: *Loading Effects on Charcoal Specimen Load-displacement Curves, (a) different displacement rates - CN-11 at 1.3E-5 mm/s and CN-12 at 6.5E-5 mm/s, (b) monotonic vs. stepwise loading (from [48])*

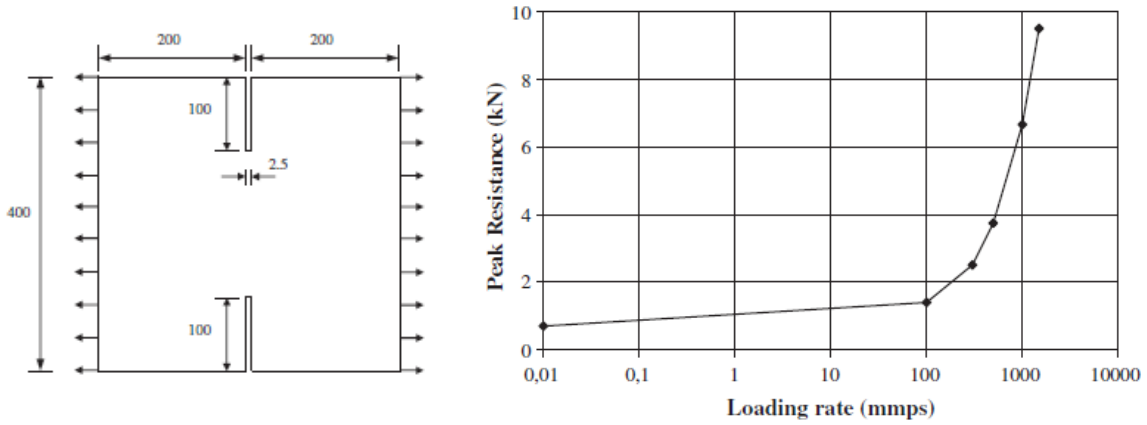

Figure 2.21: *Specimen Dimensions and Effects of High Loading Rates on Tensile Strength (from [49])*

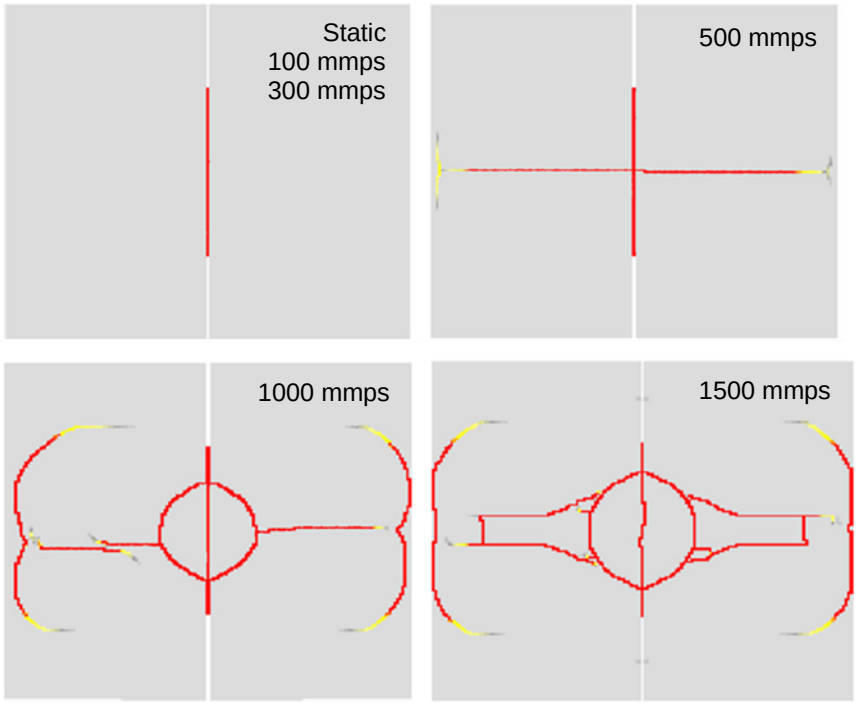

Figure 2.22: *Uniaxial Tension Failure Patterns from Different Loadings (from [49])*

static – 300 mm/s) the failure mode resembled Mode I fracture for the notched specimen. However with increasing loads (i.e. 500 mm/s – 1500 mm/s), the fracture results in an increase in mixed modes and crack branching. These higher load fracture patterns are due to structural inertia forces instead of strain rates. This inertial force prevents Mode I crack propagation and instead splits the single crack into multiple [49].

Dynamic and fatigue loadings also influence the tensile softening curve, but they will not be discussed in detail in this report. However, it has been shown that the tensile softening curves for normal and lightweight concrete are not significantly affected by cyclic loading [34, 43, 49, 50].

2.3.1.4 Temperature

Alternating the environmental temperatures of a test has similar effects as varying the loading rate. Increasing the temperature from 2˚C to 50˚C, results in an increased R_s of 1.169 and 1.205 respectively [47]. This increased fracture roughness produces a more tortuous path for crack propagation, which increases ductility. Therefore with increasing temperature, E, f_t, and the slope of the descending branch of the softening curve should decrease. This effect is shown in *Figure 2.23*.

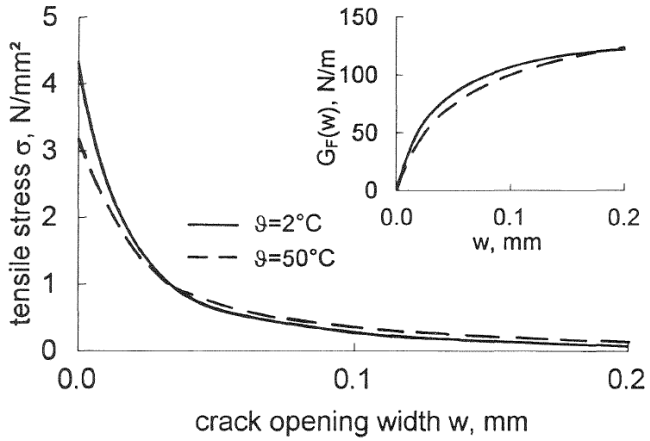

Figure 2.23: *Temperature Effects on Stress-Displacement Curve (from [47])*

2.3.2 Boundary Conditions

The FCM was developed under the assumptions of non-rotating platens and a uniform deformation distribution over the fracture zone, which is extremely difficult to maintain in an experimental test. With fixed boundaries, a bump in the stress-displacement curve will form as shown in *Figure 2.24*. This phenomenon is associated with non-uniform crack growth and redistribution of stresses throughout the specimen during testing. As the crack propagates from one side to the other, it becomes more and more eccentrically loaded introducing a counteracting, secondary moment (i.e. secondary flexure), which will stop the initial crack growth (i.e. crack arrest) and other cracks will begin to initiate. These multiple cracks allow stress transfer in the ligaments between them. This effect is ignored in the FCM and other models for concrete.

Multiple cracks increase the fracture energy by 40% in some cases, due to the more tortuous path for fracture. Also since the boundaries are fixed, the stiffness and stability of the setup increases, which results in a higher measured peak (*Figure 2.24)* [42, 51, 52, 53]. Van Mier et al. thoroughly analyzed the effects of boundary conditions through FEM models. *Figure 2.25* shows some of their results of fixed-fixed (Case C) and pinned-pinned (Case D) boundaries and their effects on both sides of a sample [51]. If the effects of fixed and rotating boundaries are understood, all other scenarios and combinations can be inferred to fall somewhere in between these two extremes.

The bump that occurs in the load-displacement diagram for fixed end conditions was explained by Van Mier and Nooru-Mohamed as a 3-dimensional, two part physical process: “(1) perimeter cracking or discrete cracking along the circumference of the

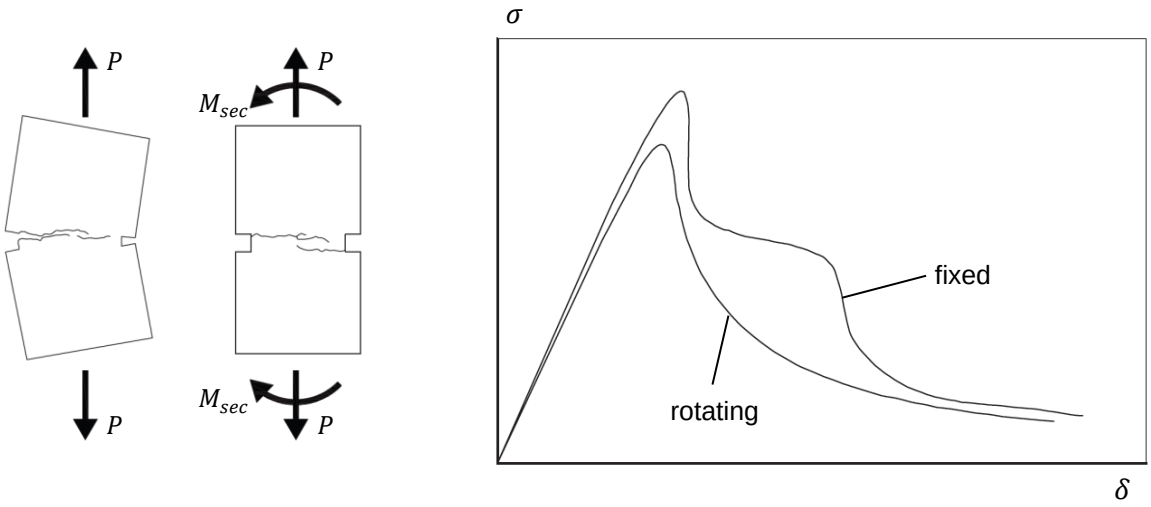

Figure 2.24: *Boundary Effects on Stress-Displacement Curve (after [5:195])*

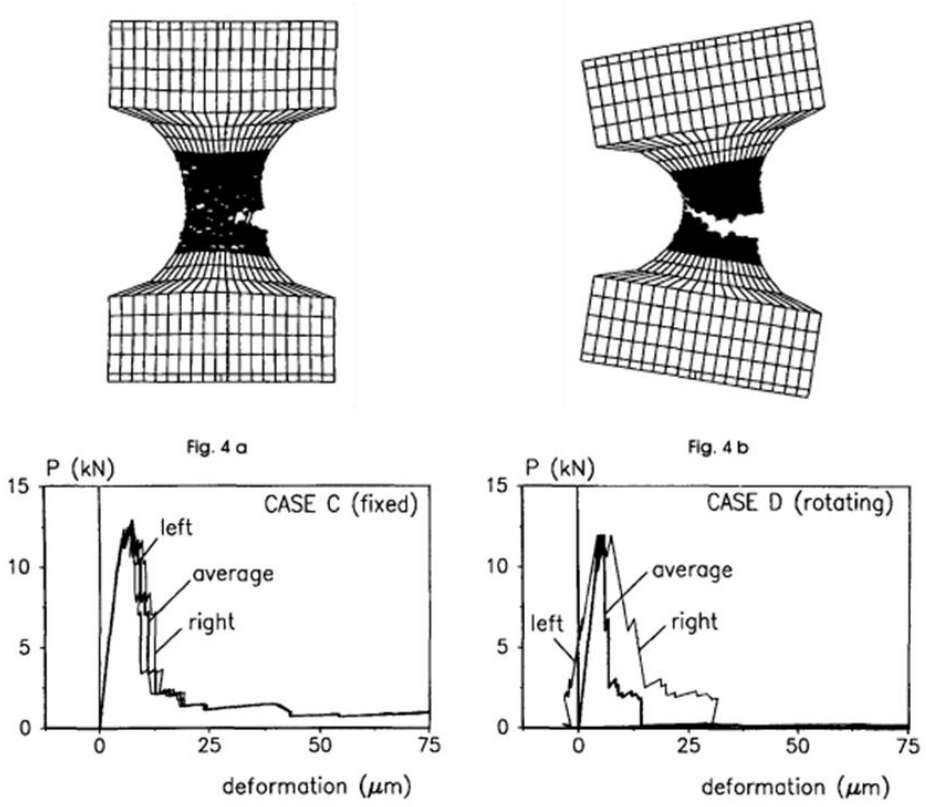

Figure 2.25: *Boundary Effects on Stress-Displacement Curve on Both Sides of Specimen (from [51])*

specimen, and (2) bending of the intact ligaments between the perimeter cracks". Ultimately, complete fracture will occur with the failure of the connecting ligaments [54]. *Figure 2.26* schematically shows on a load-displacement diagram, the two-part process. The results of one of Van Mier and Nooru-Mohamed's experiments are shown in *Figure 2.27*. As proposed, the perimeter cracking correlated exactly with the bump in the

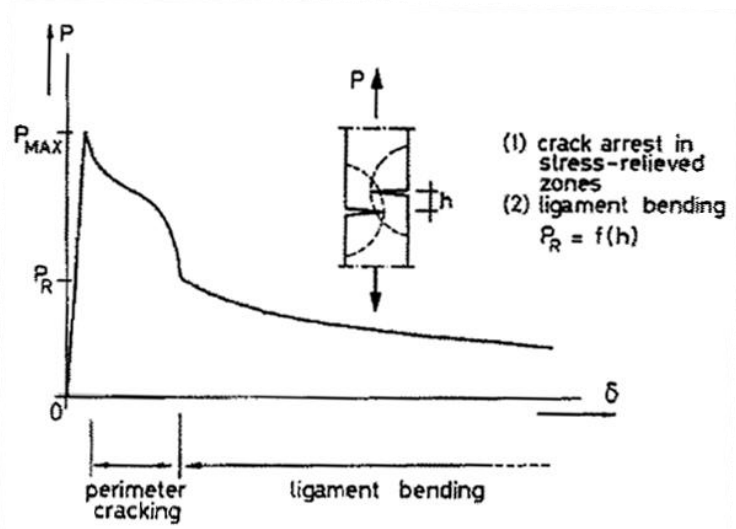

Figure 2.26: *Typical Process for Perimeter Cracking and Ligament Bending under Fixed Boundaries (from [54])*

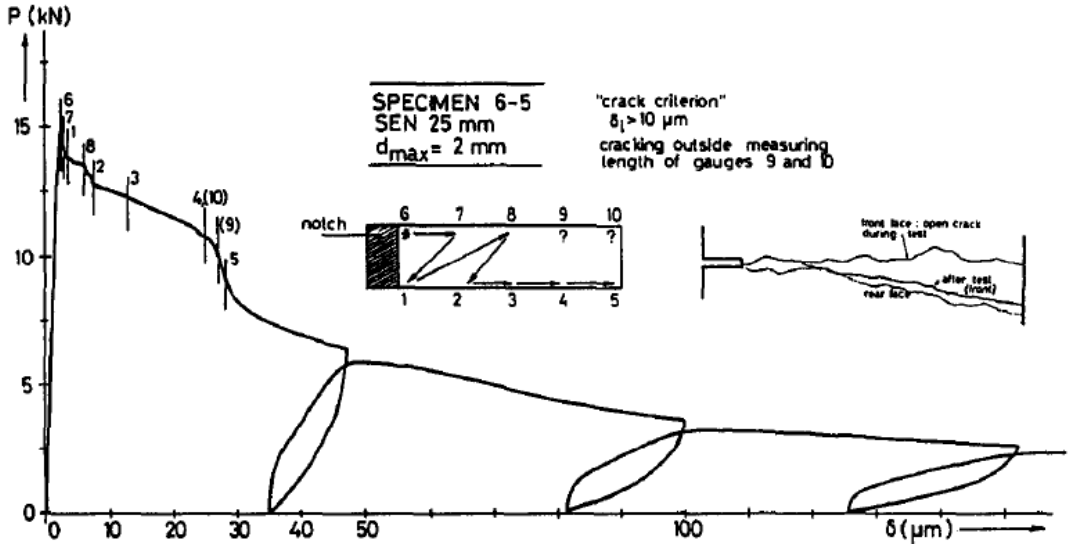

Figure 2.27: *Experimental Results of Perimeter Cracking and Ligament Bending under Fixed Boundaries (from [54])*

softening curve. Van Mier concluded that this was a structural phenomenon and cast doubt as to whether the softening behavior was actually a material property. Because of this, Van Mier thought it was best to take a conservative approach. He proposed that pinned-pinned boundaries should be used so that a lower bound of fracture energy is found [51]. However, further research presented in *Section 2.3.9* proves that process zone models, like the FCM, can appropriately explain this tensile softening phenomenon.

Many different types of uniaxial tensile tests of concrete have been performed with varying experimental setups. Some tests have utilized rotating boundaries to ensure that the applied load remains centered, eliminating secondary moment effects and resulting in lower measured fracture energies than fixed boundaries. Rotating or pinned boundaries have been created through use of a flexible chain with spherical seats and also spherical hinges, which are both displayed in *Figure 2.28.*

Some researchers have chosen to improve the rotational stiffness of their setup to behave more like fixed boundaries. For example, Cornelissen et al. experienced

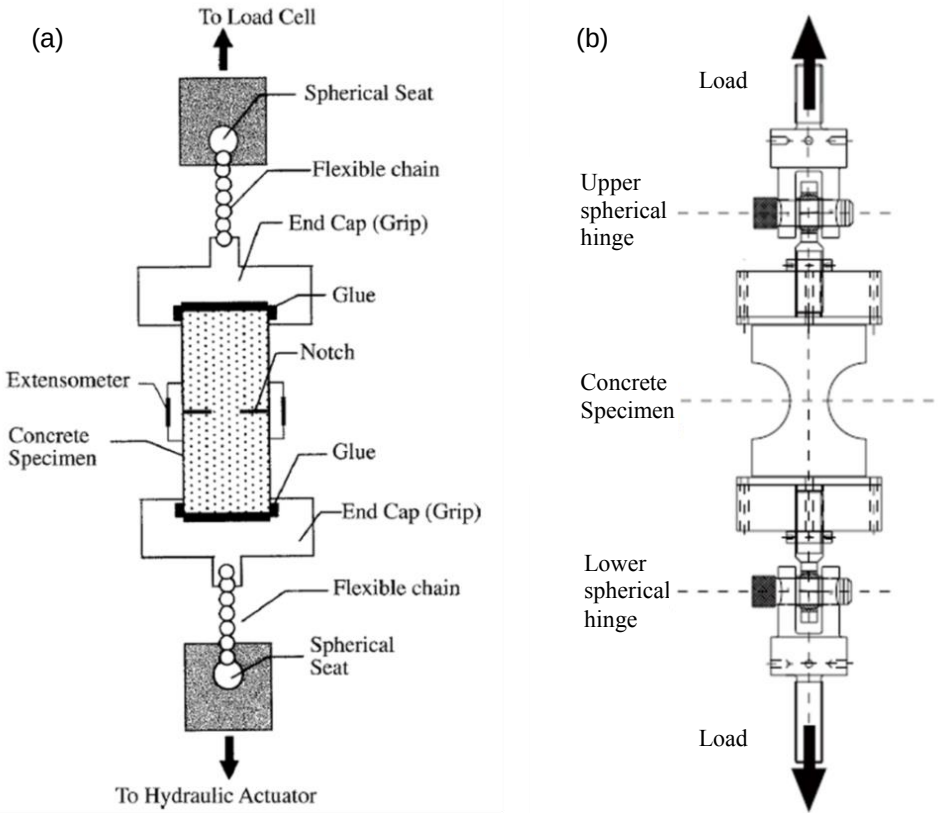

Figure 2.28: *Rotating Boundary Examples, (a) flexible chain w/ spherical seat (from [16]), (b) spherical hinge (modified from [55])*

trouble maintaining a uniform crack opening with their initial testing frame, so a stiff, ball bearing guiding system was designed to limit friction and inhibit loading platen rotation (*Figure 2.29)* [43]. Since the load cell was located outside of this guiding frame, frictional losses occurred in the ball bearings. These losses were significant enough in effecting the tail end of the softening curve that Hordijk decided to add load cells below the specimen [34:26-30]. The frictional loss solution to the stiffening system in *Figure 2.29a* is shown in *Figure 2.29b.*

Other experiments tried to mitigate secondary moments produced by fixed supports (*Figure 2.24)* by controlling the boundary so that a uniform, single crack opening occurred. A practical method to reduce lateral flexing in both directions was proposed by Akita et al. (*Figure 2.30)*. During the closed-loop uniaxial tension test the strains on each side of the sample were measured and kept uniform by hand-adjusting gears to prevent the development of secondary flexure at the steel arm boundary [44]. A similar, more complex approach was developed by Carpinteri and Maradei (*Figure 2.31a)*. Their testing machine initially utilized a simple ball joint to assist with positioning

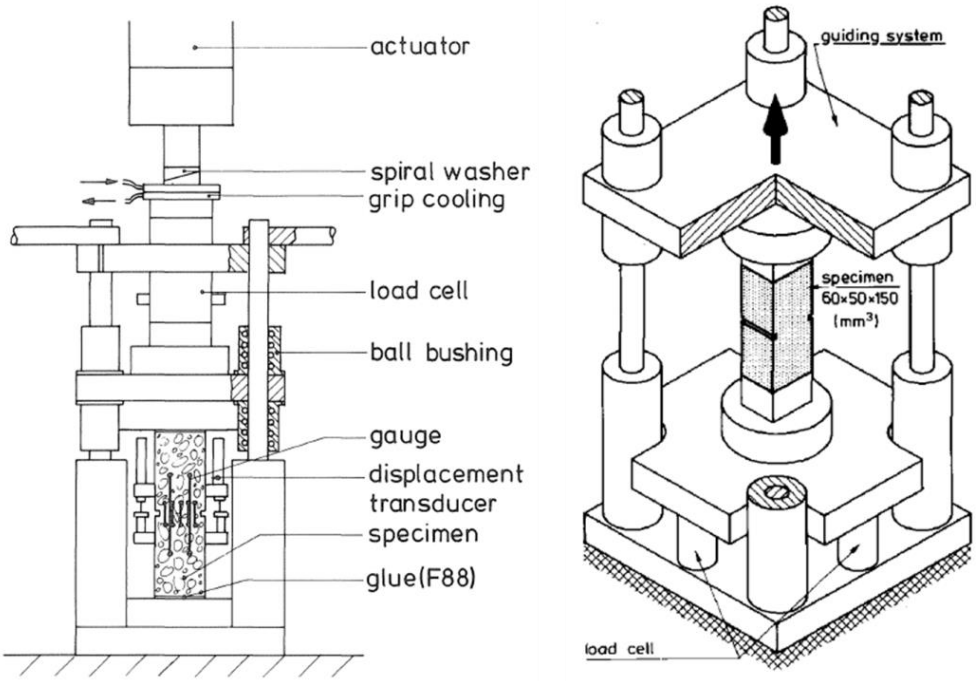

(a) (b)

Figure 2.29: *Stiff Testing Frame, (a) guiding system w/ frictional effects (from [43]), (b) frictional fix with load cells (from [34:30])*

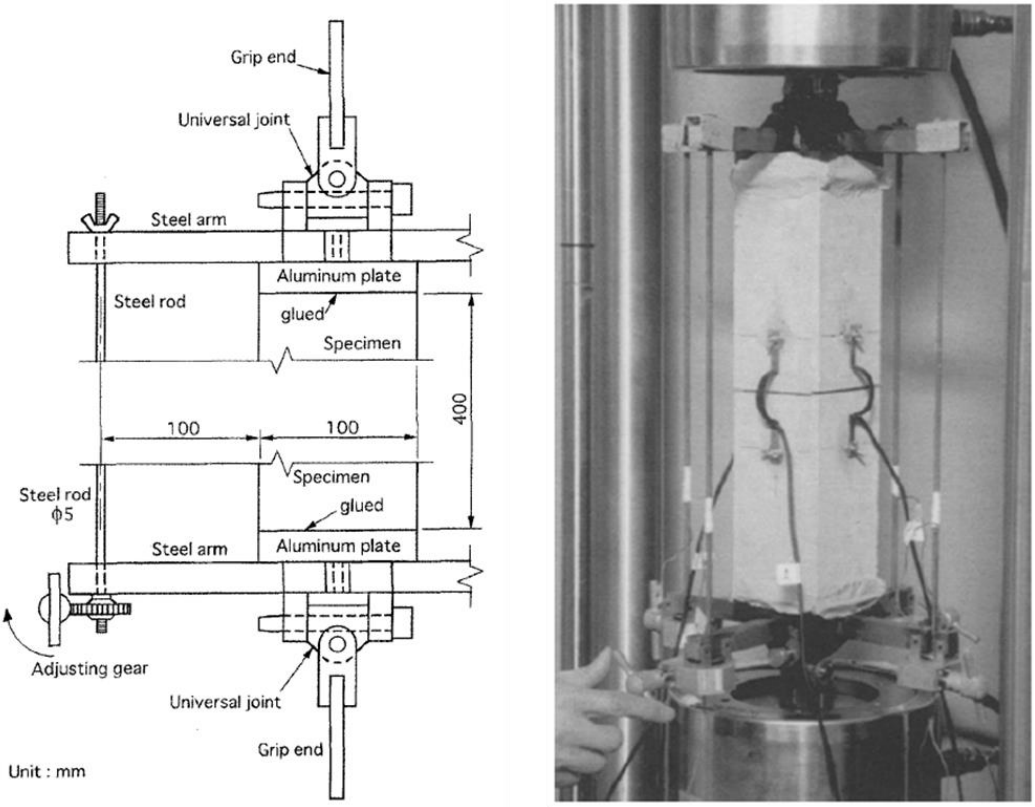

Figure 2.30: *Adjusting Gear System and Experimental Setup by Akita et. al (from [44])*

during gripping (i.e. one rotating boundary). This boundary decreased stability and did not allow for uniform deformation during testing (*Figure 2.31b)*. To mitigate this issue they implemented a three-jack solution in which overall strains were controlled to allow for uniform crack propagation and thus limiting flexural bending moments on the specimen. During testing, actuators A2 and A3 were controlled based on the following combinations of strain readings (i.e. E1, E2, E3, E4) taken from the specimen:

$$\varepsilon_x = ((\varepsilon_2 + \varepsilon_4) - (\varepsilon_1 + \varepsilon_3))/2 \qquad (2\text{-}4)$$

$$\varepsilon_y = ((\varepsilon_1 + \varepsilon_2) - (\varepsilon_3 + \varepsilon_4))/2 \qquad (2\text{-}5)$$

This technique allowed for the true tensile properties to be measured consistently. As shown in *Figure 2.31c,* the results of the three-jack soluton are stable and show a uniform deformation in all strain gauges with little to no effect of secondary forces [56].

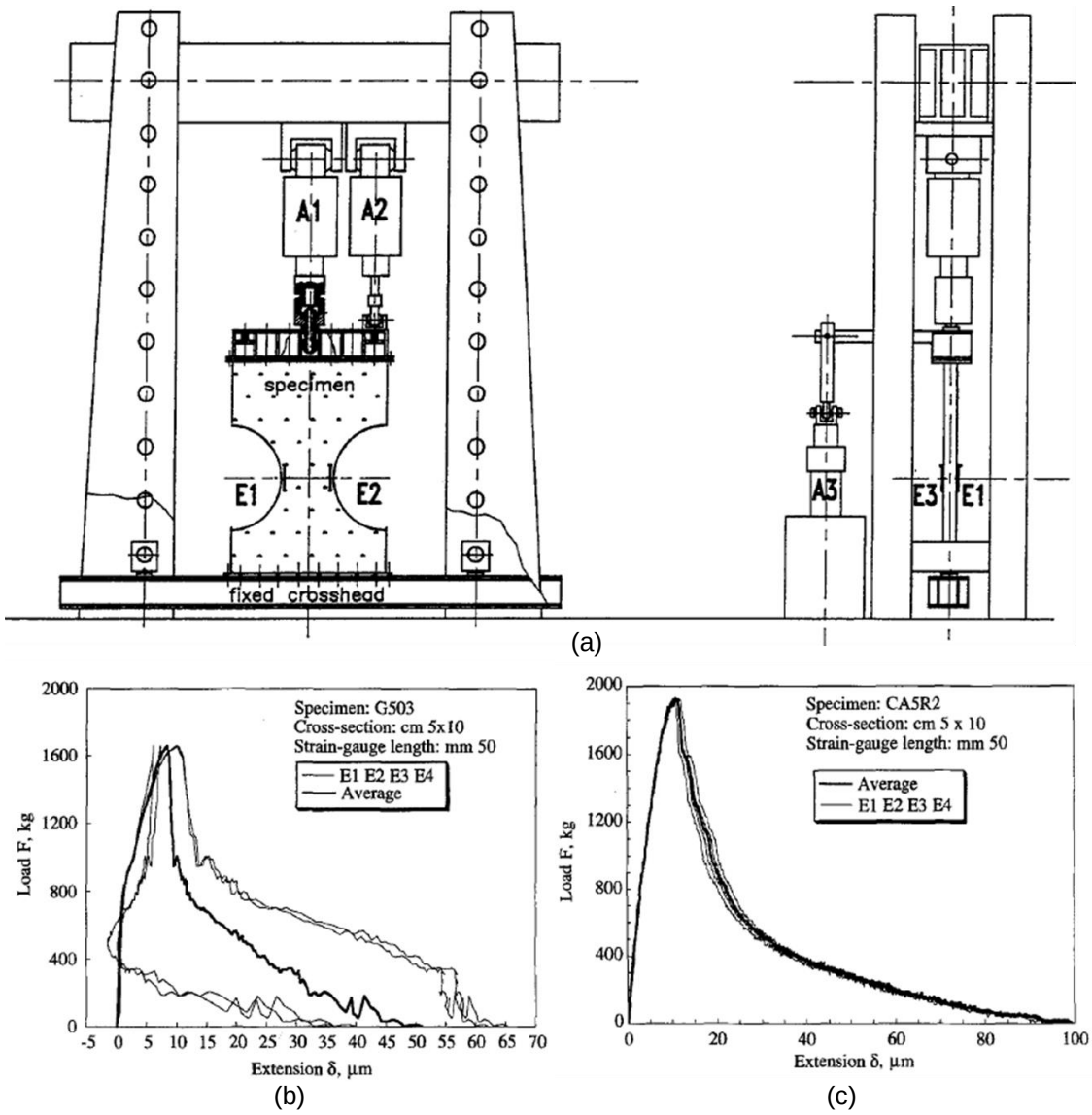

Figure 2.31: *Three-jack Solution from Carpinteri and Maradei, (a) Test Setup, (b) Rotating Boundary Results, (c) Three-jack Results (from [56])*

2.3.3 Gripping Techniques

Considering the characteristics of different gripping techniques is crucial in mitigating boundary effects in uniaxial tensile tests. If an unnotched specimen is used, stress concentrations at the boundaries (*Figure 2.32)* oftentimes result in the fracture zone forming near one of the ends. If the zone is too close to a grip, the test will not be representative of the material property. Throughout the course of uniaxial tensile tests, different gripping techniques have been developed to reduce unwanted boundary effects. Examples of these gripping techniques will be presented in this section.

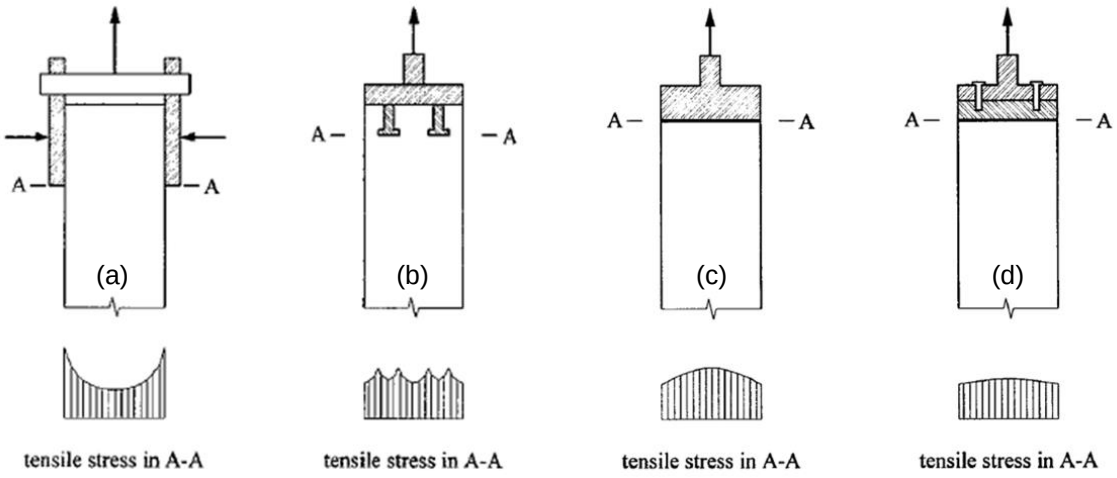

Figure 2.32: *Effects of Different Gripping Techniques on Cross-sectional Stress Distribution (from [57])*

To reduce the large stress concentrations in *Figure 2.32a* Petersson proposed a new type of grip that consisted of steel plates with wedge rubber inserts as seen in *Figure 2.33a.* These grips allowed for lower clamping forces and also a more uniform stress distribution over the critical cross sectional area. In other words the rubber inserts resulted in the stress distribution becoming fairly uniform at the grip interface, A-A. The results in *Figure 2.33b* show the gripping technique was successful in that the majority of the fracture zones occurred away from the clamping, high stress concentrations [18:104-106]. A similar technique has also been used in rock fracture mechanics [48].

Akita et al. utilized the gripping technique in *Figure 2.34a* when performing their uniaxial tensile tests. The embedded bolt was included along with glue to ensure that the stress transferred from the cover plate to the specimen. This setup introduced large stress concentrations similar to those in *Figure 2.32b.* It was reported that 5 of all 7 specimens (71.4%) suddenly broke outside of the strain gauges and were unable to be controlled. The gage orientation on the specimen is shown in *Figure 2.34b* [58]. Because of these boundary effects, Akita et al. eventually notched their specimens to insure the fracture zone occurred away from the boundaries [44].

Most concrete specimens in uniaxial tension tests are simply glued onto loading platens with high strength epoxy (*Figure 2.32c).* This creates a relatively uniform stress distribution at the boundary with a peak occurring in line with the applied force. If this applied force is better distributed over the loading grip area, a more uniform stress distribution will form. While a deeper, stiffer grip will also better distribute the force, the

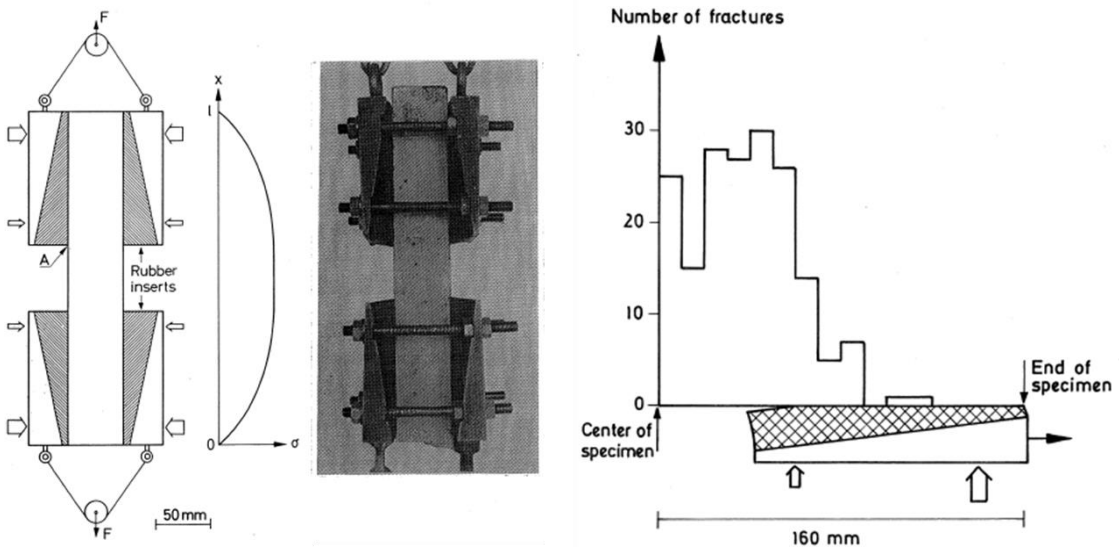

(a) (b)

Figure 2.33: *Rubber Insert Gripping Technique by Petersson, (a) Grip Setup, (b) Results of 177 uniaxial tensile tests (from [18:104-106])*

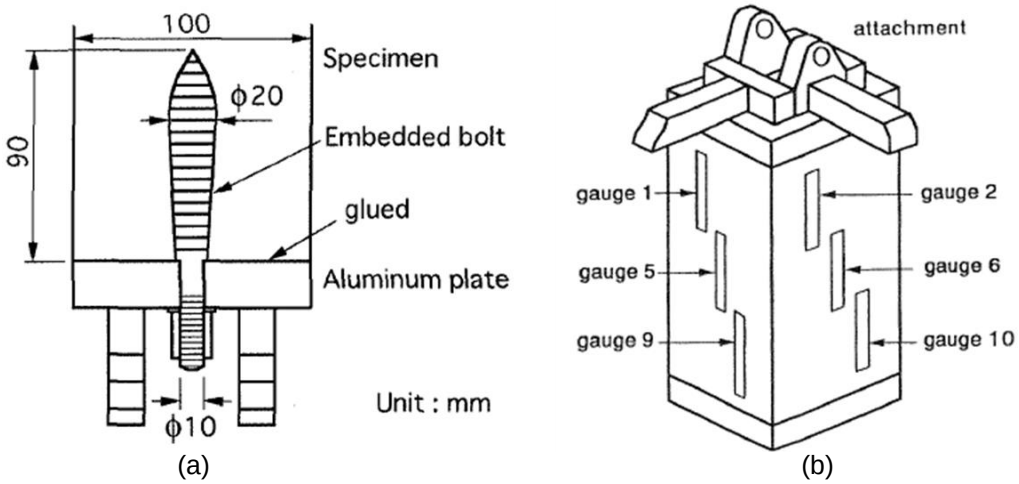

(a) (b)

Figure 2.34: *Unnotched Tensile Tests by Akita et al., (a) gripping design, (b) gage layout on specimens (from [58])*

United States Bureau of Reclamation (USBR) specifies use of a grip similar to that in *Figure 2.32d* when testing cylindrical concrete specimens in tension [59]. Zheng et al. altered USBR's gripping design to enable testing of square specimens. Their uniaxial tension test setup is displayed in *Figure 2.35a*. *Figure 2.35b* and *Figure 2.35c* show that using this gripping technique resulted in a uniform distribution of fracture zones along the specimen length with little scatter in tensile strength. It was also stated that of the nearly

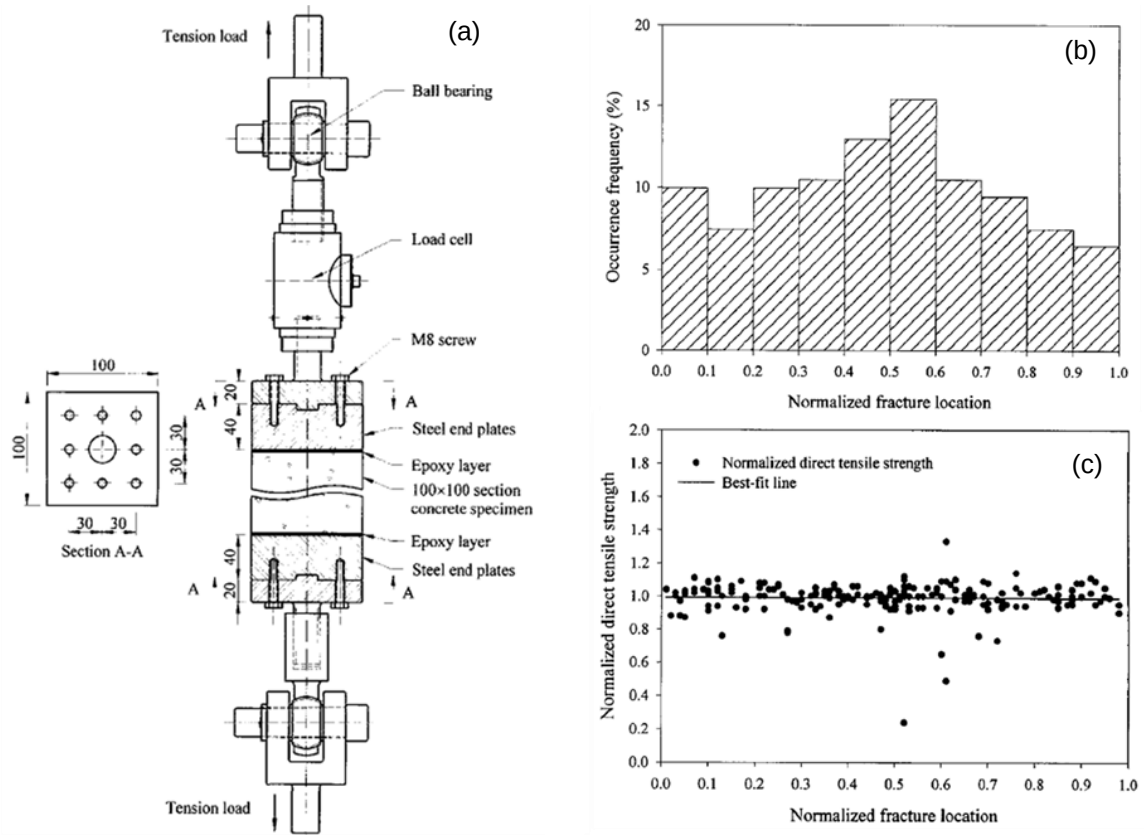

Figure 2.35: *Zheng et al. Direct Tension Gripping Technique, (a) experimental setup, (b) distribution of fracture location, (c) fracture location effect on direct tensile strength (from [57])*

200 specimens tested, none broke along the end-plate interface [57]. All in all, this gripping technique results in a uniform stress distribution along the entire length of the specimen and mitigates boundary effects.

2.3.4 Size Effects

Size/scale effects are common among concrete structures, due to concrete's inhomogeneity in its microstructure. Not accounting for these effects can have unintended consequences when determining the setup for a uniaxial tensile test. For example, when designing for the desired rotational stiffness, not only does the stiffness of the boundary conditions and loading frame need to be considered, but also the rotational stiffness of the specimen. If the specimen is too flexible, rotation across the fracture zone will occur even if the boundary is infinitely stiff. This effect is shown in *Figure 2.36*. The more slender specimens experienced greater in and out-of-plane

rotations (*Figure 2.36a*). Due to the rotation, types A, B, and D all acted as if under the influence of more rotating boundary conditions (*Figure 2.36b).* The results of the shortest specimen, C, deviated substantially from the others. Hordijk proposed that the smaller specimen length was more affected by the stiff boundary conditions preventing lateral deformations [34:44-49]. To help limit the loss of rotational stiffness effects in long and thin specimens, it has been proposed that the maximum length should be less than the characteristic length, which for most normal concrete materials is from 0.1 to 0.4 m [40].

Van Vliet and Van Mier et al. performed many uniaxial tensile tests on dog-bone specimens to determine size effects on ultimate tensile strength and variability. Six different sizes were studied and the dimensions are shown in *Figure 2.37.* All of the specimen concrete mixtures were the same with a maximum aggregate size, d_{max}, of 8mm and an average cubic compressive stress of 50 MPa. The load-displacement plot results for all of these tests are shown in *Figure 2.38*. The measuring gage length was scaled according to the specimen size, so the results would only be dependent on one variable. The control gage length was chosen as 75mm for all specimens, so that a stable test could be performed for all sizes. This is evident in *Figure 2.38b* for specimen type F's snap-back behavior. *Table 2.1* shows the ultimate tensile stress and variability in all sample types with the number of samples included in parenthesis. The results show that as the specimen size increased, the ultimate tensile strength decreased with fairly similar variability. Type A having a high standard deviation, is the one exception to

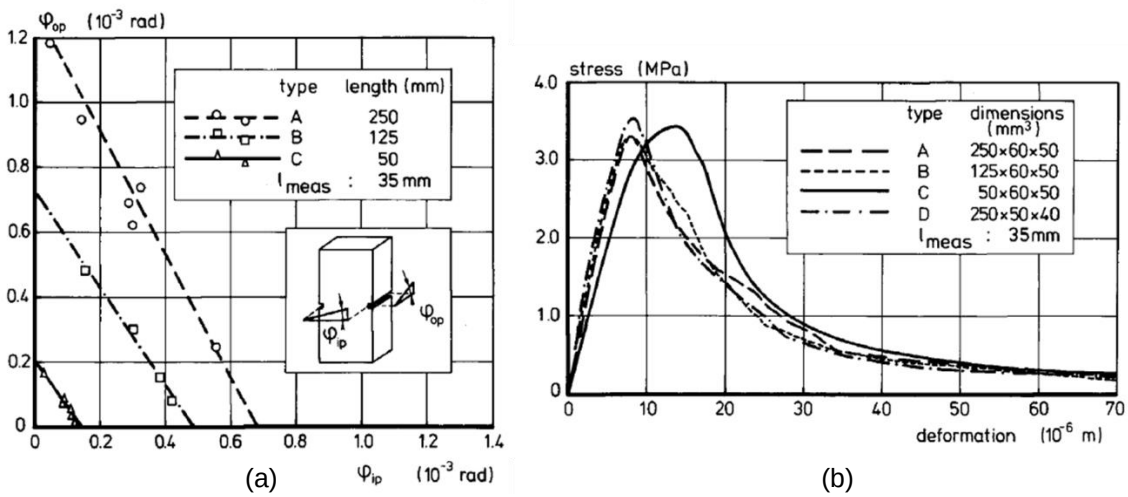

Figure 2.36: *Length Effects on Uniaxial Tensile Tests, (a) non-uniform cracking, (b) stress-displacement curves (from [34:47])*

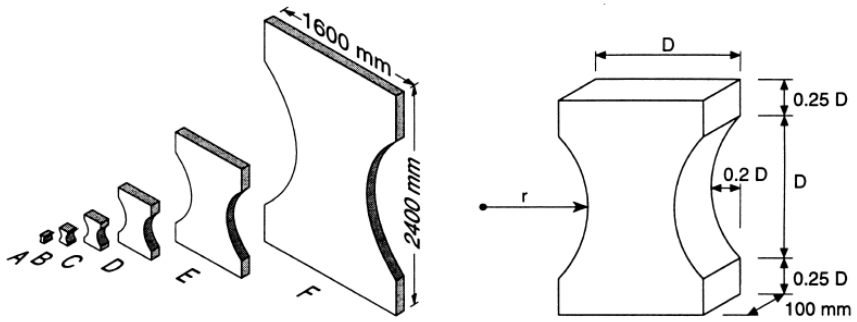

Type	A	B	C	D	E	F
D (mm)	50	100	200	400	800	1600
r (mm)	36.25	72.5	145	290	580	1160

Figure 2.37: *Dog-Bone Specimen Sizes from Vliet and Van Mier Tests (from [60])*

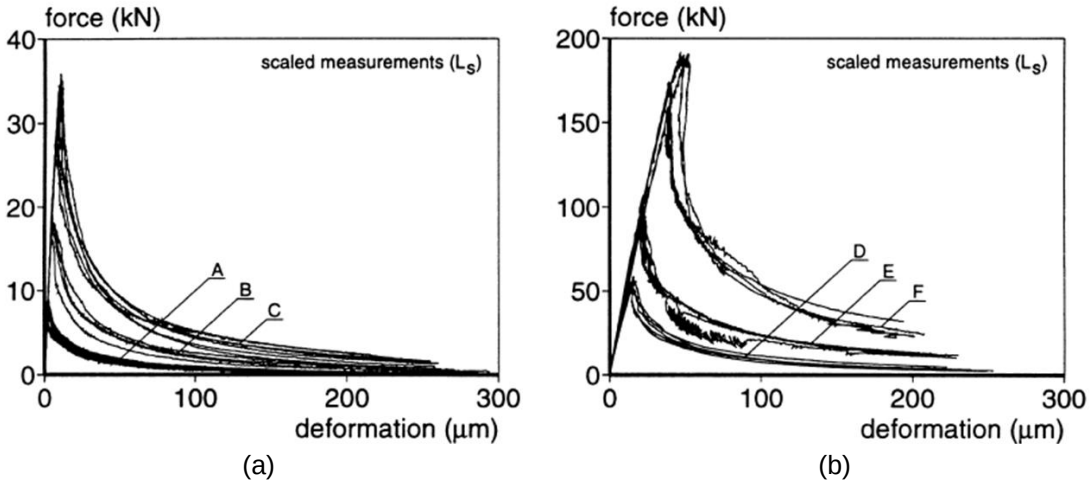

(a) (b)

Figure 2.38: *Load-deflection Plots for Specimens, (a) Types A, B, C, (b) Types D, E, F (from [60])*

Table 2.1: *Mean Ultimate Tensile Strengths and Standard Deviations for Specimen Types A-F (after [60])*

	A (10)	**B(4)**	**C (7)**	**D(5)**	**E(4)**	**F(4)**
σ (MPa) $[SD_{ft}]$	2.54 [0.41]	2.97 [0.19]	2.75 [0.21]	2.30 [0.09]	2.07 [0.12]	1.86 [0.16]

these results. Van Vliet and Van Mier explained these size effects occur due to three underlying mechanism: (1) for small specimen sizes, the micro-structural effects dominate (e.g. large aggregates located near critical cross-section, wall effects), (2) for larger specimens, the small micro-structural effects are less critical and typical material randomness are reasons for the decrease in ultimate strength, and (3) strain/stress gradients induced by boundaries, shape effects, or variation in material structure, overrule differences in material strength, which must be included in analysis. Ultimately it was shown that a critical section should have a minimum width much larger than $3.75d_{max}$ (i.e. critical section width for Type A) and has been proposed closer to $8d_{max}$ [42, 60, 61, 62].

The characteristic length developed in the FCM, l_{ch}, neglects the above mentioned size effects. To consider the influence of structural size on specimen brittleness, Elfgren proposed a number based on the ratio of stored elastic energy to required fracture energy as shown in *Eq. 2-6* [5:384-385, 63]. The characteristic size of the structure, L_C, can be assumed to be the least dimension of the cross-section where a crack will initiate and propagate [2:164-165]. If the energy required to fracture the structure is larger than the stored elastic energy, the structural behavior is more ductile and vice versa.

$$\frac{elastic\ energy}{fracture\ energy} = \frac{{L_C}^3 {f_t}^2 / E}{{L_C}^2 G_f} = \frac{L_C {f_t}^2}{E G_f} \qquad (2\text{-}6)$$

2.3.5 Specimen Alignment

Imperfect specimen alignment can be caused by manufacturing issues, gripping difficulties, and machine eccentricity. If eccentricity is introduced in the alignment the stress distribution under tensile loads becomes non-uniform, which will result in a lowered ultimate tensile stress and increased pre-peak nonlinearity [34:95-96]. Once the cracking is initiated, load eccentricity is caused by the fracturing itself [42].

Zhou presented that a 1 to 2.5 mm deviation of the loading point (i.e. 4% and 10% from center) may cause 15-20% error on measured tensile strength (*Figure 2.39a)*. Uneven deformation distribution across the cross section is also a product of load eccentricities (*Figure 2.39b)* [40]. It is understood that some eccentricities will always exist in experimental lab tests, however the magnitude of these issues need to be mitigated so that the real fracture properties of concrete are represented.

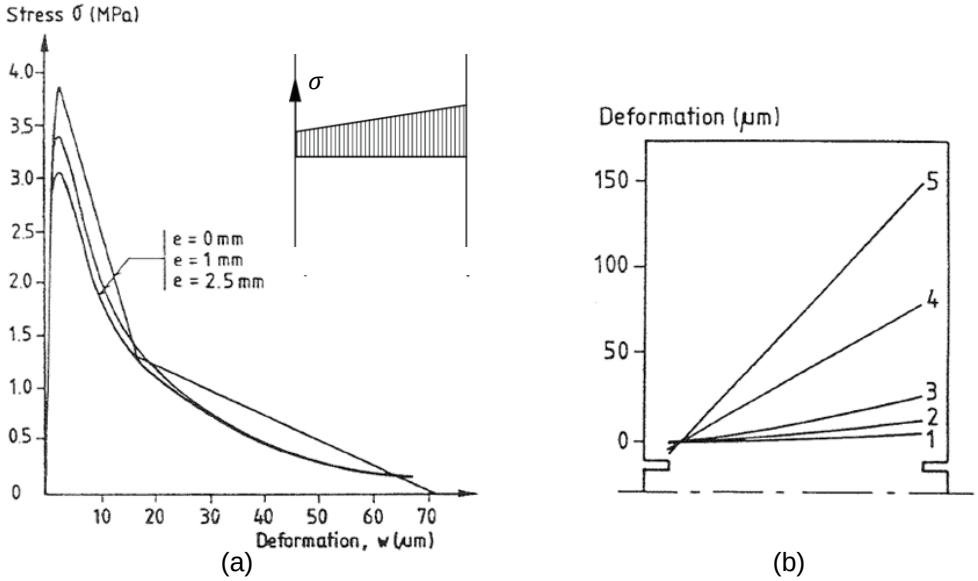

Figure 2.39: *Influences of Eccentricity, (a) Stress-displacement curves, (b) deformation distribution (modified from [40])*

2.3.6 Notch and Neck Effects

Notches or necked samples greatly decrease the difficulty in performing uniaxial tensile tests. By initiating a weak zone for fracture to occur, small gage lengths can be used at localized locations to perform a stable and controlled test. However, cross-sectional changes create stress concentrations. These non-uniform stress distributions, shown in *Figure 2.40,* have effects on fracture properties, which may result in a poor representative of the true material. Notches can also create adverse effects if included during triaxial testing inside a pressure vessel. These triaxial issues are discussed in *Section 2.4*.

Necked or dog-bone shape samples reduce the stress concentrations from notches and are also easier to reproduce to test different sizes [60]. Research performed by Petersson, however, determined that while variable, there were no substantial differences in softening curves between notched and necked specimens (*Figure 2.41)* [18:161-162]. The size of a notch has been shown to have more of an effect. As the depth of a notch increases, the post-peak plateau decreases (i.e. shifts to the left) [54]. Also notches seem to have greater effects on tensile strength when the brittleness of the material and size of the specimen increases [40].

If gripping techniques are designed properly, unnotched specimens will exhibit a more uniform stress deformation than if a notch or neck is included. Results from Hordijk show however that these stress concentrations have little effect on the softening curve [34:161-163]. *Figure 2.42* shows that the average of notched specimen tests exhibited no significant differences from the unnotched specimen. These negligible differences have also been reported in the study of rock fracture mechanics using charcoal specimens [48].

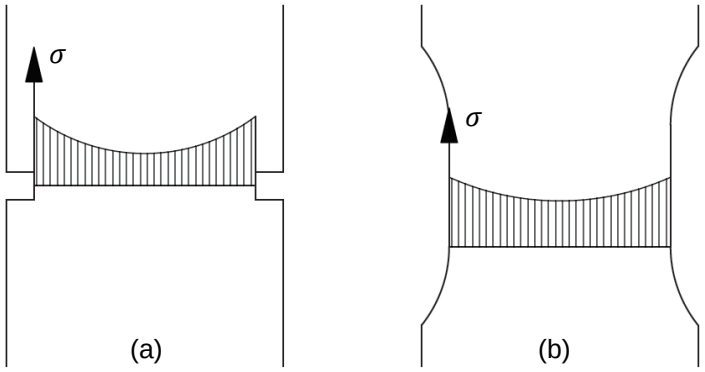

Figure 2.40: *Non-uniform Stress Distributions, (a) notched specimens (after [34:96]), (b) necked specimens (after [57])*

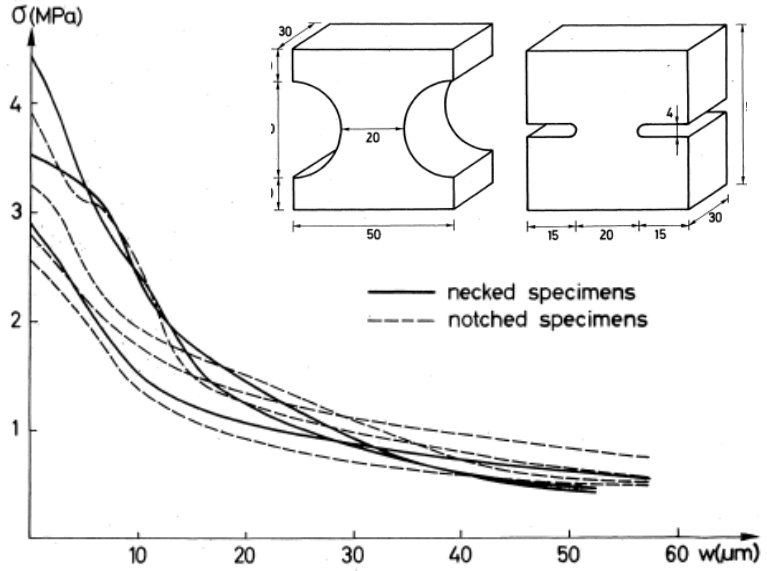

Figure 2.41: *Softening Curves for Notched and Necked Specimens (from [18:124, 18:162])*

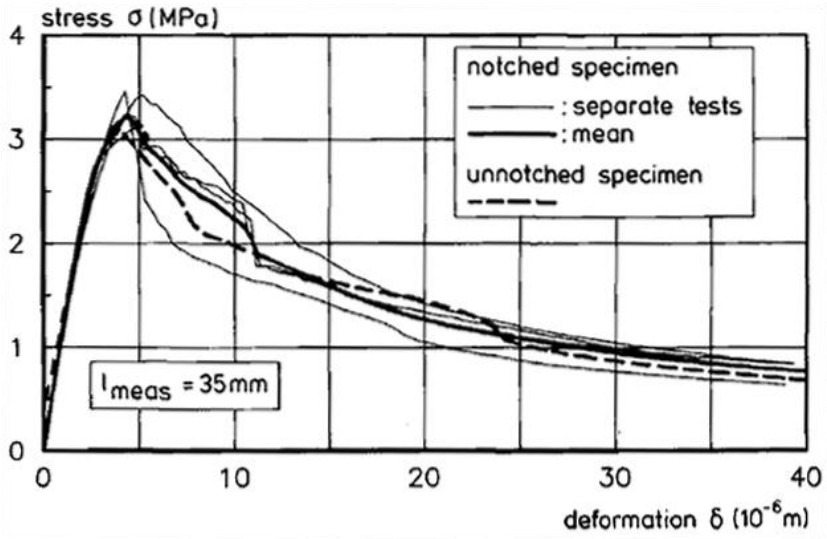

Figure 2.42: *Stress-displacement Curves for Notched and Unnotched Specimens (from [34:163])*

2.3.7 Material Composition

Due to concrete's material heterogeneity and variability, uniaxial tensile tests can produce relatively different results even when the material proportions, mixing techniques, and curing conditions are identical (*Figure 2.43)*. When the concrete material properties are altered to meet certain needs (e.g. lightweight concrete and high strength concrete), the fracture properties of concrete and their variability can greatly differ.

The results from Reinhardt et al. uniaxial tensile tests on normal weight (NC) and lightweight (LC) concrete are presented in *Figure 2.44*. These findings reflect that LC has lower fracture energy (i.e. more brittle behavior) due to less aggregate interference and a smoother fracture plane [50]. Later it was realized that the initial part of the curve for LC was biased due to certain initial stresses that were absent in the NC. Due to this, Hordijk performed new tests on LC and NC and the results can be found in *Table 2.2* [34:100-102].

In the tests by Reinhardt et al. and Hordijk, many different mix properties (e.g. cement, sand, water) were used to produce two different densities that ultimately had the same cubic compressive strength of 50 MPa. This limits the ability to predict individual property effects on concrete fracture characteristics. In the following sections specific material effects will be analyzed.

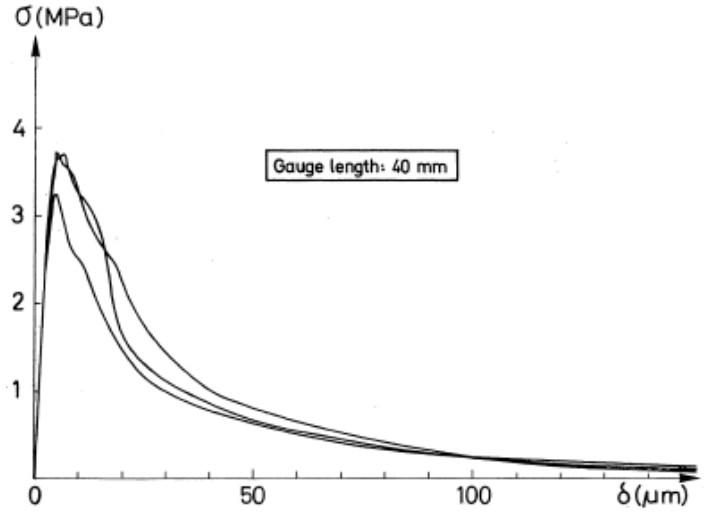

Figure 2.43: *Stress-displacement Curves for Identical Concrete Mixtures (from [18:164])*

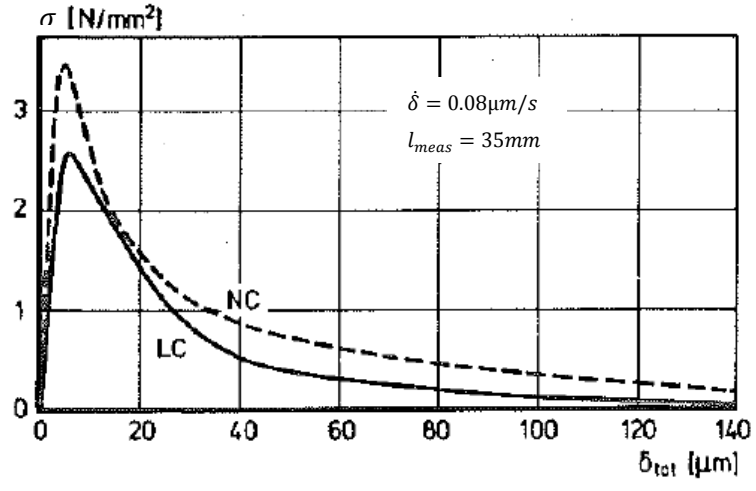

Figure 2.44: *Stress-displacement Curves for Normal weight and Lightweight concretes (modified from [50])*

Table 2.2: *Uniaxial Tensile Test Results of NC and LC (after [34:102])*

Type of concrete	E *(MPa)*	f_t (MPa)	G_f (J/m^2)	l_{ch} (mm)
normal-weight	30000	3	105	350
lightweight	18000	3	70	140

2.3.7.1 Curing Environment

The method in which concrete samples are cured can introduce unintended microcracks and stresses. *Figure 2.45a* shows a typical stress distribution due to differential shrinkage in the specimen. Hordijk performed uniaxial tensile tests on specimens that were cured under lab, oven-dry, and wet conditions (i.e. cured in water). The results are presented in *Figure 2.45b,* and the lab condition will be considered typical. When specimens were oven-dried, microcracks formed, decreasing the initial stiffness and ultimate strength of the concrete. These specimens also had lower fracture energies, which corresponds to more brittle behavior. Wet conditions show: (1) much smaller tensile strength and (2) less fracture energy than the lab conditions, which are caused by: (1) differential shrinkage stresses that were introduced after the specimens were removed from the water and (2) reduction in sliding friction due to presence of water [34:109-118]. These stresses have been shown to have greater implications on smaller sections, because more of the critical width is affected. For larger sections only small outside portions will dry out [60]

2.3.7.2 Water/Cement Ratio and Concrete Quality

Uniaxial tensile tests have shown that higher concrete cube compressive strengths (*Figure 2.46a)*, lower water/cement ratios *(Figure 2.46b)*, and increased curing time (*Figure 2.46c)* all increase the tensile strength and fracture energy of

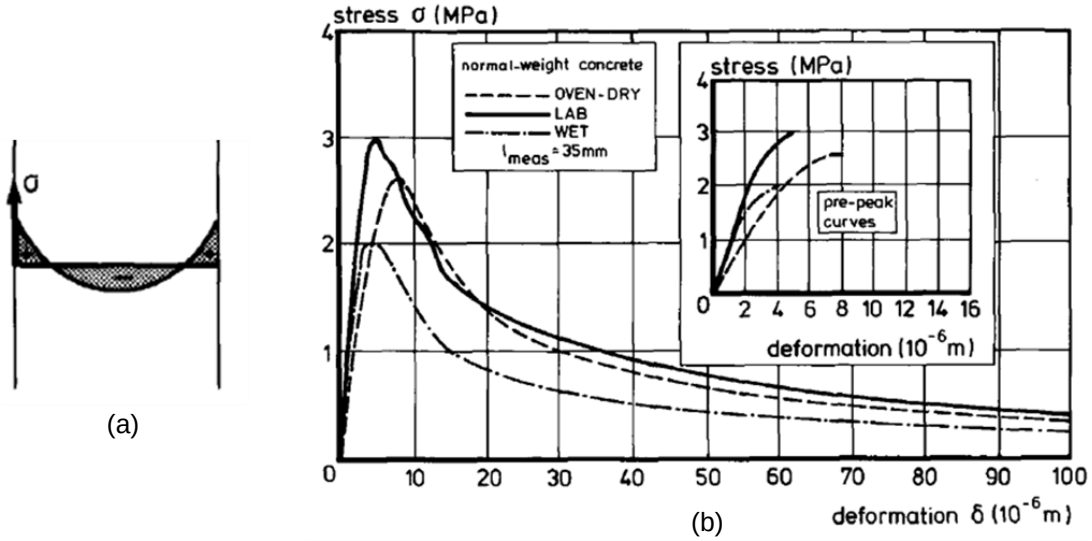

Figure 2.45: *Curing Condition Effects on (a) stress distribution (from [34:96]), (b) Concrete Tension Softening (from [34:115])*

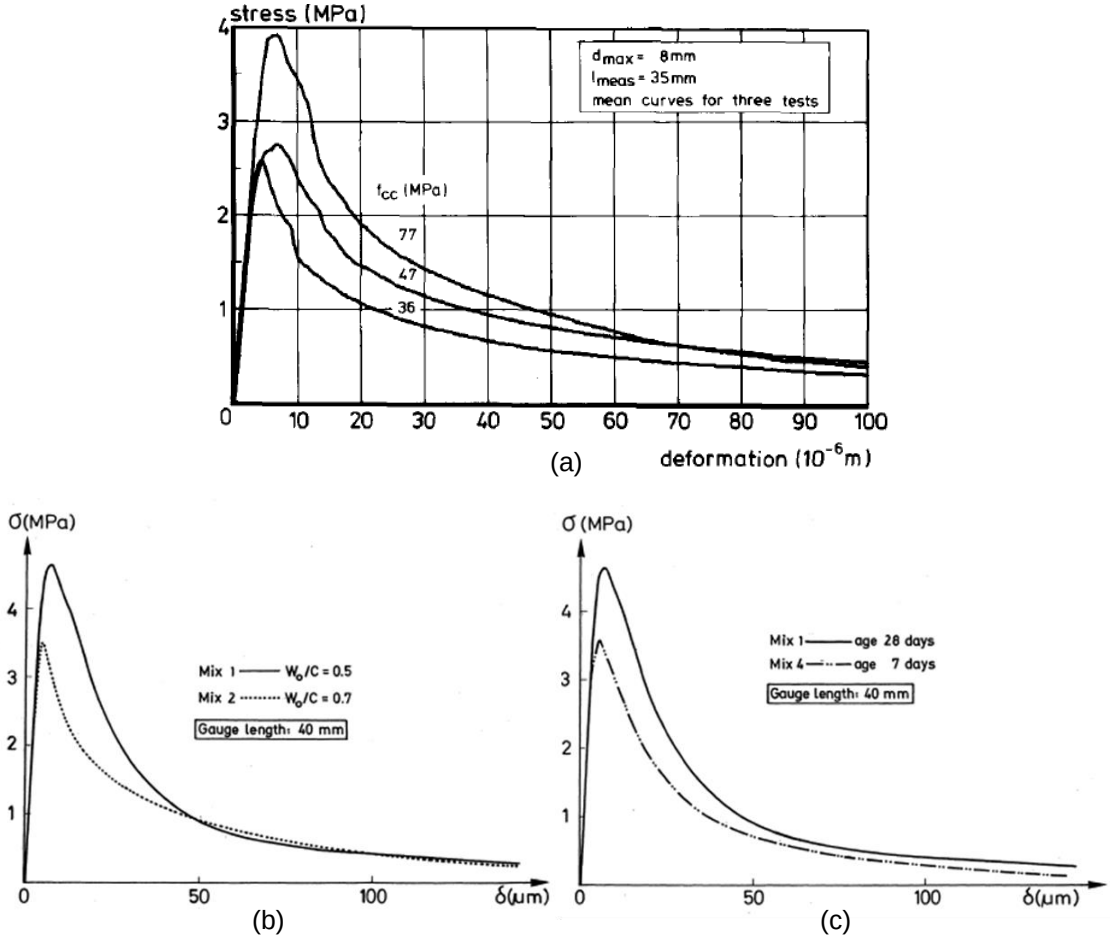

Figure 2.46: *Effects on Tension Softening Curve, (a) cube compression strength (from [34:108]), (b) water/cement ratio, (c) curing time (from [18:164-165])*

concrete [18:163-166, 34:107-109]. This is no surprise since higher strengths and longer curing times are all related to low water/cement ratios. However, other high strength concrete uniaxial tensile tests show that the tensile to compression strength ratio decreases as compressive strength increases [16].

2.3.7.3 Aggregate Size

The crack path of concrete in a uniaxial tensile test is directly related to the resulting fracture energy. Larger aggregates make for a more tortuous path for crack propagation. This increased length of crack opening results in an increase in fracture energy [18:163-166, 34:102-107, 54]. Aggregate size effect tests performed by Hordijk can be seen in *Figure 2.47.* While the softening curves show large increases in fracture energy, the characteristic lengths were all similar [34:106]. It should also be mentioned that concentration of aggregates need to be considered.

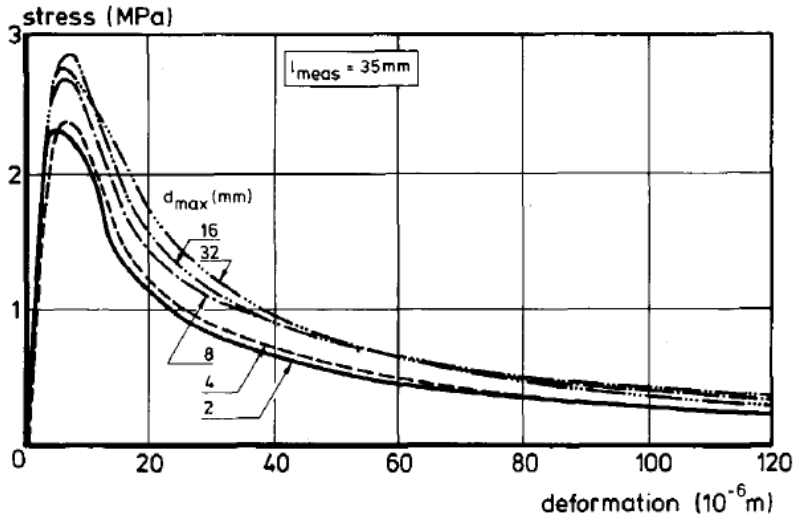

Figure 2.47: *Aggregate Size Effect on Softening Curve (Taken from [34:105])*

2.3.7.4 Fiber Inclusion

Due to their contribution to crack-face bridging (*Figure 2.48a),* fibers greatly increase the toughness of concrete in uniaxial tension. With increasing crack-face bridging, the descending branch of the softening curve will rise *(Figure 2.48b).* The maximum bridging stress depends on multiple characteristics of the fibers: strength, quantity, inclination (e.g. continuous, discontinuous), location, and pull-out behavior [5:104-106]. Fiber volume and inclination effects on stress-displacement curves have been studied by Van Mier through experiments with Slurry Infiltrated Fiber Concrete (SIFCON) [5:385-387, 64]. As displayed in *Figure 2.48b,* ductility and toughness increase with increasing volume and uniform fiber alignment crossing the fracture zone. Fiber orientation has been shown to greatly depend on the chosen mixing method. Barros et al.'s research on glass fiber reinforced concrete (GFRC) utilized two different mixing methods: (1) premix method - fibers are added to the mix following that of the aggregates, cement, water, and admixtures; (2) spray-up method – glass fibers and cement slurry are simultaneously sprayed onto a form and are mixed at moment of placement. Their results show that the fracture energy and ultimate tensile strength of the spray-up technique (4286 N/m and 10.8 MPa) were much larger than that of the premix method (3017 N/m and 5.5 MPa), due to the difficulty in uniformly distributing the mix in utilizing the latter [65].

Many other uniaxial tensile testing experiments have been performed on fiber reinforced specimens, such as those by Wang et al. who thoroughly examined effects of

different fiber types, lengths, and proportions [66, 67] and Li et al. who analyzed the differences in plain, polypropylene fiber, and steel fiber concrete [46]. The findings of Wang et al. and Li et al. are displayed in *Figure 2.49* and *Figure 2.50,* respectively. These results show that increasing the strength, volumetric proportions, and length of fibers will increase the fracture energy of concrete.

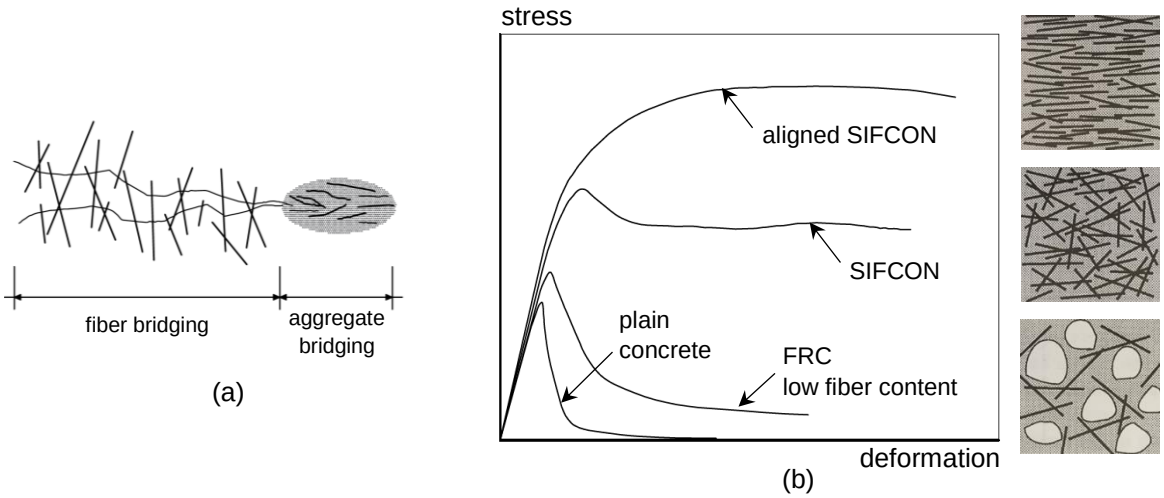

Figure 2.48: *Fiber Effects, (a) crack-face bridging schematic (after [5:105]), (b) concrete stress-displacement diagrams for varying fiber content and alignment (after [5:385-386])*

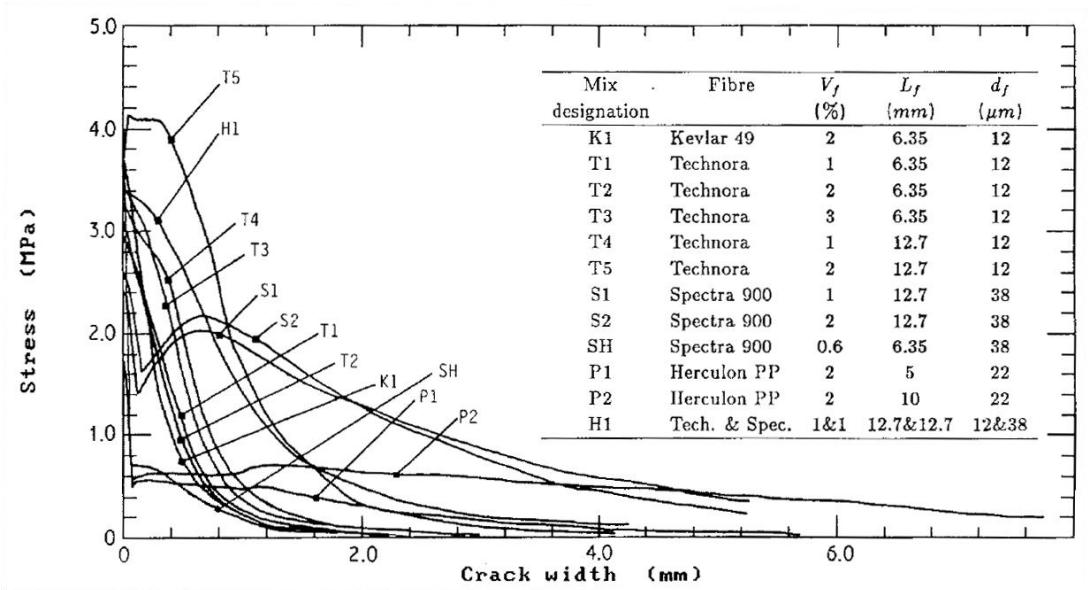

Mix designation	Fibre	V_f (%)	L_f (mm)	d_f (μm)
K1	Kevlar 49	2	6.35	12
T1	Technora	1	6.35	12
T2	Technora	2	6.35	12
T3	Technora	3	6.35	12
T4	Technora	1	12.7	12
T5	Technora	2	12.7	12
S1	Spectra 900	1	12.7	38
S2	Spectra 900	2	12.7	38
SH	Spectra 900	0.6	6.35	38
P1	Herculon PP	2	5	22
P2	Herculon PP	2	10	22
H1	Tech. & Spec.	1&1	12.7&12.7	12&38

Figure 2.49: *Tension Softening Curves for Aramid (Kevlar 49 and Technora), High-strength Polyethylene (Spectra 900), and Undrawn Polypropylene (Herculon PP) Fiber Reinforced Concrete (from [67])*

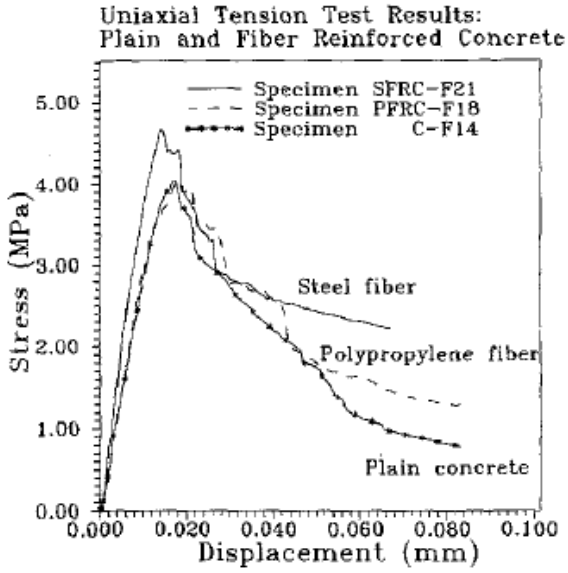

Figure 2.50: *Comparison of Plain and Fiber Reinforced Concrete (from [46])*

2.3.8 Compressive Preload

Under compressive loads, microcracks form in concrete that run parallel to the load direction (*Figure 2.51a)*. If a uniaxial tensile test is performed on a specimen with these vertical microcracks, the crack path is more likely to become discontinuous and thus more tortuous (*Figure 2.51b)*. *Figure 2.52* displays the results of uniaxial tensile tests performed following different compressive preloads [34:118-123]. These outcomes show that elastic stiffness decreases with increasing compressive preload, but these differences had little influence on the ultimate tensile strength. The reduction in stiffness is due to increasing structural damage with increasing compressive loads. Preloaded samples display much larger fracture energies and flatter peaks compared to non-loaded samples; however, the magnitude of preload seemed to have little significance.

2.3.9 Final Remarks

Extensive research has been performed on the effects of material proportions, loading conditions, boundary and gripping techniques, and testing methodology on the resulting fracture properties of concrete performed under uniaxial tension tests. As shown throughout *Section 2.3*, these conditions can greatly alter the stress-displacement curves of concrete. Some of these differences were due to structural properties of the specimens, creating non-uniform crack openings and casting doubt as to whether the

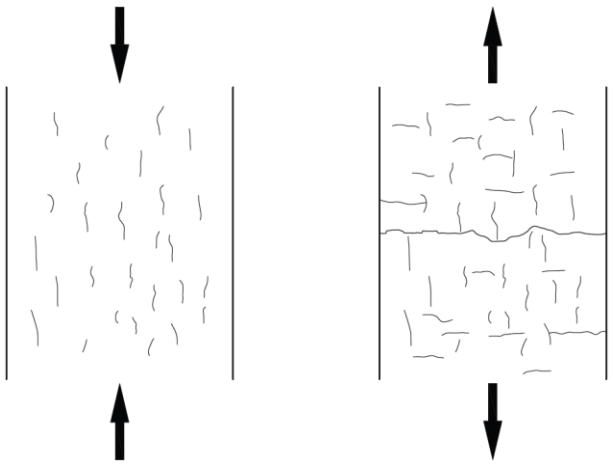

(a) (b)

Figure 2.51: *Cracking formation, (a) compressive preload, (b) tensile loads following compressive preload (after [34:160])*

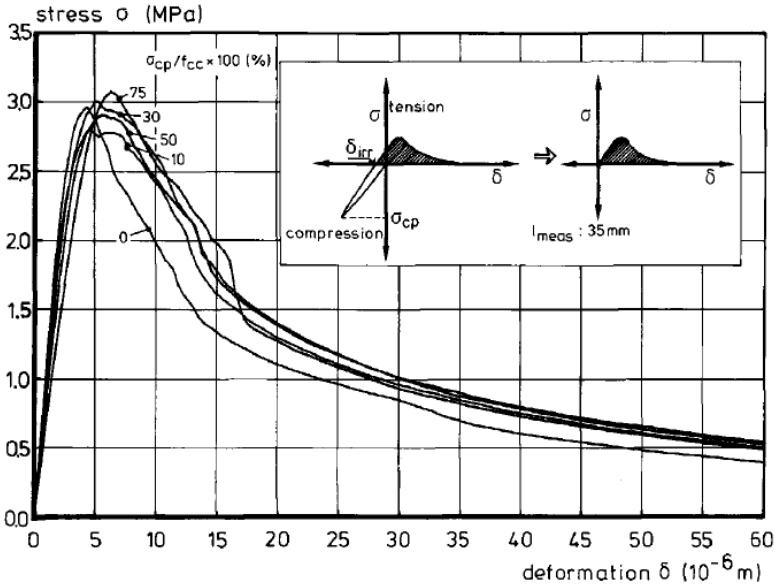

Figure 2.52: *Preload effects on Stress-displacement Curve (from [34:121])*

softening behavior was actually a material property. However after normalization, it has been shown that these effects ultimately have small influences [18:166-168, 34:69-77].

Reinhardt et al. determined a function *(Eq. 2-7)* for stress-crack opening relation based on a best fit curve of over 100 deformation controlled uniaxial tensile tests [50]. The integration of this equation, $\int \sigma dw$, results in the fracture energy, G_f *(Eq. 2-8).*

$$\frac{\sigma}{f_t} = \left\{1 + \left(c_1 \frac{w}{w_c}\right)^3\right\} exp\left(-c_2 \frac{w}{w_c}\right) - \frac{w}{w_c}(1 + {c_1}^3) exp(-c_2) \qquad (2\text{-}7)$$

$$G_f = f_t w_c \left[\frac{1}{c_2}\left\{1 + 6\left(\frac{c_1}{c_2}\right)^3\right\} - \left\{\frac{1}{c_2} + {c_1}^3\left(\frac{1}{c_2} + \frac{3}{{c_2}^2} + \frac{6}{{c_2}^3} + \frac{6}{{c_2}^4}\right) + \frac{1}{2}(1 + {c_1}^3)\right\} exp(-c_2)\right] \qquad (2\text{-}8)$$

The constants c_1 and c_2 for normal weight concrete were determined from the best fit of all the softening curves (*Figure 2.53).* Using the constants determined from the plot, the equation for critical crack opening, w_c, was determined to be equal to $5.14 G_f / f_t$ [50].

These results similarly present the same two-line stress-displacement approximation proposed by Petersson, who determined a coefficient for critical crack opening of 3.6 [18:166-167]. Hordijk used the relationship from Reinhardt et al. to compare the normalized tensile softening curves from twelve different references (*Figure 2.54).* These references had differing overall dimensions (50*30*20 – 450*300*150, 600*ø100 mm^3), measured gage lengths (25-450 mm), compressive strengths (28-58 MPa), splitting tensile strengths (2.4-3.5 MPa), water/cement ratios (0.45-0.76), maximum size aggregates (8-16 mm), and curing time (28-150 days). The results from this comparison were quite interesting. *Figure 2.54* shows that different equipment, testing procedures, material proportions, and most importantly non-uniform crack

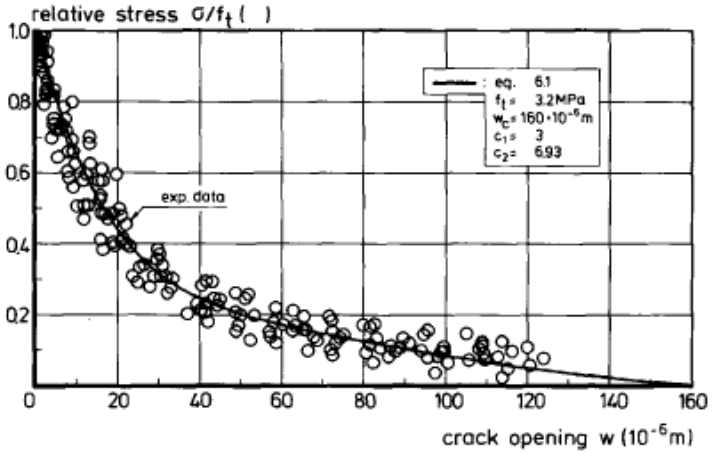

Figure 2.53: *Regression analysis and fitted equation for stress-displacement curves (from [50])*

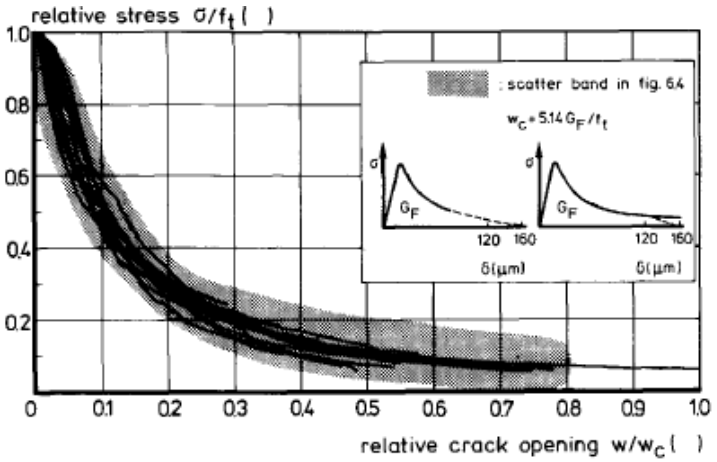

Figure 2.54: *Normalized Stress-displacement curves for 12 Different References (from [34:75])*

growth, have little influence on the relative stress-displacement relation for normal weight concrete [34:74-77]. Therefore concrete's tensile softening relation is indeed a material property and can be explained appropriately by the FCM and other process zone models.

2.4 MULTI-AXIAL CONCRETE SOFTENING BEHAVIOR

While the uniaxial tensile softening curves accurately describe concrete fracture properties under a uniform stress state, these stresses rarely act alone in three-dimensional structures. To gain a more realistic grasp of concrete fracture properties for implementation in FEM models (e.g. reinforced concrete, penetration models), multi-axial stress states need to be examined.

Biaxial experiments are some of the earliest and most performed tests used to gain insight into multi-axial stress behaviors and failure contours of concrete. *Figure 2.55* shows the typical strength and failure modes of concrete under combined stresses. Zone 2 is of special interest for the tensile softening properties of concrete. Predictably, the tensile strength of concrete decreases with increasing lateral confinement. An increase in scatter has been observed in this region for normal weight gravel concrete [5:134-135, 69] and few tests have been documented, which is most likely due to the difficulty in performing and maintaining stability in these experiments. Also concrete quality seems to have greater effects in the Zone 2 region [5:134-135]. While not shown, every point along Zone 2 could be accompanied by a tensile softening curve. Under multi-axial experiments, boundary conditions seem to be more critical. Results

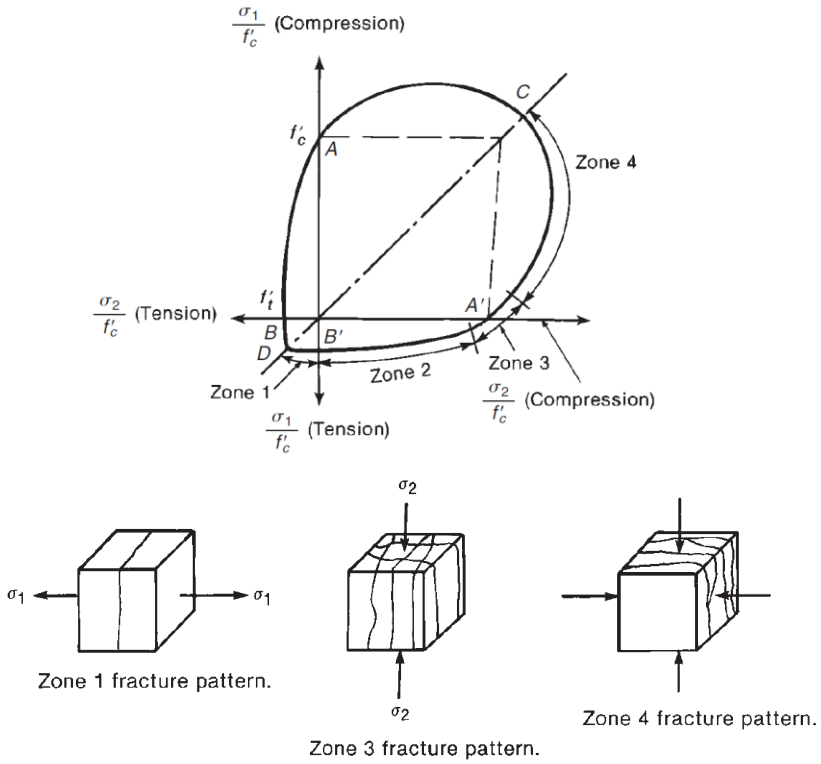

Figure 2.55: *Biaxial Failure Contour and Fracture Patterns (modified from [20:63], original results from [68])*

show that during Zone 4 conditions, higher concrete strengths correlate to increasing end restraint [70]. Due to the higher significance of triaxial loading conditions on concrete fracture, effects of biaxial states of stress will no longer be reviewed. For more information on biaxial experiments on concrete refer to Van Mier's book [5:134-135] and Ph.D. thesis [71:263-267].

Incorporating triaxial and non-linear (i.e. softening) concrete characteristics into FEM models result in more realistic material behavior predictions. However triaxial test data for concrete is limited, especially in the extension regime. "True/Full" multi-axial experiments require a specific testing machine made of three servo-valves for loading ability in three dimensions [5:173-177]. These machines are uncommon, so typically hydraulic triaxial tests are performed on cylindrical samples to gain a better understanding of concrete multi-axial behavior. This method is limited however because two stresses will always be equal. *Figure 5.56a* and *Figure 5.56b* show the failure modes of concrete under the "true" triaxial and the hydraulic triaxial stress space, respectively. Experiments for the "true" triaxial failure modes have been performed for β

values of 0, 0.05, and 0.1. Because the interest of this research is in the implementation of a uniaxial tensile test into a pressure vessel, the focus on multi-axial tests will be on hydraulic triaxial tests. For more information and results on "true" triaxial tests on concrete, refer to Van Mier's Ph.D. thesis [71].

Hydraulic triaxial failure surfaces can be split into a compressive meridian (i.e. $\sigma_3 < \sigma_1 = \sigma_2$) and a tensile meridian (i.e. $\sigma_3 > \sigma_1 = \sigma_2$), assuming compressive stresses are negative. Compression triaxial tests are common and better characterized (*Figure 2.57a)*. Typically the increase in compressive strength in the axial direction is equal to four times the concrete compressive strength plus the confining stress ($\sigma_1 = 4f'_c + \sigma_3$) [73]. More detailed relationships have been developed for larger scale specimens such as confining effects of externally bonded FRPs (fiber reinforced polymers) [74] and FRCMs (fabric-reinforced cementitious matrices) [75] on concrete structures. Also high strength concretes have been analyzed under multi-axial stress states, which can be found in spiral columns and containment vessels. The higher strength concretes showed a strong linear relationship between axial strain at peak stress and increasing level of confinement [76]. Triaxial extension tests on the other hand are rare, but extremely beneficial in characterizing realistic concrete fracture properties. The two bounds for these tests are under zero confining pressure (*Figure 2.57b, Point 1)*, which is simply a uniaxial tensile test, and under zero axial loadings (*Figure 2.57b, Point 2)*.

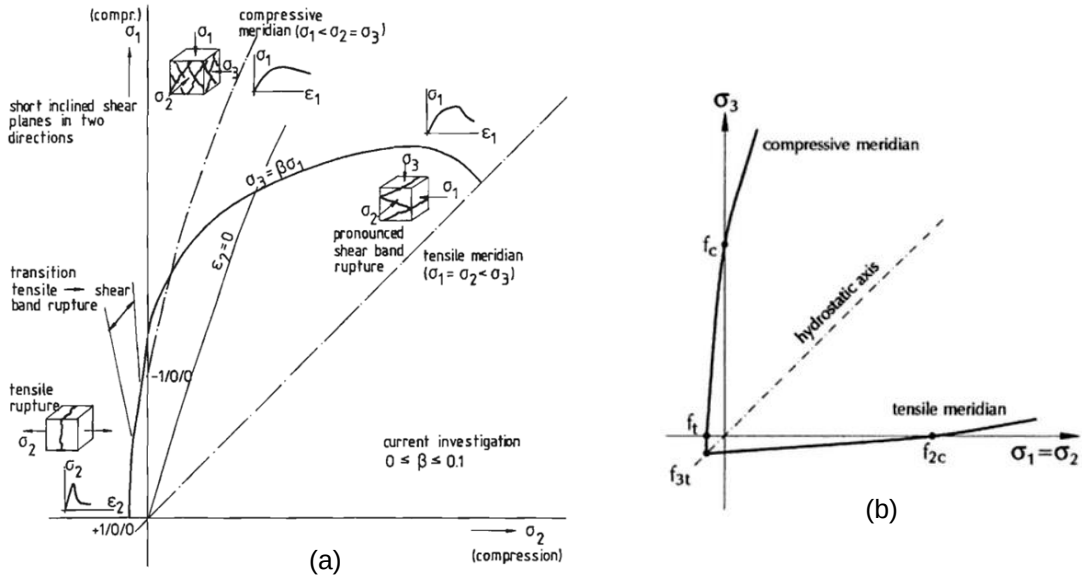

Figure 2.56: *Triaxial Failure Surfaces of Concrete, (a) "true" tests (from [71:144]), (b) hydraulic tests (from [5:395])*

Tests have shown that stable tensile softening curves for both of these extremes can be determined (*Figure 2.58*) [5:173, 78]. To define a better relationship between confining stress and concrete fracture properties, tests need to be analyzed between these two extremes.

Some difficulties in performing uniaxial tensile tests under confining pressures are dealing with the fluid flow effects. Some tests use membranes to mitigate the influence of fluid pressure on the crack opening, also known as dry fracture (*Figure 2.59a).* Others include this fluid pressure effect to get a more realistic idea of fracture

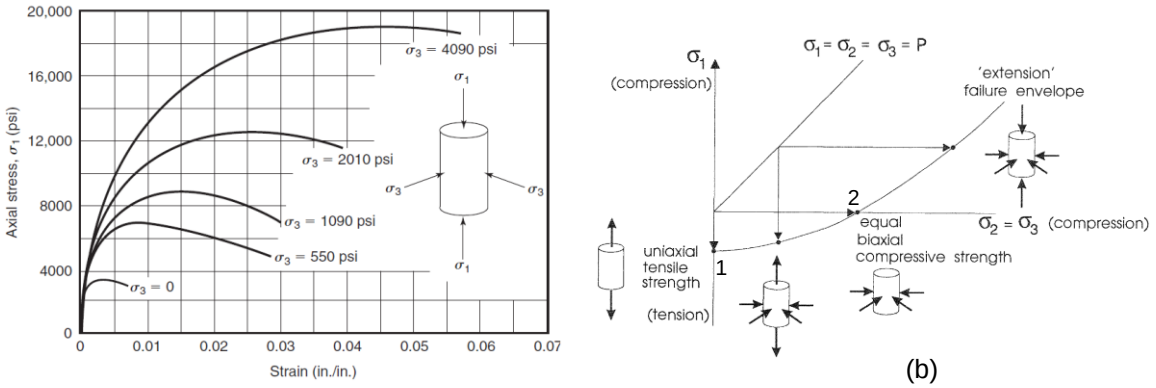

Figure 2.57: *Hydraulic Triaxial Tests for, (a) compression meridian (from [20:66], original results from [72]), (b) tensile meridian (modified from [77])*

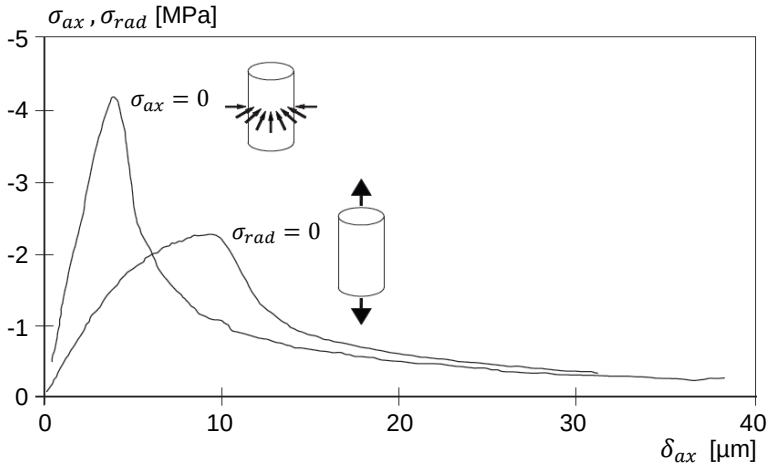

Figure 2.58: *Circumferential Stress with Zero Axial Load and Uniaxial Tension Stress-displacement Diagrams (after [5:174], original results from [78])*

mechanisms that take place in unsaturated (*Figure 2.59b)* and saturated materials (*Figure 2.59c)*. Incorporating the fluid effects, referred to as hydraulic fracturing, help estimate the fracturing process in oil wells, off-shore platforms, and dam structures [5:171-173]. Visser and Van Mier are some of the few researchers to have successfully performed stable uniaxial tensile tests under differing confining pressures. Their tests produced stress-displacement curves, including the tensile softening region, for mortar and sandstone under all three scenarios in *Figure 2.59* as well as saturated impermeable samples. *Figure 2.60* shows some of the results from their tests, where tensile stresses are negative. Ultimately it was presented that fluid pressure can contribute as much as 80% to fracture initiation, resulting in hydraulic fracturing

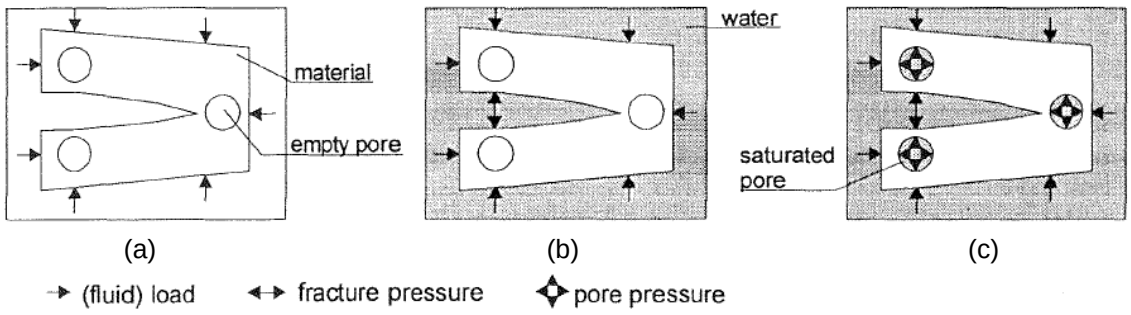

Figure 2.59: *Triaxial Test Fluid Effect, (a) dry-fracturing, (b) hydraulic fracturing, unsaturated, (c) hydraulic fracturing, saturated (from [79])*

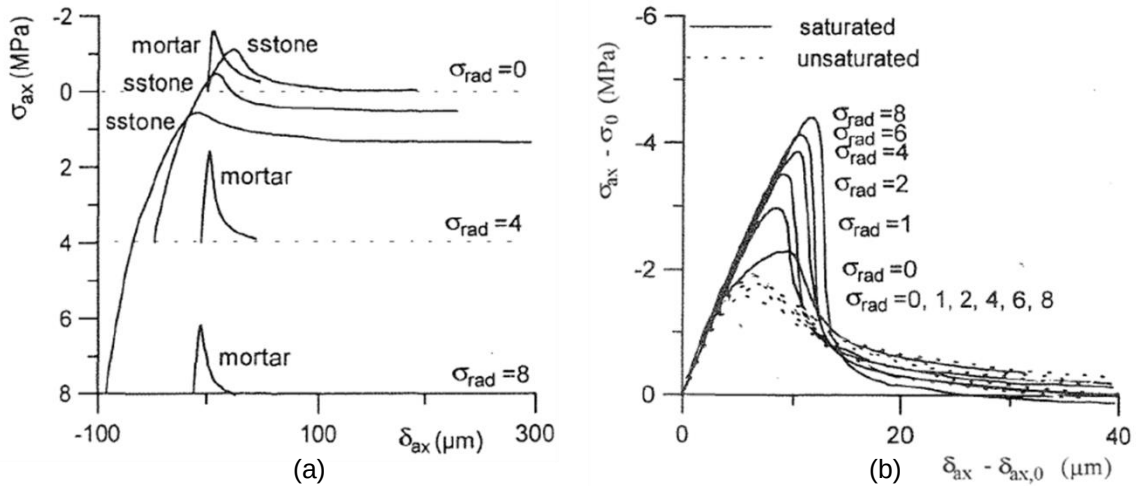

Figure 2.60: *Triaxial Stress-displacement Results, (a) hydraulic fractured, impermeable, unsaturated mortar and dry fractured, unsaturated sandstone, (b) hydraulic fractured, impermeable mortar (from [79])*

occurring under much lower tensile stress than dry fracturing. If a sample is saturated, the pore pressures generated counteract the applied stresses, which lessen the effect of fracture pressure. These counteracting pressures were more prevalent in the permeable sandstone than the cohesive mortar [77, 79].

More recently low-strength concrete at high levels of confinement and compressive axial stress have been analyzed to better understand concrete behavior under impact loadings [80]. However in spite of this, multi-axial behavior of different concretes is limited and scattered, especially in axial tension. In the field of blast/impact engineering, the particular behavior of crack opening under confining pressure for UHPC is of special interest.

2.5 STATUS OF ERDC UHPC EXPERIMENTS AND RESULTS

ERDC has developed a UHPC called Cor-Tuf for public exploration purposes, which is composed of fine aggregates and pozzolanic powders. The maximum aggregate size is approximately 0.6 mm. A superplasticizer is used to decrease the water/cement ratio (e.g. around 0.21), while retaining workability. Cor-Tuf exhibits high unconfined compressive strengths (e.g. 170 – 240 MPa). Steel fibers are also included to increase tensile capacities. This material has been extensively researched through splitting tensile, flexural, direct tensile, hydrostatic compression, unconfined compression, triaxial compression, uniaxial strain, and uniaxial strain load/constant volume strain tests [7, 81, 82].

Multiple splitting tensile tests (12) and four-point beam flexure tests (33) were performed in accordance with ASTM C496 and C1609, respectively on Cor-Tuf specimens with and without steel fibers. *Table 2.3* and *Table 2.4* display the results from these tests. While the steel fibers seemed to have little influence on the unconfined compressive strength (f_c') and tensile elastic modulus (E), the tensile strength increases with the inclusion of steel fibers by roughly 260% for splitting tensile and 175% for flexural tests. The softening curves of the flexural tests are shown in *Figure 2.61*. The two specimens without steel fibers (F1, F8) exhibit much smaller fracture energies than the others. In analyzing the fracture plane it appeared that little or no fibers ruptured. Instead all fibers were pulled from the matrix due to matrix failure, retained hooked fiber ends, or fiber straightening [82].

To analyze this pullout behavior, uniaxial tensile tests were performed on full specimens and also on individual fibers. *Figure 2.62* shows the stress-displacement

Table 2.3: *ERDC Splitting Tensile Test Results of Cor-Tuf, excluding Outliers (after [82])*

Series	Fibers	f'_c (MPa)	f_{st} (MPa)	SD_{st} (MPa)
6	with	204	25.6	1.4
7	without	182	9.8	1.1

Table 2.4: *ERDC Flexural Test Results of Cor-Tuf, excluding Outliers (after [82])*

Series	Fibers	f'_c (MPa)	E (GPa)	SD_E (GPa)	f_t (MPa)	SD_{ft} (MPa)
1	without	183	38.3	2.6	16.6	1.1
2	without	183	34.5	-	15.3	0.8
3	with	175	33.8	-	24	1.9
4	with	188	34.5	-	29.6	0.8
5	with	188/194	32.9	1.1	-	-

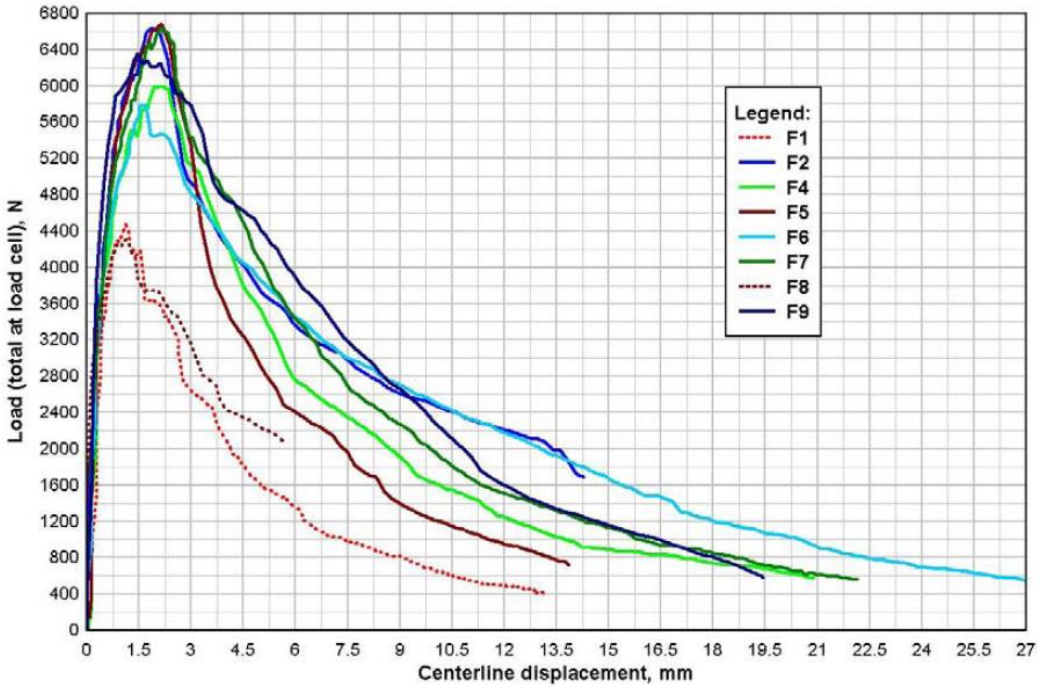

Figure 2.61: *Load-displacement Softening Curves for Cor-Tuf Flexural Tests (from [82])*

softening curves of coupon and dogbone specimens. The dogbone specimens had a square cross-section resulting in a more random fiber alignment, while the coupon was narrow which limited the fiber direction. Because of this, the coupon specimens resulted in higher ultimate tensile strengths and fracture energies. Ultimately it was shown that even with a high volume of steel fibers in a more uniaxial direction, Cor-Tuf lacked the tensile strain hardening response (i.e. higher ductility) that is evident in High Performance Fiber Reinforced Cementitious Composites (HPFRCC), also referred to as Ultra-High-Performance Fiber-Reinforced Concrete (UHPFRC). These materials have the unique ability to form numerous flat cracks bridged by fibers sustaining increasing load levels over four distinct stages as shown in *Figure 2.63* [83]. Cor-Tuf on the other

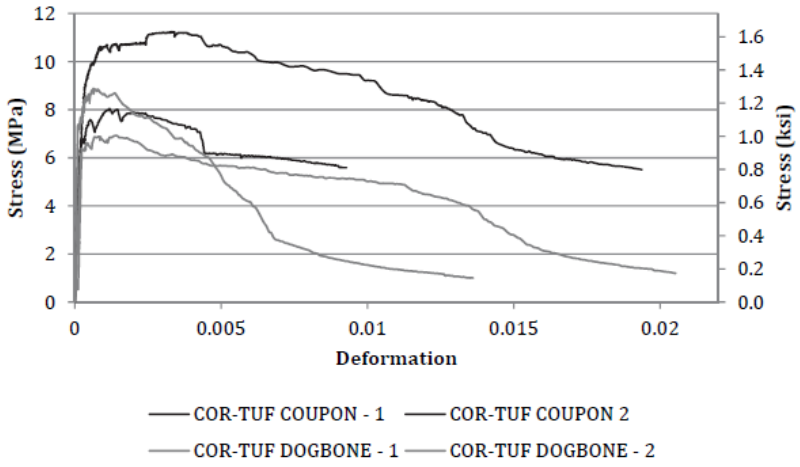

Figure 2.62: *Stress-displacement Curves for Cor-Tuf Uniaxial Tensile Tests (from [81])*

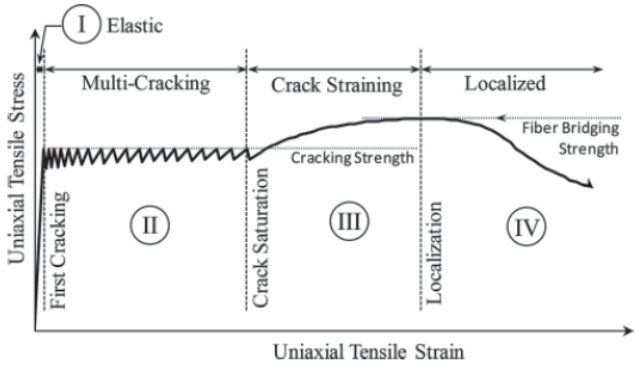

Figure 2.63: *Uniaxial Tensile Mechanical Response Schematic for UHPFRC (from [83])*

hand, exhibits a narrow zone of micro-crack formation before a localized crack is formed. To understand this difference, single fiber pullout tests were performed on straight and hooked steel fibers resulting in a four step process shown in *Figure 2.64*. Using this pullout behavior, relationships were developed between stresses from multiple fiber bridging stress and crack opening. These relationships showed that the most influential component of the stain hardening response is the type of fiber used in the design. Steel fibers, having a high lateral stiffness, resulted in matrix spalling around inclined fibers. This spalling limited the number of fibers fully engaged and thus lowered the bridging

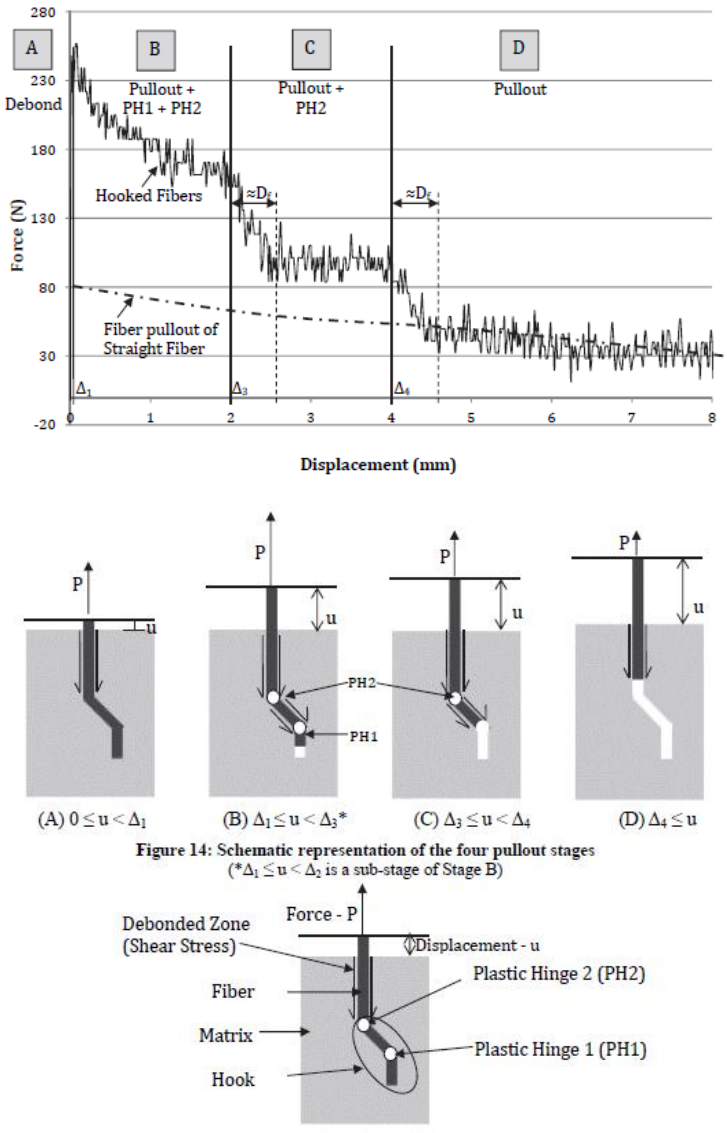

Figure 14: Schematic representation of the four pullout stages
(*$\Delta_1 \le u < \Delta_2$ is a sub-stage of Stage B)

Figure 2.64: *Fiber Pullout Stages (from [81])*

potential. All in all, it was determined that the lack of tensile ductility was due to the large fiber diameters and high matrix toughness. Because of this, Cor-Tuf material design was altered to include more ductile fibers (e.g. Spectra 1000/polyethylene). The results of this change are shown in *Figure 2.65*. It is evident that the use of the different fibers greatly increased the ductility, while retaining the ultimate tensile strength. Further experiments were performed by the University of Michigan and ERDC which consisted of altering the matrix properties as well as introducing inherent flaws in the cross-section to create a larger distribution of cracking before the main process zone was formed. This tailoring of fibers and matrix properties can lead to optimal bridging strengths that maintain high ultimate strengths while greatly increasing the strain capacity. These materials are referred to as High Strength High Ductility Concretes (HSHDC). HSHDC have both high compressive strengths and high tensile ductility, which are essential properties when dealing with high-rate loadings (e.g. blast, explosions) [81].

The increased tensile strength provided by UHPC is beneficial in many design applications, such as achieving longer spans and reducing the amount of prestressing strands in precast, prestressed bridges. However to utilize these improved tensile properties in structural design, short and long term creep need to be considered. A similar UHPC material to Cor-Tuf with short steel fibers has been studied at GT by

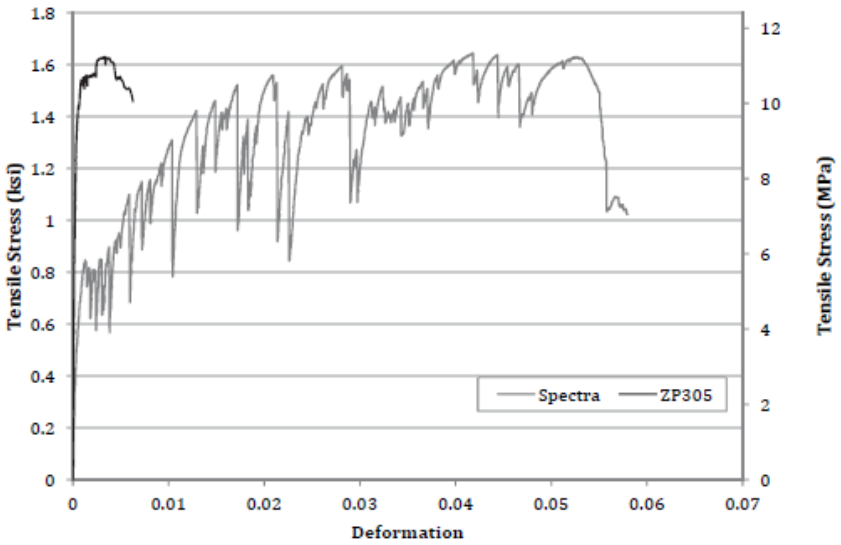

Figure 2.65: *Stress-displacement Curves for Steel (ZP305) and Polyethylene (Spectra) Fibers (from [81])*

Garas et al. for investigation into tensile creep properties for bridge applications [84, 85, 86, 87, 88]. Previous research indicated that fibers tended to increase creep in tension [89] due to the porous interfaces between paste content and fiber reinforcement initiating microcracking, as well as viscous mechanisms [90]. Garas et al. were able to increase the fiber-matrix interface strength through thermal treatment, which included placing specimens in an environmental chamber at a temperature of 194˚F (90˚C) and 100% relative humidity for 48 hours following demolding. Through the described thermal treatment and large fiber-aggregate size ratios of UHPC, short term tensile creep and shrinkage [84:68-83, 88] and long term tensile creep [84:182-229, 85, 86] were shown to decrease with increasing short steel fiber content; compression creep in UHPC however behaved differently [84:68-83, 88]. Also, tensile creep was shown to be more sensitive to thermal treatment than tensile strength [84:182-229, 85], and it was proposed that direct tensile tests be used to determine tensile strength of UHPC in place of splitting tensile tests, which seemed to overestimate the strength by 100% [84:112-181]. Ultimately Garas et al. determined that the ideal long-term properties of UHPC can be developed through thermal treatment. If appropriately developed, not only can UHPCs increase spans and decrease required prestressing strands in bridge girders, but shear reinforcement is unneeded for shear strength [87].

Triaxial compression tests were also performed on Cor-Tuf with and without fibers. The specimen setup for these tests is shown in *Figure 2.66.* Results exhibited a

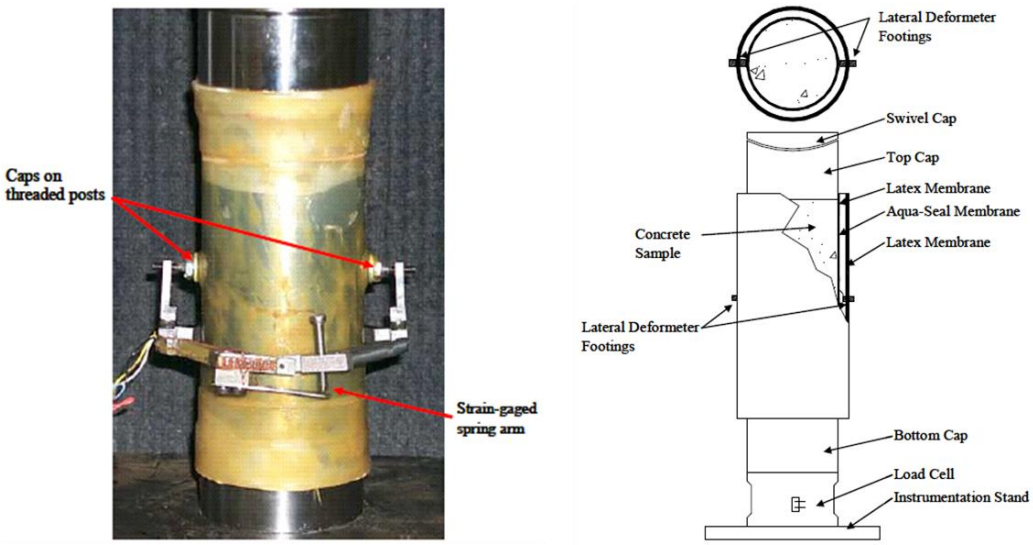

Figure 2.66: *Specimen Setup for Triaxial Compression Test (from [7])*

continuous increase in principal stress difference (axial stress – radial stress) with increasing confining stress (*Figure 2.67)* [7]. The pressure vessel used to perform these tests (similar to *Figure 1.2)* is only capable of acting in compression. Therefore to determine the tensile fracture properties of this specific concrete under confining pressures, a unique uniaxial tensile test is needed to implement into ERDC's pressure vessel.

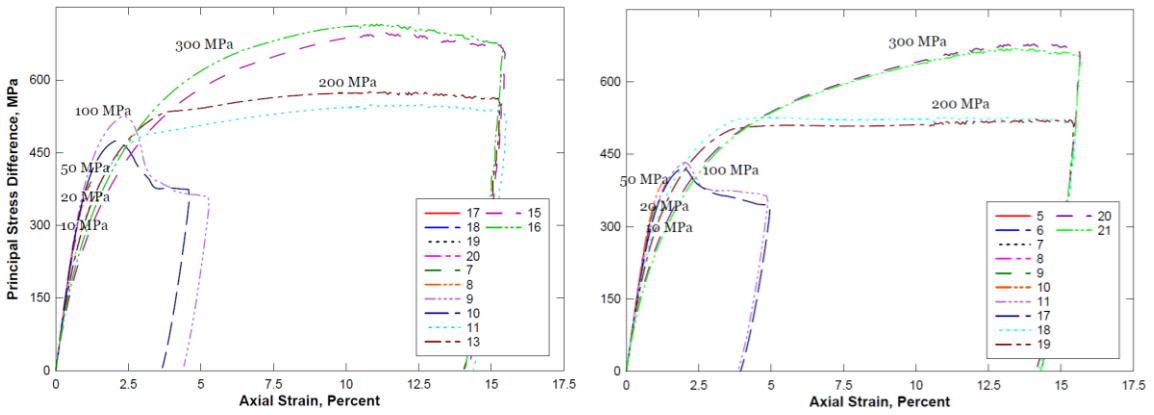

Figure 2.67: *Principal Stress Difference-Axial Strain for Triaxial Compression Tests of Cor-Tuf, (a) with steel fibers, (b) without steel fibers (from [7])*

CHAPTER 3: PREVIOUS EXPERIMENTAL PROGRAM

The experimental research presented in this thesis encompasses the latest and final developments of a larger experimental program consisting of two phases. Phase I of the program involved developing a bonding procedure for gripping of the concrete specimens and investigating instrumentation methods to be used as possible feedback signals during closed loop testing. Phase II focused on designing a stable and feasible uniaxial tensile testing setup to incorporate into ERDC's pressure vessel. The entirety of Phase I and the early stages of Phase II were performed at the University of California, San Diego (UCSD). The details and results from these earlier developments are presented in this chapter. The final stages of Phase II are discussed in chapters *4* through *6*.

3.1 UCSD PHASE I

3.1.1 Material Properties and Experimental Test Setup

The samples used during Phase I testing consisted of BERB1 (NSC), UHPC, and a brick material. All specimens were 2 inches in diameter by 6 inches long and were bonded to end caps by 3M DP460 Off-White, two part epoxy. This specific epoxy was chosen due to its high performance and toughness, which are vital in designing a test to sustain vibrations and impact. It has a full cure time of 48 hours. For more information on the epoxy specifics see the Material Safety Data Sheet [91] and Technical Data Sheet [92] from 3M. Two separate types of steel end caps were designed for insertion into UCSD's 100kip MTS machine wedge grips. Type 1 end caps (*Figure 3.1a)* had a flat surface, while Type 2 (*Figure 3.1b)* had a grooved seat for the specimens. An MTS 810 Material Testing System with the Model 318.50 Load Unit Assembly was used to perform the Phase I uniaxial tests. Important testing machine properties as reported by MTS can be found in *Appendix A.*

3.1.2 Instrumentation and Gluing Methods

Six instrumentation methods were investigated for use as viable feedback signals to control uniaxial tensile tests, including: radial strain gages, axial strain gages, axial LVDTs, radial LVDTs, circumferential extensometers, and Acoustic Emission (AE) sensors. These instrumentation techniques are shown in *Figure 3.2.*

Different aspects of gluing were analyzed and tested to determine the best procedure for epoxy application. The effects of including an additional fillet of epoxy around the base of the specimen (*Figure 3.3a)* were analyzed. An alignment jig (*Figure 3.3b)* was used during the gluing process to ensure the concrete samples and end caps were as concentric as possible.

(a) (b)

Figure 3.1: *End Caps, (a) Type I, (b) Type 2*

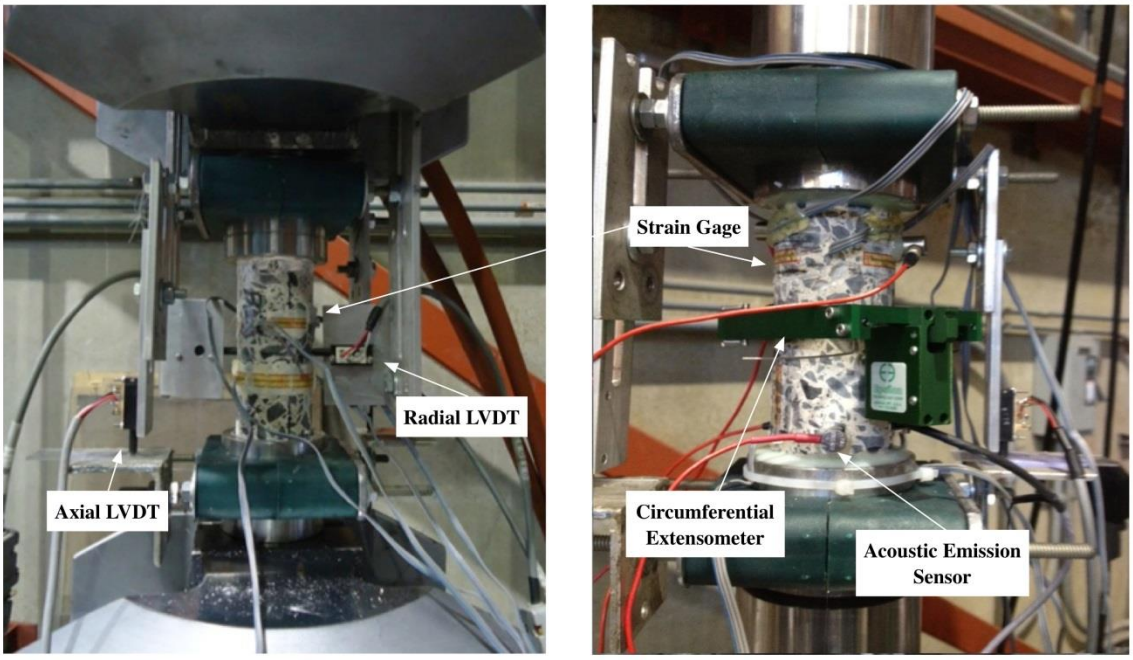

Figure 3.2: *Phase I Instrumentation*

(a) (b)

Figure 3.3: *Gluing Methods, (a) Epoxy Fillet Inclusion, (b) Alignment Jig*

3.1.3 Experimental Results

Compression tests were performed to analyze the effectiveness of the different instrumentation methods and were compared with known measurements from similar tests by ERDC. Results showed that the radial and axial strain gages were ineffective due to quality control alignment and contact issues that arose during attachment. The specific circumferential extensometer lacked needed resolution to be a viable candidate for the feedback signal. Data resulting from the AE sensors were inconclusive and their ability to perform accurately under triaxial fluid was a major concern. Because of these issues, axial LVDTs were chosen as the feedback signal, which has also seemed to be the favored method in the research presented in *Chapter 2*.

Direct tensile tests were executed to determine the appropriate grip and glue line type to include in a detailed gluing procedure and to ensure the strength and durability of the chosen 3M epoxy. There was no intention to capture the specimens' post-peak softening curves. Specific properties and results from ten of these tests are presented in *Table 3.1*. The maximum loads recorded for each material type were consistent with earlier tests. With the exception of one test, which did not utilize the centering jig, these results prove that the choice of epoxy is a suitable choice for uniaxial tensile tests. End cap types seemed to have little effect on test results. Since specimen preparation is much easier to perform with Type 1 end caps (*Figure 3.1a)*, they were selected to use during Phase II testing. To minimize effects of imperfections in the concrete sample, especially spalling around the bases, fillet glue lines were chosen over the non-fillet glue line technique.

Table 3.1: *Phase I Gluing Test Results*

Test No.	End Cap Type	Glue Line Type	Jig	Concrete Type	Glue Failure?	Max Load (lbf)
1	1	No Fillet	Yes	BERB1	No	1874
2	2	No Fillet	Yes	BERB1	No	1620
3	1	No Fillet	Yes	BERB1	No	1418
4	2	No Fillet	No	BERB1	Yes	718
5	1	Fillet	Yes	BERB1	No	1838
6	2	Fillet	Yes	BERB1	No	1671
7	1	Fillet	Yes	BERB1	N/A	-
8	2	Fillet	Yes	BERB1	No	1394
9	1	Fillet	Yes	UHPC	No	3101
10	1	Fillet	Yes	SWBrick	No	3196

3.2 UCSD PHASE II

The ultimate goal of Phase II was to demonstrate the feasibility and usefulness of implementing a strategically placed “stiffener” to measure the tensile post-peak behavior of NSC and UHPC. The effects of controlling the applied force of the stiffener (active) versus a passive approach were researched. The resulting testing method and setup will be implemented into a triaxial testing pressure vessel. Because the initial state of stress on the sample will be entirely in compression, a load train needed to be designed for a smooth transition from axial compression to axial tension. Five different test types (i.e. Tests 0, 1, 2, 3, and 4; described in *Section 3.2.3*) were performed to meet the above objectives.

3.2.1 Experimental Test Setup

Testing was performed on the same MTS 810 Material Testing System that was used throughout Phase I. A custom fabricated crosshead consisting of two MC13x50 channels was secured to the load frame columns in order to incorporate the stiffener (i.e. hollow plunger cylinder) into the test setup. The crosshead as shown in *Figure 3.4a* also improved the lateral stiffness of the testing system. Six ¾-inch diameter Grade 8 bolts per column were tensioned to 28,000 lbf each to ensure a rigid attachment. To protect the load frame columns and allow for a more uniform distribution of clamping force, two

aluminum billets, one on each side, were placed in firm contact with each of the columns.

The ability of the stiffener to separate the force system in the testing machine was made possible through the design of a custom fabricated load train. This specific component was used to implement the passive/active concepts and is composed of the following significant features: alignment mechanism, long steel shaft designed to freely pass through the crosshead, and upper and lower end caps to which the sample is secured. To fit into the 100kip MTS wedge grips, threaded rods were included at the top and bottom. A schematic diagram showing the above listed components is presented in *Figure 3.4b*.

For the stiffner used in Phase II tests, an off-the-shelf 100-ton capacity hollow plunger cylinder (HPC) (Enerpac Model No. RRH-1001) was selected. An electric pump (Enerpac Model No. ZE4420LB-FHR) and a pilot operated check valve (Enerpac Model No. V-42) were used to pump hydraulic fluid into the cylinder and to maintain cylinder pressure for passive testing, respectively. During active testing the HPC was controlled by a Parker DFplus servo proportional valve to allow for control based off of hydraulic pressure readings. *Figure 3.5a* shows important components around the HPC.

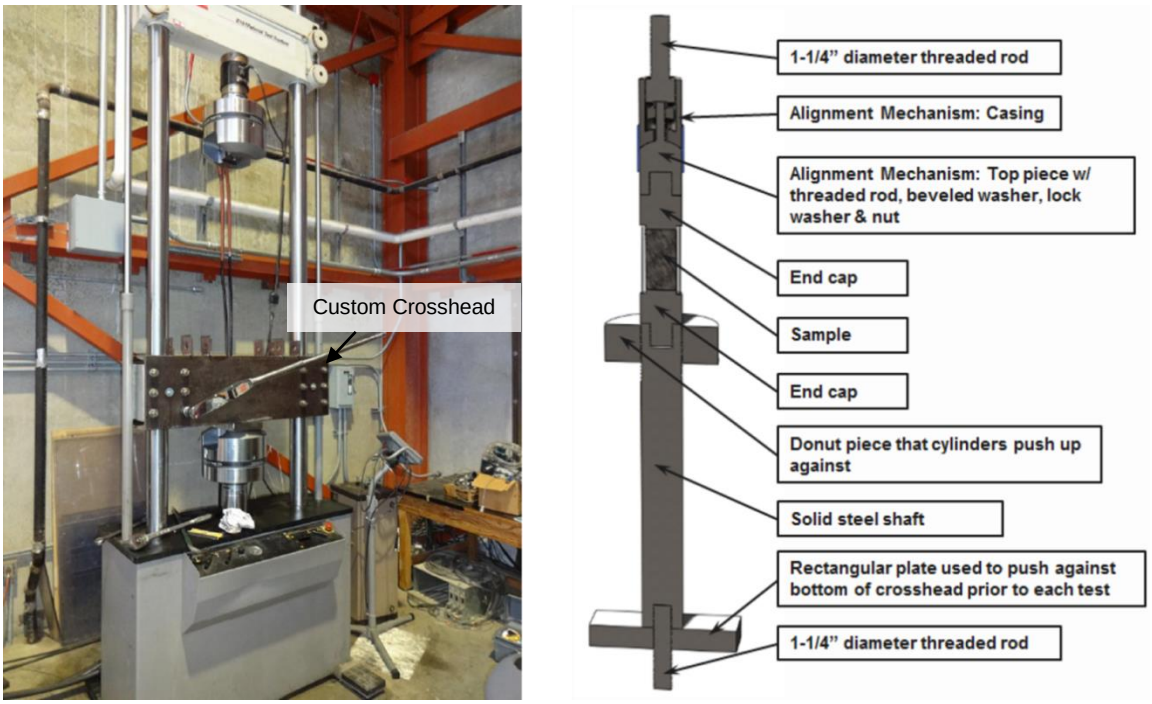

(a) (b)

Figure 3.4: *Testing System Components (1/2), (a) Custom Crosshead, (b) Load Train*

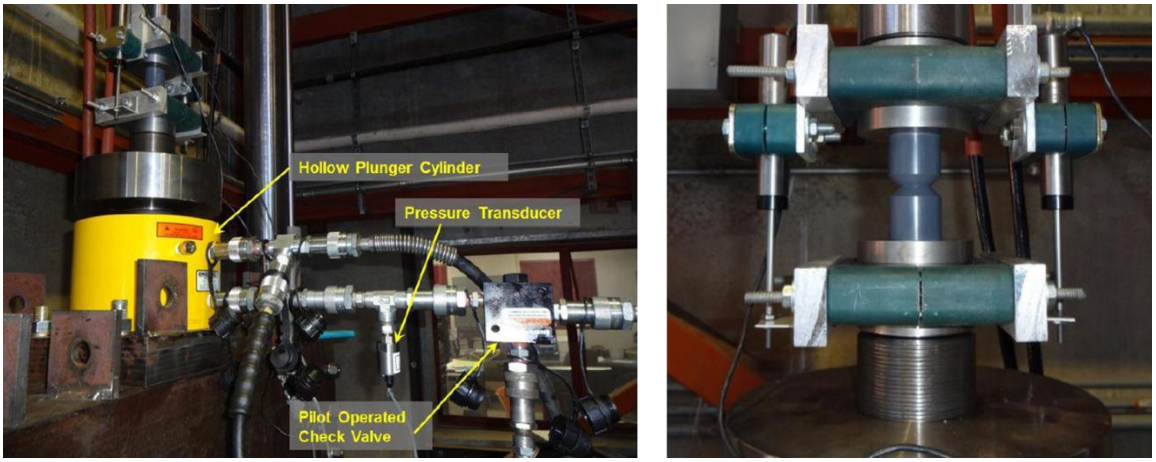

(a) (b)

Figure 3.5: *Testing System Components (2/2), (a) HPC hydraulic components, (b) Sample and LVDT setup*

From Phase I testing it was determined that DC LVDTs (250 DC-EC by Measurement Specialties) would be used to measure the axial displacement of the sample (*Figure 3.5b)*. The load cell and actuator displacement transducer in the MTS testing machine were used to measure the axial force in the sample and the measured actuator piston displacement, respectively. A pressure transducer was used to measure the fluid pressure below the HPC's piston.

3.2.2 Sample Properties

Phase II tests were performed on NSC, UHPC, and surrogate PVC and acrylic specimens. NSC and UHPC specimens were used to evaluate the effectiveness of the stiffener. Surrogate samples were used for troubleshooting of the test setup, ensuring design functionality of the load train and new crosshead, and investigating the load train's ability to allow for a smooth compression to tension transition. Important properties of these samples are listed in *Table 3.2.* *Figure 3.6* presents profiles and pictures of the different samples used.

3.2.3 Testing Descriptions and Procedures

The five different test types used in Phase II at UCSD and their relative purposes are listed below. The subsections that follow describe these tests in greater detail.

Test 0 Aid in determining k_0 and k_2 spring stiffnesses displayed in *Figure 3.7*

Test 1 Aid in determining k_0 and k_1 spring stiffnesses displayed in *Figure 3.7*

Test 2 Determine if designed load train (*Figure 3.4b*) allows for a smooth transition from compression to tension during uniaxial testing

Test 3 Evaluate the effectiveness of incorporating the HPC as a stiffener and determine the desired feedback signal in uniaxial tensile testing

Test 4 Evaluate the effectiveness of controlling the HPC displacement rate to perform uniaxial tensile testing instead of the testing machine actuator

Table 3.2: *Phase II Sample Properties*

Sample Material	Notch Inclusion?	Critical Diameter (in)	Nominal Height (in)	Elastic Modulus (ksi)	Ultimate Tensile Stress (psi)	End Cap Attachment
NSC	No	2	4.5	4,400	570	3M Epoxy
UHPC	No	2	4.5	12,000	980	3M Epoxy
Acrylic	Yes	0.75	5	440	4,500	Threaded
PVC	Yes	0.75	5	410	9,000	Threaded

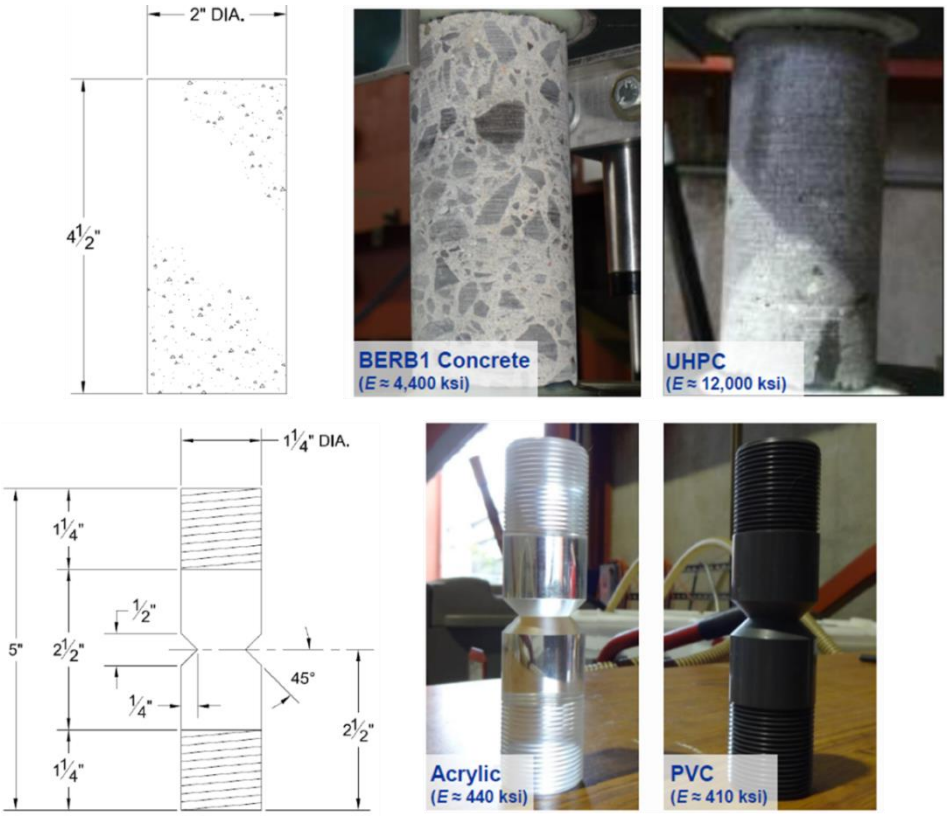

Figure 3.6: *Profiles and Images of Phase II Sample Types*

3.2.3.1 Test Types 0, 1, and 2

The ultimate goals of Tests 0 and 1 were to determine the relative axial stiffnesses of the components included in the experimental test setup. With the inclusion of the HPC jack, the force system can be split into two paths with specific stiffnesses. One path includes the test specimen stiffness (k_s) and the combined stiffness of the upper load train, upper wedge grip, load cell, machine crosshead, and upper steel columns (k_1). The other path is designated by the combined stiffness of the steel donut, HPC, and the custom crosshead (k_2). Both of these parallel paths connect in series with the combined stiffness of the lower steel posts, machine actuator, lower wedge grip, and lower load train (k_0). Significant points from the spring stiffness diagram are also labeled on a picture of the full experimental setup in *Figure 3.7*. The purpose of Test 2 was to confirm that the load train offered a smooth transition from compression to tension.

Test 0 included only the components on the right path of the spring diagram (*Figure 3.8)* to assist in determining constants k_0 and k_2. Tests were performed by pulling the machine actuator down to establish a force-displacement relationship. The setup for these tests is also shown in *Figure 3.8.*

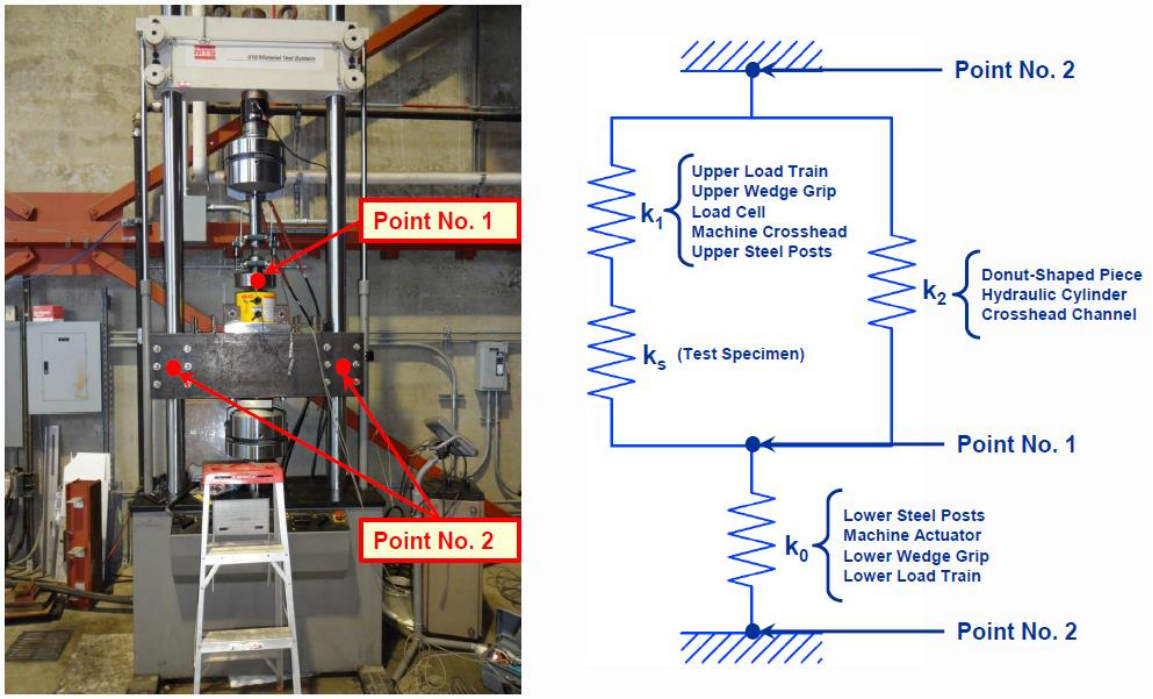

Figure 3.7: *Complete Testing System Spring Stiffness Diagram*

Tests 1 and 2 included only the components on the left path of the spring diagram (*Figure 3.9)* to aid in determining constants k_0 and k_1 and to insure the smooth transition, respectively. Test 1 utilized a simple direct tension test that controlled the machine actuator displacement at a fixed rate. Test 2 initially compressed the sample to 1,000 lbf and then either performed a direct tension test identical to Test 1 or used feedback from the average of the LVDTs to control the machine actuator. Tests 1 and 2 only utilized surrogate specimens and did not include the use of the HPC.

Figure 3.8: *Test 0 Spring Stiffness Diagram and Experimental Setup*

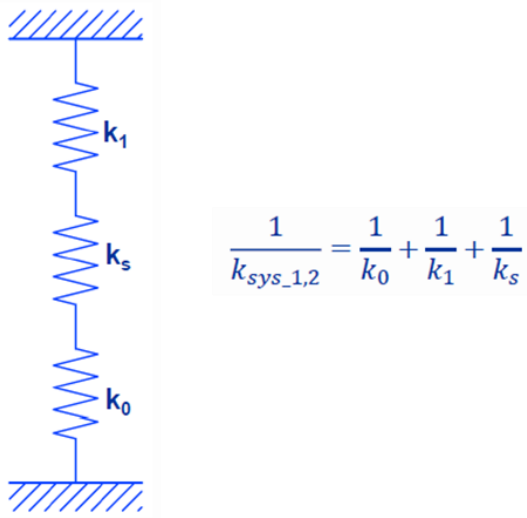

Figure 3.9: *Test 1 and 2 Spring Stiffness Diagram*

3.2.3.2 Test Type 3 (Passive HPC) and Test Type 4 (Active HPC)

Test Type 3 used the HPC in a passive sense, meaning the stiffener was not controlled by any feedback signal. These tests utilized all sample types to evaluate the effectiveness of the HPC. Specimens were initially loaded in compression followed by a direct tension test. The machine actuator was displaced either at a constant rate or based off the feedback from the LVDTs. Two separate feedback signal equations were used as shown in *Eq. 3-1* and *Eq. 3-2*. These have also been employed in other research [45] and were initially presented in *Section 2.3.1.2.* In the equations, ε is the sample strain measured from the average of the LVDTs; C is the specified stain loading rate (e.g. 10^{-6} for concrete samples); σ is the sample stress calculated from the load cell measurements; and E is the elastic modulus of the sample. *Eq. 3-2* is identical to *Eq. 2-3* with the addition of a constant for concrete properties, α.

$$\varepsilon = C \cdot t \qquad (3\text{-}1)$$

$$\varepsilon - \alpha \frac{\sigma}{E} = C \cdot t \qquad (3\text{-}2)$$

The procedure for these passive HPC experiments encompassed four steps. (1) A test would begin by loading the sample in compression to 20% of its tensile strength. (2) The sample was then loaded in tension to 75% of the tensile strength. Both of these steps utilized the force control capability of the testing system. (3) The HPC stiffener was then engaged creating the complete spring diagram shown in *Figure 3.7*. (4) Once engaged, the test was resumed in displacement control using a constant actuator displacement rate or the feedback signals described in *Eq. 3-1* and *Eq. 3-2.*

Test 4 was identical to Test 3 with a few exceptions. Acrylic specimens were not tested. The direct tensile test was only performed using the feedback signals from the average of the LVDTs. Once the HPC stiffener was engaged in (3), the feedback from the specimen was used to control the HPC and the actuator displacement was then held at a prescribed constant rate.

3.2.4 Experimental Results

Table 3.3 presents the complete test matrix of Phase II testing at UCSD. The sample type, feedback signal used, number of tests performed, and whether post-peak control was obtained are all included for each test type. Specific results and findings from a select few of these tests are presented.

Table 3.3: *Phase II Test Matrix*

Test Type	Sample Type	Feedback Signal[1]	No. of Tests[2]	Post-Peak Control?
0	N/A	TMD	4	N/A[3]
1	Acrylic	TMD	2	No
	PVC	TMD	2	No
2	Acrylic	TMD	1	No
	PVC	TMD	1	No
		SD	1	Yes
3	Acrylic	TMD	2	No
		SD	1	No
		LCSSS	1	No
	PVC	TMD	2	No
		SD	1	Yes
		LCSSS	1	Yes
	NSC	SD	2	No
	UHPC	SD	2	Yes
4	PVC	SD	1	Yes
	NSC	SD	0	N/A[4]
	UHPC	SD	0	N/A[4]

[1] TMD = Testing Machine Displacement
SD = Sample Displacement (average of the two LVDT measurements) (*Eq. 3-1)*
LCSS = Linear Combination of Sample Stress and Strain (*Eq. 3-2)*

[2] Number of tests in which sample peak strength was achieved and, if applicable, HPC was engaged

[3] No sample was used in test

[4] Sample failed violently in compression

3.2.4.1 Test Types 0,1, and 2

Results from Test 0 and 1 experiments determined that springs k_0, k_1, and k_2 had axial stiffnesses of 1,800 kip/in, 400 kip/in, and 6,000 kip/in, respectively. *Table 3.4* displays the displacement and corresponding stiffness for each of Test 0's four tests. For visual clarification, the general displacement measurement is explained in *Figure 3.10*. Representative load-displacement curves for Tests 1 and 2 are shown in *Figure 3.11*. These specific tests were performed on acrylic samples. The average of the LVDTs was used to characterize the specimen displacement. The enlarged portion of

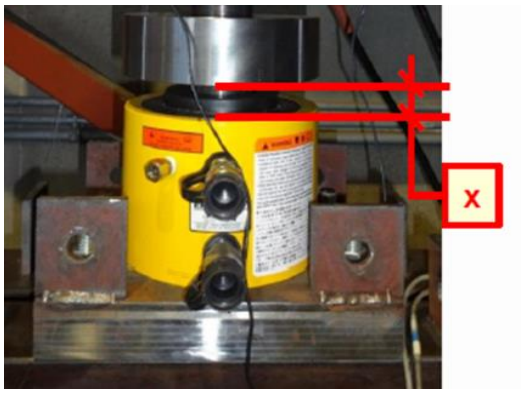

Figure 3.10: *Test 0 Measuring Origin*

Table 3.4: *Test 0 Results*

Trial No.	x (in)	k_{sys_0} (kip/in)
1	0.5670	1370
2	0.7235	1330
3	1.007	1210
4	1.238	1130

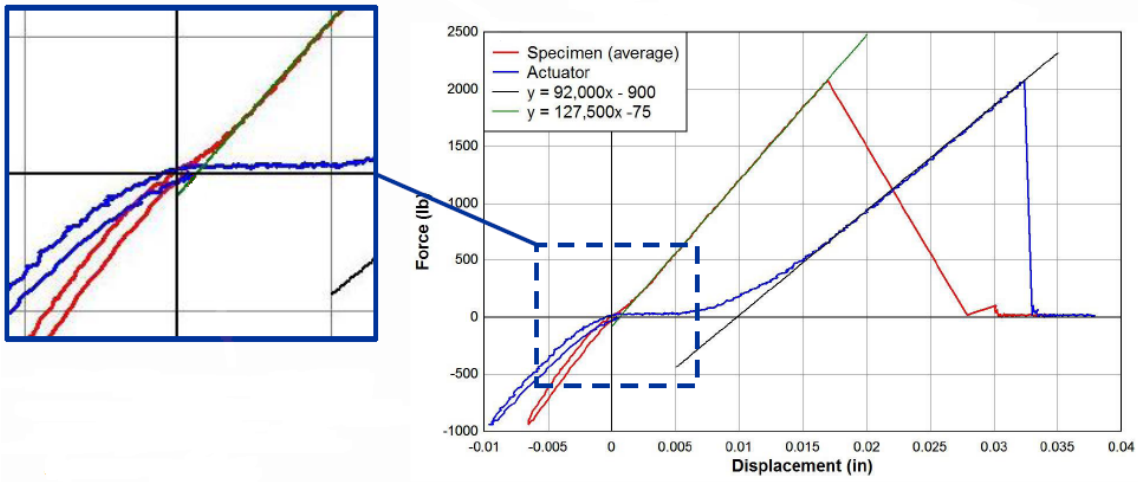

Figure 3.11: *Representative Load-displacement Curves for Tests 1 and 2 on Acrylic Samples*

Figure 3.11, indicates the presence of a fairly smooth compression to tension transition for the specimen, confirming the appropriateness of the load train design. PVC post-peak control was made possible by controlling from sample displacement feedback.

3.2.4.2 Test Type 3 (Passive HPC) and Test Type 4 (Active HPC)

Thirteen individual tests were conducted on the four different types of samples using three feedback signals. During Test 3 and 4 the HPC stiffener was incorporated for uniaxial tensile testing. Surrogate PVC and acrylic samples were initially used to shakedown the system. *Figure 3.12* shows representative load-displacement curves for Test 3 on acrylic samples. Once the stiffening jack was engaged, the axial stiffness of

the testing system increased by a factor of fifteen. This large increase greatly improves the stability of tensile testing of brittle and quasibrittle materials as evident in passive UHPC testing results presented in *Figure 3.13*.

The post-peak softening curve was unable to be obtained for any sample when the testing machine displacement was used as the feedback signal. Passive tests were performed on PVC samples to determine the effects of using *Eq. 3-1* versus *Eq. 3-2* on a

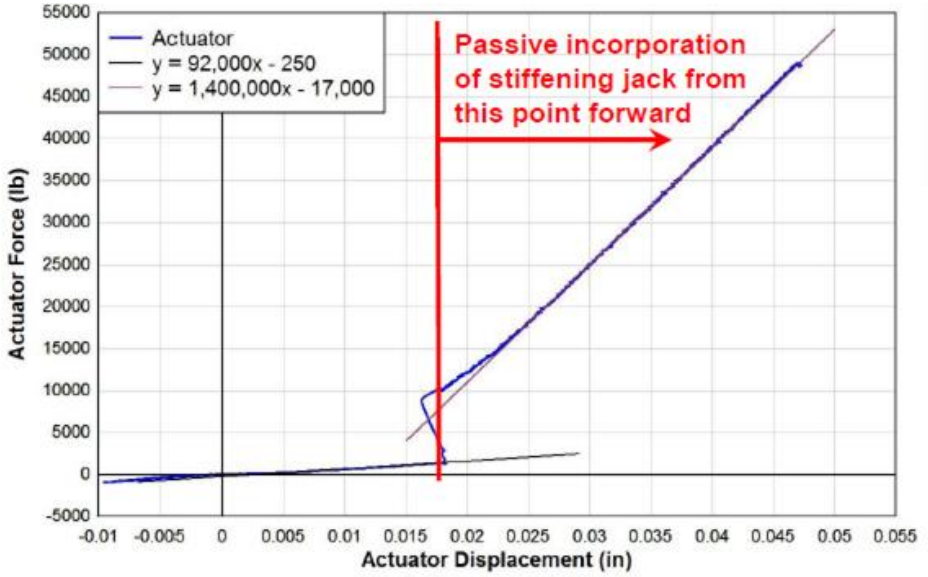

Figure 3.12: *Representative Load-displacement Curve for Test 3 on an Acrylic Sample*

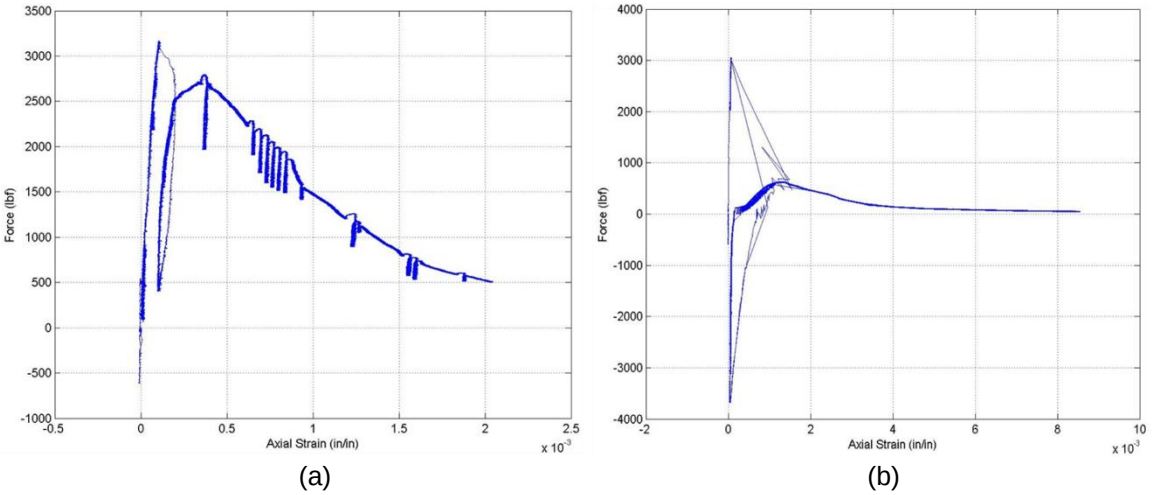

(a) (b)

Figure 3.13: *Effect of HPC Stiffener on UHPC Sample, (a) with stiffener, (b) without stiffener*

uniaxial tension test. The results of the tests are presented in *Figure 3.14* and show no significant difference in PVC behavior. Because of this, *Eq. 3-1* was deemed adequate to use as the feedback for stable direct tensile tests.

Figure 3.15 presents the results from passive uniaxial tensile tests on PVC, NSC, and UHPC. All three tests were controlled off of the feedback signal from the two LVDTs using *Eq. 3-1*. Good data were unable to be obtained for acrylic specimens due to the fracture zone occurring at the thread boundary. The plots show that as the material becomes more brittle (PVC = least brittle, NSC = most brittle), the ability to maintain stability and obtain the total post peak response becomes more difficult. For the PVC specimens, the entire softening response was captured without a drop in load. The UHPC had an initial drop around peak strength, but the system was able to recover as evident by the softening response. For the NSC test, the system was unable to respond after peak strength, failing instantly. These results were consistent through all passive (Test 3) tests.

Test 4 (active HPC) tests used the feedback from the specimen to control the HPC. The machine actuator displacement rate was held constant. Over twelve of these tests were conducted in an attempt to implement this scheme with the MTS controller. At the initial switch from force control to displacement control, the system reversed direction and loaded the specimen in compression. With the exception of one PVC trial, every test resulted in a violent compressive failure as shown in *Figure 3.16.*

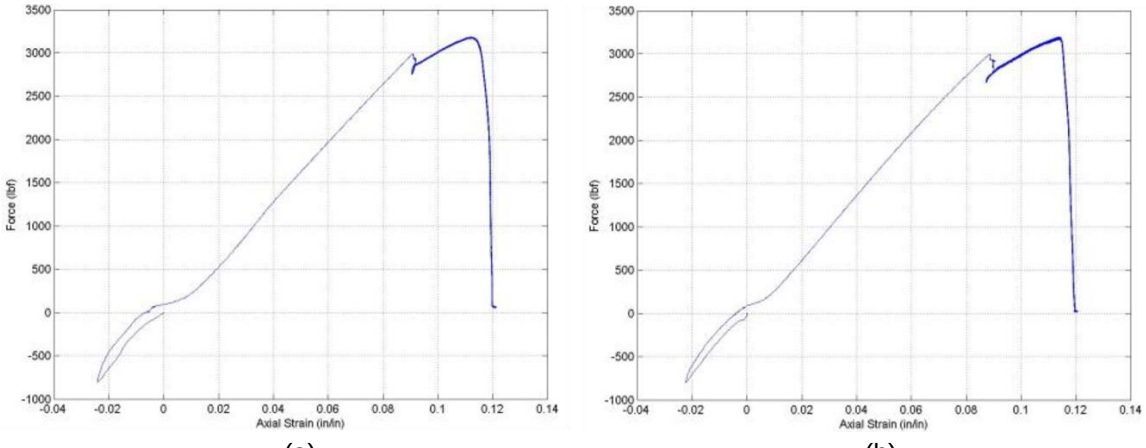

(a) (b)

Figure 3.14: *PVC Axial Strain vs. Force with Feedback from: (a) Eq. 3-1, (b) Eq. 3-2*

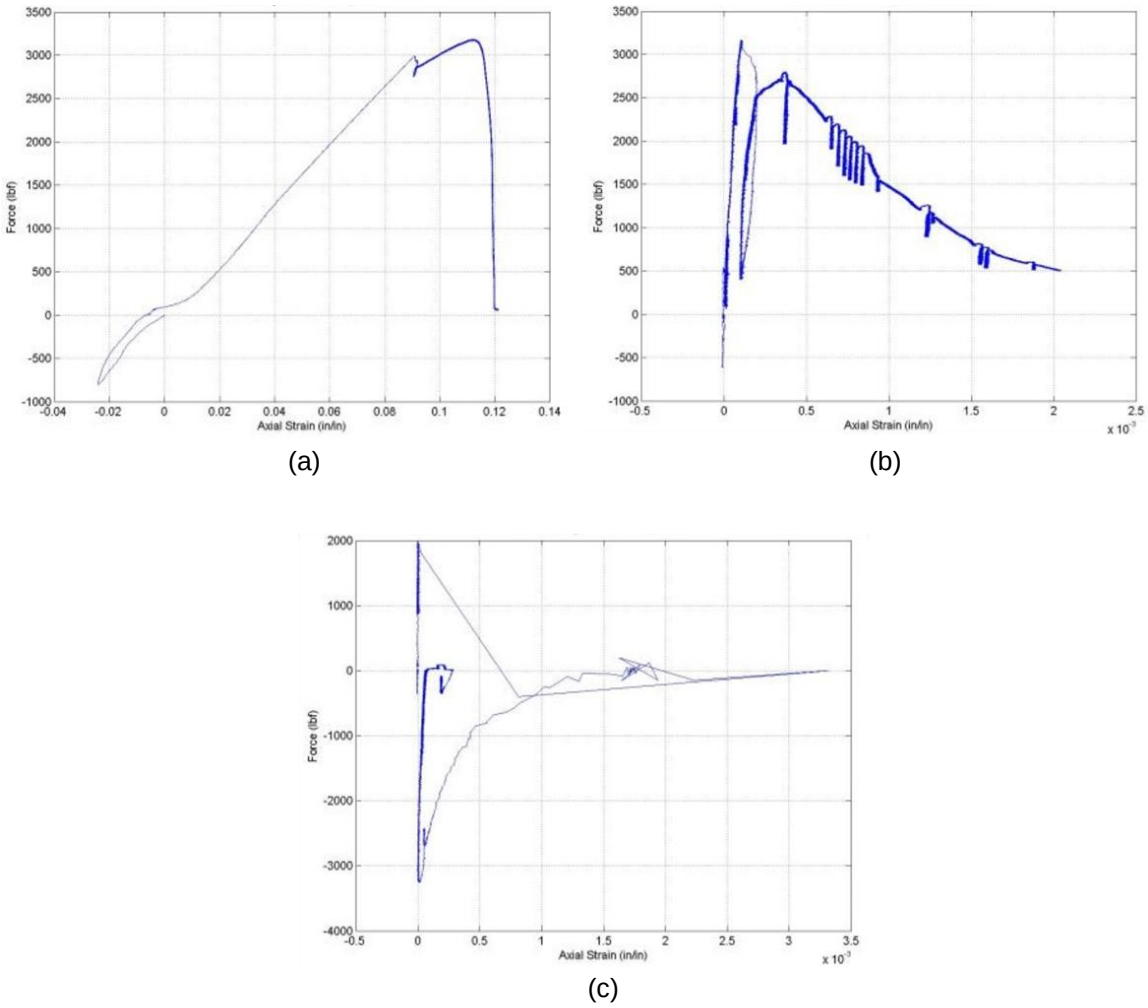

Figure 3.15: *Results of Passive Uniaxial Tensile Tests for Differing Materials, (a) PVC, (b) UHPC, and (c) NSC*

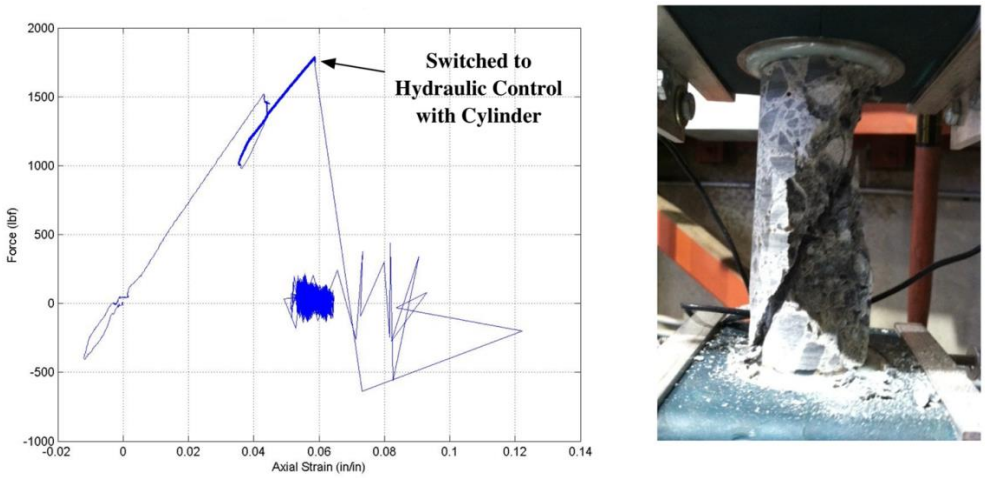

Figure 3.16: *NSC Uniaxial Tensile Test Result from Active Stiffener Concept*

CHAPTER 4: METHODOLOGY FOR UNIAXIAL TENSILE TESTING

4.1 OBJECTIVES

The main objective of the research presented in this thesis is to utilize the knowledge gained in previous phases of testing to further develop and finalize the hypothesized concept. This includes finalizing the design for a novel uniaxial tension testing scheme for UHPC, which at a later time, will be implemented into a triaxial pressure vessel for multi-axial behavior investigations. The active stiffener concept previously presented is vital to employ a uniaxial tensile testing phase into ERDC's triaxial, compression-only load frame. Active stiffener experiments performed at UCSD were unsuccessful in gaining the softening response of UHPC. These early trials are analyzed and the test setup improved upon so that stable tests can be performed.

4.2 APPROACH

The approach taken by this researcher was to (1) fully understand the successes and shortcomings of the experiments performed at UCSD discussed in *Chapter 3*, (2) perform an extensive literature review (*Chapter 2)* to give insight into possible explanations for the previous testing results, and (3) after understanding these discrepancies, make needed alterations to the experimental setup and testing procedure in hope to perform stable, uniaxial tensile tests on UHPC using the HPC as an active stiffener. The following sections pertain to the details of the final step in the design approach.

4.3 ISSUES IN PRIOR TESTING

Probable issues that may have resulted in instability during testing are described in brief below. Action/inaction taken toward these issues is presented and the reasoning behind each decision is discussed.

4.3.1 Measured and Control Gage Length

It was shown in *Section 2.3.1.1* that the control gage length greatly affects the stability of a test. If too large, the crack-opening rate becomes uncontrollable, and the specimen can rupture immediately. Even if a stable test is able to be performed, a large gage length may not report accurate local fracture zone behavior. In addition, *Section*

2.3.1.2 shows that control based upon the average of LVDTs may not be sufficiently accurate to attain post-peak behavior of concrete. Literature demonstrates that maximum displacement rate sometimes needs be used as the controlling parameter.

For these reasons, using the full sample gage length is troubling. While this large length ensures the capture of the crack location of an unnotched specimen, it makes stable testing of more brittle concretes extremely difficult. This and not controlling off the maximum LVDT displacement rate are the most likely reasons for the lack of successful NSC tests. However, due to the additional ductility in UHPC, many stable tests were achieved, but the results can be misrepresentative as they are not limited to local fracture occurrences. Also because only two LVDTs were used, three dimensional effects of crack propagation were impossible to analyze.

Due to limited funds and time constraints, research at GT did not improve on this aspect of testing but included it as a variation for possible improvement for the triaxial test setup in the discussion section. Because the main goal was to perform stable tests on UHPC specimens, controlling displacement off the average of the full specimen-length LVDTs was deemed acceptable. To approximate the stress-crack opening curve required in the FCM, an approach presented in multiple references [16, 25] was utilized. This method estimates the crack-opening width, w, by subtracting residual deformation at peak stress, δ_0, and the elastic deformation at any point on the stress-displacement curve outside the fracture zone, δ_e, from the specific deformation reading δ. This process is shown schematically in *Figure 4.1*. The described method is used to better

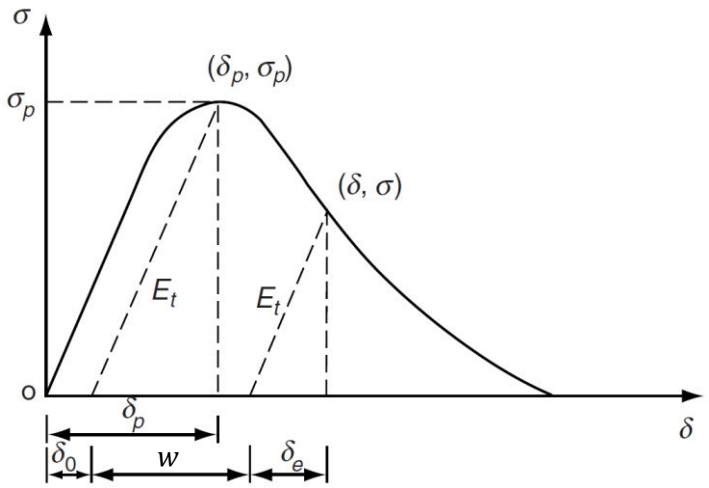

Figure 4.1: *Method for Crack Opening Approximation for Uniaxial Tensile Tests (from [25])*

interpret the results from testing at GT. However the large gage lengths influence the findings, so recorded strains and crack openings should not be taken as the UHPC's true material properties. In *Chapter 6* a solution to allow for more accurate and reliable results is presented for future implementation.

4.3.2 Loading Rate

From the literature review, the typical loading rates for NSC ranged from 1.65E-5 in/min to 1.8E-4 in/min, however the majority were closer to 2E-5 in/min. The loading rate at UCSD was 2.7E-4 in/min, which is relatively high. This may have led to instability, especially since the total length of the sample was used for feedback. Because of this, testing at GT was carried out under deformation rates close to 2.5E-5 in/min.

4.3.3 Boundary Conditions

As shown in the literature review, boundary conditions can greatly affect the results of uniaxial tensile tests. Prior testing utilized a centering mechanism to help with specimen alignment issues during gripping. The opposite end was screwed into the load train supported by the custom crosshead, creating more of a fixed boundary. The centering mechanism allowed for small rotations, which destroy any attempt at a fixed-fixed boundary. This ability for instantaneous rotation also creates stability issues in trying to perform NSC uniaxial tensile tests, which may also be responsible for the lack of a successful test. Because of this, a fixed adapter was designed for testing at GT.

4.3.4 Maximum Aggregate Size

Coarse aggregates were not included in the UHPC specimens, but were in the NSC. The maximum size aggregate for the NSC samples was roughly 0.65 in. The critical width (i.e. 2 in.) is only three times larger than the maximum aggregate, which is significantly less than the advised upon $8d_{max}$. Previous research shows that this will result in large standard deviations in ultimate tensile strengths. Because these NSC specimens were provided by the sponsor, the size effects were not improved and are most likely represented in the results.

4.3.5 Control Parameter for Active Stiffener

During active testing at UCSD, it was attempted to control the HPC based off of desired hydraulic pressure during testing. It is difficult however to perform a fine-

controlled test under pressure control. Considering the delicate process of controlling crack propagation of concrete, it is likely that regulating pressure led to the high instability during Test Type 4 (i.e. active tests). To help solve this problem, the HPC jack was controlled based off of a ± 10V error signal sent to the servo-valve. This allowed for more or less flow to be released to the HPC until the difference between the average LVDT readings and the command was zero.

4.3 EXPERIMENTAL SETUP

4.3.1 Materials

The 3M DP460 off-white epoxy and flat end caps from Phase I testing were used for specimen gripping. The NSC and UHPC specimens used during GT experiments were the same as those from earlier Phase II tests and previously described in *Section 3.2.2.* The specific material compositions of these concrete specimens were not provided. However it was determined that the UHPC specimens were reinforced with glass fibers. The PVC surrogate samples used beforehand were limited, so new specimens were manufactured for shakedown tests. During testing in this research both the old and the new surrogate PVC samples were utilized. The new samples were made identical to those presented in *Figure 3.5* except the cut angle was at 30˚ to the horizontal. This change was made due to available machining tools. Since these surrogate specimens were used only for trial runs, the difference was deemed insignificant. No acrylic samples were tested.

4.3.2 Test Setup

All of the equipment used from the previous testing was relocated to GT with the exception of the MTS load frame. The SATEC 100 kip testing frame in the Hi-bay laboratory at the Manufacturing Research Center (MARC) was chosen as the substitute due to its similar dimensions and stiffness to the MTS 810 Material Testing System with the Model 318.50 Load Unit Assembly. This allowed for the ability to use all previous components including the load train and custom crosshead with HPC assembly.

Tests performed were divided into passive and active groups, based on whether feedback was used to control the HPC. Specific details of the components used in each type of test are discussed in the following sections. More detailed information can be found in *Appendix B.*

4.3.2.1 Passive Tests

The overall testing frame setup for passive tests is shown in *Figure 4.2*. As mentioned testing was performed on a SATEC 100 kip load frame, which included a 100 kip load cell, MTS collet grip, twin Moog valves, and a Hunger Hydraulic Actuator. The load cell and machine actuator were all calibrated and tuned by MTS. The controller used for this machine was the TestStar IIs Version 3.2C 929.

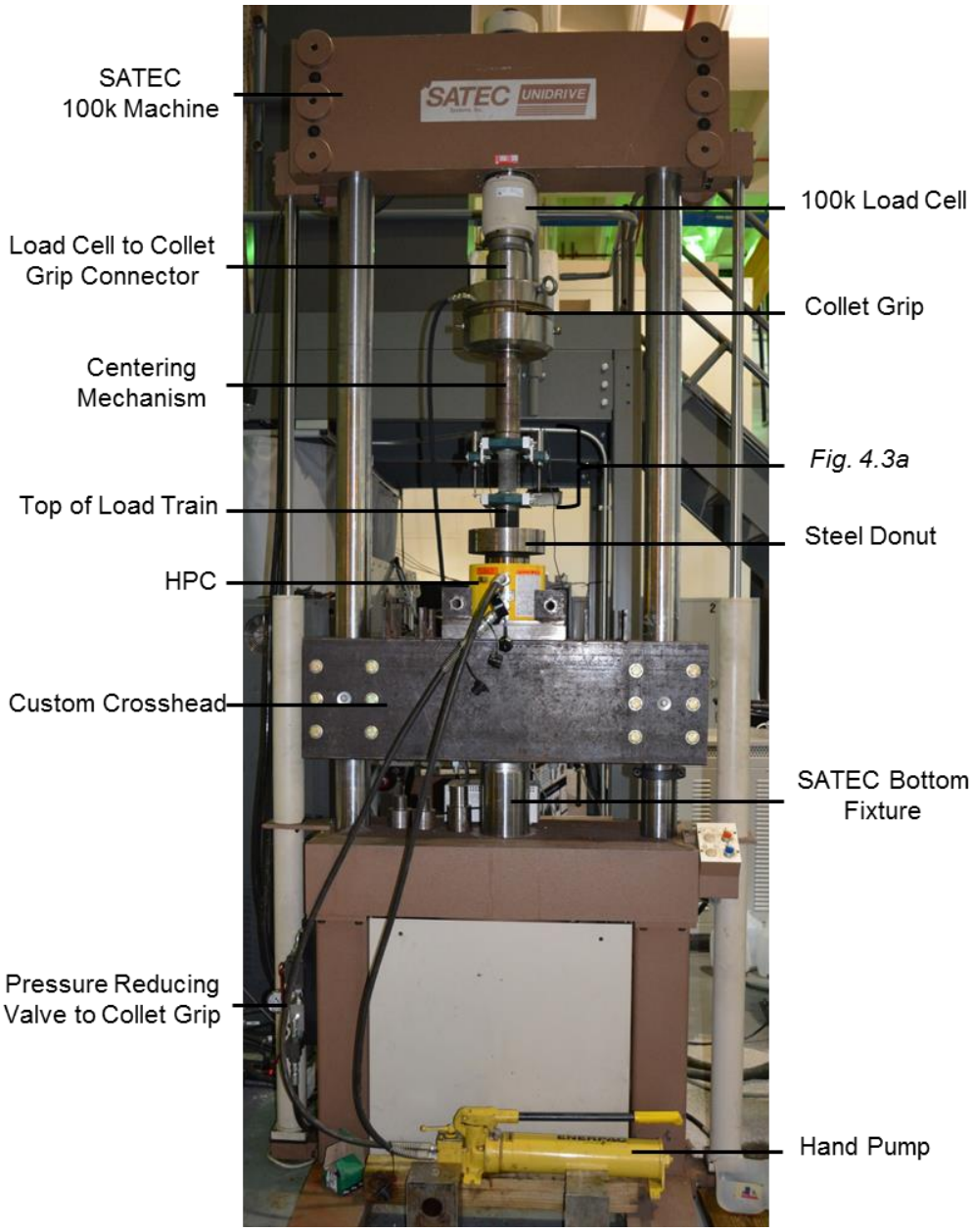

Figure 4.2: *GT Passive Testing Experimental Setup*

Connectors were designed so that the load train from *Figure 3.4b* could be screwed into the machine actuator and also properly fit into the 2 in. diameter collet shown in *Figure 4.3b.* The DC LVDTs and overall instrumentation setup from UCSD were used during tests (*Figure 4.3a)*. A fixed adapter shown in *Figure 4.3b* was designed and implemented in place of the centering mechanism to increase rotational stiffness. An Enerpac hand pump was used to control the initial pressure in the HPC. During testing the pressure would slowly increase as the deformation in the specimen increased.

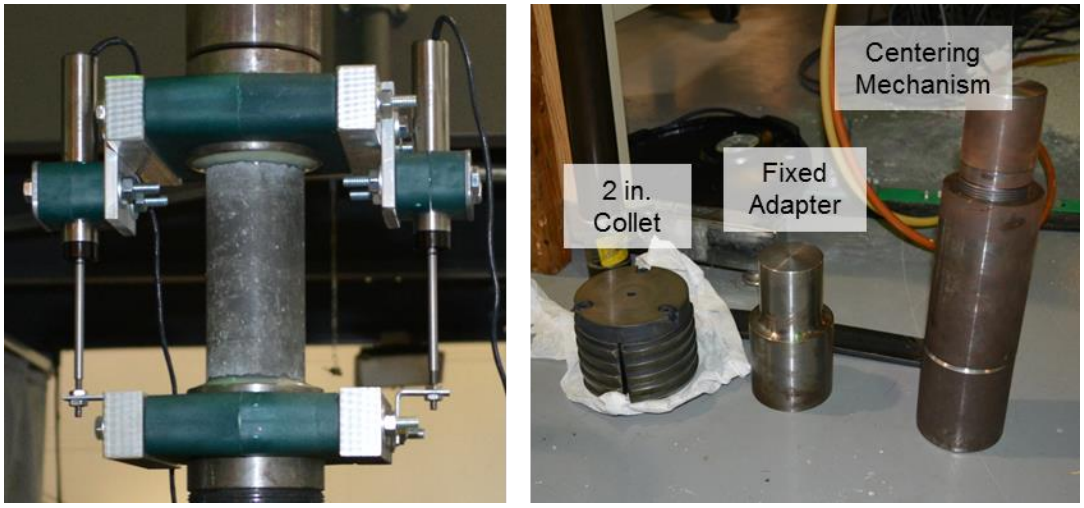

(a) (b)

Figure 4.3: *Test Setup Components, (a) Glued Specimen with LVDT instrumentation, (b) Collet, fixed adapter, and centering mechanism*

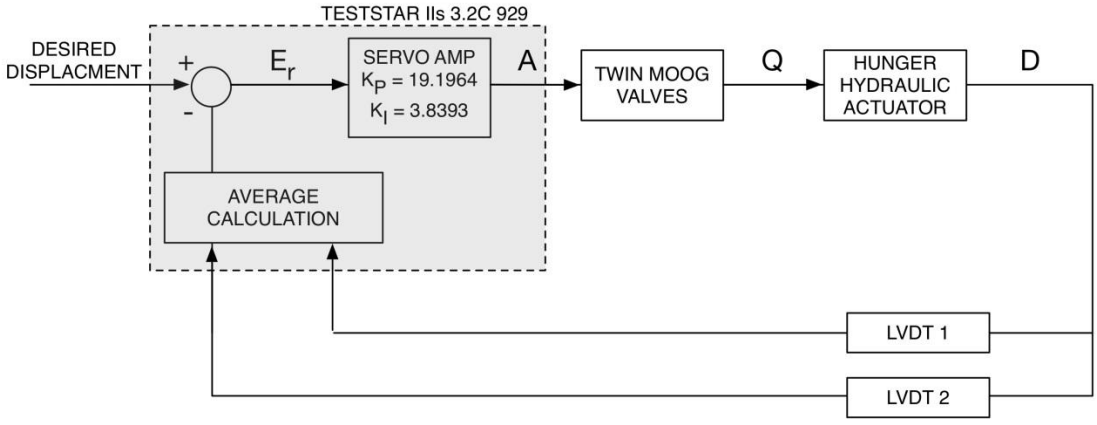

Figure 4.4: *Control Block Diagram for Passive Testing*

Most passive tests utilized feedback from the LVDT readings to control the machine actuator while the HPC pressure was left uncontrolled. This feedback was calibrated and tuned in the controller so that the machine actuator could be used to perform a uniaxial tensile test. A block diagram for the passive test control scheme is shown in *Figure 4.4* on the previous page, where E_r = error, K_P = proportional gain, K_I = integral gain, A = amperage, Q = hydraulic flow, and D = displacement.

4.3.2.2 Active Tests

To meet the research objective of devising a uniaxial tensile testing technique to implement into a compression only pressure vessel, the design of the passive tests had to be slightly altered. The two main differences between the testing schemes are the inclusion of a load cell at the bottom of the load train and utilization of the Parker DFplus servo proportional valve to control the displacement of the HPC jack during active testing. Both of these are shown in *Figure 4.5*. The significance of the bottom load cell

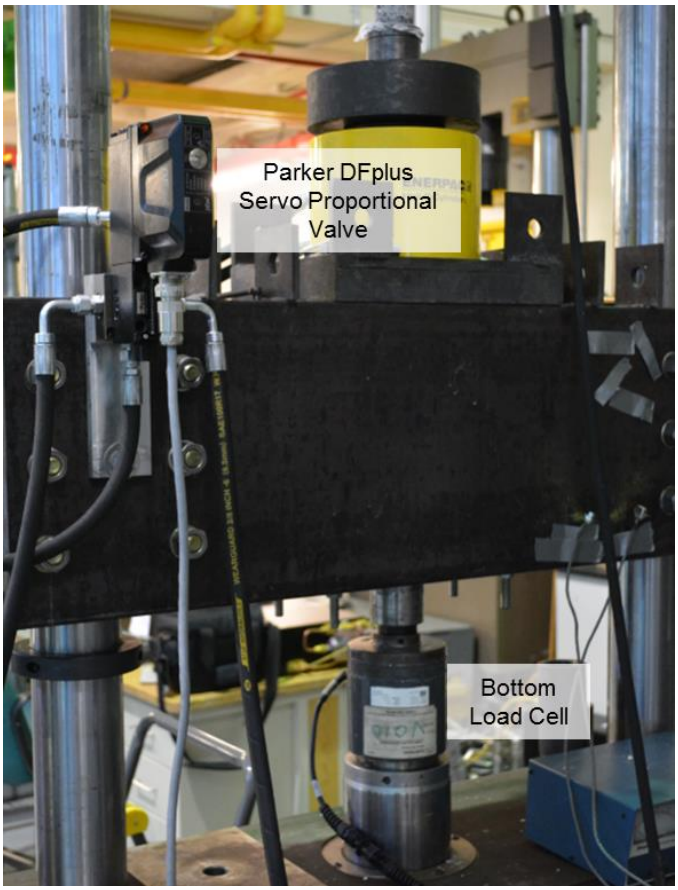

Figure 4.5: *Unique Components to GT Active Testing Experimental Setup*

is to use its readings as feedback for the machine actuator control so that constant compression can be applied, emulating a compression only load frame. Also, due to loss of vertical space with the addition of the bottom load cell, the fixed adapter had to be used in every active test.

While the changes in components from passive to active testing were slight, the control scheme (*Figure 4.6)* became much more complicated. During testing one command was sent to the machine actuator to hold the load in the bottom load cell at a constant force. At the same time, another command was sent to the HPC jack to control the displacement of the average of the LVDTs. The latter command utilized the error in the average LVDT readings to send a ± 10V signal to the Parker DFplus servo valve. This was undertaken through readout channels in the TestStar IIs controller. There was no transfer of data between these two loops. However, each loop was able to adjust to the physical variations driven by the opposing loop through use of its relative feedback signal to maintain the desired command. The variables in *Figure 4.6* are identical to the ones in *Figure 4.4* with the addition of V = voltage.

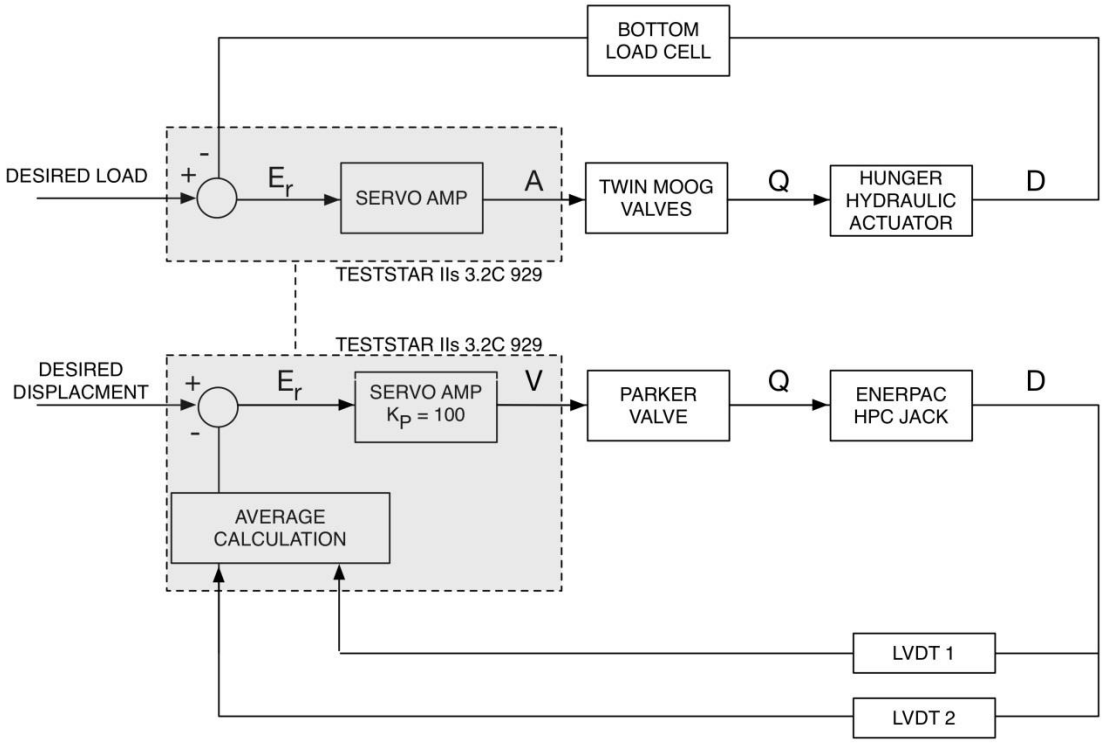

Figure 4.6: *Control Block Diagram for Active Testing*

4.4 TESTING PROCEDURE

Different variables were altered during active and passive testing to help determine the critical aspects of devising a unique uniaxial tensile testing procedure. These independent variables included test type (passive without feedback, passive with feedback, and active tests), specimen type (UHPC and NSC), load rate, length of epoxy cure time, boundary conditions (centering mechanism and fixed adapter), bottom load train stiffening force, and compressive pre-load in the specimen. The effects of these variables on load-displacement curves are compared in *Chapter 5*. All experiments performed strictly followed either a passive or active testing procedure. The specific steps in these procedures are listed as follows:

Passive Testing Procedure

1. Set sample along with instrumentation in load frame and pressurize the collet grip
2. Apply 500 psi to the steel donut through the manual hand pump
3. Preload the sample to a specified compression force
4. Begin loading the sample in tension by ramping up to a specified tensile force (e.g. 70% of tensile load capacity) in 10 sec
5. Continue tensile loading through a constant displacement rate of either the machine actuator or the average of the two LVDTs

Active Testing Procedure

1. Bolt load train donut to HPC
2. Manually command force in bottom load cell to 0 lbf
3. Set sample along with instrumentation in load frame
4. Move the top crosshead and HPC jack so that the specimen is securely located inside the collet grip and pressurize the grip
5. Manually command the bottom load cell to a specified compression force
6. Using the error of the LVDT feedback, manually command the HPC cylinder until the top load cell is at a desired preload compressive force
7. Perform the uniaxial tensile test where the specified bottom load cell force is held constant, while the HPC jack is displaced at a constant rate utilizing the feedback from the LVDT readings

4.5 DATA ACQUISITION AND VALIDATION

Data were acquired through the TestStar IIs controller at varying intervals. Earlier tests used lower data acquisition rates (e.g. 1point/3sec and 2point/sec). It was deemed necessary to increase this rate to 20point/sec. The time, force measured in each load cell, both LVDT readings, and machine actuator position were monitored for each test performed. In analyzing the rotation that occurred during testing, the single LVDT readings were projected onto the sample as discussed in *Appendix C.* Pictures were taken after every test to document crack location and path. Crack propagation was documented during a few of the tests.

Results were compared to those documented in previous phases of the experimental program. This comparison gives some validation to the repeatability of this uniaxial tensile testing scheme. Since the specific UHPC supplied included glass fibers and not steel, findings were not able to be validated by previous UHPC uniaxial tensile test data. The resulting stress-crack opening curves are compared to similar experiments found in the literature review. However it should be reminded that the objective of this research project is to develop a stable, novel uniaxial testing scheme, not to fully and precisely characterize a new concrete material.

CHAPTER 5: RESULTS AND ANALYSIS

The results of the uniaxial tensile tests performed on PVC, NSC, and UHPC specimens are presented in this chapter and are analyzed to determine whether the active stiffener testing scheme is a viable option for uniaxial, and eventual triaxial, extension tests of UHPC. Lastly, the fracture energy, G_f, and characteristic length, l_{ch}, of UHPC uniaxial tensile tests are discussed.

5.1 OVERALL RESULTS

Over the duration of this GT phase of the experimental program, seventeen different uniaxial tensile tests were performed of which ten utilized the active stiffener scheme. A test matrix including the relative test number, boundary condition (centering mechanism or fixed adapter, shown in *Figure 4.3b)*, epoxy cure time, feedback signal, displacement rate at peak load (i.e. critical load rate), sample preload, machine stiffening force, and stability of each test is presented in *Table 5.1*. The successful and semi-successful tests for PVC, NSC, and UHPC are shown in *Figure 5.1, Figure 5.2,* and *Figure 5.3* respectively. All displacement values are the average of both LVDT readings. Unless otherwise stated, this holds true for all plots in this chapter.

The PVC tests were used as trial runs for the two different testing schemes. The passive tests (*P1* and *P2)* employed the same sample type as previous UCSD tests, but differed in boundary conditions. Their results were similar to those presented in *Figure 3.13* from previous work at UCSD. The active test (*A1)* was performed using the new PVC sample machined at GT. Its result proved that the new testing scheme (*Figure 4.6)* could be used to perform stable uniaxial tensile tests

The NSC tests had a low success rate and were highly variable. Only two tests (*P4* and *P5*) were controlled past the peak load. However both of these ultimately resulted in instability during the softening branch decent. These issues were expected due to the relatively large maximum size aggregate and full specimen control gage length. Regardless, the NSC results from the current procedures were greatly improved from the previous testing attempts where not a single passive stiffener test reached the softening phase and all active stiffener tests failed violently in compression.

The UHPC tests were overall positive with a 50% success rate of maintaining stability over the duration of the test, including two successful active stiffener tests. This

Table 5.1: *GT Phase II Test Matrix*

Test Type	Sample Type	Test No.	Boundary Condition[1]	Epoxy Cure Time (days)	Feedback Signal[2]	Critical Load Rate (in/min)	Sample Preload[3] (lbf)	Stiffening Force[3] (lbf)	Post Peak Control?
Passive Stiffener	PVC	P1	CM	N/A	TMD	2.25E-5	0	N/A	Yes
		P2	FA	N/A	TMD	2.25E-5	400	N/A	Yes
	NSC	P3	CM	>2	TMD	2.25E-5	0	N/A	No
		P4	CM	>2	SD	2.25E-5	0	N/A	Yes[4]
		P5	FA	1	SD	2.25E-5	450	N/A	Yes[4]
	UHPC	P6	CM	>2	TMD	5.00E-5	100	N/A	Yes
		P7	FA	1	TMD	2.50E-5	0	N/A	Yes
Active Stiffener	PVC	A1	FA	N/A	SD	N/A	1000	500	Yes
	NSC	A2	FA	N/A	SD	2.25E-5	1100	500	No[5]
		A3	FA	1	SD	2.25E-5	450	500	No[6]
		A4	FA	>2	SD	2.25E-5	550	500	No[5]
	UHPC	A5	FA	1	SD	2.50E-5	450	750	Yes
		A6	FA	>2	SD	3.00E-5	400	500	No[6]
		A7	FA	>2	SD	3.00E-5	300	500	No
		A8	FA	>2	SD	2.50E-5	1000	1000	Yes
		A9	FA	>2	SD	2.50E-5	550	750	No[6]
		A10	FA	>2	SD	2.50E-5	350	10000	No[7]

[1] CM = Centering Mechanism, FA = Fixed Adapter (*Figure 4.3b)*

[2] TMD = Testing Machine Displacement, SD = Sample Displacement (average of the two LVDT measurements) (*Eq. 3-1)*

[3] All loads are in compression

[4] Lost stability during softening near half of peak load

[5] Damage imposed on sample during initial gripping

[6] Lost stability at peak load, but partially recovered

[7] Failure due to peeling epoxy at end cap interface

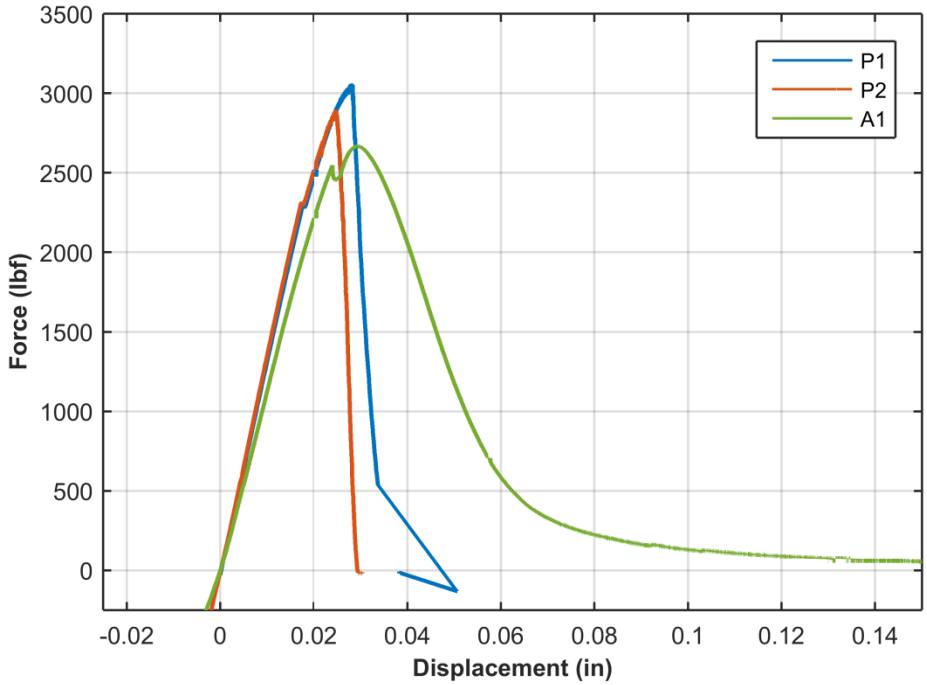

Figure 5.1: *Load-displacement Curves for P1, P2, and A1 PVC Specimens*

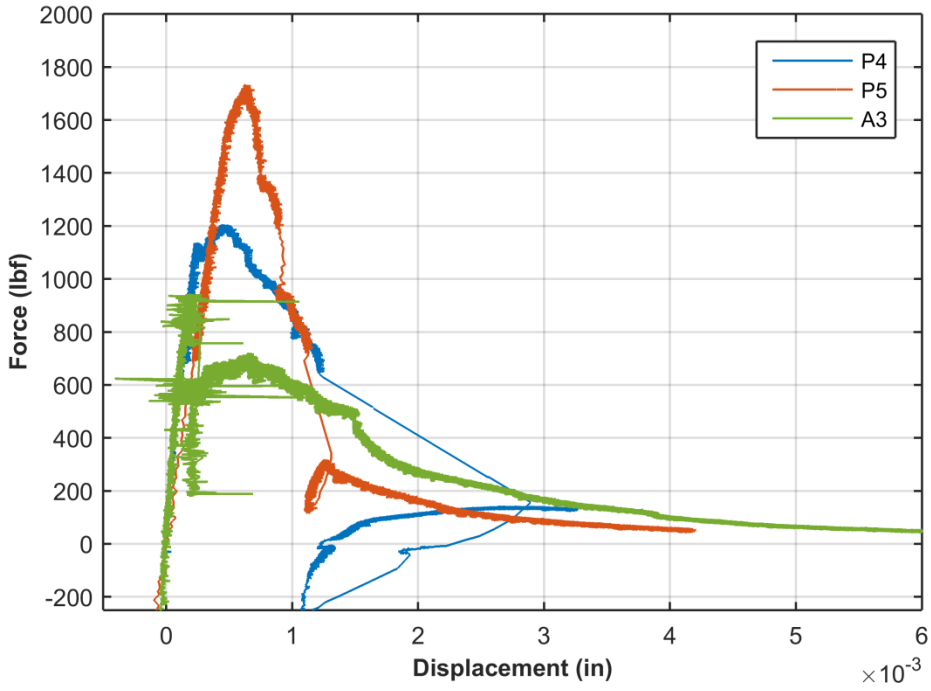

Figure 5.2: *Load-displacement Curves for P4, P5, and A3 NSC Specimens*

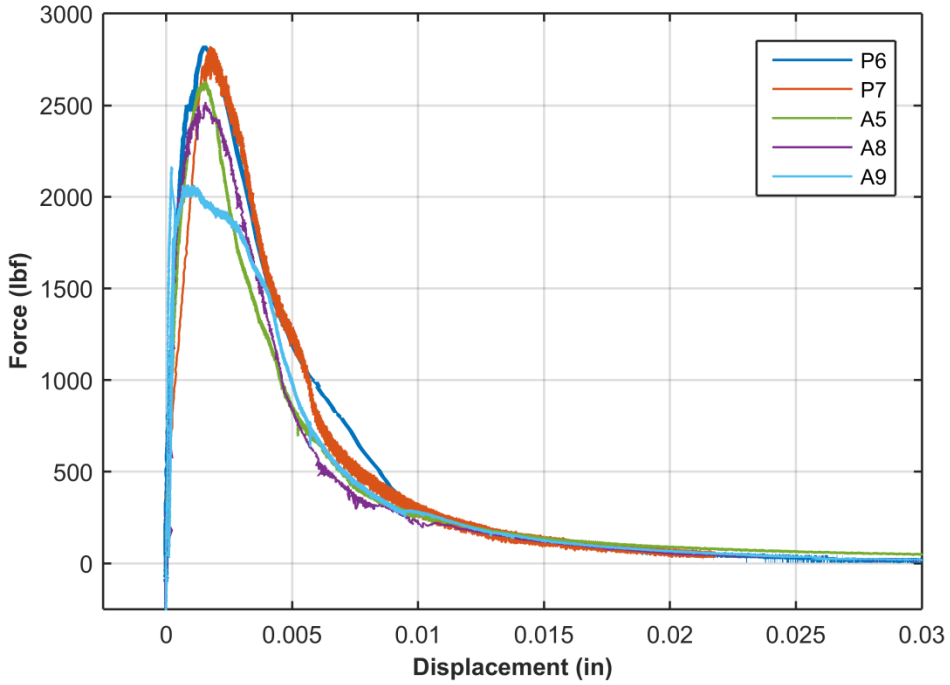

Figure 5.3: *Load-displacement Curves for P6, P7, A5, A8, and A9 UHPC Specimens*

success rate is often acceptable for uniaxial tensile tests on unnotched specimens. The load-displacement curves (*Figure 5.3)* of these successful tests and one semi-successful test are similar, showing high precision. Also the load-displacement curve of *P1,* which utilized the centering mechanism, is comparable to the UHPC results from the previous phase as shown in *Figure 5.4.* These results are promising and help validate the active stiffener scheme for uniaxial tensile testing of UHPC which was the main goal of this research. Overlapping cracks (*Figure 5.5a*) and fiber crack-face bridging (*Figure 5.5b)* were observed during UHPC tests, relating to higher fracture energy and ductility. The increase in ductility, especially due to fiber crack-face bridging, is the most likely reason UHPC tests were stable under all loading conditions and feedback signals, while the NSC tests were not.

5.2 Uniaxial Tensile Test Factors

Multiple factors were varied during the testing phase, which can be found in *Table 5.1*. Upon reviewing the load-displacement plots in their entirety, four dominating

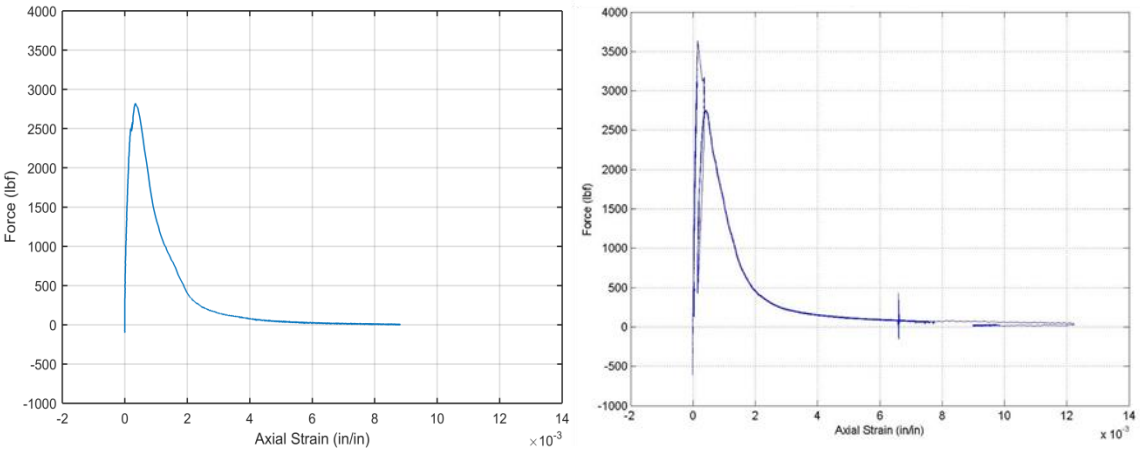

(a) (b)

Figure 5.4: *UHPC Load-displacement Comparison: (a) P1 at GT, (b) UCSD*

(a) (b)

Figure 5.5: *Fracture Phenomenon, (a) A8 Overlapping Cracks, (b) A5 Fiber Crack-face Bridging*

elements seemed to emerge as major influences in the stability and outcomes of the uniaxial testing setup and scheme utilized in this research. These include: rotational stiffness, feedback signal, specimen preload, and the bottom stiffening force in the load frame.

5.2.1 Rotational Stiffness

It should be noted that because only two LVDTs were used, out-of-plane rotation during testing is impossible to analyze. Because of this, if a specimen rotated perfectly out of plane, both LVDTs would read identical results and express that no rotation occurred. Therefore plots that attempt to present rotational effects were only used to gain insight into possible significant influences.

Figure 5.6 shows the absolute difference in LVDT readings versus normalized time up to each UHPC test's relative peak load. This plot seems to show that while the CM test (*P6)* exhibited the largest relative change in rotation near peak load, the overall rotation was not always greater than the FA tests. The two cases with the lower epoxy cure time (*P7* and *A5)* display the most rotation. It seems that the boundary conditions and epoxy cure time both influenced the rotation during testing. Because of this, these factors are further analyzed.

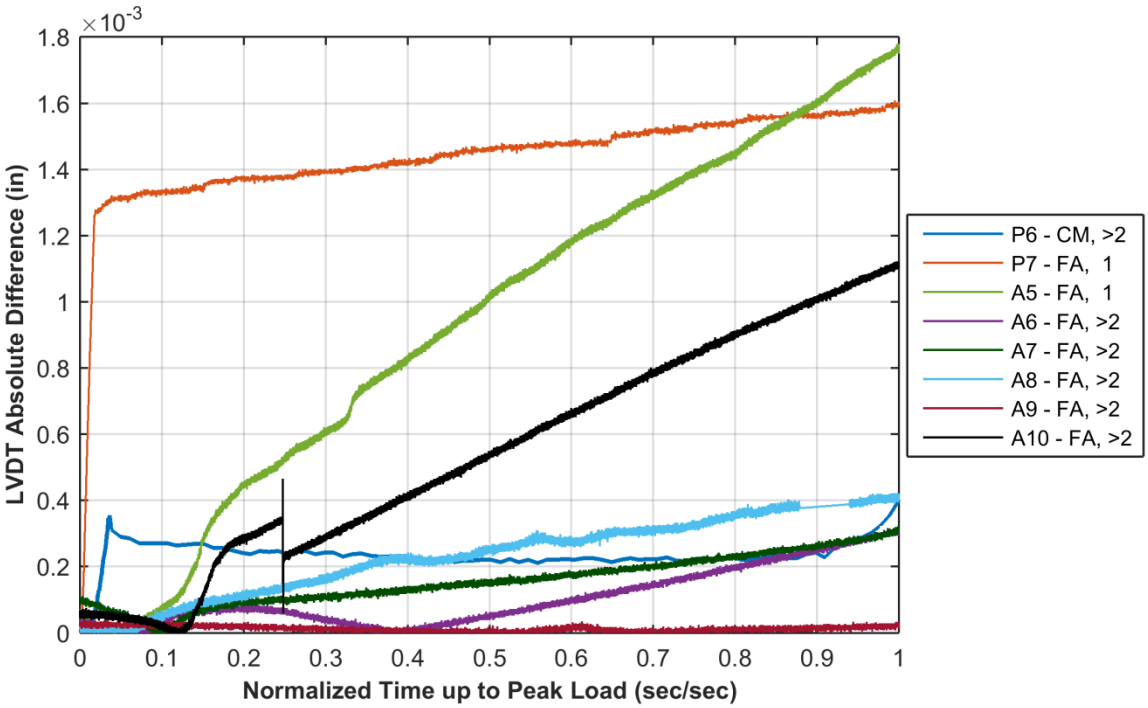

Figure 5.6: *UHPC Specimens' LVDT Absolute Difference up to Peak Load*

5.2.1.1 Boundary Condition

The fixed adapter was designed and utilized for two reasons: (1) to limit the slack between the machine actuator displacement and the specimen displacement and (2) to impede the crack opening rate when controlling off the LVDT average. Both of which would improve overall stability.

Figure 5.7 and *Figure 5.8* display the load and displacement readings over the test duration for UHPC specimens, which implemented the CM and FA, respectively. These results show that the FA did indeed limit the slack between the machine actuator and specimen. The early differences evident in *Figure 5.8* may be attributed to gaps in the threaded parts. These small openings can create a similar condition to the CM when transitioning from compression to tension.

When controlling off the feedback from the average of the LVDTs, the actual crack-opening rate is not regulated if rotation occurs. Instead, the crack is potentially propagating at a much faster rate than expected. The increased rate may limit stability during testing and is much more likely to occur when utilizing the CM. The load-displacement curves for the tests presented in *Figure 5.7* and *Figure 5.8* are shown in *Figure 5.9* and *Figure 5.10*, respectively. Around the 250 – 300 second time frame in *Figure 5.7* and the 2700 – 1700 lbf range in *Figure 5.9,* LVDT1 was opening rapidly, while LVDT2 was staying fairly constant. If the average of the LVDTs was used to control during a similar test on a more brittle material, maintaining stability would be much less likely. This is a possible reason as to why a complete, stable NSC test was not obtained.

While the FA was a good solution in theory, it made alignment and gluing difficult due to the required precision. If the specimen did not align in the collet grip perfectly, a moment would be introduced causing initial stress concentrations to form near the boundary. This adapter issue can be seen in *Figure 5.11*. After failure, the PVC specimen that utilized the CM (*Figure 5.11a)* retained the initial alignment, while the specimen which employed the FA (*Figure 5.11b)* had slightly offset failure faces. The more a specimen is initially misaligned, the greater the induced stress concentrations and built-up energy become after gripping, possibly leading to an initial failure as evident in tests *A2* and *A4* shown in *Figure 5.12*. If failure or crack initiation does not immediately occur, this built up energy may be released suddenly at a specific tensile load, causing either a momentary or permanent loss in stability such as test *A3* shown in *Figure 5.12* and all tests shown in *Figure 5.13.* Due to the increased ductility in UHPC

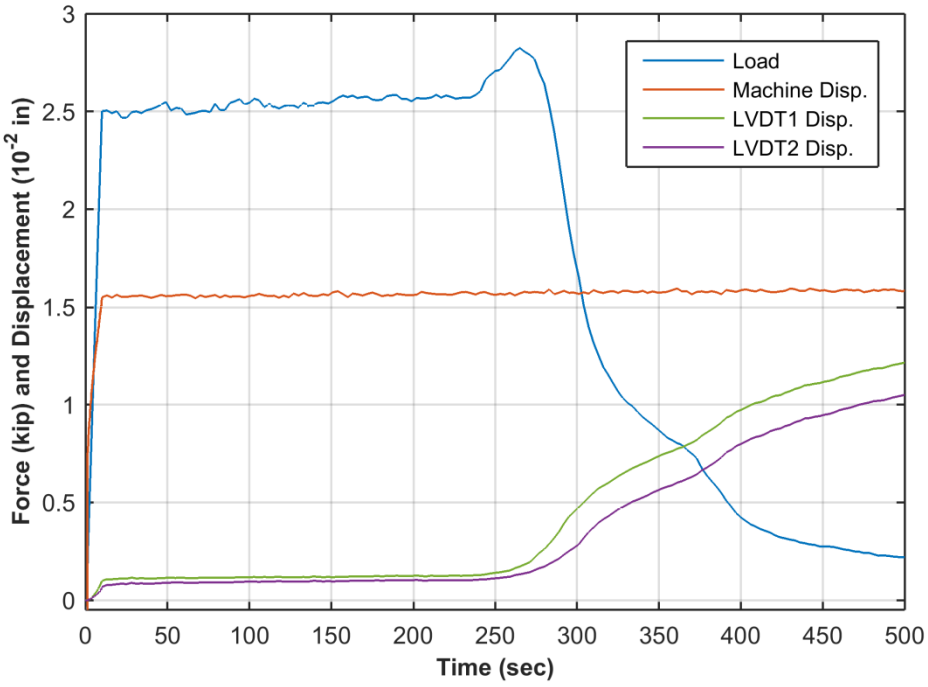

Figure 5.7: *P6 Force and Multiple Displacement Measurements over the Duration of the Test using the CM*

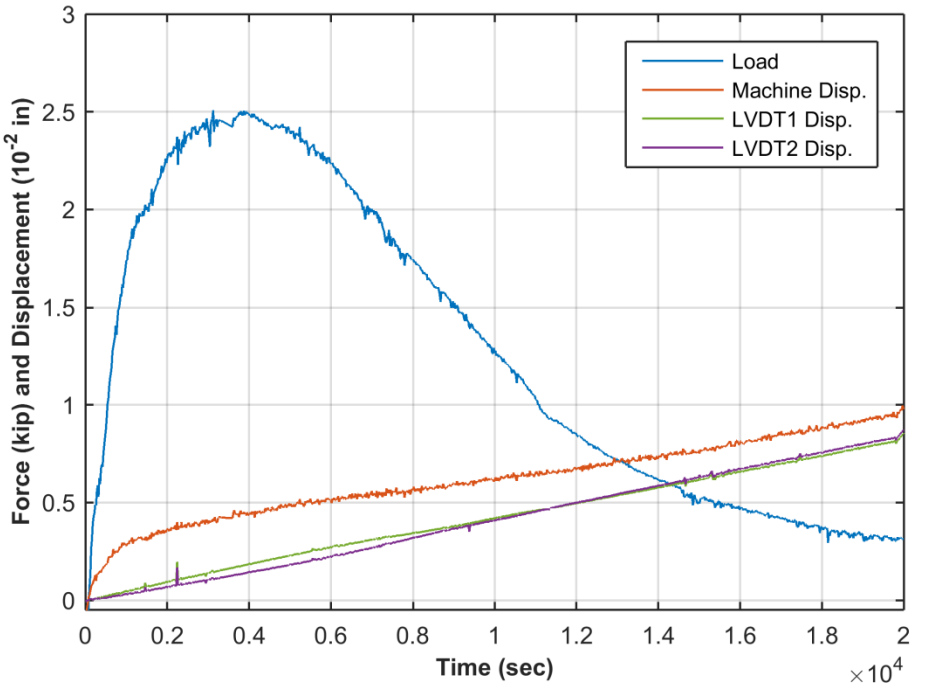

Figure 5.8: *A8 Force and Multiple Displacement Measurements over the Duration of the Test using the FA*

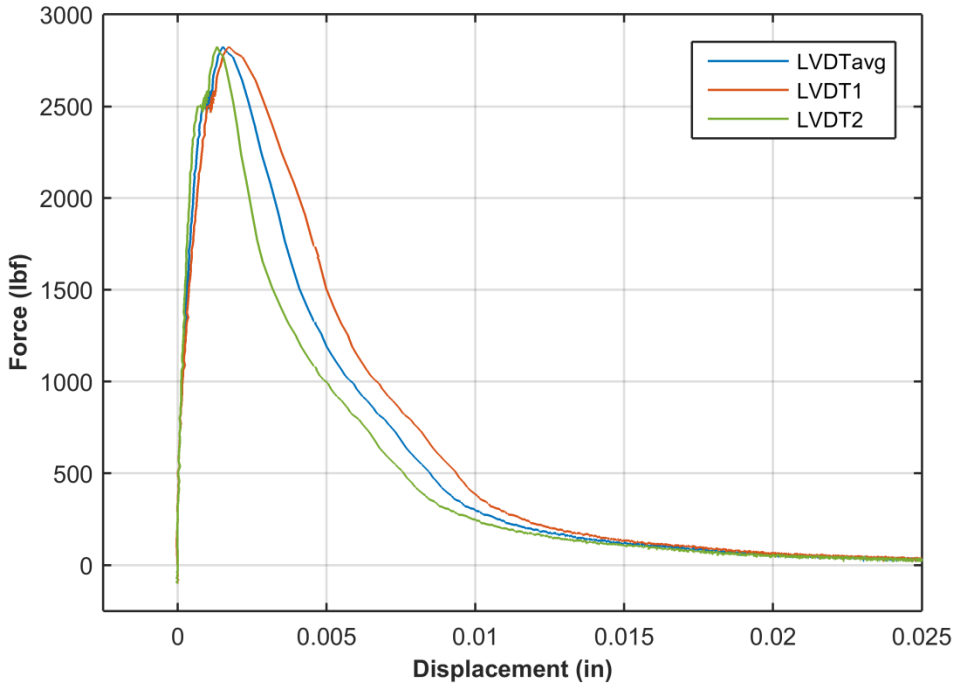

Figure 5.9 *P6 Load-displacement Curve*

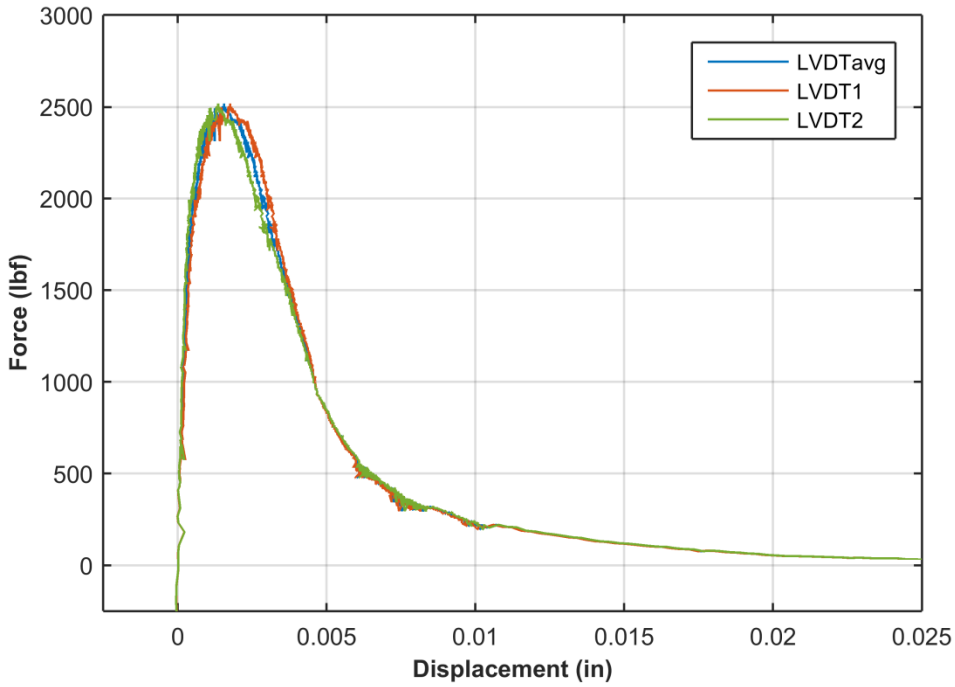

Figure 5.10: *A8 Load-displacement Curve*

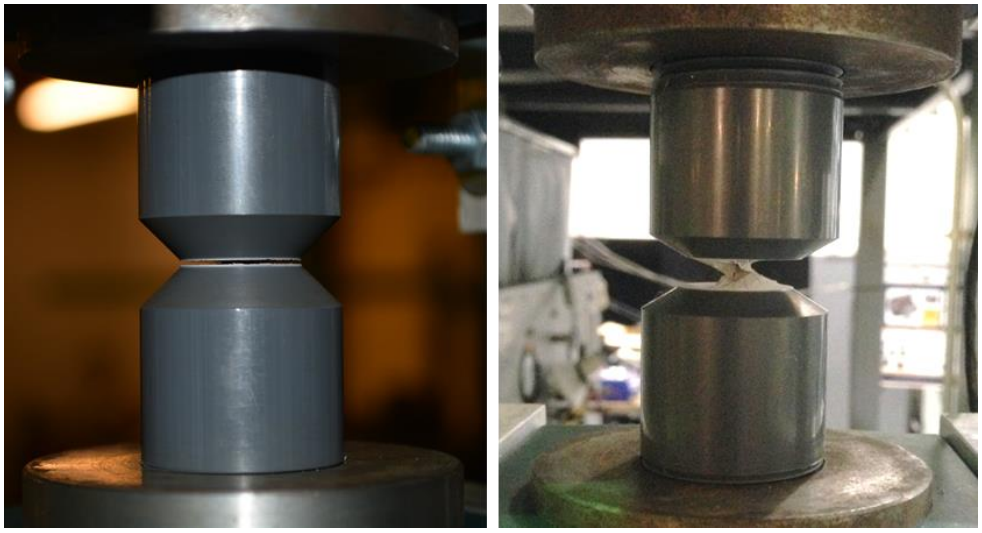

(a) (b)

Figure 5.11: *Boundary Condition Alignment, (a) P1 - CM, (b) A1 – FA*

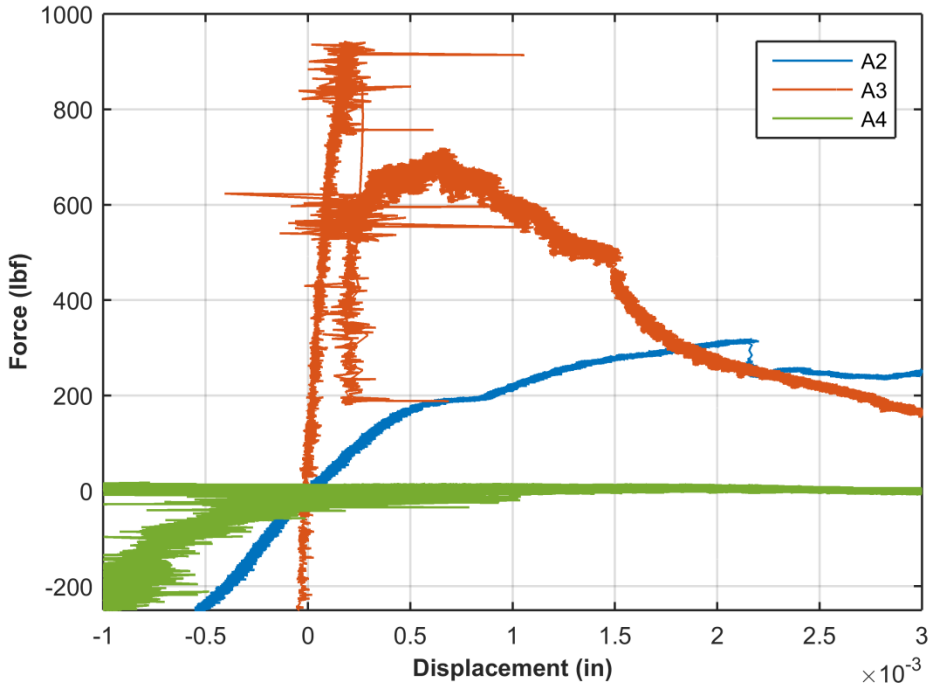

Figure 5.12: *NSC Load-displacement Curves for Unsuccessful Post-Peak Control*

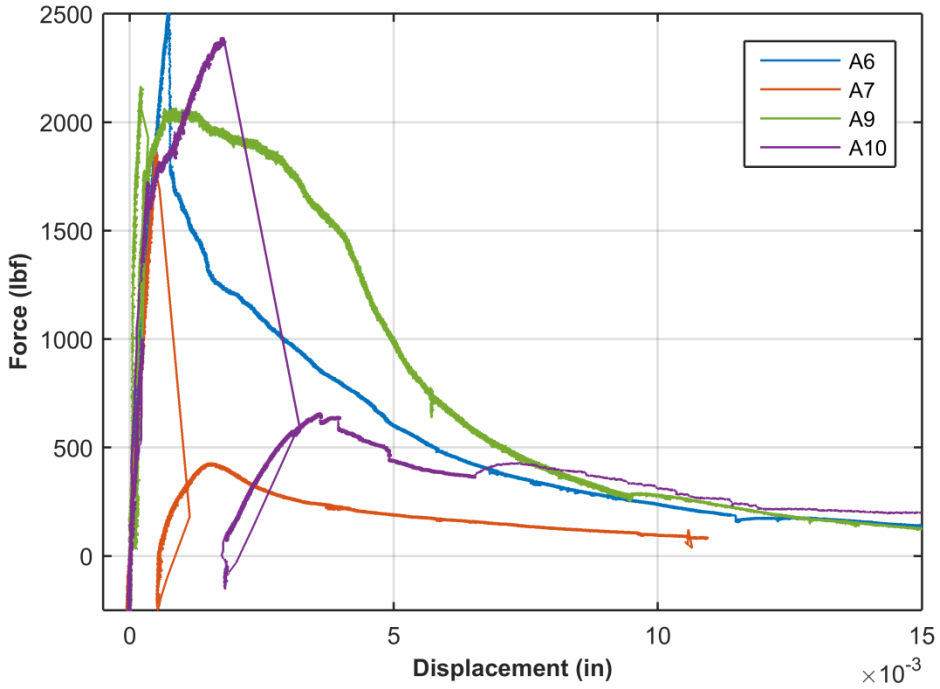

Figure 5.13: *UHPC Load-displacement Curves for Unsuccessful Post-Peak Control*

specimens, these effects are less likely to impede a stable uniaxial tensile test. The imposed stress concentrations due to gripping are also possible reasons for lower ultimate tensile strengths in UHPC specimens that used the FA compared to the CM (*Figure 5.3).*

Table 5.2 qualitatively compares the fracture zone locations for each concrete test. The boundary condition utilized and whether post-peak control was obtained is also noted. From this table two interesting correlations can be seen: (1) with the exception of test *P5*, no successful post-peak controlled tests were observed when the fracture zone occurred outside the middle half of the specimen and (2) all tests that utilized the CM formed a fracture zone in the middle half of the specimen, and with the exception of *P3* achieved at least initial post-peak control. *Figure 5.14* shows the crack locations of tests *P4* and *P5.* *Figure 5.15* presents the crack path of tests *P3* and *A2,* whose fracture zones lie in the middle half and close to boundary, respectively. Note the crack propagation through the aggregate in *Figure 5.15b* for *A2,* which typically requires more energy than avoiding aggregates and cracking through the cement paste. Only test *A10* failed due to epoxy peeling at the boundary, shown in *Figure 5.16*; a relatively large misalignment between the FA and the MTS collet grip was noted before gripping. These results correlate well with presumed boundary stress concentrations in FA tests.

Table 5.2: *Fracture Zone Locations and Boundary Conditions Comparison*

Qualitative Crack Location on Specimen	**Concrete Specimen Test No. [Boundary Condition]**
Middle Half	P3 [CM]*****, P4 [CM], P6 [CM], P7 [FA], A3 [FA]*****, A5 [FA], A8 [FA]
Outside of Middle Half	P5 [FA], A4 [FA]*****, A6 [FA]*****, A9 [FA]*****
Close to Boundary	A2 [FA]*****, A7 [FA]*****
Epoxy Interface	A10 [FA]*****

*****Did not achieve post-peak control

(a) (b)

Figure 5.14: *NSC Fracture Zone Locations, (a) P5 - FA, (b) P4 - CM*

(a) (b)

Figure 5.15: *NSC Crack Path, (a) P3 - CM, (b) A2 - FA*

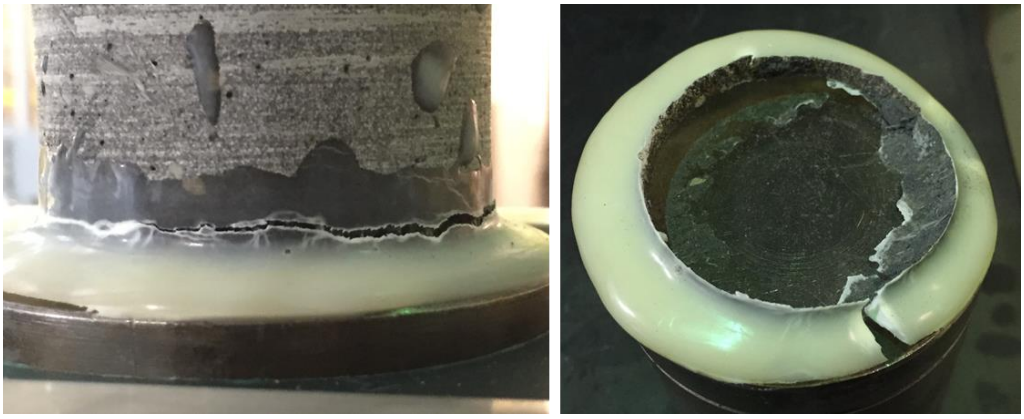

Figure 5.16: *UHPC A10 – FA Epoxy Failure*

5.2.1.2 Epoxy Cure Time

The gluing procedure proposed in Phase I stated that testing could be performed after 24 hours of epoxy application. Early FA tests followed this minimum requirement. Because concrete samples that utilized the FA were glued in the testing frame to mitigate alignment issues, only one sample was glued at a time and then after 24 hours, the sample was tested. After reviewing early FA concrete tests, it was noticed that the LVDTs seemed to rotate substantially under small applied loads. Two of these tests are shown in *Figure 5.17* for NSC test *P5* and *Figure 5.18* for UHPC test *A5.* Similar results were seen in load-displacement plots of *P7* and *A3*. All four of these tests utilized the

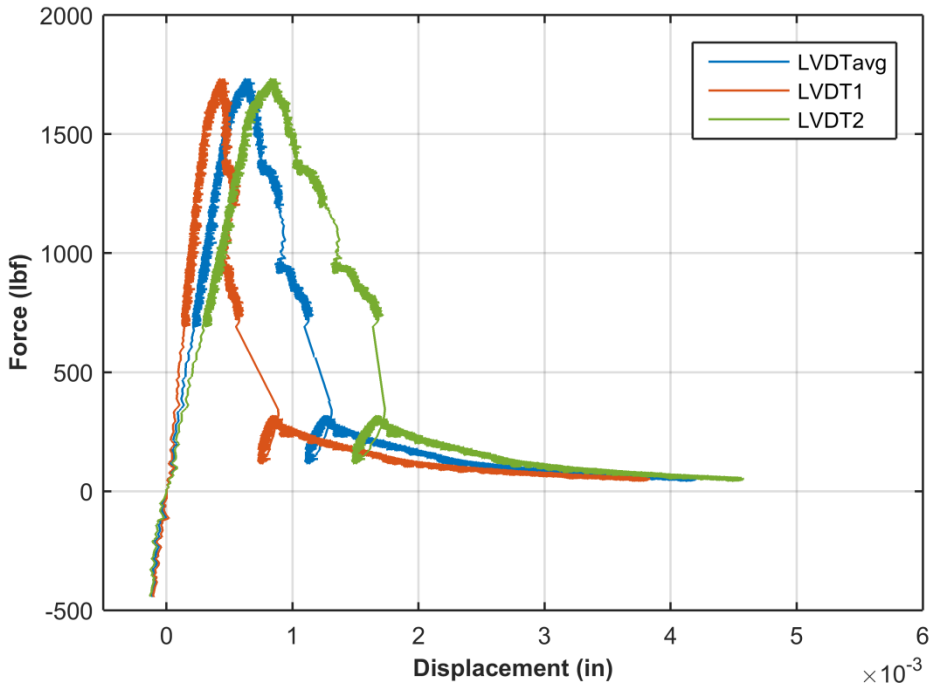

Figure 5.17: *P5 Load-displacement Curve*

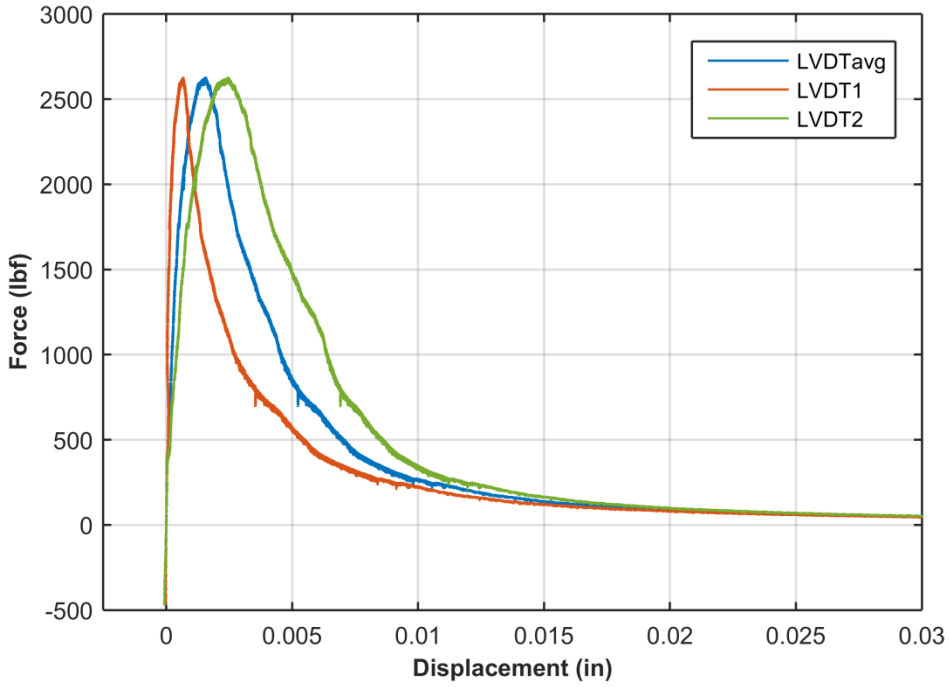

Figure 5.18: *A5 Load-displacement Curve*

FA and were tested shortly after 24 hours of gluing. Upon personally reading the technical data for the epoxy [92], it was discovered that full cure time was 48 hours. While the strength was adequate to perform uniaxial tensile tests after 24 hours, the stiffness of the epoxy may have been insufficient to limit rotation. Following this realization all tests were performed well after 48 hours of gluing. These tests included *A6* to *A10*. From *Figure 5.6*, tests *A6* through *A10* saw substantially lower in-plane rotations.

5.2.2 Feedback Signal

Three of the 14 concrete tests were performed by controlling the testing machine displacement at a constant rate. *Figure 5.19* compares the load-displacement and time-displacement for two NSC tests. Both tests utilized the CM, but *P3* was controlled by feedback from the LVDTs and *P4* by the testing machine displacement. These results show that when the machine displacement is used, the LVDT average is displaced at a faster rate than anticipated. This is a likely reason as to why *P4* achieved post-peak control while P3 failed immediately upon reaching peak load.

However, when the FA was used in UHPC testing, controlling off the machine displacement rate produced more similar LVDT average rates than those in *Figure 5.19*. While this is true, sections of test *P7* in *Figure 5.*20 show an increased LVDT average displacement rate, while *A5* displays a constant rate throughout the entirety of the test. From these two figures it is evident that a higher probability of stable testing will occur when controlling off of the feedback from the LVDTs.

5.2.3 Specimen Preload and Stiffening Force in Active Tests

During active stiffener testing, the compressive preload in the specimen and the lower stiffening force were altered. *Figure 5.21* seems to show that as the compressive preload increased, the peak tensile strength decreased and flattened out. Excluding test *P7* for having a substantially lower elastic modulus than all other UHPC tests, the slope of the descending branch of the softening curves appear to decrease with increasing preload (i.e. 450 lbf to 1000 lbf). These results are similar to those presented in *Section 2.3.8* with the exception of a decrease in elastic moduli with increasing preload. Also no discernable influence on the ultimate strength was evident in the literature review. However with such few tests, it is hard to make any conclusions with certainty.

Figure 5.22 displays all UHPC active stiffener tests with the exception of *A10,* due to failure occurring in regards to epoxy peeling. The results show that the tests with

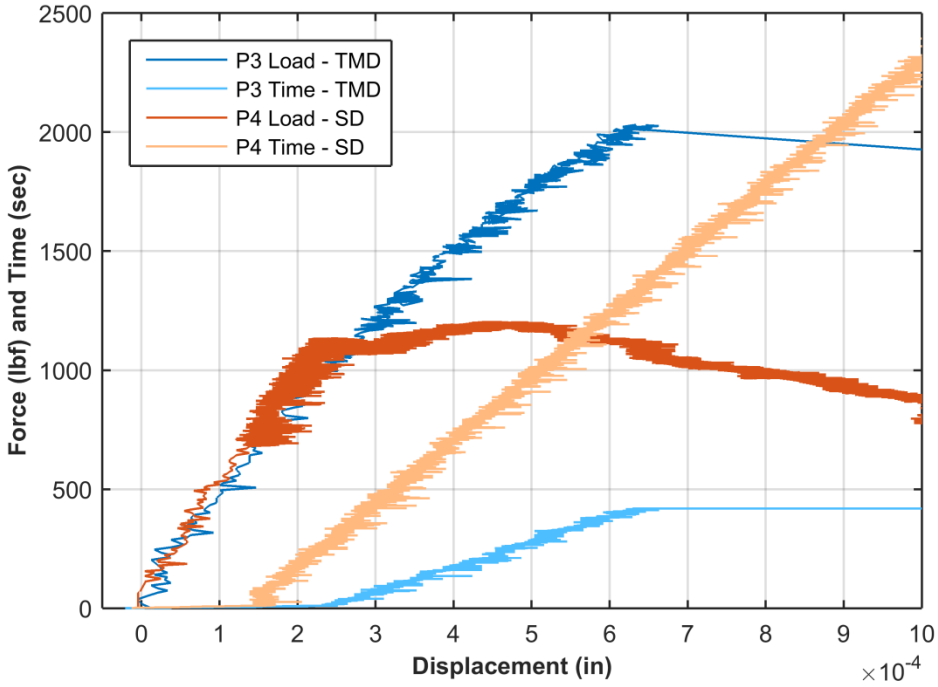

Figure 5.19: *TMD and SD Feedback Signal Comparison for NSC with CM*

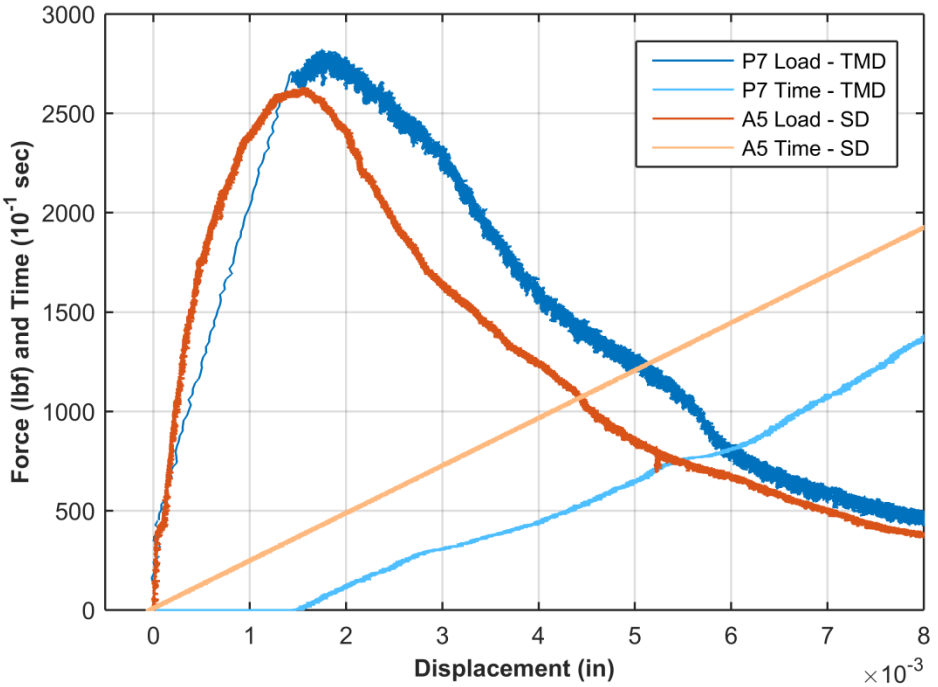

Figure 5.20: *TMD and SD Feedback Signal Comparison for UHPC with FA*

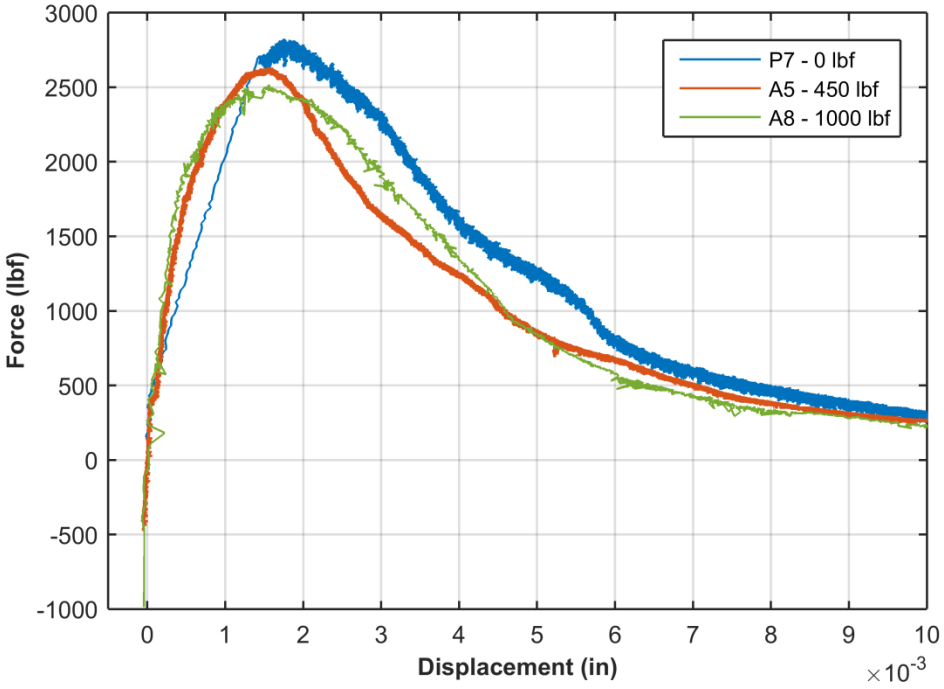

Figure 5.21: *Compressive Preload in UHPC Comparison*

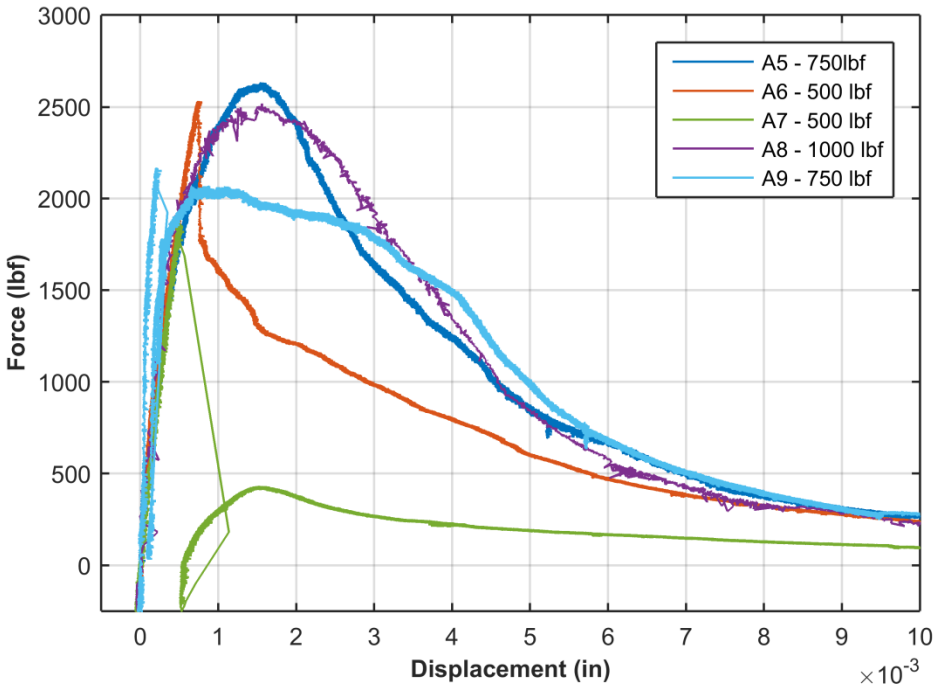

Figure 5.22: *Bottom Stiffening Force in UHPC Active Testing Comparison*

larger, lower stiffening forces (e.g. *A5* and *A8)* tended to have increased stability during softening. While test *A9* suddenly lost stability, it partially recovered and was stable throughout the remainder of the test. *A6* and *A7,* which had stiffening forces of 500 lbf, lost stability and did not recover. It seems from these results that an increase in lower stiffening force increases testing stability, but certain tests in this comparison may have been influenced more by the FA misalignment. This may have contributed to testing instability, diminishing the effect of the stiffening force.

5.3 UHPC FRACTURE ENERGY COMPARISON

By utilizing the method discussed in *Section 4.3.1*, the stress-crack opening (*Figure 5.23)* and normalized stress-crack opening (*Figure 5.24)* curves were approximated for UHPC tests *P6, P7, A5,* and *A8*. The resulting mechanical tensile properties from these tests have been calculated (*Appendix D)* and are compiled in *Table 5.3*. The results show similar softening relations for all specimens. When the stress is normalized, the differences become even less obvious. One significant discrepancy between tests is the relatively low elastic modulus of test *P7.* This difference led to the more brittle characteristic length of *P7* in spite of its high fracture energy.

From the results in *Table 5.3*, the characteristic length of the UHPC tested can be taken as 800 mm. This result makes sense when compared to typical characteristic lengths of the more brittle high strength and normal concretes (e.g. 200-500 MPa). However when compared to previous softening curves with glass fibers, the fracture energy seems low. Barros et al. tested typical GFRC specimens and determined an ultimate tensile strength and fracture energy of 4.4 MPa and 1912 N/m, respectively [65].

One possible explanation for these differences is the large measured gage length (i.e. 4.5 in) used at GT. *Figure 2.13* shows that with a larger gage length, the elastic modulus decreases and the slope of the descending branch of the softening curve increases, resulting in less apparent ductile behavior. This measured gage length effect has also been shown to occur in GFRC specimens [93]. Another possible explanation for discrepancies is the fiber alignment and distribution. As displayed in *Figure 2.48b,* alignment and volumetric proportions of fibers affect the stress-displacement curves for FRC. Barros et al. showed that the distribution of fibers due to specific mixing techniques can also greatly affect the mechanical properties [65]. While the specific mixing methods and proportions of fibers are unknown by this researcher, from

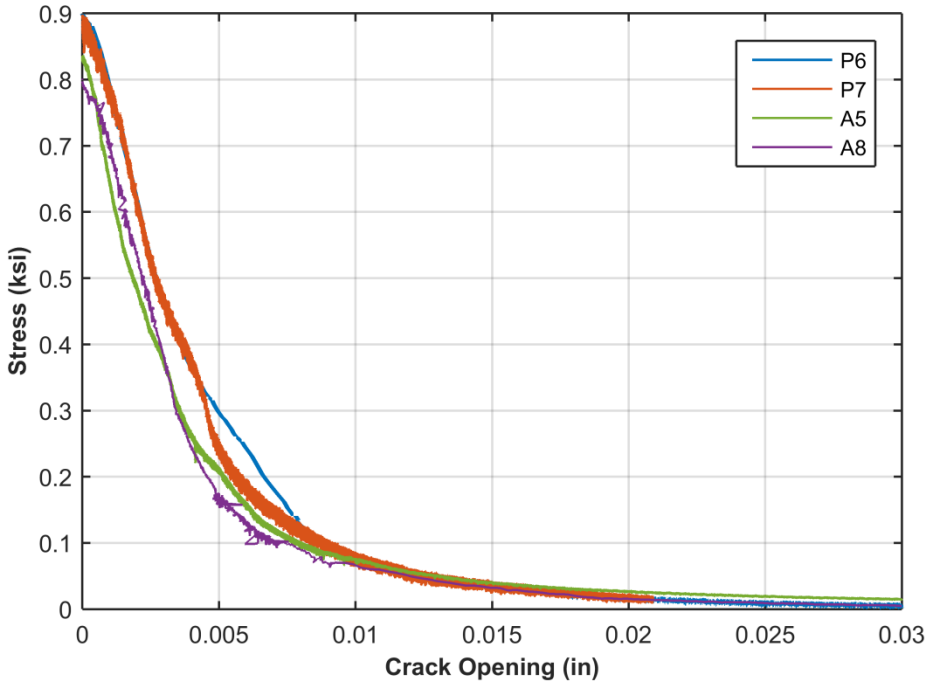

Figure 5.23: *Stress-Crack Opening Curves for UHPC Specimens P6, P7, A5, and A8*

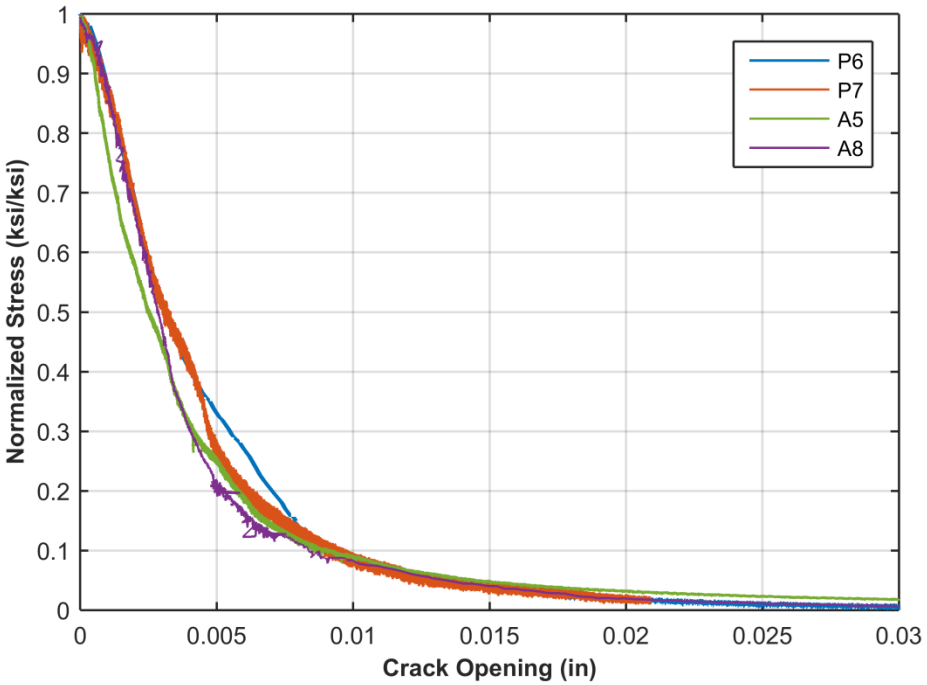

Figure 5.24: *Normalized Stress-Crack Opening Curves for UHPC Specimens P6, P7, A5, and A8*

analyzing the fracture planes of the UHPC specimens it was determined that the fiber quantity and distribution for the UHPC samples were highly variable. *Figure 5.25a* and *Figure 5.25b* show the fracture plane for tests *A8* and *A7*, respectively. Test *A8* shows a low percentage of fibers, which may attribute to the less than expected fracture energy for a FRC. Test *A7* broke at the boundary, so the softening curves are unable to be compared.

Table 5.3: *Approximate Mechanical Properties of UHPC Specimens P6, P7, A5, and A8 in Tension*

Test No.	E (ksi)[GPa]	f_t (psi)[MPa]	G_f (lbf/in)[N/m]	l_{ch} (in)[m]
P6	7096.1 [48.926]	898.9 [6.198]	4.03 [705.31]	35.367 [0.898]
P7	4605.2 [31.752]	898.0 [6.191]	3.87 [678.21]	22.118 [0.562]
A5	5923.2 [40.839]	836.9 [5.770]	3.32 [581.66]	28.089 [0.713]
A8	6520.1 [44.955]	801.3 [5.525]	3.20 [559.82]	32.463 [0.825]

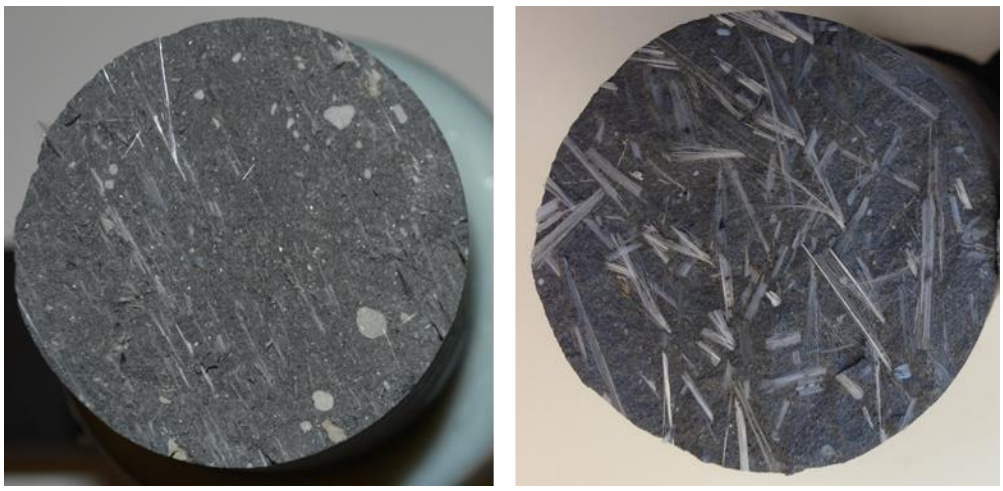

(a) (b)

Figure 5.25: *Fracture Planes of UHPC Specimens (a) A8 and (b) A7*

CHAPTER 6: DISCUSSION AND CONCLUSION

The study of concrete fracture mechanics gained significant interest with the development of the FCM in 1976. Since this time, Mode I fracture of typical plain concrete has been thoroughly researched through indirect (e.g. TPBT) and direct tensile testing experiments. The fracture parameters derived from the resulting stress-crack opening curves have been used to improve modeling capabilities for various applications (e.g. penetration simulations, bar anchorage, fatigue loadings). However in recent years more complex and unique concretes (e.g. HPFRCC, HSHDC, and UHPFRC) have been developed with only limited information on their tensile softening responses. Research concerning multi-axial behavior for these concretes is especially scarce and almost nonexistent in the extension regime.

The main objective of this research was to develop a novel, uniaxial testing scheme, so that the fracture properties of a specific UHPC could be determined under confining pressures at ERDC. The experimental program began in UCSD where initial phases were completed. However it was not until the project was brought to GT were successful tests performed on UHPC specimens with the active stiffener incorporated. The uniaxial tensile testing results of UHPC validate the following: (1) the capability of an off-the shelf HPC (Enerpac Model No. RRH-1001) to improve the stiffness of a typical MTS or SATEC load frame to allow for stable, uniaxial tensile testing of UHPC specimens, and (2) the ability to perform a uniaxial tensile test by actively controlling a HPC using specimen feedback while maintaining a constant compressive force in the machine actuator. The latter of which is vital in implementing this testing scheme into the compression only pressure vessel at ERDC.

While the overall testing scheme devised was successful, three significant aspects need to be discussed for possible improvements before implementation at ERDC. These include: boundary conditions, threaded parts and epoxy cure time, and measured and control gage lengths.

Boundary Conditions

While the fixed adapter is theoretically more appropriate for determining fracture properties of concrete, results show that the required precision when utilizing the FA is exceptionally difficult to maintain. Small misalignments can result in large moments, inducing initial stress concentrations near the ends of the specimen. In some cases

these stresses caused an immediate failure of the specimen. In most tests utilizing the FA, the fracture zone was located outside of the middle half of the specimen. Because of these issues, utilizing the CM seems to be the best choice for the boundary condition. Also the loss of rotational stiffness with the CM should be mitigated when confining pressures are applied during multi-axial testing.

Threaded Parts and Epoxy Cure Time

Results show large in-plane rotations during uniaxial testing. Insufficient early stiffness of the epoxy seemed to be the largest contributor. Rotations drastically decreased when the epoxy was allowed to cure over the specified minimum cure time of 48 hours. Because of this, it is advised to wait four days before testing, but no less than two. Threaded parts may also contribute to initial rotations. When transitioning from compression to tension, the gaps in the threads momentarily create a disconnect between parts. While this is minor compared to the rotations and slack that occur from compression to tension transition in the CM, these gaps need to be mitigated. In place of threaded end caps it would be best to connect the end caps directly to hydraulic grips. The slack in all other threads could be removed initially by tightening spiral washers (*Figure 6.1*) under larger than expected tensile loads.

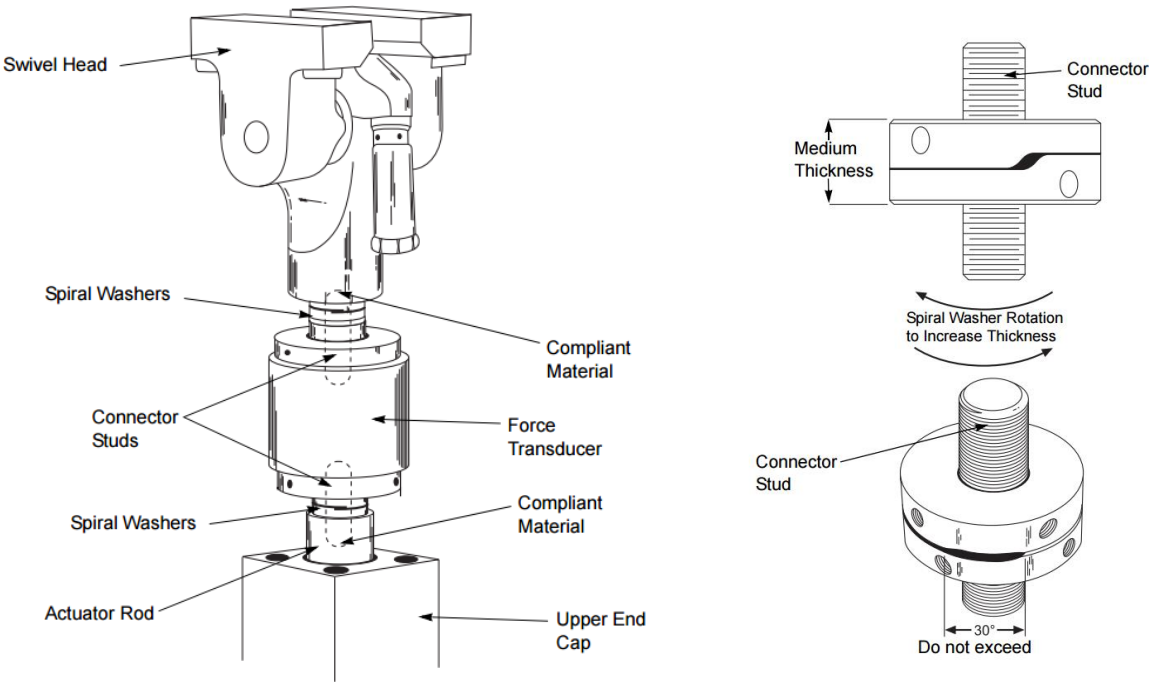

Figure 6.1: *Example of Load Train with Spiral Washers (from [94])*

Measured and Control Gage Lengths

The full-specimen gage length at GT is not small enough to confidently determine fracture material properties. For accurate and reliable stress-crack opening relations of normal concrete, it has been shown that a minimum gage length of half of the specimen length is required (*Figure 2.14)*. However more accurate results will benefit from smaller lengths assuming the fracture zone is captured. Because of this, it is the opinion of this researcher that gages closer to a quarter of the specimen length should be chosen for measurements. Therefore for the concrete specimens tested in this research (length of 4.5 in.) a gage length of 1.25 in. is much more appropriate. Since unnotched specimens are to be tested, a series of six gages will be required around the specimen to insure crack capture. Assuming accurate data will result from fracture zones occurring in the middle half of the specimen, gages will only encompass this area. Stable UHPC uniaxial tensile tests were performed using the feedback from the full-specimen gage length. However maintaining stability under confining pressures will most likely be more difficult. Therefore it is proposed that two gages, three inches in length, are to be used as feedback to control the test. If testing is still unstable, the maximum opening rate of the smaller gages may be required. A schematic of the proposed measuring and control gages on a specimen are shown in *Figure 6.2.*

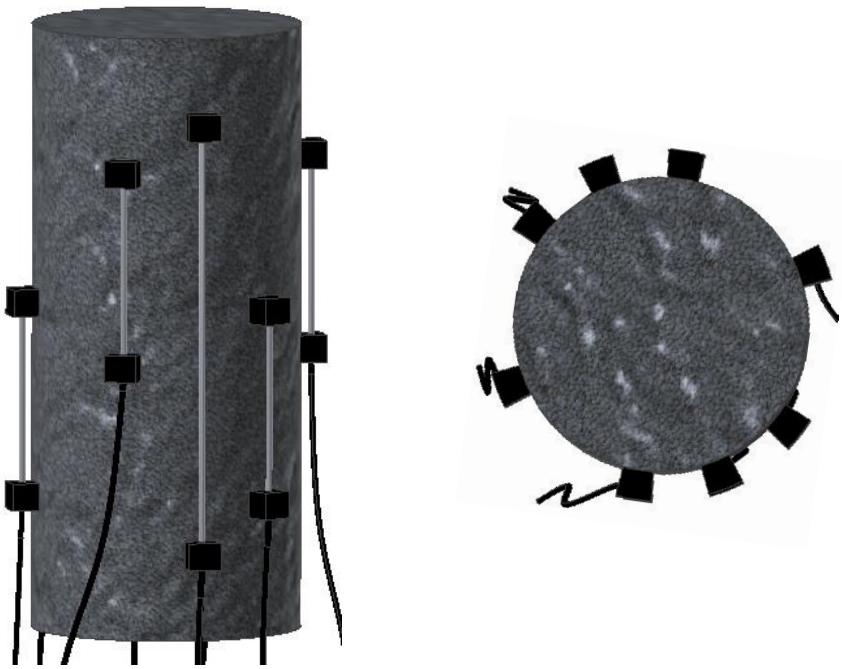

Figure 6.2: *Proposed Measured and Control Gage Length Locations on Specimen*

In conclusion, the main goal of this thesis, to develop the active stiffener testing scheme for uniaxial tensile testing of UHPC, was validated by the results gained at GT. Employing the mentioned improvements into the active testing scheme should result in reliable and accurate uniaxial tensile tests that can be implemented into ERDC's pressure vessel. *Figure 2.65* shows that ERDC has the capability to place strain-gages on a specimen that includes a membrane for protection against hydraulic pressure intrusion. Therefore it is assumed that the application of the proposed axial LVDTs (*Figure 6.2)* will not be an issue. *Figure 6.3*, on the following page, displays the proposed active test setup implemented into ERDC's pressure vessel.

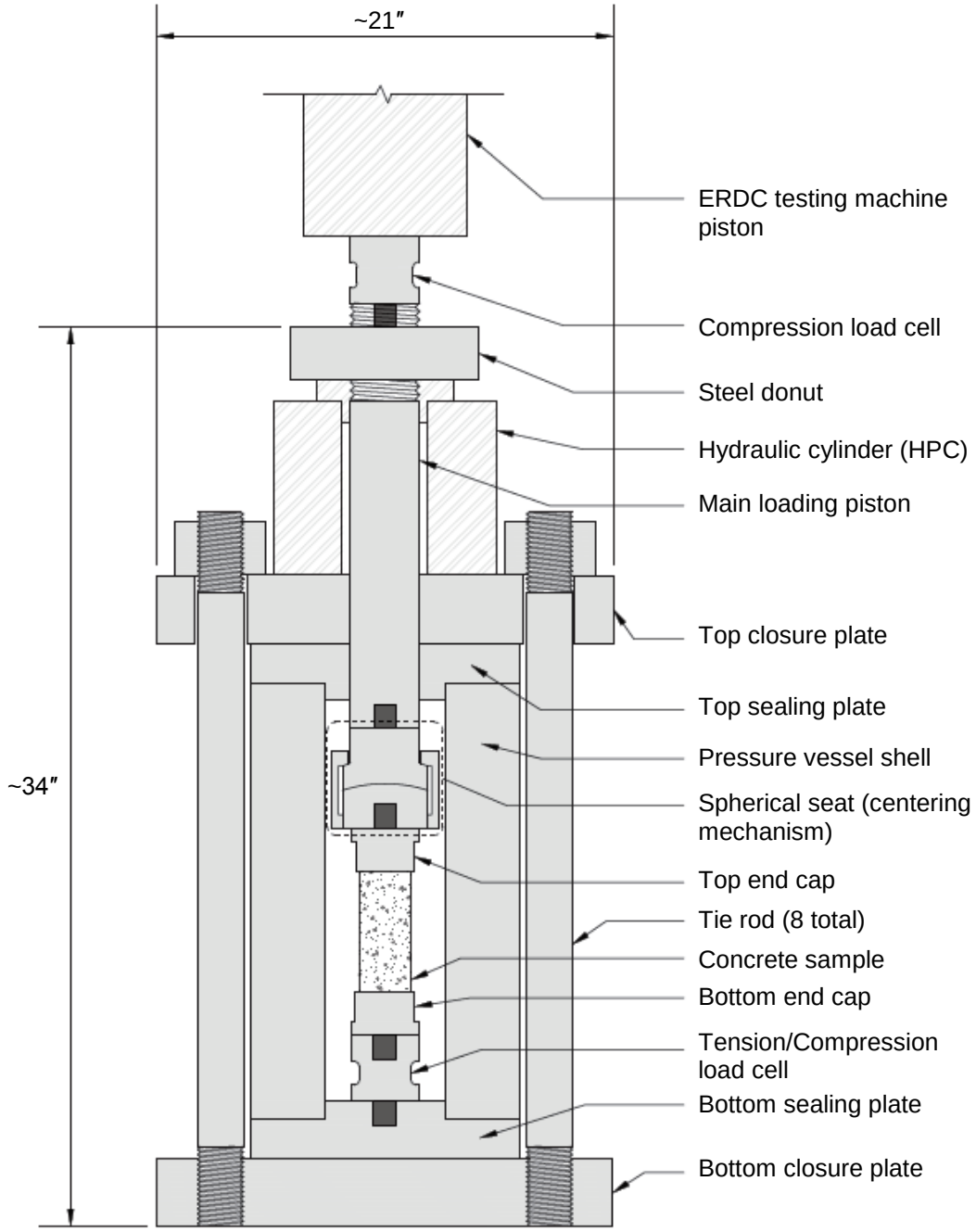

Figure 6.3: *Active Test Setup in ERDC's Pressure Vessel*

APPENDIX A

UCSD TESTING MACHINE PROPERTIES

Table A.1: *UCSD Testing Machine Properties (after [95:8])*

Parameter	**Specification**
Force capacity (maximum)	110 kip (500 kN)
Available actuator ratings	55, 100 kip (250, 500 kN)
Vertical test space[1] (A)	83 in (2108 mm)
Working height (B)	35 in (889 mm)
Column spacing (C)	30 in (762 mm)
Column Diameter (D)	4 in (102 mm)
Base width (E)	49 in (1245 mm)
Base depth (F)	36 in (914 mm)
Diagonal Clearance (G)	151 in (3835 mm)
Overall Height (H)	141 in (3581 mm)
Stiffness[2]	4.3E+06 lb/in (7.5E+08 N/m)
Weight	3900 lb (1770 kg)

[1] Test space is the maximum distance between the load cell and the actuator with the actuator fully retracted

[2] Determined at each load unit's full fatigue rating with its crosshead raised 50 in. (1270 mm) above the base

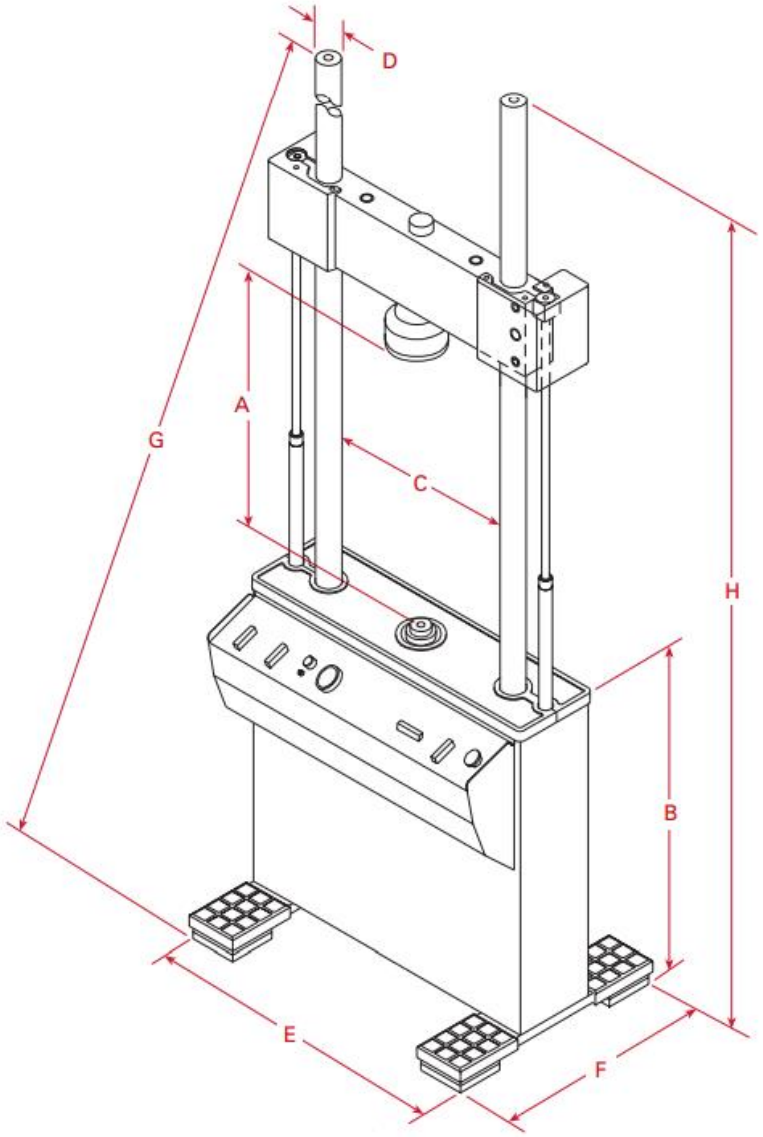

Figure A.1: *Diagram Indicating Testing Machine Dimensions (from [95:8])*

APPENDIX B

GT EXPERIMENTAL COMPONENT PROPERTIES

TestStar IIs Version 3.2C 929 Controller

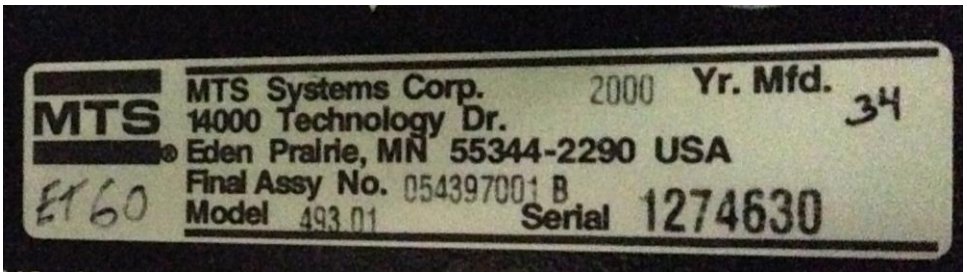

Figure B.1: *TestStar IIs Controller Name Plate*

Added Options: Model 793.03 Calculations w/ Outputs
Model 793.10 MultiPurpose TestWare

TSIIS.HWI:

```
HI RATE = 4096
LO RATE = 25.6
SYSTEM RATE=4096
MEDIUM SYSTEM RATE=256.0
LOW SYSTEM RATE=25.6
INTERRUPT LEVEL = 5

SERIAL PORT 1
NAME="EUROPA COM 1" CONNECTOR="J50"
SERIAL PORT 2
NAME="EUROPA COM 2" CONNECTOR="J51"

HPS CONTROL
NAME="HPS 1" CONNECTOR="J25"

HSM CONTROL
NAME="HSM 1" CONNECTOR="J28" TYPE=SOLENOID
/* LOW RATE=3 HIGH RATE=3 OFF RATE=2 LOW PERCENT=25 HIGH
PERCENT=100 */

LOAD FRAME CONTROL
CONNECTOR="J29"

DIGITAL INPUT CONNECTOR="J54"
CHANNEL 1 NAME="Digital Input 1"
CHANNEL 2 NAME="Digital Input 2"
CHANNEL 3 NAME="Digital Input 3"
```

```
CHANNEL 4 NAME="Digital Input 4"
DIGITAL OUTPUT CONNECTOR="J55"
CHANNEL 1 NAME="Digital Output 1"
CHANNEL 2 NAME="Digital Output 2"
CHANNEL 3 NAME="Digital Output 3"
CHANNEL 4 NAME="Digital Output 4"

READOUTS
CHANNEL 1 NAME="Analog Readout 1" CONNECTOR="J71"
CHANNEL 2 NAME="Analog Readout 2" CONNECTOR="J72"


I/O OPTION BOARDS
DAUGHTER 1 ADDRESS= 0x300000 TYPE=#493.14
FILENAME="DVD_53.OUT"
CHANNEL 3 NAME="493.14 2SVD-Slot 1" CONNECTOR="J1" RANGE=50
MODE=DUAL CLAMP=DISABLED
/*
DAUGHTER 2 ADDRESS= 0x310000 TYPE=#493.46
FILENAME="D2A_53.OUT"
CHANNEL 4 NAME="Analog Output 1-Slot 2" CONNECTOR="J2"
CHANNEL 5 NAME="Analog Output 2-Slot 2" CONNECTOR="J2"
CHANNEL 6 NAME="Analog Output 3-Slot 2" CONNECTOR="J2"
CHANNEL 7 NAME="Analog Output 4-Slot 2" CONNECTOR="J2"
CHANNEL 8 NAME="Analog Output 5-Slot 2" CONNECTOR="J2"
CHANNEL 9 NAME="Analog Output 6-Slot 2" CONNECTOR="J2" */

DAUGHTER 3 ADDRESS= 0x320000 TYPE=#493.45
FILENAME="A2D_53.OUT"
CHANNEL 1 NAME="Analog Input 1-Slot 3" CONNECTOR="J3"
CHANNEL 2 NAME="Analog Input 2-Slot 3" CONNECTOR="J3"
CHANNEL 3 NAME="Analog Input 3-Slot 3" CONNECTOR="J3"
CHANNEL 4 NAME="Analog Input 4-Slot 3" CONNECTOR="J3"
CHANNEL 5 NAME="Analog Input 5-Slot 3" CONNECTOR="J3"
CHANNEL 6 NAME="Analog Input 6-Slot 3" CONNECTOR="J3"

DAUGHTER 4 ADDRESS= 0x330000 TYPE=#493.21B
FILENAME="DUCB_53.OUT"
CHANNEL 7 NAME="493.21B DC-Slot 4" CONNECTOR="J4" MODE=DC
FILTER=1000

DAUGHTER 5 ADDRESS= 0x340000 TYPE=#493.21B
FILENAME="DUCB_53.OUT"
CHANNEL 8 NAME="493.21B DC-Slot 5" CONNECTOR="J5" MODE=DC
FILTER=1000

DAUGHTER 6 ADDRESS= 0x350000 TYPE=#493.21B
FILENAME="DUCB_53.OUT"
CHANNEL 9 NAME="493.21B AC-Slot 6" CONNECTOR="J6" MODE=AC
FILTER=1000
```

```
/*
TEMP CONTROL
TYPE="Eurotherm 2208"
HOST PORT="EUROPA COM 2"
BAUD=4800
CHANNEL 1 NAME="Temp Control 1" ADDRESS=0x1
*/

RSC
NAME="RSC 1" HOST PORT="EUROPA COM 1" FILENAME="POD.HEX"

/*
   Below here are definitions for other supported hardware.  They need to
   be uncommented, edited as necessary, and moved to the appropriate
   section if they are used.

These all go in the section I/O OPTION BOARDS

DAUGHTER 1 ADDRESS= 0x300000 TYPE=#493.15
FILENAME="D3VD_53.OUT"
CHANNEL 3 NAME="493.15 3SVD-Slot 1" CONNECTOR="J1"
CLAMP=DISABLED

DAUGHTER 2 ADDRESS= 0x310000 TYPE=#493.47
FILENAME="ENC_53.OUT"
CHANNEL 1 NAME="493.47 Encoder-Slot 2" CONNECTOR="J2"
MODE=INCREMENTAL

DAUGHTER 4 ADDRESS= 0x330000 TYPE=#493.21
FILENAME="DUC_53.OUT"
CHANNEL 7 NAME="493.21 DC-Slot 4" CONNECTOR="J4" MODE=DC
FILTER=1000

DAUGHTER 5 ADDRESS= 0x340000 TYPE=#493.21
FILENAME="DUC_53.OUT"
CHANNEL 8 NAME="493.21 DC-Slot 5" CONNECTOR="J5" MODE=DC
FILTER=1000

DAUGHTER 6 ADDRESS= 0x350000 TYPE=#493.21
FILENAME="DUC_53.OUT"
CHANNEL 9 NAME="493.21 AC-Slot 6" CONNECTOR="J6" MODE=AC
FILTER=1000
```

PASSIVE TEST PARAMETERS

Station: passive_setup.cfg Parameter Set : passive 4/29/15 1:06:34 PM
Items preceded by an asterisk (*) have been modified.

Application Information
  Name : Station Manager
  Version : 3.2C 929

ANALOG INPUT SIGNALS :-

  LVDT 1
    Hardware Name : Analog Input 1-Slot 3
    Fullscale Min : -0.2500 in
    Fullscale Max : 0.2500 in
    Manual/Auto Offset : 0.0000 in
    Sensor :
    Range :
    Conditioner : Analog Input 1-Slot 3
      Gain : 1.0000 (none)
      Auto Zero : 0.0000 (none)
      Polarity : Invert

  LVDT 2
    Hardware Name : Analog Input 2-Slot 3
    Fullscale Min : -0.2500 in
    Fullscale Max : 0.2500 in
    Manual/Auto Offset : 0.0000 in
    Sensor :
    Range :
    Conditioner : Analog Input 2-Slot 3
      Gain : 1.0000 (none)
      Auto Zero : 0.0000 (none)
      Polarity : Invert

  Aux Input 3
    Hardware Name : Analog Input 3-Slot 3
    Fullscale Min : -10.0000 in/in
    Fullscale Max : 10.0000 in/in
    Manual/Auto Offset : 0.0000 in/in
    Sensor :
    Range :
    Conditioner : Analog Input 3-Slot 3
      Gain : 1.0000 (none)
      Auto Zero : 0.0000 (none)
      Polarity : Normal

  Aux Input 4
    Hardware Name : Analog Input 4-Slot 3
    Fullscale Min : -10.0000 in/in
    Fullscale Max : 10.0000 in/in

Manual/Auto Offset	: 0.0000 in/in
Sensor	:
Range	:
Conditioner	: Analog Input 4-Slot 3
Gain	: 1.0000 (none)
Auto Zero	: 0.0000 (none)
Polarity	: Normal

Aux Input 5

Hardware Name	: Analog Input 5-Slot 3
Fullscale Min	: -10.0000 in/in
Fullscale Max	: 10.0000 in/in
Manual/Auto Offset	: 0.0000 in/in
Sensor	:
Range	:
Conditioner	: Analog Input 5-Slot 3
Gain	: 1.0000 (none)
Auto Zero	: 0.0000 (none)
Polarity	: Normal

Aux Input 6

Hardware Name	: Analog Input 6-Slot 3
Fullscale Min	: -10.0000 in/in
Fullscale Max	: 10.0000 in/in
Manual/Auto Offset	: 0.0000 in/in
Sensor	:
Range	:
Conditioner	: Analog Input 6-Slot 3
Gain	: 1.0000 (none)
Auto Zero	: 0.0000 (none)
Polarity	: Normal

Aux Input 7

Hardware Name	: 493.21B DC-Slot 4
Fullscale Min	: -1000.0000 DaN
Fullscale Max	: 1000.0000 DaN
Manual/Auto Offset	: 0.0000 DaN
Sensor	:
Range	:
Conditioner	: 493.21B DC-Slot 4
Polarity	: Normal
Excitation	: 0.0000 V
Gain	: 0.9996 (none)
Post-amp	: 0.9996 (none)
Fine Zero	: 0.0000 V
Balance Option	: 0.0000 V
DeltaK	: 1.0000 (none)
Auto Zero	: 0.0000 (none)
Manual Zero	: 0.0000 V
Pre-amp	: 1.0
Shunt Reference(+)	: 0.0000 DaN

Axial Displacement

Hardware Name	: 493.21B AC-Slot 6
Fullscale Min	: -5.0000 in
Fullscale Max	: 5.0000 in
Manual/Auto Offset	: 1.0000 in
Sensor	: Displace5inch.scf
Range	: 5 inch
Conditioner	: 493.21B AC-Slot 6
Polarity	: Normal
Excitation (peak)	: 10.0000 V
Phase	: 40.7813 deg
Gain	: 1.1426 (none)
Post-amp	: 1.1426 (none)
Fine Zero	: 0.0000 V
DeltaK	: 1.0000 (none)
Auto Zero	: 0.0000 (none)
Manual Zero	: 0.0000 V
Pre-amp	: 1.0

Axial Force

Hardware Name	: 493.21B DC-Slot 5
Fullscale Min	: -10000.0000 lbf
Fullscale Max	: 10000.0000 lbf
Manual/Auto Offset	: -331.3020 lbf
Sensor	: Force.scf
Range	: 10 kip
Conditioner	: 493.21B DC-Slot 5
Polarity	: Normal
Excitation	: 10.0000 V
Gain	: 4160.1274 (none)
Post-amp	: 16.0005 (none)
Fine Zero	: 0.0000 V
Balance Option	: 0.0000 V
DeltaK	: 0.9968 (none)
Auto Zero	: 0.0000 (none)
Manual Zero	: 0.0000 V
Pre-amp	: 260.0
Shunt Reference(+)	: 113.3926 lbf

ANALOG OUTPUT SIGNALS :-

Axial Output

Hardware Name	: 493.14 2SVD-Slot 1
Fullscale Min	: -10.0000 V
Fullscale Max	: 10.0000 V
Conditioner	: 493.14 2SVD-Slot 1
Valve Balance 1	: 0.0002 V
Valve Balance 2	: 0.0002 V
Dither Amplitude	: 0.1000 V
Dither Frequency	: 528.0000 Hz

Polarity : Invert

Readout 1
Hardware Name : Analog Readout 1
Fullscale Min : -10.0000 V
Fullscale Max : 10.0000 V
Selected Signal : None
Conditioner : Analog Readout 1
Gain : 1.0000 (none)
Offset : 0.0000 V
Polarity : Normal

Readout 2
Hardware Name : Analog Readout 2
Fullscale Min : -10.0000 V
Fullscale Max : 10.0000 V
Selected Signal : None
Conditioner : Analog Readout 2
Gain : 1.0000 (none)
Offset : 0.0000 V
Polarity : Normal

LIMIT DETECTORS :-

Axial Displacement
Upper Limit : 3.0000 in
Lower Limit : -1.0000 in
Upper Action : Interlock
Lower Action : Interlock

Axial LVDTavg
Upper Limit : 0.5118 in
Lower Limit : -0.5118 in
Upper Action : Disabled
Lower Action : Disabled

Axial Force
Upper Limit : 9799.9999 lbf
Lower Limit : -1000.0000 lbf
Upper Action : Interlock
Lower Action : Interlock

LVDT 1
Upper Limit : 0.2500 in
Lower Limit : -0.2500 in
Upper Action : Interlock
Lower Action : Interlock

LVDT 2
Upper Limit : 0.2500 in

Lower Limit : -0.2500 in
Upper Action : Interlock
Lower Action : Interlock

Aux Input 3
Upper Limit : 13.0000 in/in
Lower Limit : -13.0000 in/in
Upper Action : Disabled
Lower Action : Disabled

Aux Input 4
Upper Limit : 13.0000 in/in
Lower Limit : -13.0000 in/in
Upper Action : Disabled
Lower Action : Disabled

Aux Input 5
Upper Limit : 13.0000 in/in
Lower Limit : -13.0000 in/in
Upper Action : Disabled
Lower Action : Disabled

Aux Input 6
Upper Limit : 13.0000 in/in
Lower Limit : -13.0000 in/in
Upper Action : Disabled
Lower Action : Disabled

Aux Input 7
Upper Limit : 1300.0000 DaN
Lower Limit : -1300.0000 DaN
Upper Action : Disabled
Lower Action : Disabled

ERROR DETECTORS :-

Axial Displacement Absolute Error
Outer Limit : 1.0236 in
Inner Limit : 1.0236 in
Outer Action : Disabled
Inner Action : Disabled

Axial LVDTavg Absolute Error
Outer Limit : 1.0236 in
Inner Limit : 1.0236 in
Outer Action : Disabled
Inner Action : Disabled

Axial Force Absolute Error
Outer Limit : 5845.0325 lbf

Inner Limit : 5845.0325 lbf
Outer Action : Disabled
Inner Action : Disabled

Axial CLC Absolute Error
Outer Limit : 1.0236 in
Inner Limit : 1.0236 in
Outer Action : Disabled
Inner Action : Disabled

CONTROL CHANNELS :-

Axial
Channel Type : Program and Control
HSM : HSM 1
External Command : None
Manual Command : 0.6989 in
Setpoint Ramp Time : 2.0000 Sec
Span Ramp Time : 2.0000 Sec
Start Taper Time : 2.0000 Sec
Stop Taper Time : 2.0000 Sec
Hold Taper Time : 2.0000 Sec
Resume Taper Time : 2.0000 Sec
Start Ramp Time : 2.0000 Sec
Stop Ramp Time : 2.0000 Sec
Hold Ramp Time : 2.0000 Sec
Resume Ramp Time : 2.0000 Sec
Begin Taper Time : 2.0000 Sec
End Taper Time : 2.0000 Sec
Number of Control Modes : 4
Control Mode : Displacement
Current Span : 100.0000 %
Current Setpoint : 0.6989 in
Setpoint Ramp Time : 2.0000 Sec
Span Ramp Time : 2.0000 Sec
Number of Adaptive Compensators : 3
Adaptive Compensator : Null Pacing
Controller Type : NP CONTROLLER
Static NP Error Limit : 2.0000 %
Static NP Timeout : 0.0000 Sec
Static NP Timeout Action : Disabled
Dynamic NP Error Limit : 2.0000 %
Dynamic NP Low Cycle Timeout : 0.0000 Sec
Integrator Gain : 0.0000 (none)
Dynamic NP Low Cycle Timeout Action : Disabled
Adaptive Compensator : PVC
Controller Type : AC CONTROLLER
Convergence Rate : 10.0000 %
Sensitivity : 0.5000 %
Integrator Gain : 0.0000 (none)

Adaptation State	: Resume
Adaptive Compensator	: APC
Controller Type	: APC CONTROLLER
Convergence Rate	: 5.0000 %
Integrator Gain	: 0.0000 (none)
Adaptation State	: Resume
Controller	: Displacement
Controller Type	: PIDF CONTROLLER
P Gain	: 45.0000 (none)
I Gain	: 1.0000 (none)
D Gain	: 0.0000 (none)
F Gain	: 0.0000 (none)
S Gain	: 0.0000 (none)
FL Filter	: 2048.0000 Hz
Lower Limit	: -0.1969 in
Upper Limit	: 0.1969 in
Tracking	: 50.0000 %
Sweep Freq.	: 20.0000 Hz
Filter Type	: No Filter
Frequency	: 2048.0000 Hz
Bandwidth	: 20.4800 Hz
Stabilization Filter Type	: 1 Hz High-pass
Stabilization Filter Min	: 1.0000 Hz
Stabilization Filter Max	: 2048.0000 Hz
Control Mode	: LVDTavg
Current Span	: 100.0000 %
Current Setpoint	: 0.0000 in
Setpoint Ramp Time	: 2.0000 Sec
Span Ramp Time	: 2.0000 Sec
Number of Adaptive Compensators	: 3
Adaptive Compensator	: Null Pacing
Controller Type	: NP CONTROLLER
Static NP Error Limit	: 2.0000 %
Static NP Timeout	: 0.0000 Sec
Static NP Timeout Action	: Disabled
Dynamic NP Error Limit	: 2.0000 %
Dynamic NP Low Cycle Timeout	: 0.0000 Sec
Integrator Gain	: 0.0000 (none)
Dynamic NP Low Cycle Timeout Action	: Disabled
Adaptive Compensator	: PVC
Controller Type	: AC CONTROLLER
Convergence Rate	: 10.0000 %
Sensitivity	: 0.5000 %
Integrator Gain	: 0.0000 (none)
Adaptation State	: Resume
Adaptive Compensator	: APC
Controller Type	: APC CONTROLLER
Convergence Rate	: 5.0000 %
Integrator Gain	: 0.0000 (none)
Adaptation State	: Resume
Controller	: LVDTavg

Controller Type	: PIDF CONTROLLER
P Gain	: 19.1964 (none)
I Gain	: 3.8393 (none)
D Gain	: 0.0000 (none)
F Gain	: 0.0000 (none)
S Gain	: 0.0000 (none)
FL Filter	: 2048.0000 Hz
Lower Limit	: -0.1500 in
Upper Limit	: 0.1500 in
Tracking	: 50.0000 %
Sweep Freq.	: 20.0000 Hz
Filter Type	: No Filter
Frequency	: 2048.0000 Hz
Bandwidth	: 20.4800 Hz
Stabilization Filter Type	: 1 Hz High-pass
Stabilization Filter Min	: 1.0000 Hz
Stabilization Filter Max	: 2048.0000 Hz
Control Mode	: Force
Current Span	: 100.0000 %
Current Setpoint	: 0.0000 lbf
Setpoint Ramp Time	: 2.0000 Sec
Span Ramp Time	: 2.0000 Sec
Number of Adaptive Compensators	: 3
Adaptive Compensator	: Null Pacing
Controller Type	: NP CONTROLLER
Static NP Error Limit	: 2.0000 %
Static NP Timeout	: 0.0000 Sec
Static NP Timeout Action	: Disabled
Dynamic NP Error Limit	: 2.0000 %
Dynamic NP Low Cycle Timeout	: 0.0000 Sec
Integrator Gain	: 0.0000 (none)
Dynamic NP Low Cycle Timeout Action	: Disabled
Adaptive Compensator	: PVC
Controller Type	: AC CONTROLLER
Convergence Rate	: 10.0000 %
Sensitivity	: 0.5000 %
Integrator Gain	: 0.0000 (none)
Adaptation State	: Resume
Adaptive Compensator	: APC
Controller Type	: APC CONTROLLER
Convergence Rate	: 5.0000 %
Integrator Gain	: 0.0000 (none)
Adaptation State	: Resume
Controller	: Force
Controller Type	: PIDF CONTROLLER
P Gain	: 2.0000 (none)
I Gain	: 0.2000 (none)
D Gain	: 0.0000 (none)
F Gain	: 0.0000 (none)
S Gain	: 0.0000 (none)
FL Filter	: 2048.0000 Hz

Lower Limit	: -1124.0447 lbf
Upper Limit	: 1124.0447 lbf
Tracking	: 50.0000 %
Sweep Freq.	: 20.0000 Hz
Filter Type	: No Filter
Frequency	: 2048.0000 Hz
Bandwidth	: 20.4800 Hz
Stabilization Filter Type	: 1 Hz High-pass
Stabilization Filter Min	: 1.0000 Hz
Stabilization Filter Max	: 2048.0000 Hz
Control Mode	: CLC
Current Span	: 100.0000 %
Current Setpoint	: 1.9009 in
Setpoint Ramp Time	: 2.0000 Sec
Span Ramp Time	: 2.0000 Sec
Number of Adaptive Compensators	: 3
Adaptive Compensator	: Null Pacing
Controller Type	: NP CONTROLLER
Static NP Error Limit	: 2.0000 %
Static NP Timeout	: 0.0000 Sec
Static NP Timeout Action	: Disabled
Dynamic NP Error Limit	: 2.0000 %
Dynamic NP Low Cycle Timeout	: 0.0000 Sec
Integrator Gain	: 0.0000 (none)
Dynamic NP Low Cycle Timeout Action	: Disabled
Adaptive Compensator	: PVC
Controller Type	: AC CONTROLLER
Convergence Rate	: 10.0000 %
Sensitivity	: 0.5000 %
Integrator Gain	: 0.0000 (none)
Adaptation State	: Resume
Adaptive Compensator	: APC
Controller Type	: APC CONTROLLER
Convergence Rate	: 5.0000 %
Integrator Gain	: 0.0000 (none)
Adaptation State	: Resume
Controller	: CLC
Controller Type	: CLC CONTROLLER
Active P Gain	: 0.1000 (none)
Limiting P Gain	: 0.1000 (none)
Lower Limit	: -0.3937 in
Upper Limit	: 0.3937 in

MASTER SPAN GROUP :-

Channel List	: Axial

ACTIONS :-

CALCULATED SIGNALS :-

Axial LVDTavg
Axial LVDTavg Fullscale Min : -0.3937 in
Axial LVDTavg Fullscale Max : 0.3937 in
Expression : "Axial LVDTavg" = ("LVDT 1" + "LVDT 2") / 2;

EXTERNAL COMMAND GROUP :-

External Command Group :

MASTER COMMAND GROUP :-

Master Command Group List

ACTIVE TEST PARAMETERS

Station: active_setup.cfg Parameter Set : active 4/29/15 1:02:49 PM
Items preceded by an asterisk (*) have been modified.

Application Information
  Name : Station Manager
  Version : 3.2C 929

ANALOG INPUT SIGNALS :-

  LVDT 1
    Hardware Name : Analog Input 1-Slot 3
    Fullscale Min : -0.2500 in
    Fullscale Max : 0.2500 in
    Manual/Auto Offset : 0.0000 in
    Sensor :
    Range :
    Conditioner : Analog Input 1-Slot 3
      Gain : 1.0000 (none)
      Auto Zero : 0.0000 (none)
      Polarity : Invert

  LVDT 2
    Hardware Name : Analog Input 2-Slot 3
    Fullscale Min : -0.2500 in
    Fullscale Max : 0.2500 in
    Manual/Auto Offset : 0.0000 in
    Sensor :
    Range :
    Conditioner : Analog Input 2-Slot 3
      Gain : 1.0000 (none)
      Auto Zero : 0.0000 (none)
      Polarity : Invert

  Aux Input 3
    Hardware Name : Analog Input 3-Slot 3
    Fullscale Min : -10.0000 in/in
    Fullscale Max : 10.0000 in/in
    Manual/Auto Offset : 0.0000 in/in
    Sensor :
    Range :
    Conditioner : Analog Input 3-Slot 3
      Gain : 1.0000 (none)
      Auto Zero : 0.0000 (none)
      Polarity : Normal

  Aux Input 4
    Hardware Name : Analog Input 4-Slot 3
    Fullscale Min : -10.0000 in/in
    Fullscale Max : 10.0000 in/in

Manual/Auto Offset	: 0.0000 in/in
Sensor	:
Range	:
Conditioner	: Analog Input 4-Slot 3
Gain	: 1.0000 (none)
Auto Zero	: 0.0000 (none)
Polarity	: Normal

Aux Input 5

Hardware Name	: Analog Input 5-Slot 3
Fullscale Min	: -10.0000 in/in
Fullscale Max	: 10.0000 in/in
Manual/Auto Offset	: 0.0000 in/in
Sensor	:
Range	:
Conditioner	: Analog Input 5-Slot 3
Gain	: 1.0000 (none)
Auto Zero	: 0.0000 (none)
Polarity	: Normal

Aux Input 6

Hardware Name	: Analog Input 6-Slot 3
Fullscale Min	: -10.0000 in/in
Fullscale Max	: 10.0000 in/in
Manual/Auto Offset	: 0.0000 in/in
Sensor	:
Range	:
Conditioner	: Analog Input 6-Slot 3
Gain	: 1.0000 (none)
Auto Zero	: 0.0000 (none)
Polarity	: Normal

Axial Displacement

Hardware Name	: 493.21B AC-Slot 6
Fullscale Min	: -5.0000 in
Fullscale Max	: 5.0000 in
Manual/Auto Offset	: 1.0000 in
Sensor	: Displace5inch.scf
Range	: 5 inch
Conditioner	: 493.21B AC-Slot 6
Polarity	: Normal
Excitation (peak)	: 10.0000 V
Phase	: 40.7813 deg
Gain	: 1.1426 (none)
Post-amp	: 1.1426 (none)
Fine Zero	: 0.0000 V
DeltaK	: 1.0000 (none)
Auto Zero	: 0.0000 (none)
Manual Zero	: 0.0000 V
Pre-amp	: 1.0

Axial ForceBottom

Hardware Name	: 493.21B DC-Slot 4
Fullscale Min	: -20000.0000 lbf
Fullscale Max	: 20000.0000 lbf
Manual/Auto Offset	: 2833.3620 lbf
Sensor	:
Range	:
Conditioner	: 493.21B DC-Slot 4
Polarity	: Normal
Excitation	: 10.0000 V
Gain	: 415.2311 (none)
Post-amp	: 1.5970 (none)
Fine Zero	: 0.0000 V
Balance Option	: 0.0000 V
DeltaK	: 1.0000 (none)
Auto Zero	: 0.0000 (none)
Manual Zero	: -0.9912 V
Pre-amp	: 260.0
Shunt Reference(+)	: 0.0000 lbf

Axial ForceTop

Hardware Name	: 493.21B DC-Slot 5
Fullscale Min	: -10000.0000 lbf
Fullscale Max	: 10000.0000 lbf
Manual/Auto Offset	: -326.9008 lbf
Sensor	: Force.scf
Range	: 10 kip
Conditioner	: 493.21B DC-Slot 5
Polarity	: Normal
Excitation	: 10.0000 V
Gain	: 4160.1274 (none)
Post-amp	: 16.0005 (none)
Fine Zero	: 0.0000 V
Balance Option	: 0.0000 V
DeltaK	: 0.9968 (none)
Auto Zero	: 0.0000 (none)
Manual Zero	: 0.0000 V
Pre-amp	: 260.0
Shunt Reference(+)	: 113.3926 lbf

ANALOG OUTPUT SIGNALS :-

Axial Output

Hardware Name	: 493.14 2SVD-Slot 1
Fullscale Min	: -10.0000 V
Fullscale Max	: 10.0000 V
Conditioner	: 493.14 2SVD-Slot 1
Valve Balance 1	: 0.0002 V
Valve Balance 2	: 0.0002 V
Dither Amplitude	: 0.1003 V

Dither Frequency : 1000.0000 Hz
Polarity : Invert

Readout 1
Hardware Name : Analog Readout 1
Fullscale Min : -0.3937 in
Fullscale Max : 0.3937 in
Selected Signal : Jack Command
Conditioner : Analog Readout 1
Gain : 1.0000 (none)
Offset : 0.0000 V
Polarity : Normal

Readout 2
Hardware Name : Analog Readout 2
Fullscale Min : -0.7874 in
Fullscale Max : 0.7874 in
Selected Signal : Jack Error
Conditioner : Analog Readout 2
Gain : 100.0000 (none)
Offset : 0.0000 V
Polarity : Normal

DIGITAL INPUT SIGNALS :-

Digital Input 1
Hardware Name : Digital Input 1
Trigger : None
Action : Disabled

Digital Input 2
Hardware Name : Digital Input 2
Trigger : None
Action : Disabled

Digital Input 3
Hardware Name : Digital Input 3
Trigger : None
Action : Disabled

Digital Input 4
Hardware Name : Digital Input 4
Trigger : None
Action : Disabled

DIGITAL OUTPUT SIGNALS :-

Digital Output 1
Hardware Name : Digital Output 1

Digital Output 2
Hardware Name : Digital Output 2

Digital Output 3
Hardware Name : Digital Output 3

Digital Output 4
Hardware Name : Digital Output 4

LIMIT DETECTORS :-

LVDT 1
Upper Limit : 0.2500 in
Lower Limit : -0.2500 in
Upper Action : Interlock
Lower Action : Interlock

LVDT 2
Upper Limit : 0.2500 in
Lower Limit : -0.2500 in
Upper Action : Interlock
Lower Action : Interlock

Aux Input 3
Upper Limit : 13.0000 in/in
Lower Limit : -13.0000 in/in
Upper Action : Disabled
Lower Action : Disabled

Aux Input 4
Upper Limit : 13.0000 in/in
Lower Limit : -13.0000 in/in
Upper Action : Disabled
Lower Action : Disabled

Aux Input 5
Upper Limit : 13.0000 in/in
Lower Limit : -13.0000 in/in
Upper Action : Disabled
Lower Action : Disabled

Aux Input 6
Upper Limit : 13.0000 in/in
Lower Limit : -13.0000 in/in
Upper Action : Disabled
Lower Action : Disabled

Axial Displacement
Upper Limit : 3.0000 in

Lower Limit	: -2.0056 in
Upper Action	: Interlock
Lower Action	: Interlock

Axial ForceBottom

Upper Limit	: 4000.0001 lbf
Lower Limit	: -4000.0001 lbf
Upper Action	: Interlock
Lower Action	: Interlock

Axial ForceTop

Upper Limit	: 1000.00002 lbf
Lower Limit	: -2000.00003 lbf
Upper Action	: Interlock
Lower Action	: Interlock

Jack LVDTavg

Upper Limit	: 0.5118 in
Lower Limit	: -0.5118 in
Upper Action	: Disabled
Lower Action	: Disabled

ERROR DETECTORS :-

Axial Displacement Absolute Error

Outer Limit	: 1.0236 in
Inner Limit	: 1.0236 in
Outer Action	: Disabled
Inner Action	: Disabled

Axial ForceBottom Absolute Error

Outer Limit	: 5845.0325 lbf
Inner Limit	: 5845.0325 lbf
Outer Action	: Disabled
Inner Action	: Disabled

Axial ForceTop Absolute Error

Outer Limit	: 5845.0325 lbf
Inner Limit	: 5845.0325 lbf
Outer Action	: Disabled
Inner Action	: Disabled

Jack LVDTavg Absolute Error

Outer Limit	: 1.0236 in
Inner Limit	: 1.0236 in
Outer Action	: Disabled
Inner Action	: Disabled

CONTROL CHANNELS :-

Axial

Channel Type	: Program and Control
HSM	: HSM 1
External Command	: None
Manual Command	: 0.5196 in
Setpoint Ramp Time	: 2.0000 Sec
Span Ramp Time	: 2.0000 Sec
Start Taper Time	: 2.0000 Sec
Stop Taper Time	: 2.0000 Sec
Hold Taper Time	: 2.0000 Sec
Resume Taper Time	: 2.0000 Sec
Start Ramp Time	: 2.0000 Sec
Stop Ramp Time	: 2.0000 Sec
Hold Ramp Time	: 2.0000 Sec
Resume Ramp Time	: 2.0000 Sec
Begin Taper Time	: 2.0000 Sec
End Taper Time	: 2.0000 Sec
Number of Control Modes	: 3
Control Mode	: Displacement
Current Span	: 100.0000 %
Current Setpoint	: 0.5196 in
Setpoint Ramp Time	: 2.0000 Sec
Span Ramp Time	: 2.0000 Sec
Number of Adaptive Compensators	: 3
Adaptive Compensator	: Null Pacing
Controller Type	: NP CONTROLLER
Static NP Error Limit	: 2.0000 %
Static NP Timeout	: 0.0000 Sec
Static NP Timeout Action	: Disabled
Dynamic NP Error Limit	: 2.0000 %
Dynamic NP Low Cycle Timeout	: 0.0000 Sec
Integrator Gain	: 0.0000 (none)
Dynamic NP Low Cycle Timeout Action	: Disabled
Adaptive Compensator	: PVC
Controller Type	: AC CONTROLLER
Convergence Rate	: 10.0000 %
Sensitivity	: 0.5000 %
Integrator Gain	: 0.0000 (none)
Adaptation State	: Resume
Adaptive Compensator	: APC
Controller Type	: APC CONTROLLER
Convergence Rate	: 5.0000 %
Integrator Gain	: 0.0000 (none)
Adaptation State	: Resume
Controller	: Displacement
Controller Type	: PIDF CONTROLLER
P Gain	: 45.0000 (none)
I Gain	: 1.0000 (none)
D Gain	: 0.0000 (none)

F Gain	: 0.0000 (none)
S Gain	: 0.0000 (none)
FL Filter	: 2048.0000 Hz
Lower Limit	: -0.1969 in
Upper Limit	: 0.1969 in
Tracking	: 50.0000 %
Sweep Freq.	: 20.0000 Hz
Filter Type	: No Filter
Frequency	: 2048.0000 Hz
Bandwidth	: 20.4800 Hz
Stabilization Filter Type	: 1 Hz High-pass
Stabilization Filter Min	: 1.0000 Hz
Stabilization Filter Max	: 2048.0000 Hz
Control Mode	: ForceBottom
Current Span	: 100.0000 %
Current Setpoint	: -60.3718 lbf
Setpoint Ramp Time	: 2.0000 Sec
Span Ramp Time	: 2.0000 Sec
Number of Adaptive Compensators	: 3
Adaptive Compensator	: Null Pacing
Controller Type	: NP CONTROLLER
Static NP Error Limit	: 2.0000 %
Static NP Timeout	: 0.0000 Sec
Static NP Timeout Action	: Disabled
Dynamic NP Error Limit	: 2.0000 %
Dynamic NP Low Cycle Timeout	: 0.0000 Sec
Integrator Gain	: 0.0000 (none)
Dynamic NP Low Cycle Timeout Action	: Disabled
Adaptive Compensator	: PVC
Controller Type	: AC CONTROLLER
Convergence Rate	: 10.0000 %
Sensitivity	: 0.5000 %
Integrator Gain	: 0.0000 (none)
Adaptation State	: Resume
Adaptive Compensator	: APC
Controller Type	: APC CONTROLLER
Convergence Rate	: 5.0000 %
Integrator Gain	: 0.0000 (none)
Adaptation State	: Resume
Controller	: ForceBottom
Controller Type	: PIDF CONTROLLER
P Gain	: 3.0554 (none)
I Gain	: 0.1000 (none)
D Gain	: 0.0000 (none)
F Gain	: 0.0000 (none)
S Gain	: 0.0000 (none)
FL Filter	: 2048.0000 Hz
Lower Limit	: -1124.0447 lbf
Upper Limit	: 1124.0447 lbf
Tracking	: 50.0000 %
Sweep Freq.	: 20.0000 Hz

Filter Type	: No Filter
Frequency	: 2048.0000 Hz
Bandwidth	: 20.4800 Hz
Stabilization Filter Type	: 1 Hz High-pass
Stabilization Filter Min	: 1.0000 Hz
Stabilization Filter Max	: 2048.0000 Hz
Control Mode	: ForceTop
Current Span	: 100.0000 %
Current Setpoint	: 0.0000 lbf
Setpoint Ramp Time	: 2.0000 Sec
Span Ramp Time	: 2.0000 Sec
Number of Adaptive Compensators	: 3
Adaptive Compensator	: Null Pacing
Controller Type	: NP CONTROLLER
Static NP Error Limit	: 2.0000 %
Static NP Timeout	: 0.0000 Sec
Static NP Timeout Action	: Disabled
Dynamic NP Error Limit	: 2.0000 %
Dynamic NP Low Cycle Timeout	: 0.0000 Sec
Integrator Gain	: 0.0000 (none)
Dynamic NP Low Cycle Timeout Action	: Disabled
Adaptive Compensator	: PVC
Controller Type	: AC CONTROLLER
Convergence Rate	: 10.0000 %
Sensitivity	: 0.5000 %
Integrator Gain	: 0.0000 (none)
Adaptation State	: Resume
Adaptive Compensator	: APC
Controller Type	: APC CONTROLLER
Convergence Rate	: 5.0000 %
Integrator Gain	: 0.0000 (none)
Adaptation State	: Resume
Controller	: ForceTop
Controller Type	: PIDF CONTROLLER
P Gain	: 3.0554 (none)
I Gain	: 0.10000 (none)
D Gain	: 0.0000 (none)
F Gain	: 0.0000 (none)
S Gain	: 0.0000 (none)
FL Filter	: 2048.0000 Hz
Lower Limit	: -5000.0000 lbf
Upper Limit	: -500.0000 lbf
Tracking	: 50.0000 %
Sweep Freq.	: 20.0000 Hz
Filter Type	: No Filter
Frequency	: 2048.0000 Hz
Bandwidth	: 20.4800 Hz
Stabilization Filter Type	: 1 Hz High-pass
Stabilization Filter Min	: 1.0000 Hz
Stabilization Filter Max	: 2048.0000 Hz

Jack

Channel Type	: Program and Control
HSM	: HSM 1
External Command	: None
Manual Command	: 0.0000 in
Setpoint Ramp Time	: 2.0000 Sec
Span Ramp Time	: 2.0000 Sec
Start Taper Time	: 2.0000 Sec
Stop Taper Time	: 2.0000 Sec
Hold Taper Time	: 2.0000 Sec
Resume Taper Time	: 2.0000 Sec
Start Ramp Time	: 2.0000 Sec
Stop Ramp Time	: 2.0000 Sec
Hold Ramp Time	: 2.0000 Sec
Resume Ramp Time	: 2.0000 Sec
Begin Taper Time	: 2.0000 Sec
End Taper Time	: 2.0000 Sec
Number of Control Modes	: 1
Control Mode	: LVDTavg
Current Span	: 100.0000 %
Current Setpoint	: 0.0000 in
Setpoint Ramp Time	: 2.0000 Sec
Span Ramp Time	: 2.0000 Sec
Number of Adaptive Compensators	: 3
Adaptive Compensator	: Null Pacing
Controller Type	: NP CONTROLLER
Static NP Error Limit	: 2.0000 %
Static NP Timeout	: 0.0000 Sec
Static NP Timeout Action	: Disabled
Dynamic NP Error Limit	: 2.0000 %
Dynamic NP Low Cycle Timeout	: 0.0000 Sec
Integrator Gain	: 0.0000 (none)
Dynamic NP Low Cycle Timeout Action	: Disabled
Adaptive Compensator	: PVC
Controller Type	: AC CONTROLLER
Convergence Rate	: 10.0000 %
Sensitivity	: 0.5000 %
Integrator Gain	: 0.0000 (none)
Adaptation State	: Resume
Adaptive Compensator	: APC
Controller Type	: APC CONTROLLER
Convergence Rate	: 5.0000 %
Integrator Gain	: 0.0000 (none)
Adaptation State	: Resume
Controller	: LVDTavg
Controller Type	: PIDF CONTROLLER
P Gain	: 1.0000 (none)
I Gain	: 0.1000 (none)
D Gain	: 0.0000 (none)
F Gain	: 0.0000 (none)
S Gain	: 0.0000 (none)

FL Filter	: 2048.0000 Hz
Lower Limit	: -0.1969 in
Upper Limit	: 0.1969 in
Tracking	: 50.0000 %
Sweep Freq.	: 20.0000 Hz
Filter Type	: No Filter
Frequency	: 2048.0000 Hz
Bandwidth	: 20.4800 Hz
Stabilization Filter Type	: 1 Hz High-pass
Stabilization Filter Min	: 1.0000 Hz
Stabilization Filter Max	: 2048.0000 Hz

MASTER SPAN GROUP :-

Channel List	: Axial

ACTIONS :-

CALCULATION PARAMETERS :-

B

Fullscale Min	: 0.0000 (in)
Fullscale Max	: 2.0000 (in)
Access Level	: Configuration
Signal Value	: 1.0000 (in)

W

Fullscale Min	: 0.0000 (in)
Fullscale Max	: 4.0000 (in)
Access Level	: Configuration
Signal Value	: 2.0000 (in)

CALCULATED SIGNALS :-

Jack LVDTavg

Jack LVDTavg Fullscale Min	: -0.3937 in
Jack LVDTavg Fullscale Max	: 0.3937 in
Expression	: Jack LVDTavg" = ("LVDT 1" +"LVDT 2")/2 ;

EXTERNAL COMMAND GROUP :-

External Command Group	:

MASTER COMMAND GROUP :-

Master Command Group List

Master Command Group 1	: Axial Displacement
	: Jack LVDTavg

Hydraulic Power Supply

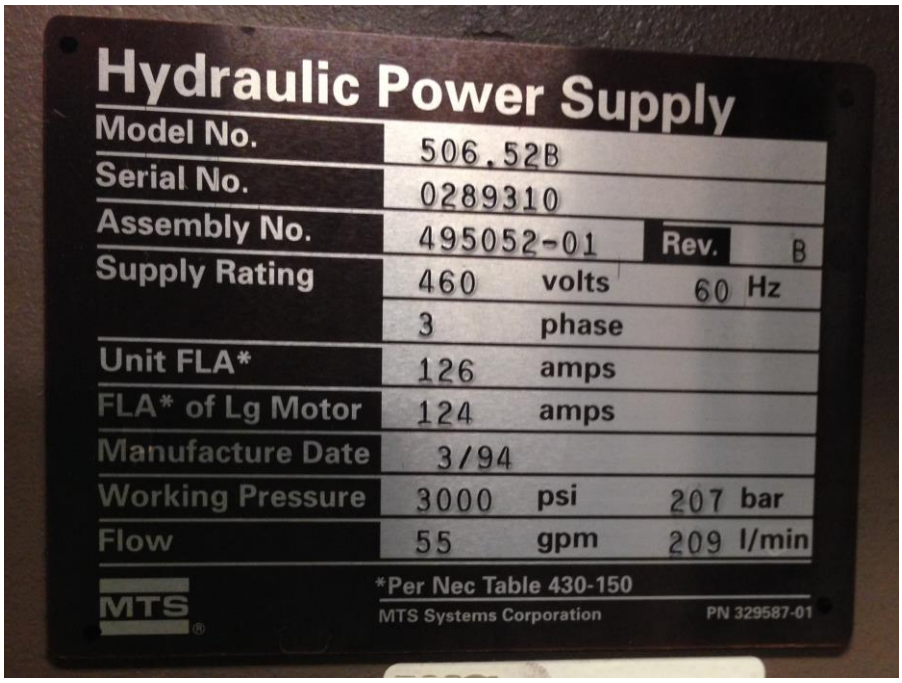

Figure B.2: *Hydraulic Power Supply Name Plate*

Hydraulic Service Manifold

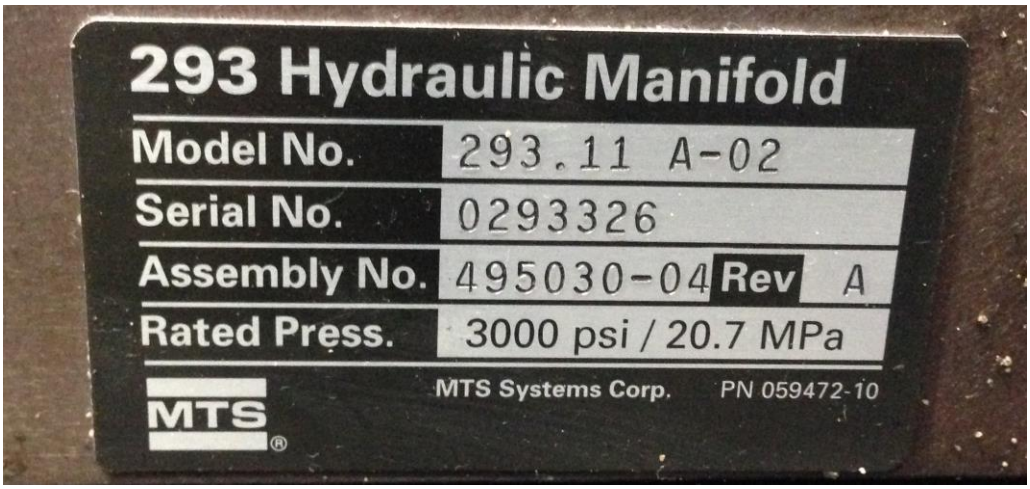

Figure B.3: *Hydraulic Manifold Name Plate*

Table B.1: *Properties for Hydraulic Service Manifold*

Parameter	Specification
Model Number:	293.11 A-02
Serial No.:	0293326
Assembly No.:	495030-04Rev A
Rated Pressure:	3000 psi / 20.7 MPa
No. of Stations:	2
Control Voltage:	24 V DC
Pilot Pressure:	No

*For more detailed information, refer to MTS Series 293.1X Hydraulic Service Manifolds Product Information [96]

100 Kip SATEC Testing Machine

Figure B.4: *100 Kip SATEC Testing Machine Name Plate*

Table B.2: *Properties for 100 Kip SATEC Testing Machine*

Parameter	Specification
Machine Model:	Model TC-110 Computer Aided Testing System
Serial No.:	TC-110-1046
Customer:	Georgia Institute of Technology Mechanical Engineering 888 Hemphill Ave. N.W. Atlanta, GA 30332
Customer Order No.:	153902204
Load System Capacity	+/- 100,000 lbs
Software Version No:	V02.04.000
Power Requirements:	460 VAC, 60 Hertz, 3 Phase (Pumping Unit) 120 VAC, 60 Hertz, 1 Phase (Console)
Machine Stroke:	6”
Vertical Test Space: (Between Crosshead and Table)	55.25” Maximum 15.25” Minimum
Piston Area:	8.765 Sq. In.
Maximum Actuator Speed:	110 Inches/Min.
Crosshead Adjustment Speed:	15 Inches/Min.
Axial Stiffness	> 2.5 million pounds/in.

Twin Moog Servo-valves

Figure B.5: *Twin Moog Servo-valves Name Plates*

Table B.3: *Properties for Twin Moog Servo-valves [S 38 F O F M 4 N P H]*

Parameter	**Specification**
Series and Model:	760-103A
Valve Version:	[S] Standard Response
Rated Flow:	[38] 38 lpm (10 gpm)
Maximum Operating Pressure:	[F] 3000 psi (210 Bar)
Main Spool (BSA) Type:	[O] 4-way/axis cut/linear
Pilot Stage Version:	[F] Standard Dynamics, Nozzle-Flapper
Spool Position Without Electrical Signal:	[M] Failsafe, Mid-position Defined
Pilot Connections:	[4] Internal Pilot Supply, Internal Return
Seal Material	[N] NBR (Buna)
Valve Connector:	[P] MS Connector over Pressure
Signal Ranges:	[H] +/- 7.5 mA series (+/- 15 mA parallel)

*Box Car Information was supplied by Jim Breeding at Power Systems Inc. (770-475-1680)

Hunger Hydraulic Cylinder

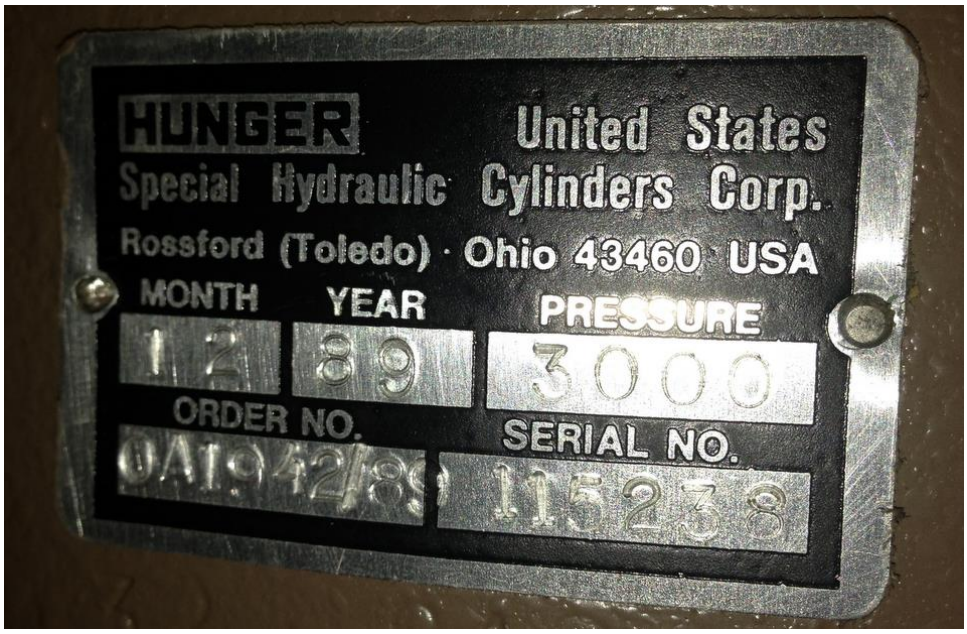

Figure B.6: *Hunger Hydraulic Cylinder Name Plate*

Table B.4: *Properties for Hydraulic Hunger Cylinder, Series OA*

Parameter	Specification
Order No.:	OA1942/89
Serial No.:	115238
Bore Size:	230 mm
Rod Type:	Double Rod, 140 mm rod on both sides
Stroke:	155 mm [6.1 in]
Operating Pressure:	21 MPa [3045 psi]
Test Pressure:	33.6 MPa [4873 psi]

*Information on Series OA was supplied by Hunger Hydraulics CC, Ltd. | 63 Dixie Hwy, Rossford, OH 43460 | phone: 419-666-4510

MTS Hydraulic Collet Grip

Figure B.7: *MTS Hydraulic Collet Grip Name Plate*

Table B.5: *Properties for MTS Hydraulic Collet Grip*

Parameter	Specification
Model:	646.25 Hydraulic Collet Grip
Serial No.:	189
Part No.:	417135-02
Max. Pressure:	6500 psi/45 MPa
Force Capacity	55 kip/250 kN Axial 20,000 in-lb/2200 N-m Torsional

Testing Machine Load Cells

*For load cell specifications, see photos below; both load cells were calibrated by MTS

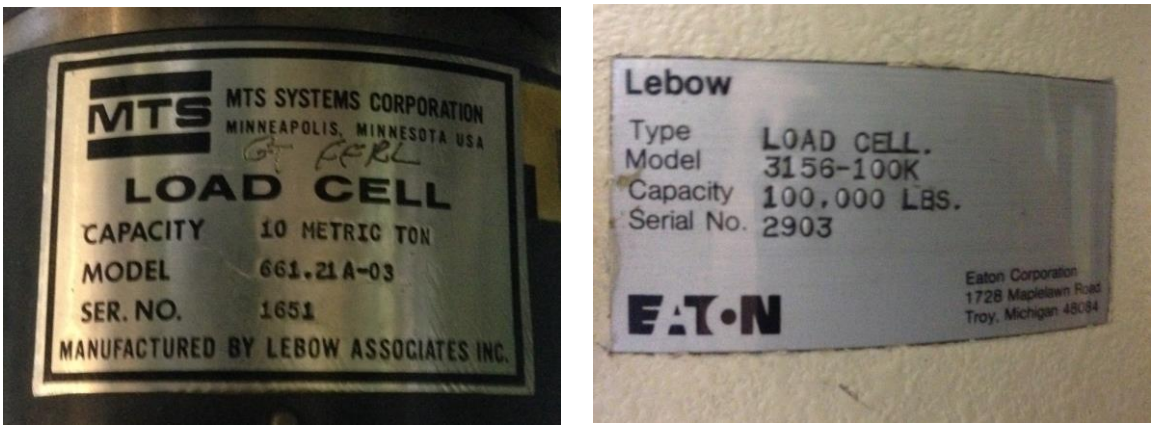

Figure B.8: *Tension/Compression Load Cells (a) Bottom Load Cell, (b) Top Load Cell*

Parker DFplus Servo-valve

Figure B.9: *Parker DFplus Servo-valve Name Plate*

Table B.6: *Properties for DFplus Servo-valve*

Parameter	Specification
Model Number:	DF plus
Order Code:	D1FPE50BA9NB00 20
Supply Voltage:	24 V DC
Nominal Pressure::	350 bar max. P, A, B 35 bar max. T

*For more detailed information, refer to the Operation Manual Series DFplus Design > 20 [97]

Hydraulic Plunger Cylinder (ENERPAC RRH1001)

Figure B.10: *ENERPAC Hydraulic Plunger Cylinder (HPC)*

Table B.7: *Properties for ENERPAC Hydraulic Plunger Cylinder*

Parameter	**Specification**
Hydraulic Jack Model Number:	RRH-1001
Maximum Pressure	10,000 psi
Cylinder Capacity:	100 ton
Stroke:	1.5 in.
Maximum Cylinder Capacity:	Adv.:103 ton Retr.: 68 ton
Cylinder Effective Area:	Adv.: 20.63 in^2 Retr.: 13.54 in^2
Oil Capacity:	Adv.: 30.94 in^3 Retr.: 20.32 in^3
Coll. Height:	6.50 in.
Ext. Height:	8.00 in.
Outside Dia.:	8.38 in.
Center Hole Dia:	3.13 in.
Weight	85 lbs

*information from ENERPAC website [98]

APPENDIX C

PROJECTED SPECIMEN DISPLACEMENT BASED OFF LVDT READINGS

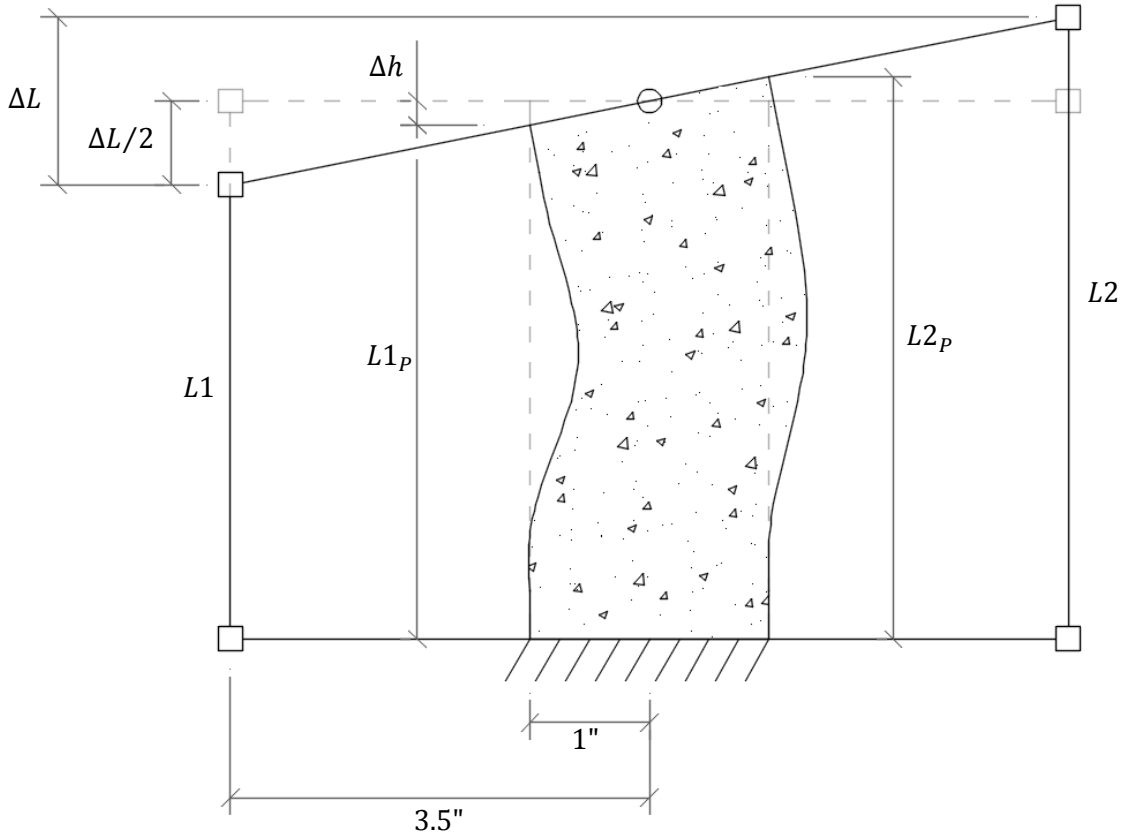

Figure C.1: *Schematic Showing Variables used in Projected Sample Displacement Derivation*

To project the LVDT readings onto the specimen a simple derivation was used based on geometry and symmetry. Any time during the test, the difference between the LVDT1 ($L1$) and LVDT2 ($L2$) readings can be expressed as ΔL (*Eq. C-1)*. Utilizing similar triangles the relative change in vertical displacement of each side of the specimen, Δh, can be determined based off of the differences in LVDTs (*Eq. C-2).*

$$\Delta L = L2 - L1 \qquad \textit{(C-1)}$$

$$\frac{\Delta h}{1"} = \frac{\Delta L/2}{3.5"} \quad \Rightarrow \quad \Delta h = \frac{\Delta L}{7} \qquad \textit{(C-2)}$$

The projected LVDT readings on each side of the specimen ($L1_P$ and $L2_P$) are a function of the current relative LVDT reading, the change in vertical displacement with respect to the horizontal, and the difference between LVDT readings. From *Figure C.1*, these projections can be expressed by *Eq. C-3* and *Eq. C-4*. Substituting in *Eq. C-1* and *Eq. C-2* results in the projected specimen displacements in terms of the known LVDT readings as shown in *Eq. C-5* and *Eq. C-6*.

$$L1_P = L1 + \Delta L/2 - \Delta h \qquad \textit{(C-3)}$$

$$L2_P = L2 - \Delta L/2 + \Delta h \qquad \textit{(C-4)}$$

$$L1_P = \frac{9}{14}L1 + \frac{5}{14}L2 \qquad \textit{(C-5)}$$

$$L2_P = \frac{9}{14}L2 + \frac{5}{14}L1 \qquad \textit{(C-6)}$$

APPENDIX D

FRACTURE ENERGY DETERMINATION FOR SELECT UHPC SPECIMENS

The elastic stiffnesses for the tests discussed in *Section 5.*3 are shown in *Figure D.1a-d* for *P6, P7, A5,* and *A8*, respectively. From these values the elastic moduli were determined by *Eq. D-1*, where A (cross-sectional area) = π in^2 and l (specimen length) = 4.5in for all specimens. All data collected was in units of force, so values were needed to be converted to stress *(Eq. D-2).*

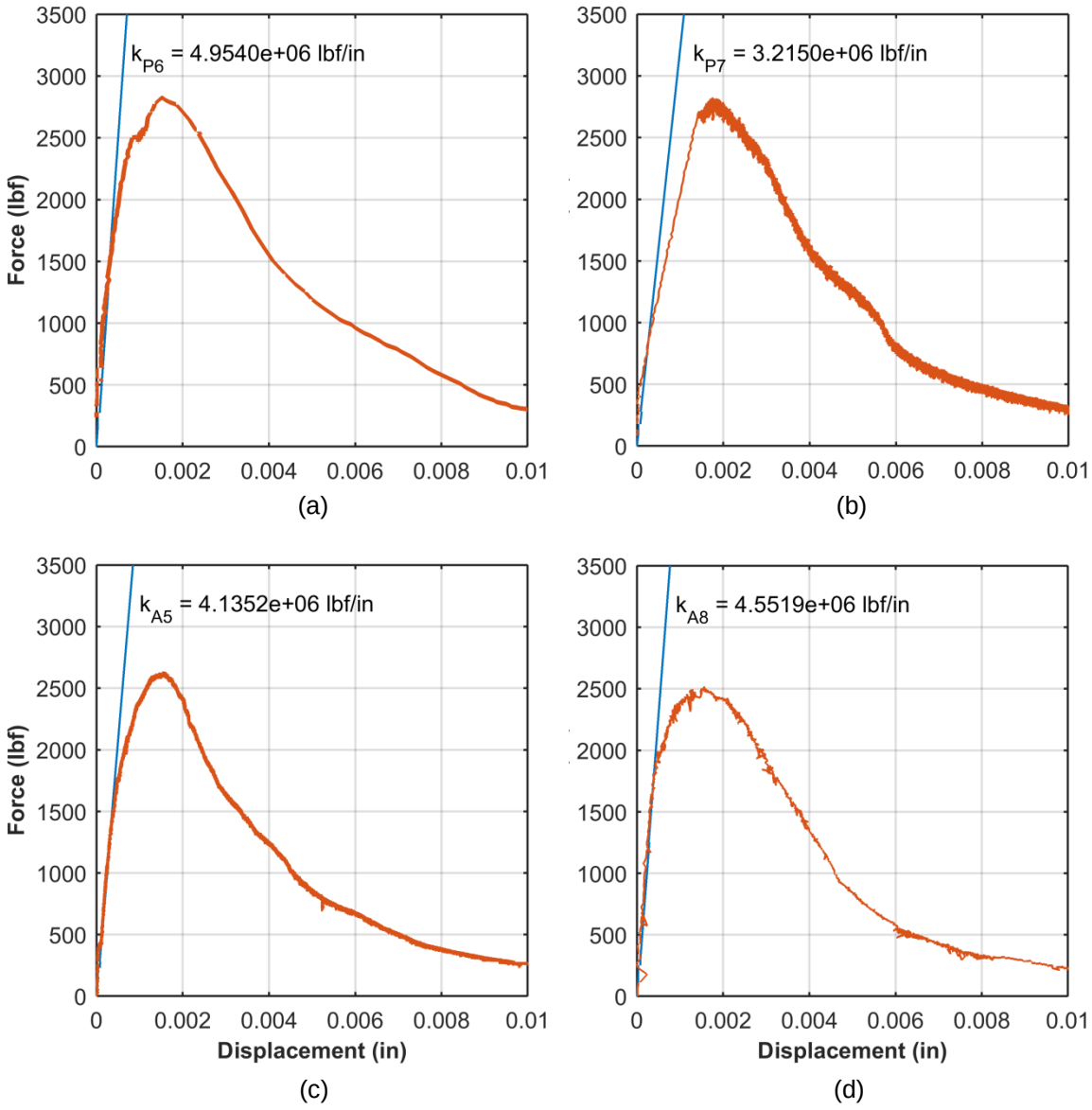

Figure D.1: *Load-displacement Plots for Elastic Stiffness Determination for (a) P6, (b) P7, (c) A5, and (d) A8*

$$E = \frac{k}{A} l \tag{D-1}$$

$$\sigma = \frac{F}{A} \tag{D-2}$$

To determine the stress-crack opening relation from the stress-displacement curve, the method discussed in *Section 4.3.1* [40, 18] was utilized. The crack width, *w*, can be determined by subtracting the elastic deformation at any point on the stress-displacement curve outside the fracture zone, δ_e, and the residual deformation at the peak stress point, δ_0, from the total displacement beyond peak stress, δ. The equations for crack width determination are shown in *Eq. D-3* to *Eq. D-6.* The stress-crack width opening for each UHPC specimen is displayed in *Figure D.2a.*

$$\delta_e = \frac{\sigma}{E} l \tag{D-3}$$

$$\delta_{ep} = \frac{\sigma_p}{E} l \tag{D-4}$$

$$\delta_0 = \delta_p - \delta_{ep} \tag{D-5}$$

$$w = \delta - \delta_e - \delta_0 \tag{D-6}$$

Using a tenth degree polynomial with centered and scaled x data to best fit the scatter, equations for the experimental data were determined. The generic equations are expressed in *Eq. D-7* and *Eq. D-8* with needed constants for each test listed in *Table D.1*. The plotted equations are displayed in *Figure D.2b.*

$$z(w) = \frac{w - \mu_w}{SD_w} \tag{D-7}$$

$$\sigma(w) = \sum_{i=0}^{10} p_i z(w)^i \tag{D-8}$$

Table D.1: *Constants for Stress-Crack Opening Curves for UHPC Tests*

Constants (ksi)	***P6***	***P7***	***A5***	***A8***
μ_w [1]	0.028348	0.012	0.0077319	0.0048492
SD_w [1]	0.0067224	0.0055494	0.009879	0.0050181
p_0	0.0055507	0.052931	0.103293	0.180588
p_1	-0.004403	-0.057321	-0.217362	-0.325756
p_2	0.001055	0.036995	0.379709	0.443831
p_3	-1.303415e-04	0.019627	-0.427258	-0.254335
p_4	0.001411	-0.003496	0.287743	-0.083958
p_5	-5.867845e-04	-0.046526	-0.118187	0.191473
p_6	-7.085055e-04	0.008263	0.030183	-0.109807
p_7	5.325071e-05	0.016271	-0.004778	0.032428
p_8	1.383538e-04	0.001040	4.513613e-04	-0.005361
p_9	2.507647e-05	-0.002304	-2.296360e-05	4.712702e-04
p_{10}	9.181023e-07	-6.787197e-04	4.724393e-07	-1.719053e-05

[1] Units are in inches

The fracture energy, G_f, is determined by taking the integral of the stress-crack opening equation (*Eq. D-9*) from 0 to the maximum crack opening displacement, w_c. For the values in *Table 5.3,* the maximum crack opening displacement for all tests was taken as 0.0209 in.

$$G_f = \int_0^{w_c} \sigma(w)dw \qquad \textit{(D-9)}$$

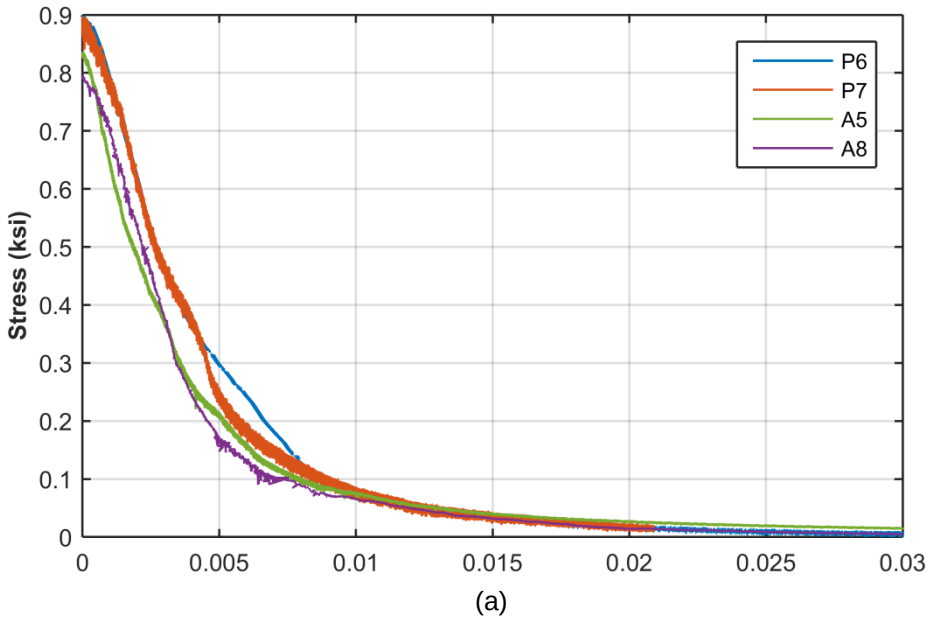

(a)

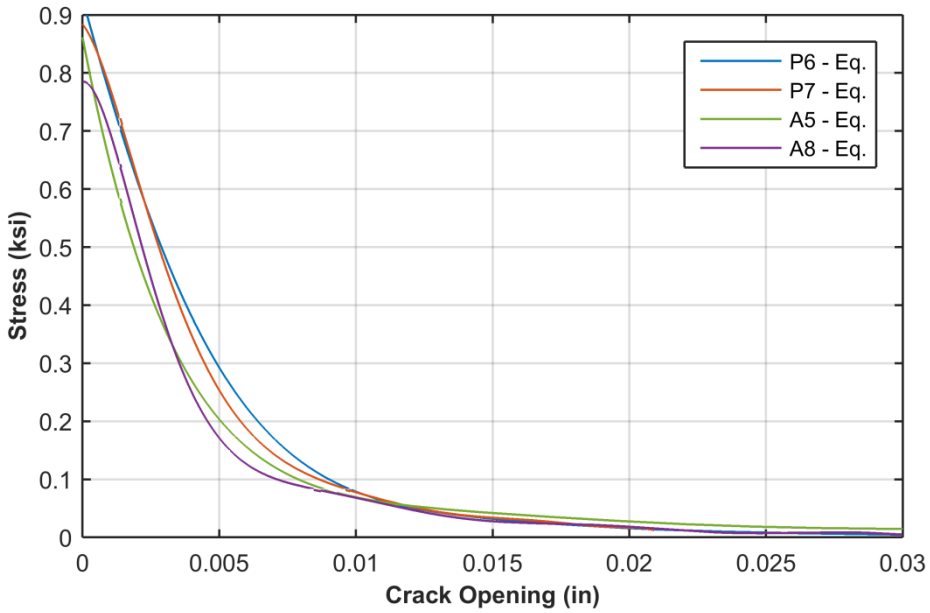

(b)

Figure D.2: *Stress-Crack Opening Curves for UHPC Tests P6, P7, A5, and A8 using (a) Experimental data, (b) Curve fitting equations*

REFERENCES

[1] S. Kumar and S. V Barai. *Concrete Fracture Models and Applications*. Springer, 2011.

[2] J.G.M. van Mier. *Concrete Fracture: A Multiscale Approach*. CRC Press, 2012.

[3] T.W. Aure and A.M. Ioannides. Simulation of crack propagation in concrete beams with cohesive elements in abaqus. *Journal of the Transportation Research Board*, 2(2154):12-21, 2010.

[4] S.V. Chaudhari and M.A. Chakrabarti. Modeling of concrete for nonlinear analysis using finite element code abaqus. *International Journal of Computer Applications*, 44(7):14-18, 2012.

[5] J.G.M. van Mier. *Fracture Processes of Concrete: Assessment of Material Parameters for Fracture Models*. CRC Press, 1996.

[6] K. Farah and Y. Sato. Uniaxial tension behavior of reinforced concrete members strengthened with carbon fiber sheets. *Journal of Composites for Construction*, March/April:215-228, 2011.

[7] E.M. Williams, S.S. Graham, P.A. Reed, and T.S. Rushing. Laboratory characterization of cor-tuf concrete with and without steel fibers. Technical Report ERDC/GSL TR-09-22, Geotechnical and Structures Laboratory U.S. Army Engineer Research and Development Center, Vicksburg, MS, July 2009.

[8] ACI Committee 446 on Fracture Mechanics (Bazant, Z.P. princ. author & chairman). “Fracture mechanics of concrete: concepts, models and determination of material properties (446.R1-91).” Fracture Mechanics of Concrete Structures (Proc. FraMCoS1-Int. Conf. on Fracture Mechanics of Concrete Structures, Breckenridge, Colorado, June), ed. by Z.P. Bazant, Elsevier Applied Science, London, 1-140 (reprinting of S25), 1992 (Reapproved 1999).

[9] K. Otsuka, H. Date, and T. Kurita. Fracture Process Zone in Concrete Tension Specimens by X-ray and AE Techniques. In *Proceedings FRAMCOS-3, Fracture Mechanics of Concrete Structures*, pages 3-16, AEDIFICATIO Publishers, D-79104 Freiburg, Germany, 1998.

[10] V.C. Li, C. Chan, and C.K.Y Leung. Experimental determination of tension softening relations for cementitious composites. *Cement and Concrete Research*, 17(3):441-452, 1987.

[11] D.S. Dugdale. Yielding of Steel Sheets Containing Slits. *Journal of Mechanics and Physics of Solids*, 8(2): 100-104, 1960.

[12] A. Hillerborg, M. Modeer, and P.E. Petersson. Analysis of Crack Formation and Crack Growth in Concrete by means of Fracture Mechanics and Finite Elements. *Cement and Concrete Research*, 6(6):773-782, 1976.

[13] B.L. Karihaloo, *Fracture Mechanics and Structural Concrete*, Longman Publishing Group, 1995.

[14] H.H. Bache. Fracture mechanics in design of concrete and concrete structures, *In G-23*, pages 577-586, 1986.

[15] A. Hillerborg. Analysis of one single crack, *In G-18*, pages 223-249, 1983.

[16] Q. Li and F. Ansari. High-strength concrete in uniaxial tension. *ACI Materials Journals*, 97(1):49-55, 2000.

[17] E. Bruhwiler, J.J. Broz, and V.E. Saouma. Fracture Model Evaluation of Dam Concrete. *Journal of Materials in Civil Engineering*, 3(4): 235-251, 1991.

[18] P. Petersson. *Crack growth and development of fracture zones in plain concrete and similar materials*. PhD thesis, Lund University, 1981.

[19] E.M.R. Fairbairn and F.J. Ulm. A Tribute to Fernando L.L.B. Carneiro (1913-2001) Engineer and Scientist who invented the Brazilian Test. *Materials and Structures*, 35:195-196, 2002.

[20] J.K. Wight and J.G. MacGregor, *Reinforced Concrete Mechanics & Design 6E*, Person, 2012.

[21] ASTM Standard C496, 1962 (2011), Standard Test Method for Splitting Tensile Strength of Cylindrical Concrete Specimens. *ASTM International*, West Conshohocken, PA, 2011, DOI: 10.1520/C0496_C0496M-11, www.astm.org.

[22] A. Hillerborg. Concrete Fracture Energy Tests Performed by 9 Laboratories According to a Draft Rilem Recommendation. Technical Report TVBM-3015, Division of Building Materials Lund Institute of Technology, Lund, Sweden, 1983. Report to Rilem TC50-FMC.

[23] A. Hillerborg. The theoretical basis of a method to determine the fracture energy G_F of concrete. *Materials and Structures*, 18(106):291-296, 1985.

[24] M. Elices, G.V. Guinea, and J. Planas. Measurement of the fracture energy using three-point bend tests: Part 3 – Influence of cutting the P-δ tail. *Materials and Structures,* 25(6): 327-334, 1992.

[25] Z. Zhao, J. Zhang, H. Zhou, S.P. Shah, and Z. Zhao. Two methods for determining softening relationships of dam concrete and wet-screened concrete. *Advances in Structural Engineering*, 15(7):1125-1138, 2012.

[26] RILEM TC 89-FMT Fracture Mechanics of Concrete – Test Methods, "Size Effect Method for Determining Fracture Energy and Process Zone Size of Concrete," *Materials and Structures*, 23: 461-465, 1985.

[27] H.M. Abdalla and B.L. Karihaloo. A method for constructing the bilinear tension softening diagram of concrete corresponding to its true fracture energy. *Magazine of Concrete Research*, 56(10):597-604, 2004.

[28] G.V. Guinea, J. Planas, and M. Elices. Measurement of the fracture energy using three-point bend tests: Part 1 – Influence of experimental procedures. *Materials and Structures,* 25(4): 212-218, 1992.

[29] J. Martin, J. Stanton, N. Mitra, and L.N. Lowes. Experimental Testing to Determine Concrete Fracture Energy Using Simple Laboratory Test Setup. *ACI Materials Journals*, 104(6):575-584, 2007.

[30] R.K.L. Su, H.H.N. Chen, and A.K.H. Kwan. Incremental displacement collocation method for the evaluation of tension softening curve of mortar. *Engineering Fracture Mechanics,* 88: 49-62, 2012.

[31] H.H. Chen and R.K.L. Su. Tension softening curves of plain concrete. *Construction and Building Materials*, 44:440-451, 2013.

[32] ASTM Standard C78, 1930 (2010e1), Standard Test Method for Flexural Strength of Concrete (Using Beam With Third-Point Loading). *ASTM International*, West Conshohocken, PA, 2010, DOI: 10.1520/C0078_C0078M-10E01, www.astm.org.

[33] ASTM Standard C1609, 2005 (2012), Standard Test Method for Flexural Performance of Fiber-Reinforced Concrete (Using Beam With Third-Point Loading). *ASTM International*, West Conshohocken, PA, 2012, DOI: 10.1520/C1609_C1609M-12, www.astm.org.

[34] D.A. Hordijk. *Local approach to fatigue of concrete*. PhD thesis, Delft University of Technology, 1991.

[35] ASTM Standard E399, 1970 (2012e3), Standard Test Method for Linear-Elastic Plane-Strain Fracture Toughness K_{Ic} of Metallic Materials. *ASTM International*, West Conshohocken, PA, 2011, DOI: 10.1520/E0399-12E03, www.astm.org.

[36] H. Schorn and T. Berger-Bocker. Test method for determining process zone position and fracture energy of concrete. *Experimental Techniques*, June:29-33, 1989.

[37] R. Gettu, B. Mobasher, S. Carmona, and D.C. Jansen. Testing of Concrete Under Closed-Loop Control. *Advanced Cement Based Material,* 3(2): 54-71, 1996.

[38] S. Okubo, K. Fukui, and Y. Nishimatsu. Control performance of servo-controlled testing machines in compression and creep tests. *International Journal of Rock Mech. Min Sci. and Geomech.*, 30(3):247-255, 1993.

[39] W.R. Wawersik and C. Fairhurst. A study of brittle rock fracture in laboratory compression experiments. *International Journal of Rock Mech. Min Sci.*, 7:561-575, 1970.

[40] F.P. Zhou. Influences of notch size, eccentricity and rotational stiffness on fracture properties determined in tensile tests. In F.H. Wittmann, editor, *Proceedings FRAMCOS-2, Fracture Mechanics of Concrete Structures*, pages 65-73, AEDIFICATIO Publishers, D-79104 Freiburg, Germany, 1995.

[41] H. Akita, H. Koide, M. Tomon, and S.M. Han. Three misunderstandings in uniaxial tension test of concrete. In *Proceedings of the 5th ACI International Conference. Innovations in Design with Emphasis on Seismic, Wind, and Environmental Loading; Quality Control and Innovations in Materials/Hot-Weather Concreting*, pages 405-414, Cancun, Mexico, 2002.

[42] J.G.M. van Mier and M.R.A van Vliet. Uniaxial tension test for the determination of fracture parameters of concrete: state of the art. *Engineering Fracture Mechanics*, 69:235-247, 2002.

[43] H.A.W Cornelissen, D.A. Hordijk, and H.W. Reinhardt. Experimental determination of crack softening characteristics of normalweight concrete. *Heron*, 31(2):45-56, 1986.

[44] H. Akita, H. Koide, M. Tomon, and D. Sohn. A practical method for uniaxial tension test of concrete. *Materials and Structures*, 36:365-371, 2003.

[45] S. Okubo and K. Fukui. Complete stress-strain curves for various rock types in uniaxial tension. *International Journal of Rock Mech. Min Sci. and Geomech.*, 33(6):549-556, 1996.

[46] Z. Li, S.M. Kulkarni, and S.P. Shah. New test method for obtaining softening response of unnotched concrete specimen under uniaxial tension. *Experimental Mechanics*, September:181-188, 1993.

[47] V. Mechtcherine, H. Garrecht, and H.K. Hilsdorf. Effect of temperature and loading rate on fracture behavior of concrete subjected to uniaxial tension. In F.H. Wittmann, editor, *Proceedings FRAMCOS-2, Fracture Mechanics of Concrete Structures*, pages 719-728, AEDIFICATIO Publishers, D-79104 Freiburg, Germany, 1995.

[48] J.F. Labuz, S.P. Shah, and C.H. Dowding. Experimental analysis of crack propagation in granite. *International Journal of Rock Mech. Min Sci. and Geomech.*, 22(2):85-98, 1985.

[49] J. Ozbolt and A. Sharma. Numerical simulation of dynamic fracture through uniaxial tension and L-specimen. *Engineering Fracture Mechanics*, 85:88-102, 2012.

[50] H.W. Reinhardt, H.A.W. Cornelissen, and D.A. Hordijk. Tensile tests and failure analysis of concrete. *Journal of Structural Engineering*, 112(11):2462-2477, 1986.

[51] J.G.M. van Mier, E. Schlangen, and A. Vervuurt. Tensile cracking in concrete and sandstone: Part 2 - effect of boundary rotations. *Materials and Structures*, 29:87-96, 1996.

[52] J.G.M. van Mier and A. Vervuurt. Micromechanical analysis and experimental verification of boundary rotation effects in uniaxial tension tests on concrete. In G. Baker and B.L. Karihaloo, editors, *Proceedings of The International Union of Theoretical and Applied Mechanics (IUTAM) Symposium on fracture of Brittle, Disordered Materials: Concrete, Rock and Ceramics*, pages 406-420. E and FN Spon, 1993.

[53] A. Vervuurt, E. Schlangen, and J.G.M. van Mier. Tensile cracking in concrete and sandstone: Part 1 – basic instruments. *Materials and Structures*, 29:9-18, 1996.

[54] J.G.M. van Mier and M.B. Nooru-Mohamed. Geometrical and structural aspects of concrete fracture. *Engineering Fracture Mechanics*, 35(4/5):617-628, 1990.

[55] A. Carpinteri and S. Invernizzi. Fractal characterization of concrete damage during the strain-softening regime. In *Atti del XV Convegno Nazionale del Gruppo Italiano Frattura, IGF2000,* Bari, pages 407-414, 2000.

[56] A. Carpinteri and F. Maradei. Three-jack Solution to Obtain a Truly Stable and Symmetric Tensile Concrete Test. *Experimental Mechanics*, March:19-23, 1995.

[57] W. Zheng, A.K.H. Kwan, and P.K.K. Lee. Direct tension test of concrete. *ACI Materials Journals*, 98(1):63-71, 2001.

[58] H. Akita, H. Koide, and M. Tomon. Uniaxial tensile test of unnotched specimens under correcting flexure. In *Proceedings FRAMCOS-3, Fracture Mechanics of Concrete Structures*, pages 367-376, AEDIFICATIO Publishers, D-79104 Freiburg, Germany, 1998.

[59] Materials Engineering and USBR Research Lab. Procedure for direct tensile strength, static modulus of elasticity, and poisson's ratio of cylindrical concrete specimens in tension, usbr 4914-92. In *Concrete Manual Part 2*, pages 726-731. U.S. Department of the Interior Bureau of Reclamation, 1992.

[60] M.R.A van Vliet and J.G.M. van Mier. Experimental investigation of size effect in concrete and sandstone under uniaxial tension. *Engineering Fracture Mechanics*, 65:165-188, 2000.

[61] M.R.A van Vliet and J.G.M. van Mier. Effect of strain gradients on the size effect of concrete in uniaxial tension. *International Journal of Fracture*, 95:195-219, 1999.

[62] M. Vorechovsky and V. Sadilek. Computational modeling of size effects in concrete specimens under uniaxial tension. *International Journal of Fracture*, 154:27-49, 2008.

[63] L. Elfgren. *Fracture Mechanics of Concrete Structures*. Chapman & Hall/E&FN Spon, London/New York, Ed. 1989.

[64] J.G.M. van Mier. Fracture mechanics of concrete: Will applications start to emerge? *HERON,* 40(2):147, 1995.

[65] J.A.O. Barros, J.A. Figueiras, and C.V.D. Veen. Tensile behavior of glass fibre reinforced concrete, In J.F. Silva Gomes et al., editors, *Recent Advances in Experimental Mechanics,* pages 1073-1080, Lisbon, Portugal, 2, 1994.

[66] Y. Wang, V.C. Li, and S. Backer. Experimental Determination of Tensile Behavior of Fiber Reinforced Concrete. *ACI Materials Journals*, 87(5):461-468, 1990.

[67] Y. Wang, V.C. Li, and S. Backer. Tensile failure mechanisms in synthetic fibre-reinforced mortar. *Journal of Materials Science,* 26(24):6565-6575, 1991.

[68] H. Kupfer, H.K. Hilsdorf, and H. Rusch. Behavior of Concrete under Biaxial Stresses, *ACI Journal Proceedings*, 66(8): 656-666, 1969.

[69] H. Kupfer. Behavior of Concrete under Multiaxial Short Term Loading, with Emphasis on Biaxial Loading, In *Deutscher Ausschuss fur* Stahlbeton, Vol. 254, Berlin, Germany, 1973.

[70] K.H. Gerstle, D.L. Linse, P. Bertacchi, M.D. Kotosovos, H.-Y Ko, J.B. Newman, P. Rossi, G. Schickert, M.A. Taylor, L.A. Traina, R.M. Zimmerman, and R. Bellotti. Strength of Concrete under Multiaxial Stress States. In *Proceedings Douglas McHenry Int'l Symposium on 'Concrete and Concrete Structures'*, pages 103-132, ACI SP 55, American Concrete Institute, Detroit, MI, 1978.

[71] J.G.M. van Mier. *Strain-softening of concrete under multiaxial loading conditions*. PHD thesis, Eindhoven University of Technology, Netherlands, 1984.

[72] F.E. Richart, A. Brandtzaeg, and R.L. Brown. A Study of the Failure of Concrete under Combined Compressive Stresses. *University of Illinois Engineering Experiment Station,* Bulletin No. 185, 1928.

[73] F.E. Richart, A. Brandtzaeg, and R.L. Brown. The failure of plain and spirally reinforced concrete in compression. *University of Illinois Engineering Experiment Station*, Bulletin No. 190, 1929.

[74] ACI Committee 440, "Guide for the Design and Construction of Externally Bonded FRP Systems for Strengthening Concrete Structures (ACI 440.2R-08)," American Concrete Institute, Farmington Hills, MI, 2008.

[75] ACI Committee 549, “Guide to Design and Construction of Externally Bonded Fabric-Reinforced Cementitious Matrix (FRCM) Systems for Repair and Strengthening Concrete and Masonry Structures (ACI 549.4R-13),” American Concrete Institute, Farmington Hills, MI, 2013.

[76] D.C. Candappa, J.G. Sanjayan, and S. Setunge. Complete triaxial stress-strain curves of high-strength concrete. *Journal of Materials in Civil Engineering*, 13(3):209-215, 2001.

[77] J.H.M. Visser and J.G.M. van Mier. Tensile Hydraulic Fracture of Concrete and Rock. In F.H. Wittmann, editor, *Proceedings FRAMCOS-2*, *Fracture Mechanics of Concrete Structures,* pages 261-270, AEDIFICATIO Publishers, D-79104 Freiburg, Germany, 1995.

[78] J.H.M. Visser and J.G.M. van Mier. Hydraulic fracturing in the tensile regime, In H.J. Siriwardane and M.M. Zaman, editors, *Computer Methods and Advances in Geomechanics 8th International Conference*, pages 1647-1652, Balkema, Rotterdam, 1994.

[79] J.H.M. Visser and J.G.M. van Mier. The Mechanical Behaviour of Hydraulic Fractured, Possibly Saturated Materials. In *Proceedings FRAMCOS-3, Fracture Mechanics of Concrete Structures*, pages 269-280, AEDIFICATIO Publishers, D-79104 Freiburg, Germany, 1998.

[80] T. Gabet, Y. Malecot, and L. Daudeville. Triaxial behavior of concrete under high stresses: Influence of the loading path on compaction and limit states. *Cement and Concrete Research*, 38:403-412, 2008.

[81] V.C. Li, M. Stults, and R. Ranade. Development of high strength high ductility concrete. Technical Report UM/ERDC Annual Report, Department of Civil and Environmental Engineering University of Michigan, Ann Arbor, MI, December 2009.

[82] M.J. Roth, T.S. Rushing, O.G. Flores, D.K. Sham, and J.W. Stevens. Laboratory investigation of the characterization of cor-tuf flexural and splitting tensile properties. Technical Report ERDC/GSL TR-10-46, Geotechnical and Structures Laboratory U.S. Army Engineer Research and Development Center, Vicksburg, MS, October 2010.

[83] B. A. Graybeal and F. Baby. Development of Direct Tension Test Method for Ultra-High-Performance Fiber-Reinforced Concrete. *ACI Materials Journal,* 110(2):177-186, 2013.

[84] V.Y. Garas. *Multi-Scale Investigation of Tensile Creep of Ultra-High Perfomance Concrete for Bridge Applications.* PhD thesis, Georgia Institute of Technology, 2009.

[85] V.Y. Garas, L.F. Kahn, and K.E. Kurtis. Tensile Creep Test of Fiber-Reinforced Ultra-High Performance Concrete. *Journal of Testing and Evaluation*, 38(6):1-9, American Society of Testing and Materials (www.astm.org) paper JTE102666, 2010.

[86] V.Y. Garas, L.F. Kahn, and K.E. Kurtis. Preliminary investigation of the effect of steel fibers on the tensile creep and shrinkage of ultra-high performance concrete. In Tanabe et al., editors, *Proceedings 8th International Conference on Creep, Shrinkage and Durability Mechanics of Concrete and Concrete Structures*, Ise-shima, Japan, pages 741-744, CRC Press, Taylor & Francis Group, London, 2009.

[87] V. Garas, C.K. Crane, L.F. Kahn, and K.E. Kurtis. Ultra-High Performance Concrete for Precast Prestressed Bridge Girders. Final Report No. 09-8 for Office of Materials and Research Georgia Department of Transportation, School of Civil and Environmental Engineering Georgia Institute of Technology, Atlanta, GA, June 2009.

[88] V.Y. Garas, L.F. Kahn, and K.E. Kurtis. Short-term tensile creep and shrinkage of ultra-high performance concrete. *Cement & Concrete Composites*, 31:147-152, 2009.

[89] B. Bissonnette and M. Pigeon. Tensile Creep at Early Ages of Ordinary, Silica Fume and Fiber Reinforced Concretes. *Cement and Concrete Research,* 25(5):1075-1085, 1995.

[90] B. Bissonnette, M. Pigeon, and A.M. Vaysburd. Tensile Creep of Concrete: Study of Its Sensitivity to Basic Parameters. *ACI Materials Journal,* 104(4):360-368, 2007.

[91] 3M, *Scotch-Weld Epoxy Adhesive DP-460, Off-White* [Material Safety Data Sheet], St. Paul, MN, January 4, 2012.

[92] 3M, *Scotch-Weld Epoxy Adhesives DP-460 Off-White, DP460 NS* [Technical Data Sheet], St. Paul, MN, March, 2004.

[93] B. Mobasher and S.P. Shah. Test Parameters for Evaluating Toughness of Glass-Fiber Reinforced Concrete Panels. *ACI Materials Journal,* 86(5):448-458, 1989.

[94] MTS Systems Corp., *Series 247 Actuators Product Information*, Manual Part Number 011-560-000 D, Eden Prairie, MN, 2008.

[95] MTS Systems Corp., *MTS 810 & 858 Material Testing Systems*, Number 100-154-137, Eden Prairie, MN, 2006.

[96] MTS Systems Corp., *Series 293.1X Hydraulic Service Manifolds Product Information*, Manual Part Number 015-081-000 D, Eden Prairie, MN, 2001.

[97] Parker Hannifin Corp. Hydraulic Controls Division, *Operation Manual Series DFplus Design > 20 Proportional Directional Control Valve*, Bulletin HY11-5715-658/UK, Kaarst, Germany, 2011.

[98] ENERPAC, *RRH-Series, Double Acting Hollow Plunger Cylinders*. Internet: http://www.enerpac.com/en-us/, 2015 [Feb. 20, 2015].